TUM School of Life Sciences
Technische Universität München

A cellular model for the prodromal phase of sporadic Parkinson's disease

Sebastian Schmidt

Vollständiger Abdruck der von der TUM School of Life Sciences der Technischen Universität München zur Erlangung des akademischen Grades eines

Doktors der Naturwissenschaften (Dr. rer. nat.)

genehmigten Dissertation.

Vorsitzende:

Prof. Angelika Schnieke, Ph.D.

Prüfende der Dissertation:

1. Prof. Dr. Wolfgang Wurst
2. Prof. Dr. Ilona Grunwald Kadow

Die Dissertation wurde am 17.05.2021 bei der Technischen Universität München eingereicht und durch die TUM School of Life Sciences am 30.08.2021 angenommen.

Abstract

Parkinson's disease (PD) is a progressive neurodegenerative disorder characterized in advanced stages by motor disabilities. The pathological hallmark of PD is a slow, but progressive and irreversible loss of dopaminergic neurons specifically in the substantia nigra pars compacta. About 15 % of PD are associated with heritable familial mutations whereas the vast majority is sporadic with the contribution of genetic and environmental risk factors. Analysis of model systems carrying inherited PD-associated mutations have been harnessed to unravel molecular and cellular mechanisms contributing to disease etiology such as mitochondrial impairment. Still, the relevance of these mechanisms for sporadic PD etiology and in translational studies was diminished by the lack of suitable human models.

To establish a model system for sporadic PD, the effect of long-term *in vitro* cultivation on PD-related phenotypes like mitochondrial dysfunction should be investigated. Fibroblasts from sporadic PD patients and age- and sex-matched control individuals were reprogrammed into human induced pluripotent stem cells (hiPSCs) and cultivated for up to 70 passages. hiPSCs were then differentiated towards dopaminergic neurons and screened for mitochondrial function and known aging marker. Interestingly, exclusively high-passage neural cells derived from sporadic PD hiPSCs exhibited a mitochondrial dysfunction including a complex I deficiency comparable to postmortem brain tissue. Notably, mitochondrial dysfunction is accompanied by aging-associated genomic and epigenomic alterations such as telomere attrition. Thus, long-term *in vitro* cultivation induced a premature aging phenotype in neural cells which recapitulates known PD-associated alterations. The cellular model system described in this thesis is a suitable model to study the etiology of sporadic PD. It is up-to-date the first cellular model that recapitulates PD phenotypes associated with mitochondrial function. Almost every stage of the prodromal phase is recapitulated, from a no symptoms phase to severe mitochondrial alterations e.g. complex I deficiency. Thus, this model system can provide unique insights into cellular processes and molecular mechanisms contributing to sporadic PD etiology.

To unravel these mechanisms, an unbiased molecular characterization of high passage neuronal precursor cells was performed. The new technology of multiplexed single-cell RNA sequencing of pooled cells from different individuals allowed a detailed analysis of differentially expressed genes without confounding technical batch effects. A strong disease-associated alteration appeared in pathways associated with primary cilia (PC), which was also observed in transcriptome studies of postmortem PD patients. This finding was validated by demonstrating a disease-specific impairment in PC-associated signaling and alterations in PC morphology. Notably, neuronal precursor cells and neurons, but not astrocytes, derived from sporadic PD patients exhibited shorter PC. In addition, shortened PC were observed in striatal cholinergic neurons of *Pink1* knock-out mice as a model system for familial PD. Thus, altered PC signaling and morphology emerge as a convergence point in the etiology of sporadic and familial PD.

Based on the data presented in this thesis, it can be hypothesized that sporadic PD etiology follows a predefined process that is at least in our cellular model independent of environmental stimuli and intensified or accelerated in the midbrain dopaminergic lineage. The observed alterations might create a positive feedback loop and a downward spiral of disease progression due to the reduced efficiency of almost every cellular pathway and compensatory capacity.

Zusammenfassung

Die Parkinson-Krankheit (PD) ist eine fortschreitende neurodegenerative Störung, die durch motorische Beeinträchtigungen geprägt ist, welche hauptsächlich durch einen langsamen, aber fortschreitenden und irreversiblen Verlust dopaminerger Neuronen in der Substantia nigra pars compacta verursacht werden. Etwa 15 % der PD sind mit vererbbaren familiären Mutationen assoziiert, während die überwiegende Mehrheit bedingt durch genetische und Umwelt-Risikofaktoren sporadisch ist. Modellsysteme mit PD-assoziierten Mutationen wurden bisher genutzt, um krankheitsrelevante molekulare Mechanismen wie mitochondriale Dysfunktion aufzudecken. Die Relevanz dieser Mechanismen für die sporadische PD und in translationalen Studien ist jedoch unbekannt, dank des Fehlens geeigneter menschlicher Modelle.
Um ein Modellsystem für die sporadische PD zu etablieren, sollte der Einfluss einer langen *In-vitro*-Kultivierung auf PD-assoziierte Phänotypen wie mitochondriale Dysfunktion untersucht werden. Fibroblasten von sporadischen PD-Patienten und Kontrollpersonen gleichen Alters und Geschlechts wurden in induzierte pluripotente Stammzellen (hiPSCs) reprogrammiert und für bis zu 70 Passagen kultiviert. hiPSCs wurden zu dopaminergen Neuronen differenziert und auf Mitochondrien Funktion hin untersucht. Interessanterweise sind ausschließlich neuronale Zellen, die von sporadischen PD-hiPSCs mit hoher Passage differenziert wurden, von einer mitochondrialen Dysfunktion betroffen, einschließlich einer mit postmortem Hirngewebe vergleichbaren Komplex-I Dysfunktion. Diese neuronalen Zellen sind auch von altersbedingten genomischen und epigenomischen Veränderungen wie einer Telomerverkürzung betroffen. Eine lange *In-vitro*-Kultivierung induziert somit einen Alterungsphänotyp, der bekannte PD-assoziierte Veränderungen rekapituliert. Das in dieser Arbeit beschriebene zelluläre Modellsystem ist daher geeignet zur Untersuchung der Ätiologie der sporadischen PD. Fast jedes Stadium der Prodromalphase ist vertreten, von einer Phase ohne Symptome bis zu schweren mitochondrialen Veränderungen, z.B. einer Komplex-I Dysfunktion. Somit kann dieses Modellsystem einzigartige Einblicke in zelluläre Prozesse und molekulare Mechanismen liefern, die zur Entwicklung sporadischer PD beitragen.
Um diese Mechanismen aufzudecken, wurden neuronale Vorläuferzellen mit hoher Passage unvoreingenommen weiter charakterisiert. Die neue Technologie der multiplexierten Einzelzell-RNA-Sequenzierung von gepoolten Zellen verschiedener Individuen ermöglichte eine detaillierte Analyse differentiell exprimierter Gene unbeeinträchtigt von technischen Batch-Effekten. Eine starke krankheitsassoziierte Veränderung konnte in primären Zilien (PC) beobachtet werden, welche ähnlich ist zu Transkriptomstudien an postmortalen PD-Patienten. Dies wurde durch Beeinträchtigung der PC-vermittelten Signalübertragung und durch Veränderungen der PC-Morphologie bestätigt. Bemerkenswerterweise hatten neuronale Vorläuferzellen und Neuronen, jedoch keine Astrozyten, von sporadischen PD-Patienten kürzere PC. Zusätzlich wurden verkürzte PC in striatalen cholinergen Neuronen von *Pink1*-Knockout-Mäusen als Modell für familiäre PD beobachtet. PC-Dysfunktion scheint somit ein Konvergenzpunkt in der Ätiologie der sporadischen und familiären PD zu sein.
Basierend auf diesen Daten kann angenommen werden, dass die sporadische PD einem vordefinierten Prozess folgt, der zumindest in unserem Zellmodell unabhängig von Umwelteinflüssen ist und in der dopaminergen Linie des Mittelhirns verstärkt oder beschleunigt wird. Die beobachteten Veränderungen können aufgrund einer verringerten Effizienz fast aller Kompensationskapazitäten eine positive Rückkopplungsschleife und eine Abwärtsspirale des Krankheitsverlaufs erzeugen.

Contents

1. Introduction

Our generation must overcome great challenges without precedents reaching from climate change to pandemics and population aging in a globalized world. The often neglected aging society is a powerful and transforming demographic force and is one of the most fundamental changes of our time (*1*). As population aging is accompanied by an increase in lifespan, a key question arises: Will aging also be accompanied by a longer period of good health, productivity and social engagement, or will it be marked by disabilities and illness? Age is the main risk factor for diseases of developed countries such as cancer, cardiovascular and neurodegenerative diseases. Unfortunately, for most neurodegenerative diseases, conventional drugs only treat symptoms but do not allow to stop or even slow disease progression. These drugs usually interfere with secondary phenotypes, not the underlying cause. Thus, for developing cures it is essential to understand and learn about disease etiology which, however, remains often elusive. This creates an urgent need for human systems to model the onset and prodromal phase of these complex diseases.

1.1. Parkinson's disease

1.1.1. Epidemiology

The typical motor symptoms of Parkinson's disease (PD) have been known for thousands of years. Already in the ancient Indian medical system a tremor-causing disease named Kampavata has been described and treated methodically (*2, 3*). In western society, these symptoms have been first reported by Galen of Pergamon in 175 AD (*2*). However, it was not until 1690 that the occurrence of all four cardinal motor symptoms of PD has been described in the medical text *Pax Corporis* by Ferenc Pápai Páriz (*2, 4*). Similar observations have been reported by James Parkinson in his famous article *An Essay on the Shaking Palsy* (*5*) in 1817. Around 70 years later, the symptoms were refined and the disease was named Parkinson's disease by the French neurologist Jean-Martin Charcot (*6*). Today, PD is the second most common neurodegenerative disorder after Alzheimer`s disease with an incidence rate of 1-2 % of the population or 5-35 per 100.000 persons per year [reviewed in (*7*)]. Interestingly, the prevalence is higher in the western world compared to Asian or African countries, possibly caused by ethnic and geographic differences such as diet, lifestyle, environment and genetics. Another risk factor is gender, as men are twice as often affected by PD (*8*). However, the greatest risk factor is age (*7, 9*). Before the age of 50, the PD prevalence is quite low, while after the age of 85 the incidence rate increases up to 3-5 % of the population. In our aging society, the amount of PD patients is predicted to double between 2005 and 2030. This underlines the need for global efforts to understand and develop cures for age-related diseases like PD.

1.1.2. Symptoms

PD is a very heterogeneous disorder and symptoms can vary for different people. The most characteristic ones are motor symptoms, which are noticeable from the outside and used by physicians for diagnosis. The three cardinal motor symptoms are slowness or bradykinesia, resting tremor, and stiffness or rigidity. These symptoms are progressive and may be accompanied by further motor dysfunctions such as postural instability and later in disease progression by freezing of gait. Interestingly, motor symptoms are often preceded by non-motor symptoms sometimes referred to as the "invisible" symptoms of PD. These include olfactory dysfunction or neuropsychiatric alterations such as depression, constipation, pain, genitourinary problems, and REM-sleep-behavior-disorder (RBD) [reviewed in (*10*–*12*)]. The pre-motor or prodromal phase of PD can start up to 20 years before motor symptoms occur and a diagnosis can be finalized (*13*). Although symptoms vary between patients, studies showed that up to 90 % of patients suffered from non-motor symptoms. In addition, it was shown that mortality rates of PD patients double after 10 years of disease progression, hence strengthening the need for early diagnosis and treatment (*7*).

1.1.3. Etiology

Responsible for PD etiology are both genetic as well as acquired factors. According to these factors, PD can be subdivided into different forms namely toxin or drug-induced, familial inherited (fPD), and sporadic PD (sPD) (*14*). The most common form is sPD, but about 10-15 % of patients can nowadays be defined as familial cases with a positive family history of PD.

1.1.3.1. Familial Parkinson's disease

Over the last 2 decades, important progress has been made in discovering monogenic causes and genetic risk factors for PD. Monogenic PD is mostly inherited in an autosomal dominant or autosomal recessive manner (*15*). The age of disease onset can be useful in distinguishing autosomal dominant (typically age >50 years) from autosomal recessive PD (typically age <40 years) (*16*). Depending on the gene mutations the etiology and pathogenesis of fPD present itself highly variable. Currently identified genes associated with juvenile-onset PD (onset age generally <20 years), early-onset adult PD (age 20-50 years), and late-onset adult PD (age >50 years) and their phenotypic characteristics are listed in ***Table 1*** [reviewed in *(17, 18)*]. In addition, like symptoms, the age of onset can differ between individuals with the same genetic variant.

The most common causes for fPD and autosomal dominant PD are mutations in *GBA* and *LRRK2* with a frequency of 3-7 % and 1-2 % of adult-onset PD, respectively. However, the first mutations associated with autosomal-dominant PD were described for *SNCA*, which is probably also the most intensively studied PD-associated gene. Mutations in *PRKN* are the most common known cause of early-onset PD, accounting for approximately 50 % of familial cases with a mode of autosomal recessive inheritance (*19*).

PINK1 is, after *PRKN*, the second most common cause for autosomal recessive familial PD (*20*). Patients carrying *PINK1* mutations develop clinical phenotypes that resemble those suffering from sPD, including

Table 1 | Monogenic causes of PD. AD: autosomal dominant; AR: autosomal recessive. Table modified from (*17, 18*).

Gene	Inheritance	% of adult PD	Disease onset	Comments
SNCA (PARK1/4)	AD	Rare	early-onset	Onset age may be <50 yrs Cognitive & psychiatric features more likely Aggregates in a misfolded state – Lewy bodies/neurites
PRKN (PARK2)	AR	1 % (4.6-10.5 % of early-onset PD)	early-onset	Slow progression Mild non-motor manifestations
PARK3	AD	Rare	late-onset	
UCHL1 (PARK5)	AD	Rare	early-onset/ late-onset	
PINK1 (PARK6)	AR	Rare (3.7 % of early-onset PD)	early-onset	Phenotype similar to PRKN Non-motor manifestations more common
PARK7 (DJ1)	AR	Rare	early-onset	Phenotype similar to PRKN ID &/or seizures occasionally
LRRK2 (PARK8)	AD	1-2 %	late-onset	Classic manifestations with less non-motor involvement Variable penetrance dependent on age, variant & ethnicity
ATP13A2 (PARK9)	AR	Rare	juvenile-onset	Wide variability; Triad of spasticity, supranuclear gaze palsy & dementia Also referred to as Kufor-Rakeb syndrome or juvenile-onset atypical PD
PARK10	Risk factor	Rare	late-onset	
PARK11	AD	Rare	late-onset	
PARK12	Risk factor	Rare	late-onset	
HTRA2 (PARK13)	AD or risk factor	Rare	early-onset	
PLA2G6 (PARK14)	AR	Rare	early-onset	
FBXO7 (PARK15)	AR	Rare	juvenile-onset	Juvenile or early-onset, rapidly progressive, may have corticospinal signs Early-onset parkinsonism with bradykinesia in some families
PARK16	Risk factor	Rare	early-onset	
VPS35 (PARK17)	AD	Rare	late-onset	Classic PD with tremor Fewer non-motor manifestations
EIF4G1 (PARK18)	AD	Rare	late-onset	
DNAJC6 (PARK19)	AR	Rare	juvenile-onset	2 subtypes identified: • Slowly progressing, levodopa-responsive parkinsonism; onset in 3rd-4th decade • Rare juvenile-onset with rapid disease progression; atypical features of hyperreflexia, seizures & intellectual disability
SYNJ1 (PARK20)	AR	Rare	juvenile-onset	Variants in the SAC1-like domain cause juvenile-onset dystonia with dyskinesia 1 family with early-onset PD reported
TMEM230 (PARK21)	AD	Rare	late-onset	
CHCHD2 (PARK22)	AD	Rare	late-onset	
VPS13C (PARK23)	AR	Rare	early-onset	Early-onset PD with very rapid progression; truncating variants cause severe disease
GBA	AD	3-7 %	late-onset	Onset age may be <50 yrs; Associated with dementia and Lewy bodies Higher likelihood of cognitive impairment, atypical motor findings & severe progression

slow disease progression (*21, 22*). *PINK1* is ubiquitously expressed throughout the body and encodes a protein with an N-terminal mitochondrial targeting sequence, a transmembrane domain, a highly conserved serine-threonine kinase domain and a C-terminal domain. Up to now, more than 50 mutations in *PINK1* are known, which are preferably localized in the kinase domain and result in a loss of function (*23*). Nevertheless, the pathophysiology of many *PINK1* mutations is still unknown.

PINK1 is known amongst others for regulating proper mitophagy, but also mitochondrial transport (*24, 25*). In cell culture, it has been shown that PINK1 can initiate mitophagy of damaged mitochondria to prevent cell death. During this process, PINK1 accumulates on the outer mitochondrial membrane (OMM) of mitochondria with a disrupted mitochondrial membrane potential (MMP) to phosphorylate ubiquitin that is bound to mitochondrial proteins. Consequently, PRKN with an affinity to phosphorylated ubiquitin is recruited to dysfunctional mitochondria and starts to poly-ubiquitinate proteins in the OMM. A positive feedback loop is established which ultimately results in the recruitment of the autophagy machinery to damaged mitochondria (*26–28*). Furthermore, Rab GTPases were identified as other downstream target proteins of the PINK1 kinase (*29*).

In addition to the known monogenic causes of PD, additional genes and loci have been identified in genome-wide association studies (GWAS) (*30*). These genetic modifiers may influence the risk of developing PD or clinical aspects such as disease onset and progression. Up to now, 90 independent risk signals across 78 genomic regions were identified and may explain 16-36 % of the heritable risk for developing PD. Interestingly, many of these risk genes were found to be associated with mitochondrial function, metabolism and dynamics (*30*).

The findings that genetic variants can deterministically drive or alter the risk for developing PD, provided the opportunity to use genetically modified organisms as model systems. Animal models have enhanced the understanding of the molecular pathogenesis and helped to develop candidate therapies. They have been harnessed to unravel molecular mechanisms involved in PD such as mitochondrial impairment [further reviewed in chapter 1.3], autophagy, protein aggregation, proteasomal degradation, and lysosomal dysfunction (*20*). Still, the relevance of these mechanisms especially in translational studies was diminished by the lack of suitable human model systems as up to now no animal model fully reassembled the etiology and pathophysiology of PD, especially of sPD. Major limitations such as the use of rare genetic variants for understanding sPD, genomic and developmental differences, and the short lifespan of rodents may contribute to incomplete development of pathological hallmarks (*31*).

1.1.3.2. Sporadic Parkinson's disease

Although progress has been made in investigating the pathogenesis of fPD, the etiology of sporadic PD remains largely elusive. A sporadic disease is defined as a disease that occurs infrequently and irregularly with no known cause, which limits the availability of useful model systems. In most PD cases the cause is thought to be a combination of environmental, probably toxins, and genetic contributions, which makes PD a multifactorial disease (*6*). Recent studies suggested that environmental factors like rural residences, toxins/pesticides as well as certain occupations (farming, mining, or welding) are associated with an increased risk of developing PD (*14*). Since the initial discovery that exposure to the neurotoxin 1-methyl-4-phenyl-1,2,3,6-tetrahydropyridine (MPTP) can cause PD, several other studies identified further PD causing pesticides such as rotenone or paraquat (*32*). MPTP itself is not toxic but can penetrate the blood-

brain barrier and enter brain cells due to its lipophilic character. In astrocytes and serotonergic neurons, which express the enzyme MAO-B, MPTP is oxidized to 1-methyl-4-phenylpyridinium (MPP^+). A substrate that can be transported into dopaminergic neurons (DAns) by DAT, which has a high affinity for the toxic compound. MPP^+ interferes with the mitochondrial complex I of the electron transport chain and causes enhanced production of superoxides and eventually cell death. Interestingly, also rotenone and paraquat interfere with mitochondrial complex I and cause the enhanced formation of superoxides (*32*).
The greatest risk factor for developing PD, however, is aging. The prevalence increases almost exponentially and peaks after 80 years of age (*20*). One theory is, that age-related changes in several cellular processes may increase cell vulnerability so that a further insult e.g. caused by environmental factors leads to cell death during and after the prodromal phase. Age-related changes include the accumulation of mitochondrial DNA (mtDNA) defects, oxidative stress as well as accumulation of neuromelanin [further reviewed in chapters 1.2 and 1.3]. Another theory is, that the pathogenic mechanisms caused by genetic or environmental factors may already start in the prenatal period (*33*). Thus, some patients may be born with fewer than normal DAns and due to the normal age-related neuronal attrition eventually reach the critical threshold of neuronal loss needed for PD onset.
In contrast, also environmental factors associated with a reduced risk of developing PD could be identified. The risk for a cigarette smoker is reduced by ~50 % compared to non-smokers and a dose-dependent effect could be observed. However, it was also shown that PD patients can quit smoking more easily, suggesting a decreased responsiveness to nicotine during the prodromal phase (*20, 34*). Additionally, consumption of coffee or tea reduces the risk for PD by ~60 % in men and to a much lesser extent in women (*35, 36*).
In summary, epidemiological studies demonstrated that environmental factors, as well as lifestyle, have an impact on PD etiology. However, their interactions with genetic variants remain largely elusive and emphasize the need for further investigations.

1.1.4. Pathophysiology

The adult brain contains more than 100 billion neurons, however, only a small number seems to be affected in PD (*37*). The pathological hallmark of PD is a slow, but progressive and irreversible loss of DAns specifically in the substantia nigra pars compacta (SNpc). It has been estimated that an adult brain contains ~400,000 DAns in the substantia nigra (SN) and about 60-80 % are lost before the characteristic motor symptoms begin to emerge (*33, 38*). The SN is a region in the midbrain and a part of the basal ganglia, which are proposed to be a part of four different thalamo-coritco-basal ganglia circuits that are involved in the control of action and goal-directed behavior. They are thought to control limbic, prefrontal-associative, oculomotor, and motor functions by linking the thalamus and basal ganglia to the respective cortical areas (*39*). In PD the degeneration of DAns in the SNpc causes activity changes in the motor cortex circuitry and thus motor disabilities (***Figure 1***) [reviewed in (*7*)]. The dopaminergic innervations to the motor areas of the striatum are reduced with opposing effects on the direct and indirect pathways from the striatum to the globus pallidus internus and the substantia nigra pars reticulata, respectively. Eventually, this causes increased activation of γ-aminobutric acid (GABA)-ergic interneurons which inhibit projections from the thalamus to the motor cortex, resulting in PD-specific motor symptoms. Consequently, balancing striatal dopamine levels by substituting the dopamine precursor L-DOPA is

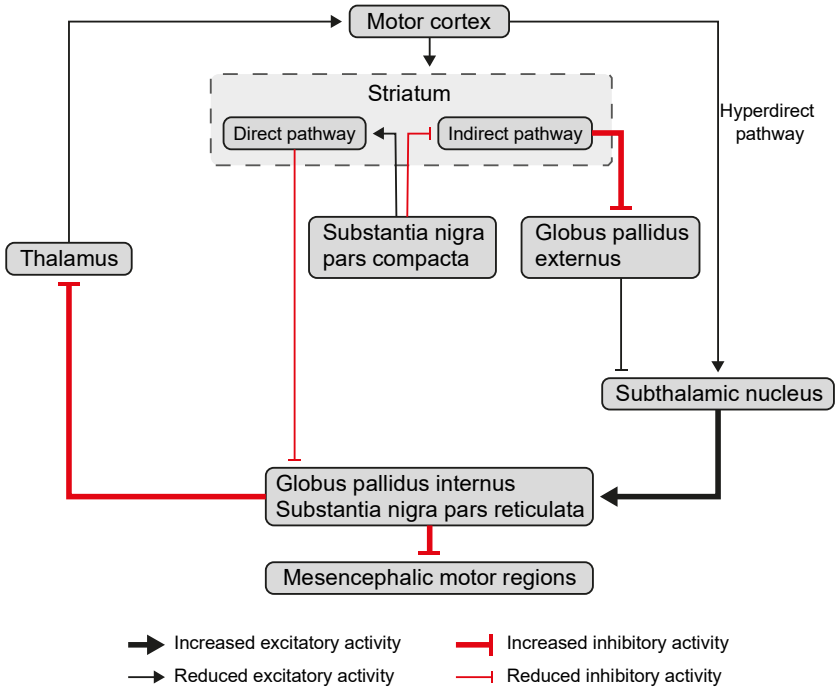

Figure 1 | Activity changes in the motor cortex circuitry. Loss of DAns in the SNpc alters striatal projections to the globus pallidus internus and the substantia nigra pars reticulata via the direct and indirect pathway. Consequently, the activity of the thalamus and motor cortex is strongly reduced which causes the characteristic motor symptoms observed in PD patients. Figure adapted from (*7*).

currently the gold standard to treat most PD-specific motor symptoms. However, alterations in firing rates alone cannot fully explain the pathophysiology of PD. They are thought to be accompanied by abnormal neural synchronization and cortico-subcortical coupling in specific frequency bands (*40*). Additionally, neural loss in PD was also observed in the locus ceruleus, nucleus basalis of Meynert, pedunculopontine nucleus, raphe nucleus, and hypothalamus (*41*).

Another pathological hallmark of PD found in the majority of cases (familial + sporadic) is the development of intracellular inclusions within the cell body (Lewy bodies - LBs) and neuronal processes (Lewy neurites). Protein aggregations have emerged as a common thread of neurodegenerative diseases, which are categorized by the abnormally folded protein that is most abundant in the protein inclusions (*42*). The major component of LBs in PD is SNCA, which becomes insoluble and aggregates in a misfolded state (*43*). In 2003, Braak and colleagues proposed a mechanism for SNCA propagation based on the observations that LB formation seemed to start in the peripheral nervous system and progressively affected the central nervous system (*20, 44*). A theory reinforced by observations of SNCA aggregations in patients receiving embryonic DAn transplants as treatment (*45, 46*). Braak and colleagues suggested categorizing PD in 6 different stages according to LB formation in the brainstem and olfactory bulbs as well as propagation from caudal to rostral within the brain (*44*). Interestingly, the Braak model may explain the clinical course

of PD. Braak stages 1 and 2 seem to correspond with the onset of premotor symptoms, stage 3 corresponds with the characteristic motor symptoms caused by a nigrostriatal dopamine deficiency, and stages 4 – 6 occur with non-motor symptoms that manifest in later stages of PD (*20*). Furthermore, mutated SNCA can also cause a monogenic form of PD.

Although probably not the initial trigger, neuroinflammation is another pathological hallmark of PD. A close link between certain genes, protein aggregations, and neuroinflammation has been suggested, as SNCA aggregations can induce the innate and adaptive immune response (*47*). Inversely, neuroinflammation can also promote SNCA misfolding and aggregation. The innate immune system is the first line of defense against various threats, causing a rapid short-term response (*48*). In the central nervous system, this response is triggered amongst others by microglia and monocytes. The adaptive immune system causes a slow but long-lasting response, which is mediated by T- and B-lymphocytes (*49*). Astrocytes, like microglia, respond to inflammatory stimuli and in an activated state produce more proinflammatory cytokines (*50*). Interestingly, both reactive astrogliosis, as well as microgliosis, was observed within areas of neurodegeneration in PD (*50, 51*). Astrocytes are involved in the clearance of extracellular debris, the release of neurotrophic factors such as GDNF, and nutritional support to neurons. Using specific shuttle systems such as the malate-aspartate and glutamate-glutamine shuttle (*52*). However, whether the balance of these functions is beneficial or harmful to neurons remains largely elusive.

Nevertheless, the question arises why specifically these DAns in the SNpc tend to degenerate in PD, as most previously described pathogenic hallmarks are not restricted to these neurons in general. It seems to be a combination of several circumstances [reviewed in (*41, 53, 54*)]. Firstly, DAns are marked by a high energetic burden. This demand is a result of their anatomical structure with diffuse axonal projections, their dopamine metabolism, and their spontaneous tonic activity. A second factor that makes DAns particularly vulnerable is the unstable nature of the neurotransmitter dopamine itself (*55*). The spontaneous auto-oxidation of dopamine can cause aminochrome formation, a reactive species that triggers superoxide formation and depletion of cellular nicotinamide adenine dinucleotide (NADH) and/or nicotinamide adenine dinucleotide phosphate (NADPH) pools (*56, 57*). To prevent auto-oxidation, cellular dopamine is either stored in vesicles and released into the synaptic cleft upon excitation of DAns or degraded by the neuronal enzyme MAO-A or the glial enzymes MAO-A and MAO-B. However, dopamine degradation by MAO-B produces as by-product H_20_2 which can further elevate oxidative stress levels (*58*). Thus, dopamine metabolism may be crucial for cellular redox homeostasis and could trigger oxidative stress, another pathological hallmark of PD. Furthermore, SNpc DAns are marked by a high content of iron, which can cause hydroxide formation and thus oxidative stress via the Fenton reaction, as well as low levels of antioxidants like glutathione (*59*).

1.2. Hallmarks of aging

The phenomenon of growth, decline, and death that affects most living organisms is known as aging. It is defined as a time-dependent and progressive loss of homeostasis, leading to impaired functions and increased cell vulnerability (*60*). The pathological hallmarks of aging can be grouped into three categories (***Figure 2***) [reviewed in (*61*)]. The primary hallmarks (genomic instability, telomere attrition, epigenetic

Figure 2 | Proposed hallmarks of aging. The primary hallmarks (genomic instability, telomere attrition, epigenetic alterations, loss of proteostasis) are thought to be the initial causes of cellular damage. The antagonistic hallmarks (deregulated nutrient sensing, mitochondrial dysfunction, cellular senescence) are considered to be compensatory or antagonistic responses to the primary causes. The integrative hallmarks (stem cell exhaustion, altered intercellular communication) are proposed to be the culprits of aging-associated phenotypes. Figure adapted from (*61*).

alterations, loss of proteostasis) are thought to be the initial causes of cellular damage. In contrast, antagonistic hallmarks (deregulated nutrient sensing, mitochondrial dysfunction, cellular senescence) are considered to be compensatory or antagonistic responses to the primary causes. They can have opposite effects depending on their intensity. At low levels, they may be beneficial, but at high levels, they can become harmful. Finally, integrative hallmarks (stem cell exhaustion, altered intercellular communication) are proposed to be the result of the previous two categories and eventually cause the functional decline associated with aging (*61*). Up to now, many theories have tried to elucidate the underlying mechanisms of these hallmarks but failed to fully explain the complex processes. These theories can be classified into two categories: 1) Programmed aging and 2) the accumulation of damage and errors. Theories about

programmed aging hypothesize programmed longevity and imply that the aging process may follow a biological time course which is, at least to some extent, controlled by genetic pathways and biochemical processes conserved in evolution (*62, 63*). In contrast, theories classified into the second category imply that endogenous or exogenous cellular stressors lead to the failure of repair mechanisms and the accumulation of cellular and molecular damage (*64, 65*). Interestingly, there is a remarkable overlap in the aging and PD-associated hallmarks. In particular, PD seems to be affected by aging-associated mitochondrial dysfunction and loss of proteostasis (*9*). The following chapters will highlight the biological function of selected primary hallmarks relevant for this thesis and their contribution to cellular aging. Mitochondrial dysfunction in aging and PD will be reviewed in chapter 1.3.

1.2.1. Epigenetic alterations

Epigenetic modifications cause stable and heritable alterations in cellular function independent of genetic variations. These modifications alter chromatin structure and DNA accessibility, thereby causing a specific gene expression pattern. These processes are highly dynamic and essential for establishing distinct cell lineages as well as preserving cell identity and function. There are two types of epigenetic modifications - DNA methylation and post-translational modifications of histones (*66*). These modifications are known to be influenced by various factors such as environment, exercise, smoking, and age (*67–69*).

DNA methylation involves the addition of methyl groups to either adenine or cytosine and is thought to cause stable, long-term epigenetic modifications (*70*). The most commonly studied modification is the conversion of cytosine to 5-methylcytosine (5-mC), which is usually directly adjacent to a guanine so that two methylated cytosine residues sit diagonally on opposing DNA strands. In humans, approximately 28 million CpG dinucleotides (reference sequence GRCh37) are sparsely, but globally distributed throughout the genome and enriched in 28,890 CpG islands (*71–73*). Interestingly, CpG sites appear to be underrepresented in the human genome with a frequency of 0.98 %, less than one-quarter of the expected frequency (*71*). On average only 1 % of all DNA bases are methylated in human, whereas 70 % of all CpG sites are methylated (*71, 74*). This global pattern of methylation makes it difficult to state if methylation is targeted to specific regions or is a default state. However, CpG islands are often found to be in close proximity to or within gene promotor regions, indicating that there might be a specific recognition system (*75*). Most DNA methylation is thought to be without significant biological function, due to the heterogeneous nature of methylation patterns within tissue types and the high rate of loss of CpG sites during evolution (*76, 77*). Methylated cytosine residues are prone to spontaneous hydrolytic deamination to thymine and it could be shown that CpG to TpG/CpA conversions accounts for up to 28% of exonic single-nucleotide polymorphisms (SNPs) (*78, 79*). Up to now, the exact function of DNA methylation in gene expression is still unknown. It has been observed, that methylation near or in gene promotors can vary considerably between cell types and that promotor methylation levels correlate negatively with gene expression levels (*80*). Recently, DNA hydroxymethylation has been identified as a further type of DNA modification in which 5-mC is converted to 5-hydroxymethylcytosine (5-hmC). Hydroxymethylation has been observed in various organisms including mammals where its levels are highest in the central nervous system. It has been proposed that DNA hydroxymethylation may function as DNA demethylation intermediates. However, there is also evidences that DNA hydroxymethylation may play an important regulatory role in gene transcription (*81*).

Chromosomal DNA is condensed by histones to fit into the microscopic space of eukaryotic nuclei. The energy to fold DNA is provided in form of electrostatic interactions between the positively charged histone proteins and the negatively charged DNA, in units referred to as nucleosomes (*82*). A nucleosome consists of approximately 146 bp of DNA that is wrapped in 1.67 left-handed turns around a histone octamer. These octamers contain two H3-H4 histone dimers and two H2A-H2B dimers (*83*). The N-terminal histone tails protrude into the nuclear lumen and are accessible for post-translational modifications. Histone modifications are in general quite flexible and contribute to short-term epigenetic modifications. These modifications can affect either the binding of effector molecules or directly the overall chromatin structure by determining nucleosome spacing. The chromatin structure can be divided into two geographically distinct environments - a transcriptional inactive, densely packed heterochromatin, and a transcriptional permissive, less densely packed euchromatin [reviewed in (*84, 85*)]. Both chromatin structures are enriched and also depleted of certain histone modifications. However, there is a high degree of variance within heterochromatin and euchromatin structures as well as a high degree of overlap between the different regions. Nevertheless, specific histone modifications such as H3K9me2, H3K9me3, and H3K27me3 appear to be associated with heterochromatin, whereas H3K4me3, H3K27ac, and H3K79me2 modifications often appear to be present in euchromatin (*86–89*).
A variety of epigenetic alterations has been observed in age, ranging from DNA methylation patterns to post-translational modifications of histones and chromatin remodeling (*61*). Alterations of epigenetic marks are thought to affect most nuclear processes such as gene expression and silencing, DNA repair, cell-cycle progression as well as telomere and centromere structure. Associated with age are increased levels of H3K16ac, H3K4me3, or H4K20me3, as well as decreased levels of H3K9me or H3K27me3 (*90, 91*). Especially histone methylations fulfill the criteria for a hallmark of aging in invertebrates. Mutation of histone methylation complexes (for H3K4 and H3K27), as well as inhibition of histone demethylases (for H3K27), may extend longevity in nematodes, flies, and worms (*92–94*). Another promising marker for studying human development and aging is DNA methylation. Age-related global DNA hypomethylation has long been described for various species, however, more recent studies also associated hypermethylation of specific genomic loci such as CpG islands, promoters that are associated with key developmental genes, or Polycomb-group protein targets with age (*61, 95*). Furthermore, Horvath proposed an epigenetic clock that allows predicting the DNA methylation age of human tissues and cell types based on the methylation levels of 353 CpG sites (*96*). It is thought, that the epigenetic clock has a high tick rate until adulthood and slows down to a constant tick rate afterward. He could show, that the DNA methylation age is close to zero for embryonic and induced pluripotent stem cells. Furthermore, he showed that age acceleration, the difference between DNA methylation age and chronological age, is highly heritable. Nevertheless, there is no proof that the lifespan could be extended by altered patterns of DNA methylation.

1.2.2. Genomic instability

The accumulation of genetic mutations throughout life is a common denominator of aging (*97*). Genome stability and integrity are permanently challenged by various exogenous as well as endogenous threats, such as reactive oxygen species (ROS), DNA replication errors, and spontaneous hydrolysis (*98*). These stressors can cause diverse genetic lesions, including point mutations, translocations as well as copy number variations. To avoid these lesions, cells maintain a complex network of DNA repair mechanisms

that is efficient, but not capable of preventing all genetic damage (*61*). Especially in age, the accumulation of genetic damage is accelerated as the repair capacity is thought to decline. In addition to the direct influence of mutagenesis on gene expression and protein function, these mutations may cause replication stalling, senescence, apoptotic cell death, or transform cells into a cancerous state (*99*). This is especially critical when DNA damage leads to stem cell exhaustion, which may jeopardize tissue homeostasis (*100*). mtDNA has been considered as a main target for aging-associated mutations. It is particularly challenged by the oxidative environment of mitochondria (chapter 1.3), the lack of protective histones, and the limited capacity of mtDNA repair mechanisms (*61*).

The most common form of oxidative DNA lesion is 8-oxo-7,8-dihydroguanine (8-oxoG), which can cause a G:C to T:A transversion if not repaired properly (*101*). Additionally, 8-oxoG can generate a DNA double-strand break if it is inserted instead of guanine during DNA replication. Oxidative damage is repaired in general by the base excision repair pathway. The oxidized base is recognized and excised by a DNA glycosylase such as OGG1, leaving an abasic site (AP-site). In a second step, these are cleaved by the AP-endonuclease APE1 and 3' / 5' ends are repaired. Next, missing nucleotides are added by the DNA polymerase POLB and the DNA ends are ligated by LIG1 (*102*). Interestingly, single and double-strand DNA breaks activate the enzyme PARP1, which is essential for 3' / 5' end repair (*103*). Excessive activation of PARP1 can lead to a depletion of NAD^+, which may further alter the intracellular redox homeostasis as well as cellular metabolism such as neurotransmitter and myelin synthesis (*99*). Due to the strong relationship between ROS production and 8-oxoG formation, oxidative DNA damage is a commonly used cellular biomarker of oxidative stress (*99*).

Besides, defects in nuclear architecture can cause genomic instability (*61*). The nuclear lamina is a dense meshwork of filaments at the nuclear periphery which provides structural support to the nucleus and is involved in chromatin organization, DNA repair, and nuclear assembly/disassembly (*104*). The mammalian nuclear lamina is predominantly composed of the two A-type lamin isoforms A and C as well as of the two B-type lamins B1 and B2. Interestingly, each isoform is thought to form a distinctive separate meshwork with unique properties such as lamin edge length and edge connectivity (*105*). It appears that A and B-type lamin meshworks do not overlap and only interact indirectly also via lamina-associated proteins (LAPs) (*106*). Hundreds of LAPs were identified to interact directly or indirectly with lamins, including most inner nuclear membrane proteins as well as nuclear peripheral proteins (*107, 108*). These LAPs are thought to be involved in nuclear architecture, chromatin organization, cell-cycle regulation, and signaling (*108, 109*). Both lamin filaments and LAPs can directly interact with chromatin and DNA *in vitro*, however, regions close to the nuclear lamina are mostly occupied by heterochromatin (*110, 111*). In C. elegans, the association of repressed chromatin regions with the nuclear periphery is regulated by histone methyltransferases as well as by the protein CEC-4, which preferentially localizes to the inner nuclear membrane and specifically binds methylated H3K9 (*112*). Therefore, it is not surprising that dysregulation of lamin isoforms A/C and B1 cause chromatin reorganization (*113*).

It was of particular interest for aging researchers, that mutations in genes involved in nuclear lamina function can cause premature aging syndromes such as Hutchinson-Gilford (HGPS) and Néstor-Guillermo progeria syndromes (*114*). HGPS is caused by mutations in the LMNA gene, that result in the production of an abnormal version of lamin A called progerin. This causes the loss of nucleoplasmic LAP2α and lamin A and C (*115*). LAP2α is a non-membrane-associated isoform of the LAP2 family, which specifically interacts with A-type lamins and maintains their nucleoplasmic pool (*116*). Interestingly, progerin production was also observed during normal human aging and is further promoted by telomere dysfunction (*117*). In

addition to age-associated alterations in A-type lamins, lamin B1 levels have been shown to decline during replicative senescence, highlighting even further the importance of genomic integrity mediated by the nuclear lamina (*118*).

1.2.3. Telomere attrition

Accumulation of DNA damage with age is randomly distributed over the whole genome, however, there are some chromosomal regions, such as telomeres, that are particularly susceptible to age-associated decay (*119*). Telomeres are regions of repetitive sequences (5'-TTAGGG-3') at each end of a linear eukaryotic chromosome. These repetitive elements are bound by a multiprotein complex known as shelterin, which protects the chromosome ends from deterioration or fusion (*120, 121*). They prevent the access of the DNA repair machinery to telomeres, which would treat and repair telomeres as double-strand breaks leading to chromosome fusion. Thus, it has been shown, that DNA damage at telomeres is irreparable and highly efficient in inducing senescence or apoptosis (*119, 122*).
Replicative DNA polymerases lack the ability to copy the absolute ends of linear chromosomes. With the replication of nuclear DNA during mitosis, telomere length is progressively shortened by approximately 50-200 bp per replication (*123*). Telomere attrition is continued until a critical threshold is reached, which triggers cell-cycle arrest and ultimately cellular senescence or apoptotic cell death. This allows telomeres to act as a mitotic clock and can explain the limited proliferation capacity of most mitotic cells, also known as replicative senescence or Hayflick limit (*123, 124*). In general, cells would be capable to balance telomere length with the enzyme telomerase, however, telomerase expression is restricted to only a few cell types such as embryonic stem cells, germ cells, activated lymphocytes, and certain adult stem cells (*125*). Telomerases are ribonucleoproteins that consist of an RNA template and a highly specialized reverse transcriptase. The RNA template includes a sequence complementary to the telomere repeats, which allows telomerases to bind and extend telomeres (*126*).
Up to now, determinants of telomere length *in vivo* are poorly understood. Already at birth, telomere length is highly variable and declines during normal aging by 20-40 bp/year, ranging in humans from 5 to 15 kb (*127, 128*). These telomere shortening rates may be used to predict a species life or health span (*128*). It has been described that telomere shortening increases the risk of developing age-related diseases associated with restricted cell proliferation and tissue degradation such as cardiovascular diseases (*129, 130*). Telomere shortening is thought to be affected by 2 processes in particular, namely cellular replication and oxidative stress (*123, 131*). In most somatic cells telomerase activity is diminished after birth, only adult stem cells and lymphocytes maintain low telomerase activity levels leading to an elongated proliferative capacity (*125*). However, also reduced activity levels can cause telomere shortening so that even the majority of stem cells are subjected to a mitotic clock. Furthermore, multiple factors are known that can affect the rate of telomere shortening such as genetic and epigenetic predispositions, social and economic status, exercise, body weight, and smoking (*132*). Interestingly, the telomere length of post-mitotic neurons remains relatively stable throughout life (*133*). Thus, it is more likely that the accumulation of persistent DNA damage contributes to cellular aging of post-mitotic neurons in vivo, whereas telomere exhaustion is a hallmark of mitotic cells.

1.3. Cellular energy metabolism

Metabolism is the sum of physical and chemical processes by which material is produced, maintained, and destroyed and by which energy is provided. These processes can be divided into constructive (anabolism) and destructive (catabolism) metabolism. Anabolism requires energy to construct complex molecules from smaller units. These complex molecules can be degraded in catabolic processes into smaller units that are oxidized to release energy or to be used in other anabolic processes (*134*). In the brain, glucose is the main energy substrate and is delivered across the blood-brain-barrier (BBB) to fuel neuronal cell activity (*135*). The first step in the degradation of glucose is glycolysis which takes place in the cytoplasm, followed by the citric acid cycle and oxidative phosphorylation (OXPHOS) which take place in the mitochondria. The main purpose of glucose degradation is thereby the production of adenosine triphosphate (ATP), a ubiquitously used intracellular chemical energy carrier. The energy needed for energetically unfavorable reactions such as anabolic processes (nucleotide and protein biosynthesis) is then regained by hydrolyzing the terminal phosphoanhydride bond of ATP, producing energy, and adenosine diphosphate (ADP) (*134*). The following chapters will outline the principles of cellular ATP production in glycolysis, the citric acid cycle, and OXPHOS.

1.3.1. Glycolysis

Glycolysis is an ancient metabolic pathway that is common to a great majority of organisms alive today. It serves as the first step in both aerobic and anaerobic cellular respiration [reviewed in (*134, 136*)]. In glycolysis, one molecule of intracellular glucose is stepwise converted into two molecules of pyruvate, generating two molecules of ATP in the process. All glycolytic enzymes are found exclusively in the cytosol and an overview of the ten glycolytic reactions is depicted in ***Figure 3***. These reactions can be grouped into two main phases. The first five reactions are the energy-requiring phase, during which two molecules of ATP are invested and the last five reactions are the energy-releasing phase, during which four molecules of ATP are generated.

In a first step, glucose is irreversibly phosphorylated by the enzyme hexokinase to glucose-6-phosphate consuming one molecule ATP, which has two remarkable consequences. Glucose molecules are not only captured within cells, as glucose-6-phosphate is no longer a substrate for glucose transporters, it is also destabilized which facilitates further conversion steps. After isomerization of glucose-6-phosphate to fructose-6-phosphate, another ATP molecule is invested and the energetically unstable fructose-1,6-bisphosphate is generated by phosphofructokinase. Subsequently, fructose-1,6-bisphosphate is split into two phosphorylated three-carbon molecules: dihydroxyacetone phosphate and glyceraldehyde-3-phosphate, which exist in equilibrium as they can be isomerized into each other. However, only the three-carbon molecule glyceraldehyde-3-phosphate can be further processed in glycolysis. In the second half of glycolysis, both glyceraldehyde-3-phosphates are oxidized and phosphorylated into two molecules of 1,3-bisphosphoglycerate by glyceraldehyde-3-phosphate dehydrogenase, yielding two molecules of NADH. The further conversion of 1,3-bisphosphoglycerate to pyruvate generates in total four molecules of ATP (*134, 136*). Glycolysis is a fast, but inefficient process to generate ATP. Only approximately 5 % of

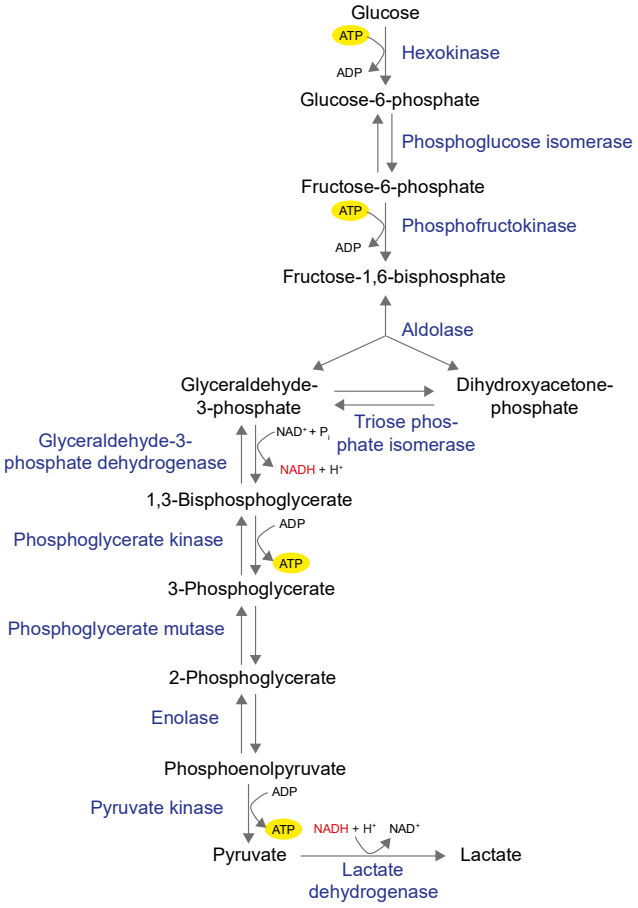

Figure 3 | The glycolytic pathway. Cytosolic degradation of glucose to pyruvate yields two molecules ATP and NADH. Figure adapted from (*137*).

glucose's energy potential is actually used (*138*). However, many intermediate products are used for other metabolic pathways. An important pathway to mention is the pentose phosphate pathway (PPP), which uses glucose-6-phosphate as educts. The PPP serves a pivotal role in supporting cell survival and growth by producing NADPH, an electron donor used amongst others in the defense against oxidative damage, as well as ribose-5-phosphate, a precursor for the synthesis of nucleotides, and erythrose 4-phosphate used in the synthesis of aromatic amino acids. Other intermediate products are used for lipid and also amino acid synthesis (*134, 136, 139*).

In general, enzymes catalyzing irreversible reactions are potential control sites. In glycolysis, the reactions catalyzed by hexokinase, phosphofructokinase, and pyruvate kinase serve as important check points. Their amount and activity are regulated by binding of allosteric effectors, by posttranscriptional modifications or on the transcriptional level. The principal rate-limiting enzyme of glycolysis is phosphofructokinase. Its activity is enhanced by high levels of reduced forms of ATP such as adenosine monophosphate (AMP) and

ADP, meaning glycolysis is stimulated as the cellular energy pool depletes. Contrary, high levels of ATP allosterically inhibit phosphofructokinase by lowering its affinity for fructose-6-phosphate.
Glycolysis itself only produces NADH but is not capable of regenerating NAD^+. However, this is necessary to restore the redox balance. This occurs downstream of pyruvate and depending on the cellular environment (oxygen availability, energy demand, presence of functional mitochondria). Under anaerobe conditions, pyruvate and NADH are converted to lactate and NAD^+ by the enzyme lactate dehydrogenase, which leads to the accumulation of lactic acid. In mitochondria containing cells and if oxygen is available, pyruvate can be further metabolized in the citric acid cycle and the NAD^+/NADH redox couple is maintained by OXPHOS [reviewed in chapter 1.3.2] (*134, 136, 139*).

1.3.2. Mitochondria

Mitochondria are semi-autonomous organelles that are found in most eukaryotic cells. Unlike any other organelle, mitochondria originate only from other mitochondria. They contain their own circular DNA (mtDNA), similar to those of bacteria, and maintain their own transcriptional and translational machinery (*140, 141*). It is believed that mitochondria evolved from a symbiotic relationship between primordial eukaryotic cells and aerobic bacteria (*141*). The endosymbiotic theory suggests that these aerobic bacteria somehow survived endocytosis by another species and became incorporated into the cytoplasm (*142*). The ability of primordial eukaryotic cells that relied on anaerobic glycolysis beforehand to now metabolically use oxygen for energy generation would have been a considerable evolutionary advantage. The aerobic processing of glucose in the citric acid cycle and OXPHOS enables cells to generate 16 times more ATP than could be produced during anaerobic glycolysis (*134*). In the course of endosymbiosis, a large part of the mtDNA was transferred to the nucleus, and mitochondria got specialized for various metabolic processes such as the citric acid cycle, the metabolism of amino acids and fatty acids, as well as OXPHOS (*143*). These processes are assigned to four distinct structural compartments: the outer mitochondrial membrane (OMM), the intermembrane space (IMS), the inner mitochondrial membrane (IMM), and the matrix. The matrix contains the mtDNA as well as citric-acid-cycle-associated enzymes, while the OXPHOS complexes are located in the IMM (*143*).
Even though mitochondria have a complex structure, they are highly dynamic organelles (*144*). An adequate balance of mitochondrial fission and fusion is essential for an appropriate mitochondrial function or the generation of new mitochondria. Mitochondrial fusion generates extended mitochondrial networks, which facilitate the transfer of mitochondrial content and increase the mitochondrial respiratory capacity. Thus, the formation of mitochondrial networks is advantageous under conditions of high energy demand. Contrary, mitochondrial fission generates fragmented mitochondria, which are transportable or can be removed through mitophagy. Mitophagy is defined as the selective autophagic degradation of mitochondria, which is necessary to adjust the mitochondrial number to changing metabolic requirements as well as to remove dysfunctional mitochondria (*144–147*).
Cellular energy requirements differ between cell types, but also within subcellular locations. As a consequence, mitochondria of certain cell types like e.g. neurons undergo more fission than others. This simplifies the distribution of mitochondria, which are often associated with the microtubular system, and their clustering at locations of high energy demand, mainly in dendritic spines and synapses where they are essential to maintain the appropriate function (*147–150*).

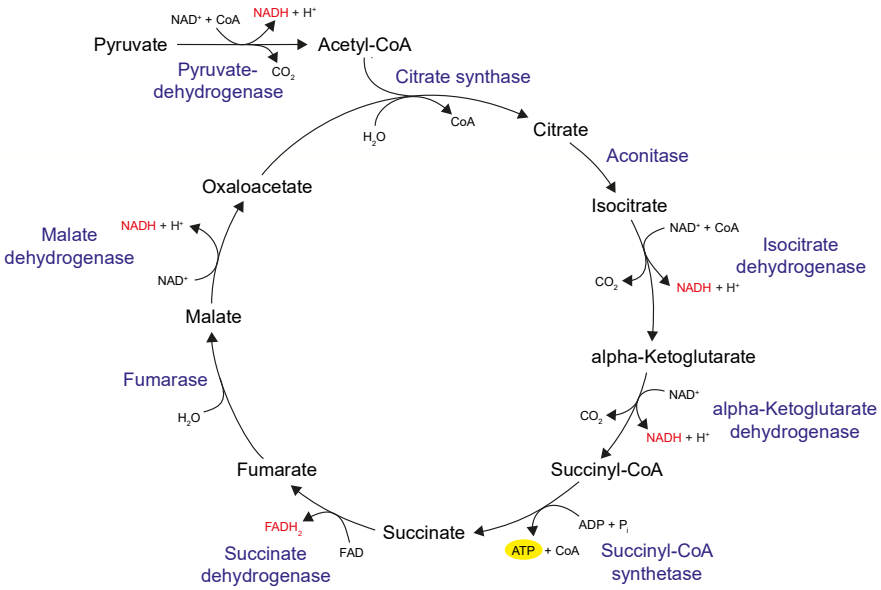

Figure 4 | The citric acid cycle. Degradation of pyruvate to CO_2 yields four molecules NADH, one $FADH_2$, and one ATP. Figure adapted from (*134*).

1.3.3. Citric acid cycle and oxidative phosphorylation

Glucose can be metabolized to pyruvate to generate ATP anaerobically through the glycolytic pathway. As mentioned before, this only uses about 5 % of glucose's total energy potential. Aerobic processing of glucose is the main source of ATP in metabolism, generating 16 times more ATP than produced during anaerobic glycolysis. Aerobic processing starts with glucose being degraded to pyruvate through the glycolytic pathway. Pyruvate is then further metabolized in the citric acid cycle, which takes place in the mitochondrial matrix and is the final common pathway for the oxidation of fuel molecules like carbohydrates, amino acids, and fatty acids. Most fuels enter the citric acid cycle as acetyl coenzyme A (acetyl-CoA). The citric acid cycle includes a series of redox reactions resulting in the oxidation of an acetyl-CoA into two molecules of CO_2, yielding 3 molecules of NADH, one $FADH_2$, and one ATP (***Figure 4***). The electrons from the electron carriers NADH and $FADH_2$ are then transferred through several membrane-bound mitochondrial complexes to one molecule of O_2, producing H_2O (OXPHOS) (***Figure 5***). The electron transfer is coupled to the pumping of protons out of the mitochondrial matrix across the IMM into the IMS. This causes a proton gradient that provides the potential energy to generate ATP from ADP [reviewed in (*134, 136, 139*)].

In detail, the pyruvate generated from glucose is oxidatively decarboxylated to acetyl-CoA by pyruvate-dehydrogenase, yielding one additional molecule of NADH. In the first step of the citric acid cycle, the two carbon molecule acetyl-CoA condenses with the four-carbon molecule oxaloacetate to yield the six-carbon

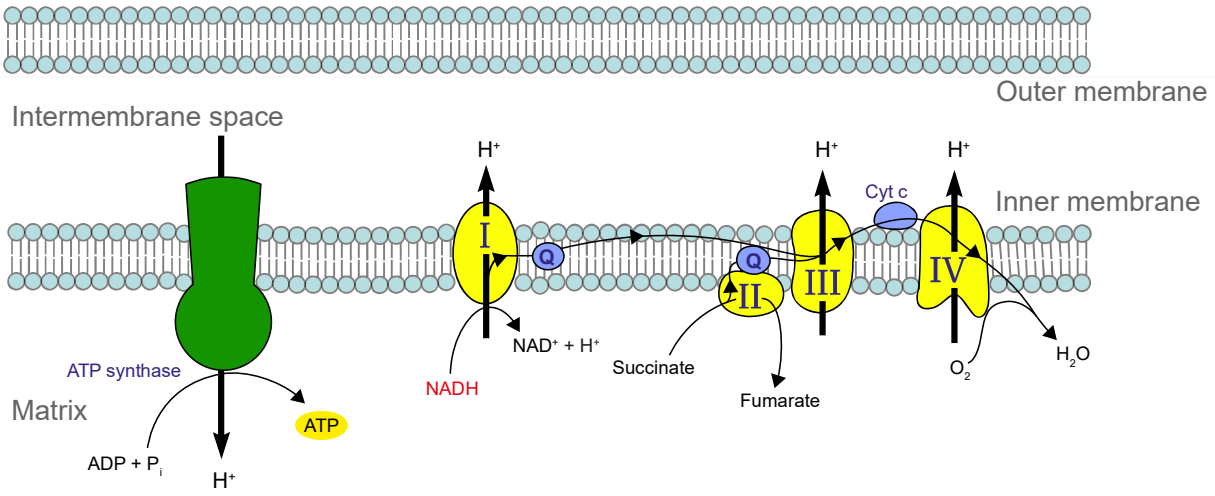

Figure 5 | Oxidative phosphorylation. The energy of electrons released by NADH and $FADH_2$ is used in a step-wise manner to create a proton gradient across the inner mitochondrial membrane. The proton gradient powers the ATP synthase which catalyzes the formation of ATP from ADP. Figure adapted from (*134*).

molecule citrate. Isocitrate, an isomer of citrate, is then oxidatively decarboxylated to the five-carbon molecule α-ketoglutarate (synonym: 2-oxoglutarate) by isocitrate dehydrogenase, yielding the first molecule of NADH. α-ketoglutarate is further decarboxylated to the four-carbon molecule succinate, which generates a second molecule of NADH as well as one ATP. In the last two steps, oxaloacetate is regenerated from succinate, yielding the third molecule of NADH and one $FADH_2$. Oxaloacetate can then accept another acetyl-CoA to restart the cycle. In total, only one molecule of ATP is generated directly in the citric acid cycle, whereas most of the energy is stored in NADH or $FADH_2$, which are used in oxidative phosphorylation to generate ATP. As a major metabolic hub, the citric acid cycle is also an important source of precursors for storage forms of fuels, but also for various other biosynthesis pathways. For example, most carbons in porphyrins are derived from succinyl-CoA. Citrate is used for fatty acid synthesis and many amino acids are derived from oxaloacetate (e.g. aspartate) or α-ketoglutarate (e.g. glutamate). However, citric acid cycle intermediates have to be replenished if they are used for other biosynthesis pathways, otherwise, the cycle will operate to a reduced extent. Thus, oxaloacetate, for example, can be generated by the carboxylation of pyruvate, which is catalyzed by the enzyme pyruvate carboxylase [reviewed in (*134, 136, 139, 151*).

NADH and $FADH_2$ generated in glycolysis, fatty acid oxidation, and citric acid cycle are energy-rich storage molecules as each contains a pair of electrons with a high transfer potential. In OXPHOS the electrons are transferred through several membrane-bound mitochondrial complexes to O_2, producing H_2O. This transport chain consists of four multimeric protein complexes located in the IMM which contain specific redox cofactors such as hemes, flavins, or iron-sulfur clusters. These complexes are known as NADH:ubiquinone oxidoreductase (complex I, approximately 44 subunits), succinate dehydrogenase

(complex II, four subunits), ubiquinone-cytochrome c oxidoreductase (complex III, 11 subunits), and cytochrome c oxidase (complex IV, 13 subunits) [reviewed in (*134, 136, 139*)].
Complex I is the first enzyme of the respiratory chain. The functional mammalian complex contains 44 different subunits which form an L-shaped arm composed of a hydrophilic (peripheral) and a lipophilic part (transmembrane). The peripheral part protrudes into the mitochondrial matrix and is responsible for the transfer of two electrons from NADH through 8 iron-sulfur clusters to ubiquinone, which is reduced to ubiquinol. The electron transfer is linked to the translocation of four protons from the mitochondrial matrix through the transmembrane part to the IMS. In total, complex I is thought to provide approximately 40 % of the proton motive force. Complex II or succinate dehydrogenase is a component of both the citric acid cycle and the electron transport chain. It catalyzes the oxidation of succinate to fumarate and transfers the yielded electrons through an immobile FAD to ubiquinone. However, electron transport in complex II is not accompanied by the translocation of protons. Complex III transfers the electrons from ubiquinol to cytochrome c and thereby pumps four additional protons across the IMM. Both ubiquinone and cytochrome c are freely mobile electron carriers that are loosely connected to the surface of the IMM and can thus move between the complexes. Finally, complex IV accepts the electrons from cytochrome c and transfers them to the terminal electron acceptor ½ O_2 to generate H_2O using protons from the matrix. The electron transfer is linked to the translocation of two more protons into the IMS. The movement of protons from the matrix to the IMS has two major consequences. It generates both a pH gradient across the IMM, with a high pH in the matrix and physiological pH in the IMS, as well as a voltage gradient (membrane potential), with the negative side in the matrix and the positive side in the IMS. The pH gradient forces H^+ into the matrix and OH^- into the IMS, thereby reinforcing the voltage gradient. Together, the pH and voltage gradients are said to generate an electrochemical proton gradient. The ATP synthase (complex V, approximately 16 subunits) finally generates ATP using the proton flow along the electrochemical gradient to mechanically unite ADP and P_i. In total, OXPHOS is responsible for the generation of 26 of the 30 molecules of ATP that are formed when glucose is completely oxidized to CO_2 and H_2O. Thus, OXPHOS is a highly efficient process to generate ATP but compared to glycolysis is more time-consuming [reviewed in (*134, 136, 139*)]. A critical point in OXPHOS is an inefficient electron transfer to O_2 instead of ubiquinone, which causes the generation of ROS [further reviewed in chapter 1.3.4]. This can be enhanced by subtle defects in complex I assembly as well as by changes in the expression level of complex I subunits or mutations in these subunits (*152, 153*).

1.3.4. Mitochondrial function in aging and Parkinson's disease

The free-radical theory of aging was originally described by Denham Harman in 1956 (*154*). It postulates that the process of aging is a consequence of the accumulation of oxidative damage caused by free radicals or ROS. Free radicals are molecules with single unpaired electrons and thus unstable and highly reactive. They can oxidize nearly all organic molecules such as proteins, lipids, DNA, or RNA. Oxidation of lipids may disrupt cell membranes, while oxidation of proteins may result in the accumulation of defective proteins in cells, which potentially overstrains cellular protein clearance mechanisms (*155*). Particularly dangerous is the oxidation of nucleotides, which introduces mutations that may cause genomic instability, mutations of proteins, or results in their misexpression (*101, 102, 155*). Free radicals are generated *in vivo* primarily in mitochondria during the mitochondrial electron transport as a consequence of an inefficient electron

transfer at complex I to e.g. O_2 instead of ubiquinone, but also by various other cellular processes (*152, 153*). As the mtDNA is stored in the mitochondrial matrix in close proximity to the respiratory chain, it is particularly vulnerable to oxidative damage caused by ROS (*155*). The mtDNA encodes a total of 37 genes - 13 subunits of mitochondrial complexes, two rRNAs, and 22 tRNAs (*156*). Thus, mtDNA mutations may cause the expression of defective proteins associated with the cellular respiratory system. This may not only result in a reduced mitochondrial respiratory efficiency and capacity but may further increase ROS production, which creates a vicious circle of oxidative stress that ultimately leads to cell death (*157*). It has been described in numerous studies that ROS levels and oxidative damage increase with age as well as that reducing oxidative damage can extend the lifespan of various organisms (*158*). In line with these observations, increased production of ROS seems to shorten the lifespan of organisms, however, in some organisms increased ROS levels are also associated with increased lifespans (*158–160*). Interestingly, a recent study revealed that the number of mtDNA mutations acquired during aging can vary between different cell types, while SN neurons were severely affected such a trend was not observed in cortical or cerebellar neurons (*161*). Thus, the questions arising are whether a progressive mitochondrial dysfunction acquired during aging is actively contributing to the aging process as well as whether this dysfunction is also contributing to the development of neurodegenerative diseases like PD (*161*).

The first link between mitochondrial dysfunction and PD became evident in 1983 when several people consumed a new synthetic drug and suffered from parkinsonian-like symptoms afterward (*162*) [further reviewed in chapter 1.1.3.2]. The drug they consumed was contaminated with MPTP which caused mitochondrial complex I dysfunction, an enhanced production of superoxides, and selective neurodegeneration in both the human and mouse SN (*32*). Similarly, also exposure to toxins like rotenone and paraquat results in mitochondrial complex I deficiency and parkinsonian-like symptoms. However, the toxicity of these molecules may not only be due to the inhibition of complex I, as some also interfere with other cellular processes such as intracellular dopamine oxidation (*163, 164*).

Also in post-mortem studies, varying degrees of complex I and complex II deficiency (from ~30 - 60 %) have been described in the SN and cortex of sPD patients (*165–167*). Due to the high number of mtDNA encoded subunits required for complex I assembly, this complex is more likely to be affected by mtDNA mutations which seem to accumulate in SN neurons of PD patients (*168, 169*). In line with this, the dysregulation of genes involved in the electron transport chain could be detected on the transcriptional level already early in PD etiology (*170*). Apart from complex I deficiency, the decreased activity of the citric acid cycle enzyme α-ketoglutarate dehydrogenase found in PD brains likely contributes to energetic failures in PD (*171, 172*). Additionally, PD-associated genes including *PARK7* (*DJ1*), *PINK1*, *PRKN*, *SNCA,* and *LRRK2* were shown to be involved in, amongst others, mitochondrial homeostasis and quality control. Thus, mutations in these genes may reduce the cells' ability to adapt their mitochondrial networks to cellular requirements and to remove damaged mitochondria, possibly causing their accumulation (24) as well as elevated ROS generation and susceptibility to oxidative stress (*173*).

Thus, experimental evidence suggests that a substantial contributor to dopaminergic neuronal loss is oxidative stress, which may be the consequence of a dysfunctional electron transport chain, low glutathione levels, and high levels of iron and calcium in the SNpc (*41, 54*).

1.4. Development and maintenance of midbrain dopaminergic neurons

Various neuronal subtypes are subjected to degradation in the prodromal phase or early PD. These subtypes share a selective vulnerability with phenotypic characteristics such as neurotransmission (high levels of cytosolic monoamines), electrophysiology (autonomous activity, broad action potentials), morphology (long, unmyelinated, and highly branched axons), and connectivity (*174*). However, the cell type that is most affected and also responsible for most motor symptoms are midbrain DAns [reviewed in chapter 1.1]. Our ability to understand their developmental lineage may not only provide us with insights into their selective vulnerability but may also improve our attempts to generate subtype-specific human midbrain DAns *in vitro* for future regenerative medicine.

During gastrulation, the formation of the three germ layers is accompanied by a posterior to anterior migration of cells. At the rostral end, a set of specific transcriptions factors (e.g. *DKK1*, *NOG,* and *LEFTY1*) inhibits posterior signals to pattern the neural ectoderm, which leads to the formation of the neural tube (*175*). During these developmental stages, a genetic network of transcription factors from two organizing signaling centers, the isthmic organizer (IsO) and the floor plate (FP) defines the regional identity and controls specification and proliferation of neuroepithelial cells as well as midbrain DAn differentiation and maintenance (***Figure 6***) (*175*).

One of the most crucial patterning events in the neural tube is the formation of the IsO, which defines the midbrain-hindbrain boundary (MHB). The IsO is formed through the coordinated repression of *OTX2* in the midbrain and *GBX2* in the hindbrain (*176, 177*). These transcription factors also control the expression of the morphogen *WNT1* in the midbrain and *FGF8* in the hindbrain. Importantly, only the appropriate expression of *FGF8*, but not *WNT1*, is required for the formation of the IsO. High concentrations of FGF8 in the hindbrain induce the hindbrain fate, whereas low concentrations in the anterior region drive midbrain identity. The second important event in neural tube patterning is the secretion of the morphogen SHH by the notochord, which induces the expression of *FOXA2* and thus specifies the most ventral region of the neural plate as FP. FOXA2 has a central role in the SHH signaling network and is essential for ventral patterning and thus notochord and FP development. Interestingly, FOXA2 directly upregulates *SHH* expression and secretion. Thus during development, also the FP starts to secrete SHH and becomes a secondary organizer. The concentration gradient of SHH secreted by the FP is thought to regulate the ventro-dorsal patterning by inducing the expression of different sets of transcription factors in ventral and dorsal progenitors. The low concentration of SHH in the dorsal region induces the upregulation of *NKX6-1* and *OTX2*, whereas *NKX2-2* expression is suppressed in the midbrain FP (mFP) by FOXA2 [reviewed in (*175*)].

Midbrain dopaminergic progenitors are marked by the expression of *LMX1A* and *LMX1B*, which is regulated by both OTX2 and FOXA2 (*175*). Whereas LMX1B is required for the differentiation of midbrain dopaminergic progenitors, LMX1A is essential for the specification of midbrain DAns in the mFP (*178, 179*). Overall, temporal and spatial regulation of the *WNT1-LMX1A* autoregulatory loop as well as SHH-*FOXA2* and *OTX2* expression plays an important role in the specification and proliferation of midbrain dopaminergic progenitors (*175*).

Generally, neurogenesis begins with neuroepithelial cells switching to asymmetric differentiative cell division. This switch is accompanied by the transformation of neuroepithelial cells into radial glia (RG). RG

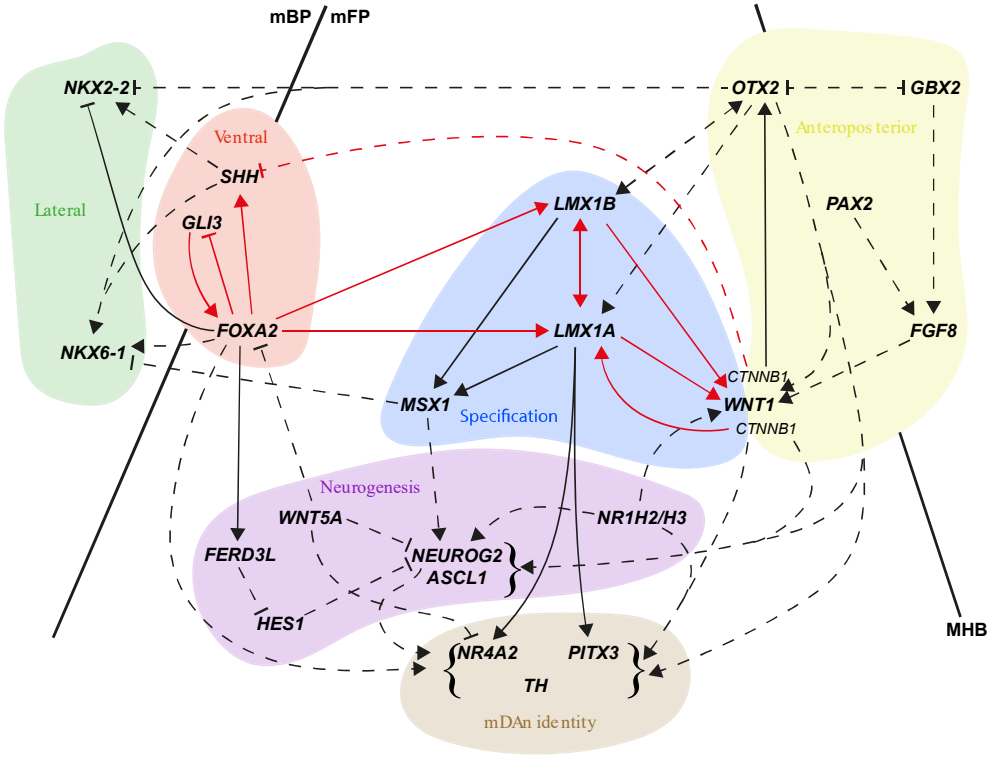

Figure 6 | Genetic networks controlling the development of midbrain DAns. The *SHH-FOXA2* (red) and *LMX1A/B-WNT1-OTX2* (blue/yellow) networks coordinately control both midbrain dopaminergic specification and neurogenesis as well as differentiation and survival. Genes are assigned to specific categories: anteroposterior patterning - yellow area; midbrain floor plate (mFP) specification – blue area; ventral patterning – orange area; lateral phenotypes – green area; neurogenesis - purple area; midbrain DAn identity and maintenance – brown area. MHB, midbrain-hindbrain boundary. mBP, midbrain basal plate. Solid lines indicate direct interactions validated by chromatin immunoprecipitation. All other interactions are shown by dashed lines. Arrowheads indicate activation and perpendicular lines indicate inhibition. Figure adapted from (*175*).

express astroglial markers such as *GFAP* or *GLAST* and upregulate specific transcription factors such as *PAX6 (180, 181)*. These RG reside in the embryonic ventricular zone of the FP and migrate through the intermediate zone (*181–183*). The *SHH-FOXA2* and *LMX1A/B-WNT1-OTX2* networks also coordinately control midbrain dopaminergic neurogenesis by regulating the expression of the proneural genes *ASCL1* and *NEUROG2 (175)*.

After neurogenesis, the migratory midbrain dopaminergic neuroblasts in the intermediate zone differentiate into TH^+ midbrain DAns on reaching the mantle zone. Differentiation is regulated by the early genes LMX1A/B, FOXA2, OTX2 as well as by EN1/2 that induce the expression of late transcription factors such as *PITX3* and *NR4A2 (175)*. These maintenance factors are thought to control the dopaminergic neurotransmitter phenotype as well as DAn maintenance and survival through an appropriate supply of neurotrophic factors such as GDNF (*184*).

In conclusion, the two morphogen-controlled genetic networks *SHH-FOXA2* and *LMX1A/B-WNT1-OTX2* coordinately control both midbrain dopaminergic specification and neurogenesis as well as differentiation and survival. Understanding the developmental process that specifies midbrain DAns *in vivo*, it is now possible to differentiate induced pluripotent stem cells (iPSCs) or embryonic stem cells into vulnerable or pathogenic cell types such as DAns *in vitro*. This has opened up immense possibilities in disease modeling, drug discovery, or cell replacement therapies [further reviewed in chapter 1.6].

1.5. Primary cilia

Cilia are microscopic, hair-like cellular organelles that extend from the surface of almost all mammalian cells. The length of a single cilium can range from 1-10 µm with a diameter of less than 1 µm. Each cilium comprises a microtubular backbone, the ciliary axoneme which is surrounded by the cell membrane. Depending on their axonemal arrangement and protein content, cilia can be divided into two classes - motile cilia or signaling units. Motile cilia are found for example in the respiratory tract or the middle ear where they protrude from the cell surface in large numbers. They exhibit a rhythmic waving or beating motion which allows them to move extracellular fluids. These 'classical' cilia are characterized by axonemes with nine outer doublets and a central pair of microtubules (9+2 axoneme) which are connected by radial spokes as well as by dynein arms that promote motility. Non-motile or primary cilia (PC) lack the central pair of microtubules (9+0 axoneme) and protrude as a single appendage from the cell surface. PC typically emanate from the mother centriole, also known as the basal body, which is docked to the apical cell membrane through transition fibers. These transition fibers may also form a ciliary pore complex, similar to the nuclear pore, and together with the apically adjacent transition zone function as a permeability barrier between the cytoplasm and the PC, called the ciliary gate. The ciliary gate is also a physical barrier between the ciliary membrane and the plasma membrane that maintains their distinct lipid and protein composition. The transition zone is characterized by Y-links that connect the proximal axoneme to the membrane of the ciliary pocket and has a sophisticated modular organization that allows regulating appropriate intracellular transport to and from the PC (***Figure 7***) [reviewed in (*185–187*)].
The assembly and maintenance of PC are dependent on a specific transport system, known as intraflagellar transport (IFT) (*188*). The ciliary gate is thought to restrict the size of proteins that can diffuse into PC to about 10 nm hydrodynamic diameter (~50 kDa) (*189, 190*). Larger cargo molecules accumulate either at the transition fibers, where IFT complexes are thought to assemble and bind cargo molecules, as well as at the ciliary pockets, which are thought to be involved in vesicular trafficking to the PC (*186, 191–193*).
Vesicles containing ciliary cargo molecules originate from the *trans*-Golgi network and are directed to the ciliary base by the Rab family (RAB11 and RAB8), where RAB3IP binds to the exocyst complex subunit SEC15. The exocyst complex attaches the vesicle to the ciliary pocket and RAB8-dependent membrane-vesicle fusion is mediated by CEP290 and CC2D2A (*186, 187, 192*).
A second pathway involves the BBSome, an octameric complex (BBS1, BBS2, BBS4, BBS5, BBS7, BBS8, BBS9, and BBS18) which is thought to be evolutionarily related to transmembrane protein trafficking complexes such as clathrin coats and the COPI/COPII coatomeres (*194*). The BBSome recognizes ciliary targeting sequences of transmembrane proteins such as the G-protein coupled receptor (GPCR) RHO and mediates their trafficking to the ciliary membrane. Vesicles containing ciliary transmembrane proteins are bound by

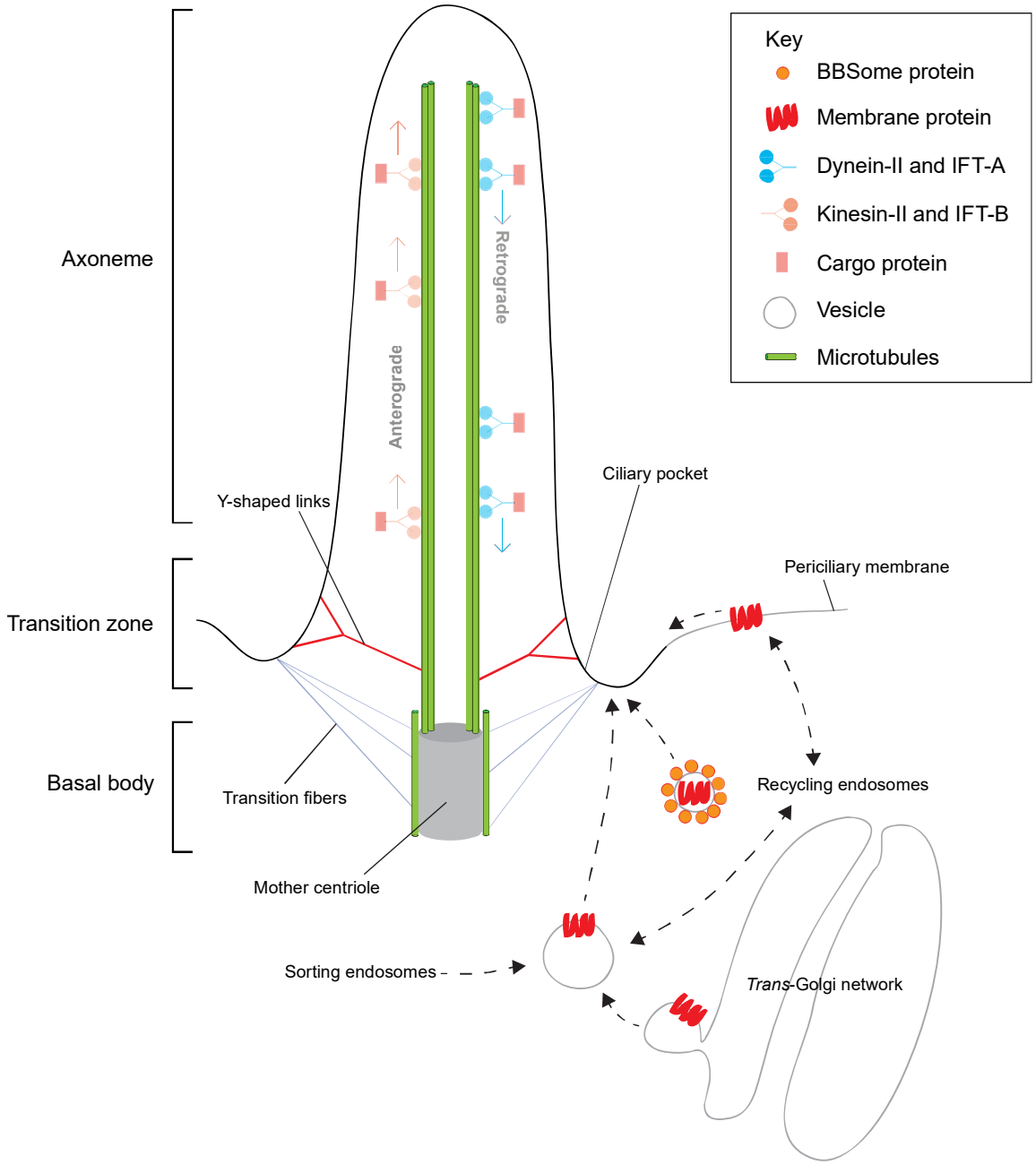

Figure 7 | Simplified schematic of cilia structure and ciliary protein trafficking. Proteins are transported to the ciliary base by several pathways. IFT complexes and motor proteins mediate the anterograde and retrograde intraflagellar transport along the axoneme. Vesicular transport and protein movements are indicated by black, red, and blue arrows. Figure adapted from (*186*).

the BBSome and directed to the ciliary base. Vesicle fusion with the ciliary pocket membrane is presumably facilitated by SNARE complexes (*186, 187, 192, 195*).

The larger cargo molecules that accumulate at the ciliary base are bound by IFT-B complexes which mediate their transition through the ciliary gate and along the axonemal doublet microtubules by linking the cargo to motor proteins. Kinesin-II family motors mediate the anterograde transport towards the

ciliary tip, whereas retrograde transport is mediated by dynein-II and IFT-A complexes, which are thought to assemble at the ciliary tip (*188, 193, 196*). However, there is also evidence that some cargo particles can bind directly to kinesin-II motors, possibly circumventing the participation of IFT complexes. These include tubulins and the GLI transcription factors that are involved in hedgehog-related signaling (*193*). Even though the BBSome is enriched at the transition zone where it mediates the transport of vesicles containing ciliary proteins, it has been shown that it also migrates bidirectionally during IFT and that some transmembrane proteins e.g. SMO accumulate in BBSome-deficient cilia (*197*). This led to the hypothesis that the BBSome promotes also the retrieval and export of specific transmembrane proteins from the cilium.

Proteins that can be transported into and thus concentrate in PC are amongst others ion channels, receptor tyrosine kinases, transforming growth factor beta receptors, NOTCH receptors, receptors for extracellular matrix proteins, class A, B, and F GPCRs as well as proteins involved in cellular signal transduction (*187*). Thus, PC are thought to function as mechano-, osmo- and chemosensory units or in other words as 'cellular antenna' that receive and process signals from the extracellular environment, and by transmitting these signals to the cytoplasm and nucleus they control gene expression and cell function. This unique feature allows them to control cellular processes during development and tissue homeostasis (*187, 198*). Dysfunction or defects in motile and primary cilia underlie many severe human disorders termed ciliopathies [reviewed in chapter 1.5.3] (*199*).

1.5.1. Primary cilia assembly

Ciliogenesis is tightly coupled to the cell cycle as centrioles must be released from the plasma membrane to function in the mitotic apparatus. Cilia formation typically starts during the G1 phase and cilia continue to grow during the G0 phase. They appear to be resorbed in two waves, the first one occurs before the G1/S transition and the second one before the mitotic entry. Ciliary resorption allows the centrosomes to contribute to the formation of the mitotic apparatus and thus the suppression of ciliogenesis is essential for proliferating cells. Bidirectional crosstalk between cilia formation and cell division has been observed as improper division can result in abnormal ciliogenesis and vice versa, dysfunctional ciliogenesis can result in cell cycle alterations [reviewed in (*186, 200*)].

In detail, during the G1 phase, the mother centrioles are thought to mature and acquire a variety of distal appendages which correspond to the transition fibers (***Figure 8***). This distal region can interact with a ciliary vesicle that flattens upon ciliary extension. Upon docking to a vesicle, the mother centriole is referred to as the basal body. It is also thought that the mother centriole can remain associated with a remnant of the ciliary membrane during the cell cycle so that the daughter cell that inherits this centriole can quickly undergo ciliogenesis during the G1 phase (*200–202*). The ciliary vesicle associated with the basal body then translocates to the cell surface and fuses with the plasma membrane. The final step of ciliogenesis is the axoneme nucleation and extension by assembling tubulin at the distal growing end, called the ciliary tip (*186, 200, 202*). Cilia typically lack the machinery that is necessary for protein synthesis, hence they rely on intracellular and intraflagellar transport systems for the delivery of new axonemal building blocks to their site of assembly (*188*). Microtubule assembly is thought to be intrinsically unstable and highly dynamic. Dimeric α/β-tubulin subunits are added preferentially to the (+) end of a preexisting microtubule, while the (-) end is associated with the basal body. After incorporation of the

tubulin dimer, the GTP bound to the β-tubulin is hydrolyzed to GDP, but not the GTP bound to α-tubulin. At high concentrations of unpolymerized GTP-tubulin, microtubules grow as the rate of tubulin incorporation is faster than the rate of hydrolysis of GTP bound to α-tubulin or the dissociation of GTP-tubulin from the (+) end. At low concentrations, the incorporation rate is decreased and a GDP cap forms at the (+) end. The GDP cap is unstable and thus microtubule ends peel apart and dissociate (*139*). The IFT regulates the continuous tubulin turnover at the distal end of the axoneme and determines the concentration of unpolymerized GTP-tubulin that is available for microtubule assembly. The balance point model proposes that the assembly rate, similar to the IFT, is length-dependent, whereas disassembly is length-independent. Thus, the two rates can only reach a balance point at a single length. Defects in IFT complexes or motor proteins can prevent ciliogenesis or affect normal ciliary assembly, which may lead to an altered ciliary morphology e.g. shortened or prolonged cilia.

One obvious mechanism to regulate ciliogenesis, but also cilia length is to interfere with the dynamic equilibrium between assembly and disassembly of microtubules. Although the exact mechanisms remain elusive, several centrosomal and ciliary proteins have been identified to regulate ciliogenesis such as CEP97 or CEP110 and their function depends partly on their phosphorylation by cell cycle kinases. A second mechanism is to regulate microtubule stability by post-translational modifications such as ubiquitination, methylation, or acetylation. For example, the Aurora A (AURKA) kinase is involved in the axonemal disassembly of cells emerging from G0. The association of AURKA with HEF1 and PIFO elevates their catalytic activity and induces the histone deacetylase HDAC6, which leads to tubulin deacetylation and presumably destabilization [reviewed in (*186, 203*)]. Furthermore, ciliary resorption can be caused by the katanin-mediated severing of microtubules at the transition zone (*204*).

Interestingly, cilia have also the ability to adjust their morphology in response to environmental conditions. They seem to self-adjust their size and shape depending on the strength of signals they need to detect. PC can be enlarged to enhance its signal detection capacity, but can also be resorbed to decrease its response. For example, leptin or prostaglandin signaling is thought to enhance ciliogenesis, potentially creating a positive feedback loop (*186*).

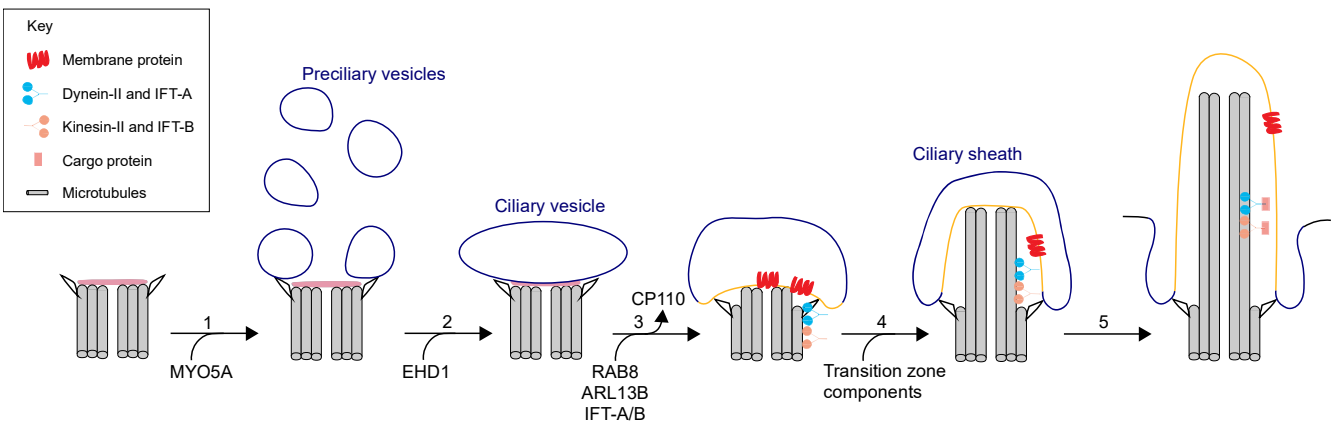

Figure 8 | Primary cilia assembly. The mother centriole serves as a base for PC assembly. The intracellular pathway includes 5 steps: 1) Maturation of the mother centriole and MYO5A-dependent recruitment of preciliary vesicles to the distal appendages; 2) EHD1-mediated fusion of the preciliary vesicles to the ciliary vesicle; 3) Growth of the ciliary vesicle; 4) Growth of the axoneme and formation of the transition zone; 5) Fusion of the ciliary sheath with the ciliary membrane. Figure adapted from (*201*).

1.5.2. Primary cilia function

The PC is a sensory organelle that responds to mechanical and chemical stimuli in the environment and communicates these external signals to the cytoplasm and nucleus to control gene expression and cell function [reviewed in chapter 1.5]. The concept of ciliary signal transduction will be discussed in this chapter exemplarily for SHH signaling which affects amongst others GLI3 processing.

One of the foremost tasks of PC is to regulate SHH signaling, which relies on the dynamic trafficking of SMO into and out of the PC to control tissue homeostasis or cell proliferation [reviewed in (*205, 206*)]. For SHH signaling, three transcription factors are known to mediate signal transduction namely GLI1, GLI2, and GLI3 (*207*). GLI1 acts as a transcriptional activator whose expression is low in neuronal precursor cells (NPCs) and its activity is thought to be neglectable during neural development (*208, 209*). In contrast GLI2 and GLI3 exhibit an evolutionarily conserved transcriptional duality - acting as activators or repressors depending on post-translational processing - and are thought to be the primary mediators of SHH signaling (*208, 210*). Furthermore, the restriction of the GLI3 repressor activity has been shown to be essential to adopt specific cell fates in the developing brain (*211*).

In the absence of SHH, the receptor PTCH1 is localized in the ciliary membrane and prevents the translocation of SMO to the PC. In the presence of SHH, PTCH1 is removed and SMO is translocated to the PC and transported to the ciliary tip. At the ciliary tip, SMO subsequently prevents the degradation of full-length GLI3 (GLI3-FL) to GLI3-repressor (GLI3-R) (*205, 212*). GLI3-FL is thought to be neutral or functions as a weak transcriptional activator, whereas the degradation product GLI3-R acts as a repressor (*213*). In addition, proteolytic processing of GLI protein depends on the inhibition of SUFU as well as on phosphorylation by cAMP-dependent PKA which are key regulatory components of SHH signaling. However, the signal transduction pathways from SMO to SUFU and PKA remain poorly understood (*212–215*). Finally, processed GLI3-FL or GLI3-R has to be exported from the PC and imported into the nucleus to function as transcription factors. In the presence of SHH, the ratio of GLI3-FL to GLI3-R is thought to increase which results in target gene activation (*216, 217*).

Recently, PC were also found to have a role in regulating protein homeostasis by influencing several key maintenance mechanisms including the ubiquitin-proteasome system (UPS) or autophagy. For example, some ciliary proteins including BBS4, OFD1, and RPGRIP1L have been shown to directly interact with proteasomal components such as RPT6, the regulatory component of the 19S proteasome subunit. This may lead to a reduction of proteasomal activity. Contrary, UPS-mediated protein degradation is also crucial for regulating cilia formation and disassembly (*186, 218*).

1.5.3. Ciliopathies

Ciliopathies are human disorders caused by dysfunctional motile or non-motile cilia. Today, at least 35 different ciliopathies are known that cause many phenotypes and affect a wide variety of organs (*199*). These include cystic kidneys, retinal degeneration, hippocampal dysgenesis, corpus callosum agenesis, and cognitive deficits such as intellectual disability and autism spectrum disorder. Ciliopathies are mostly recessive disorders and genetically heterogeneous, due to the many genes involved in ciliary structure and function (*219, 220*). However, proteins encoded by mutated genes that are associated with different

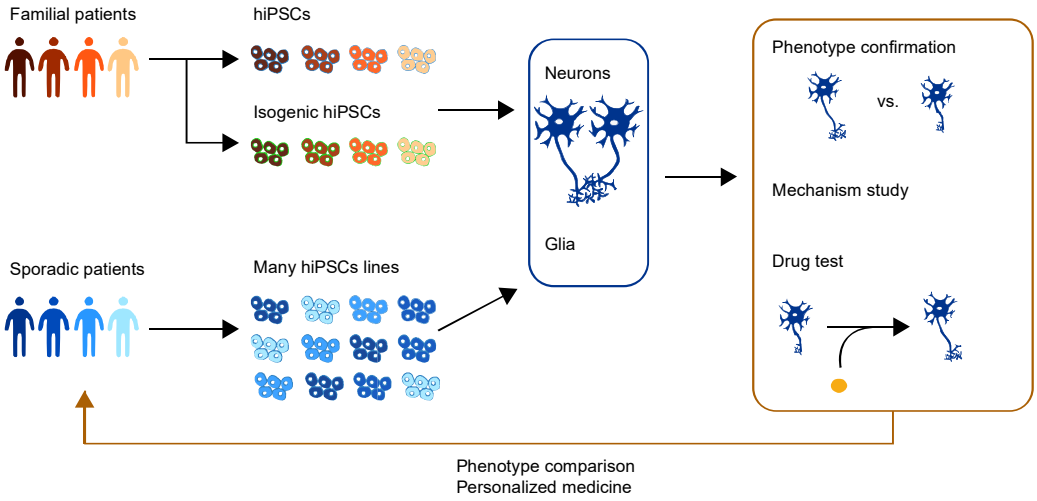

Figure 9 | hiPSCs used for neurological disease modeling - phenotype confirmation, mechanism study, and drug test. Figure adapted from (*221*).

disease groups seem to cluster to distinct subcellular localizations (*222*). Hotspots for ciliopathies are the basal body, transition zone, and the IFT system. Interestingly, mutations in the same gene or even the same mutation can result in clinically distinct ciliopathies (*199, 222*).

One example of a ciliopathy is the Bardet-Biedl syndrome (BBS) which causes retinal degeneration, limb abnormalities, obesity, developmental delay, reproductive anomalies, and renal tract abnormalities (*223*). BBS is caused by the disruption of BBSome components (BBS1, BBS2, BBS4, BBS5, BBS7, BBS8), the disruption of BBSome trafficking (ARL6 or BBS3), or alterations in BBSome assembly (BBS6, BBS10, BBS12) (*223–225*). This results in delivery problems of key receptors to PC. Altered ciliary protein localization of cell type-specific receptors such as DRD1, SSTR3, and MCHR1 is the probable etiology of different BBS-associated phenotypes (*226*). However, the molecular mechanisms underlying many phenotypes remain elusive and could be multifactorial.

1.6. hiPSCs as a model for neurodegenerative diseases

Genetic or toxin-induced cell and animal models have been harnessed to unravel molecular and cellular mechanisms contributing to disease etiology. However, most of these models cannot faithfully recapitulate the pathology in disease-relevant cells which often hampers the search for potential mechanisms underlying sporadic diseases (*227, 228*). Also, the relevance of these mechanisms in translational studies was diminished by the lack of suitable human models. With the advent of human iPSCs (hiPSCs) an advancement of our knowledge on human physiology at the cellular level is now possible. hiPSCs were first described in 2007 by Shinya Yamanaka as a type of pluripotent stem cells that are capable of self-renewal *in vitro* (*229*). Overall, hiPSCs are similar to embryonic stem cells, however, can be generated and used without complex social issues involved. In addition, while embryonic stem cells are

obtained from abandoned embryos generated for *in vitro* fertilization, hiPSCs can be directly reprogrammed from various somatic cell types (skin fibroblasts and peripheral blood mononuclear cells) donated from patients. The introduction of four transcription factors (OCT4, SOX2, KLF4, MYC) was sufficient to reverse the cellular differentiation and aging pattern of somatic cells (*230*). Using these patient-derived hiPSCs, it is now possible to obtain pathogenic cell types directly from patients that possibly share disease mechanisms for drug discovery. For neurodegenerative disease modeling, hiPSCs can be differentiated into various neuronal populations, glial cells, or even brain organoids which allow mimicking processes of the central nervous system (***Figure 9***) (*221*).

To explore mechanisms underlying PD etiology, PD patient-derived hiPSCs can be differentiated towards midbrain DAns. hiPSCs with mutations in *SNCA*, *LRRK2*, *PINK1*, and *PRKN* were used for fPD modeling and characterized for PD-associated phenotypes (*231*). These hiPSCs were either generated from wild type hiPSCs or patient-derived hiPSCs carrying these mutations were gene-corrected allowing a comparative analysis. For example, *LRRK2* mutated DAns displayed PD-specific phenotypes including mitochondrial dysfunction, DAn degeneration as well as deficient autophagy (*231, 232*). Similar phenotypes could be also observed in a few sPD-derived hiPSCs (*233*). Nevertheless, generating pathogenic cells for sPD modeling that display disease-relevant phenotypes remains challenging due to the multifactorial causes that underlie sPD etiology such as environmental factors or aging (*234*). Therefore, strategies to induce or accelerate aging are thought to be essential to mimic late-onset sporadic diseases. Amongst others, this can be achieved by overexpressing progerin, a truncated form of LMNA that contributes to the premature aging syndrome HGPS (*114*). hiPSCs exposed to progerin exhibit an accelerated aging phenotype which was sufficient to induce some PD-specific phenotypes (*235*). However, this strategy does not allow to fully recapitulate natural aging as nuclear aging, for example, is only one part of the normal aging process [reviewed in chapter 1.2]. Another strategy is the direct reprogramming of somatic cells to induced neurons without undergoing a state of pluripotency (*236*). These induced neurons were shown to exhibit aging-associated epigenetic marks as well as disease phenotypes. However, the reprogramming efficiency, as well as the purity of induced neurons, is not sufficient for detailed studies or drug screenings.

1.7. Aim of this thesis

The molecular and cellular mechanisms involved in sPD are still not entirely elucidated, also, due to the lack of suitable human model systems (*229*). The ascent of hiPSCs allowed the use of patient-specific stem cells as model systems to expand our knowledge on human physiology at the cellular level. However, during the reprogramming of patient-derived fibroblasts into hiPSCs, these cells are rejuvenated regarding their epigenetic state, transcriptome, telomeres, DNA damage, and mitochondrial function (*112, 237–240*). Thus, there is a concern that rejuvenated hiPSCs cannot recapitulate the phenotype of a late-onset disease like sPD.

This thesis aimed to establish a cellular model for sPD, which should be used to explore molecular alterations underlying the etiology and progression of sPD. Therefore

1) the effect of long-term in vitro cultivation on PD-related phenotypes like mitochondrial dysfunction should be investigated. To address this question, fibroblasts from sPD patients and age- and sex-matched Ctrl individuals were reprogrammed into hiPSCs by the ForiPS consortium(*241*) and should be cultivated for up to 70 passages. These hiPSCs should then be differentiated towards DAns and screened for known PD-associated phenotypes.
2) this cellular model system should be used to unravel cellular processes and molecular mechanisms contributing to sPD etiology by using unbiased molecular characterization methods such as transcriptome and non-targeted metabolomics analysis.
3) the discovered cellular processes should be validated by using various model systems for PD.

Parts of the following chapters were taken from yet unpublished manuscripts (Schmidt et al.) submitted to peer-reviewing journals.

2. Results

2.1. Model systems and the ForiPS consortium

In this thesis, hiPSCs derived from 7 late-onset sPD patients and 5 Ctrl individuals (with two clones per patient) were used for bioenergetic as well as multi-omic analysis. PD patients were extensively clinically examined and defined as having sPD by the absence of known PD-causing familial mutations (***Table 1***; PARK 1-18). The hiPSC clones were established, characterized, and provided by the ForIPS consortium (*241*). A complete list of received hiPSC clones is given in ***Table 2***.

Table 2 | Detailed description of retroviral hiPSC clones received from the ForIPS consortium.

hiPSC clone ID	Patient ID	Gender	Age at biopsy [years]	Time between diagnosis and biopsy [years]
UKERiJ2C-R1-012	J2C	Male	73	3
UKERiJ2C-R1-015	J2C	Male	73	3
UKERiM89-R1-005	M89	Male	64	3
UKERiM89-R1-006	M89	Male	64	3
UKERiC99-R1-007	C99	Male	68	7
UKERiC99-R1-008	C99	Male	68	7
UKERiR66-R1-007	R66	Male	54	3
UKERiR66-R1-014	R66	Male	54	3
UKERiAY6-R1-003	AY6	Male	37	4
UKERiAY6-R1-004	AY6	Male	37	4
UKERiPX7-R1-001	PX7	Male	49	1
UKERiPX7-R1-002	PX7	Male	49	1
UKERi88H-R1-001	88H	Female	63	6
UKERi88H-R1-002	88H	Female	63	6
UKERi1JF-R1-011	1JF	Male	42	Ctrl
UKERi1JF-R1-018	1JF	Male	42	Ctrl
UKERiG3G-R1-032	G3G	Female	69	Ctrl
UKERiG3G-R1-039	G3G	Female	69	Ctrl
UKERi1E4-R1-003	1E4	Male	53	Ctrl
UKERi1E4-R1-012	1E4	Male	53	Ctrl
UKERiO3H-R1-001	O3H	Male	71	Ctrl
UKERiO3H-R1-005	O3H	Male	71	Ctrl
UKERi82A-R1-001	82A	Female	66	Ctrl
UKERi82A-R1-002	82A	Female	66	Ctrl

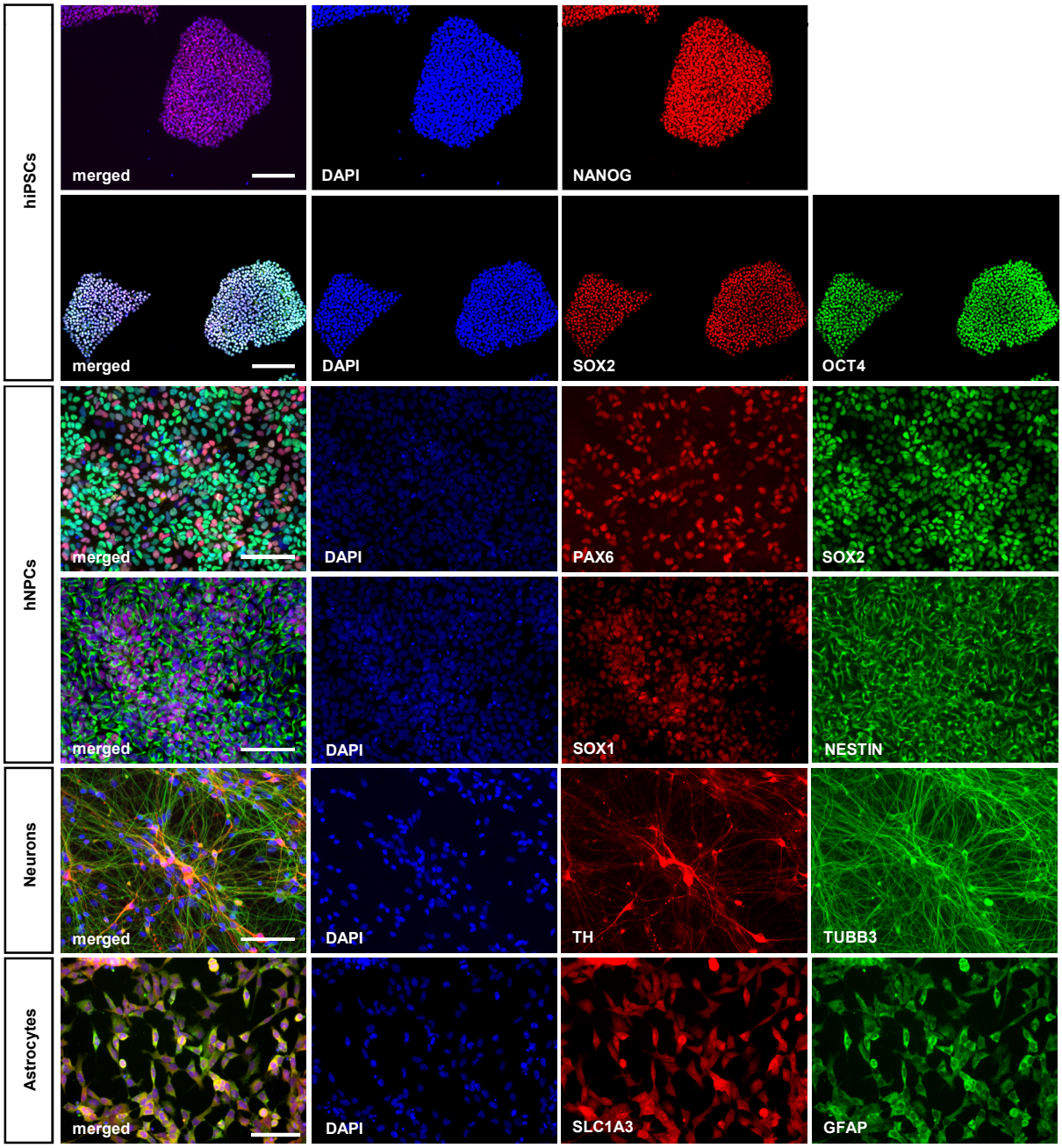

Figure 10 | Characterization of high-passage hiPSC derived hNPCs, neurons, and astrocytes. Immunostainings are exemplarily shown for iO3H-R1-003. hiPSC pluripotency staining for markers OCT4, NANOG, SOX2. Scale bar = 200 µm. hNPC staining for markers SOX1, SOX2, NESTIN, PAX6. Scale bar = 100 µm. Neuron staining for markers TUBB3 and DAn marker TH. Scale bar = 100 µm. Astrocyte staining for markers GFAP and SLC1A3. Scale bar = 100 µm. In parts taken from a manuscript (Schmidt et al.) submitted to peer-reviewing journals.

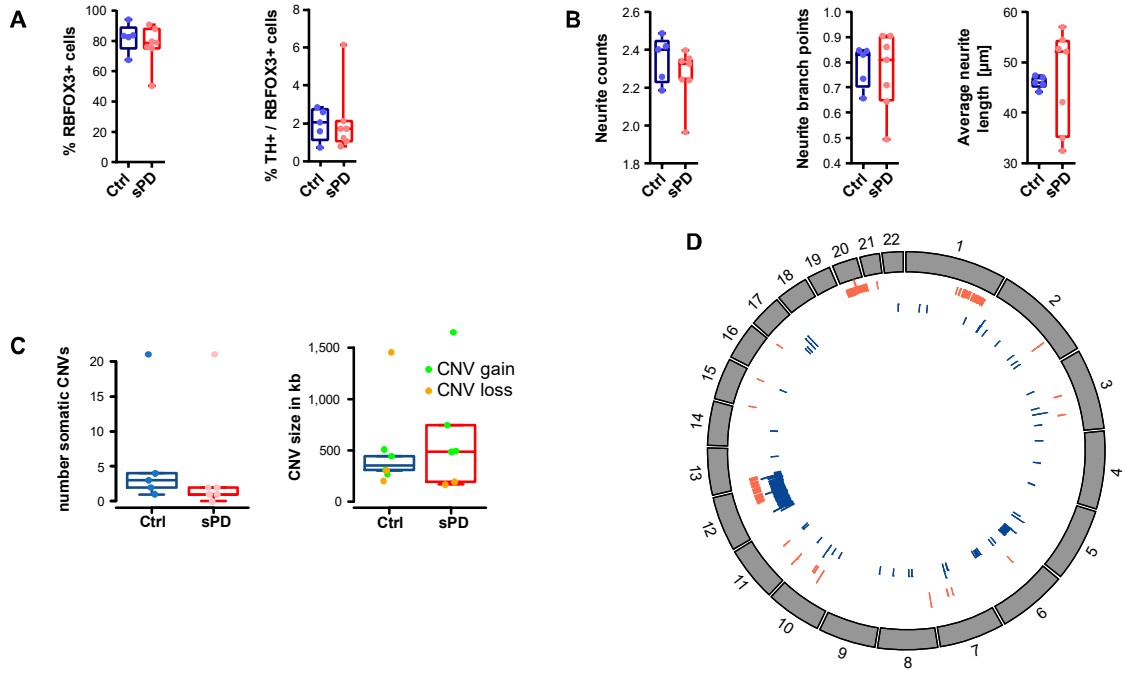

Figure 11 | Copy number variation of high-passage hiPSC derived cells. (A) Quantification of RBFOX3 (synonym: NeuN) positive as well as TH / RBFOX3 double-positive cells in a neuronal population derived from high-passage hiPSCs. **(B)** Quantification of neurites emerging from TH positive cells in a neuronal population derived from high-passage hiPSCs. Boxplots show the average number of neurites emerging from one cell body, their average number of branch points and their average length (in collaboration with Michael Ziller). **(C)** Summary of somatic CNVs identified in hNPC clones by chromosomal microarray analysis is shown as (left) the total number of somatic CNVs detected per analyzed clone (dots) and the (right) average length of CNVs (in kb; green dots = copy number gain; orange dots = copy number loss) per analyzed clone. No significant differences regarding the number and size of somatic CNVs between Ctrl and sPD clones were detected. n = 5 Ctrl and 7 sPD clones. **(D)** Circos plot showing the genomic distribution of somatic CNVs in Ctrl (blue) and sPD (red) clones. Boxplots are displayed from min to max values with all data points shown. P values are determined by (t-test A; Mann-Whitney-U test **C**). *, $p < 0.05$; **, $p < 0.01$; ***, $p < 0.001$. In parts taken from a manuscript (Schmidt et al.) submitted to peer-reviewing journals.

To explore mechanisms underlying sPD etiology, the patient-derived hiPSCs were differentiated towards the midbrain dopaminergic lineage. In a first step, hiPSCs were differentiated into hNPCs which are thought to mimic neuroepithelial cells at the border between the neural plate and neural crest, and thus to have the developmental potential to form neural tube- as well as neural crest-derived lineages (*242*). These precursor cells showed correct expression of the pluripotency markers SOX1 and SOX2, as well as of the neuronal precursor markers NES, Pax6, and SOX10 (staining not shown) (***Figure 10***). The expression of PAX6 indicates midbrain identity, whereas SOX10 is implicated in neural crest formation. In a second step, these hNPCs were further differentiated into astrocytes which showed correct expression of the astrocyte markers SLC1A3 and GFAP, as well as a neuronal population enriched for midbrain DAns which showed correct expression of the neuronal markers TUBB3 and TH (***Figure 10***).

Aging has been considered the greatest risk factor for developing sPD. Thus, it is thought that hiPSCs per se could be unsuitable for modeling sPD, as during reprogramming a process of rejuvenation seems to occur. Although several strategies to induce or accelerate aging in hiPSCs such as progerin overexpression have been tested, the generation of pathogenic cells for sPD modeling that display disease-relevant

phenotypes remains challenging. In this thesis, it was attempted to recapitulate an aging phenotype in hiPSCs by prolonged *in vitro* cultivation as published by (*243*). hiPSCs were cultivated in vitro after reprogramming for approximately 60 passages. hiPSCs at passage ~25 are hereinafter referred to as low-passage hiPSCs and at passage ~60 as high-passage hiPSCs.
To exclude an effect of copy number variations (CNVs) that may accumulate during passaging, an CNV analysis was performed in high-passage hiPSCs using an Infinium CoreExome-24 v1.3 microarray. The number (Ctrl: 6.2±8.3; sPD: 4.0±7.5) and size (Ctrl: 986.4±623.2; sPD: 623.2±548.5) of CNVs were slightly increased in comparison to those published for low-passage hNPCs (*241*) but did not show significant differences between sPD and Ctrl (***Figure 11C***, ***D***). However, various genes were affected by CNVs in some Ctrl clones (*PRKG1, DKK1, PRKG1-AS1, IQSEC3, RP11-598F7.3, RP11-598F7.4, RP11-598F7.5, RP11-598F7.6, SLC6A12*) and some sPD clones (*RP11-38L15.3, SYT15, GPRIN2*). So far none of these genes have been associated with sPD. Furthermore, the CNVs did not seem to have an effect on neuronal differentiation efficiency. Neuronal populations derived from both sPD and Ctrl clones contained approximately 80 % neurons positive for RBFOX3 (synonym: NeuN) (Ctrl: 82.2±9.5; sPD: 77.0±13.2) as well as around 2 % DAns double-positive for RBFOX3 and TH (Ctrl: 1.96±0.85; sPD: 2.11±1.84) (***Figure 11A***). However, quantification is likely to underestimate the actual values, as neurons especially DAns tend to grow in neurospheres which had to be excluded from the analysis. Interestingly, also the neurite morphology (average length Ctrl: 46.03±1.27; sPD: 46.55±9.93) (average count per cell Ctrl: 2.35±0.12; sPD: 2.27±0.14) (average branch points Ctrl: 0.78±0.08; sPD: 0.76±0.15) was similar in DAns derived from sPD and Ctrl hiPSC clones (***Figure 11B***). Thus, it can be concluded that high-passage numbers did not have a differential effect on the genomic integrity as well as on the differentiation and maturation potential of cells derived from patients and Ctrls.
To establish our cellular system as a model for sPD, we analyzed the cellular respiration of hiPSCs and their derivatives, which is known to be impaired in postmortem brain tissue of sPD patients (*244, 245*).

2.2. Respiratory analysis of the dopaminergic lineage

Cellular respiration was assessed in fibroblasts, low- and high-passage hiPSCs, hNPCs, and DAns derived from sPD patients and Ctrls using Seahorse XF analysis. This system allows the parallel assessment of the oxygen consumption rate (OCR) and the extracellular acidification rate (ECAR) of cell monolayers. As oxygen consumption is coupled to mitochondrial ATP synthesis, the measurement of cellular respiration is in consequence a measurement of mitochondrial energy metabolism. Furthermore, the sequential injection of chemicals that target components of the electron transport chain allows the assessment of multiple parameters, like basal respiration, proton leak, ATP-linked respiration, and maximal respiratory capacity (***Figure 12A***).
Basal respiration is the OCR measured during cellular homeostasis. It is the combination of oxygen consumption linked to ATP synthesis and oxygen consumption used to compensate for the proton leakage across the IMM. Substitution of the ATP-synthase inhibitor oligomycin (Olig) results in a decreased OCR, which can now be solely correlated to the respiration used to compensate for mitochondrial proton leak. The difference to the basal respiration thus determines the ATP-linked respiration. The uncoupling reagent FCCP is added to achieve the maximal mitochondrial respiration. The difference between maximal and basal respiration is defined as reserve capacity. This reserve capacity reflects the mitochondrial spare

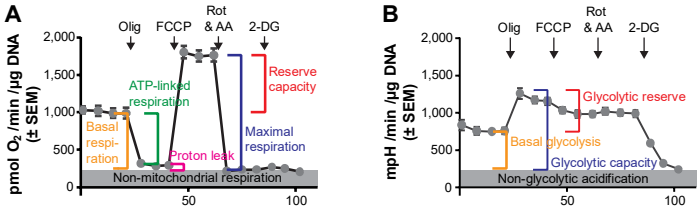

Figure 12 | Mitochondrial and glycolytic stress tests performed using a Seahorse XFe96 Extracellular Flux Analyzer. Cells were measured in Seahorse XF assay medium supplemented with 25 mM glucose or 5 mM pyruvate. (a) Oligomycin (Olig; 1 µg/ml), (b) FCCP (0.5 µM), (c) Rotenone (Rot; 5 µM)/Antimycin A (AA; 2 µM) and (d) 2-Deoxyglucose (2-DG; 100 mM) were injected in the indicated order. Measurement progression is shown with means ± standard error of the mean (SEM).

capacity to increase ATP synthesis in periods of high energy demand. For example, post-mitotic neurons that have to fire and respond to environmental changes are thought to have a higher reserve capacity than mitotic cells which constantly have a high energy demand. In a last step rotenone (Rot) and antimycin-A (AA), inhibitors of complex I and III, are injected which will completely shut down the mitochondrial electron transport chain and thus respiration. This yields the non-mitochondrial respiration which has to be subtracted from the cellular respiration to gain the OCR solely linked to mitochondrial respiration.

Different energy substrates allow to investigate the contribution of specific metabolic pathways to cellular respiration and can be used to determine possible bottlenecks. Thus, cells were analyzed in a minimal medium (Seahorse XF assay medium) supplemented with either 25 mM glucose or 5 mM pyruvate. 25 mM glucose was chosen to provide excess substrate for cells that are exposed to high-stress levels during Seahorse measurements. Similarly, 5 mM pyruvate was chosen as a higher intracellular concentration might result in free diffusion rather than controlled transport of pyruvate into mitochondria.

Using glucose as an energy substrate, we observed no difference in the OCR between Ctrl and sPD in fibroblasts, as well as in hNPCs and DAns derived from low-passage hiPSCs (***Figure 14A**,**C**,**D***; ***Table 16***). However, there was a significant decrease in the maximal respiratory capacity of high-passage sPD hiPSCs, hNPCs, and a trend in high-passage DAns. The basal respiration is also decreased in low-passage and high-passage sPD hiPSCs and high-passage hNPCs (***Figure 14A**-**D***; ***Table 16***). As the low-passage cells did not show changes in the maximal respiratory capacity, these results indicated an sPD specific defect of mitochondrial respiration in neural cells derived from high-passage hiPSCs.

To determine the bottleneck of the respiratory defect, pyruvate, which can be fed directly into the citric acid cycle whereas glucose has to pass through glycolysis, was additionally supplied as substrate. As observed for glucose before, mitochondrial respiration of fibroblasts, low-passage hiPSCs, hNPCs, and DAns was not altered between sPD and Ctrl (**Figure *13A-D***; ***Table 16***), except for the basal mitochondrial respiration of low-passage hiPSCs which was reduced in sPD. Although there was no significant difference in the maximal respiration of high-passage hiPSCs, the high-passage hNPCs, and DAns showed an sPD specific decrease. Again, low-passage hiPSCs, as well as high-passage hNPCs and DAns, exhibited a significantly reduced basal mitochondrial respiration and a trend was observed in high-passage hiPSCs (**Figure *13B-D***; ***Table 16***). As mitochondrial respiration was still impaired when pyruvate was used as an energy substrate, this indicated a defect downstream of glycolysis, either in substrate delivery for the respiratory chain by the citric acid cycle or the respiratory chain itself. Furthermore, these results hinted

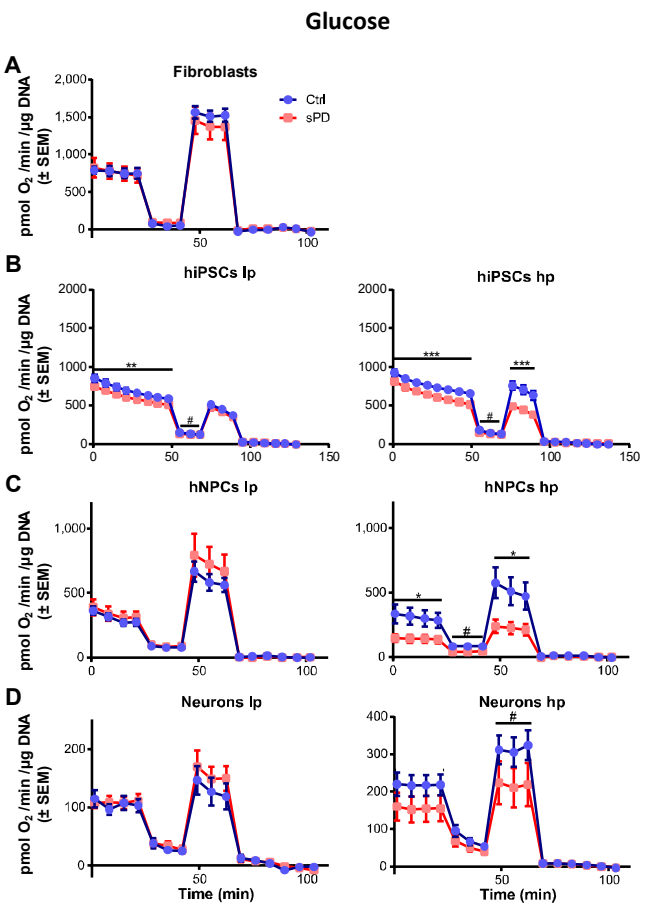

Figure 14 | Respiratory characterization of Ctrl and sPD cell lines using glucose as energy substrate. (A) Mitochondrial stress test performed in fibroblast lines, **(B)** (left) low-passage and (right) high-passage hiPSC clones (data provided by (*245*)), **(C)** hNPC lines and **(E)** DAns using a Seahorse XFe96 Extracellular Flux Analyzer. Cells were measured in Seahorse XF assay medium supplemented with 25 mM glucose as described in ***Figure 12A***. Measurement progression is shown with means ± standard error of the mean (SEM). n = 5 Ctrl and 7 sPD clones, in triplicates. P values are determined by (***Table 16***). #, $p < 0.1$; *, $p < 0.05$; **, $p < 0.01$; ***, $p < 0.001$. In parts taken from a manuscript (Schmidt et al.) submitted to peer-reviewing journals.

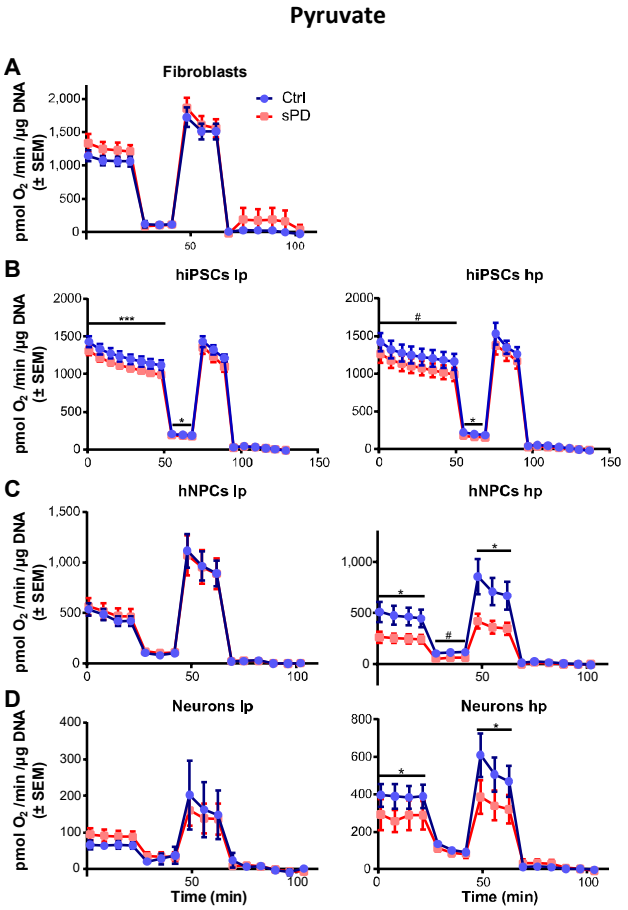

Figure 13 | Respiratory characterization of Ctrl and sPD cell lines using pyruvate as energy substrate. (A) Mitochondrial stress test performed in fibroblast lines, **(B)** (left) low-passage and (right) high-passage iPSC clones (data provided by (*245*)), **(C)** hNPC lines and **(D)** DAns using a Seahorse XFe96 Extracellular Flux Analyzer. Cells were measured in Seahorse XF assay medium supplemented with 5 mM pyruvate as described in ***Figure 12A***. Measurement progression is shown with means ± standard error of the mean (SEM). n = 5 Ctrl and 7 sPD clones, in triplicates. P values are determined by (***Table 16***). #, $p < 0.1$; *, $p < 0.05$; **, $p < 0.01$; ***, $p < 0.001$. In parts taken from a manuscript (Schmidt et al.) submitted to peer-reviewing journals.

towards a defect of cellular respiration not due to long-term cultivation per se, but rather due to a specific sPD background.

To get a more comprehensive overview of cellular metabolism, the glycolytic flux was assessed in parallel to mitochondrial respiration. The oxidation of glucose during glycolysis depends on ATP hydrolysis and results in the production of protons and anions like pyruvate or lactate. These processes acidify the medium, thus, the ECAR is thought to correlate with glycolytic activity. However, the ECAR only offers a rough overview of glycolytic rates as various other cellular processes also contribute to extracellular acidification and it is therefore much more complex to interpret.

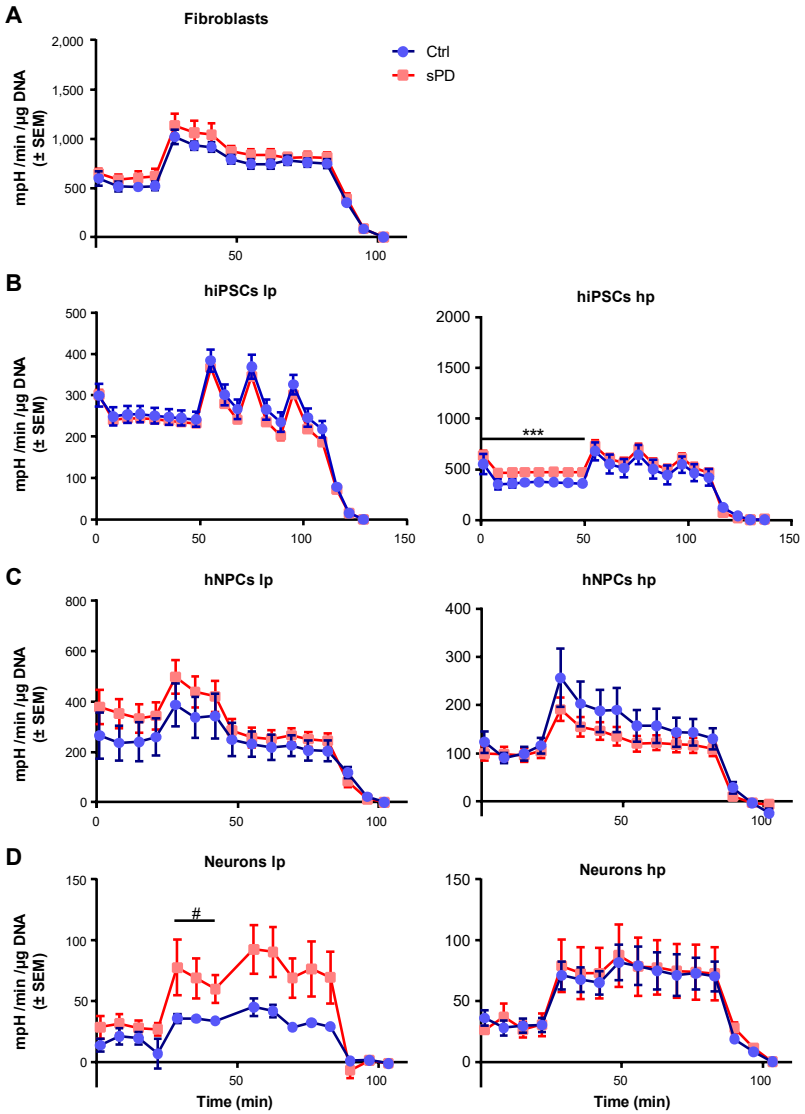

Figure 15 | Glycolytic flux analysis of Ctrl and sPD cell lines with glucose as energy substrate. (A) Extracellular acidification rate (ECAR) analyzed in fibroblast lines, **(B)** (left) low-passage and (right) high-passage iPSC clones (data provided by (*246*)), **(C)** hNPC lines, and **(D)** DAns using a Seahorse XFe96 Extracellular Flux Analyzer. Cells were measured in Seahorse XF assay medium supplemented with 25 mM glucose as described in ***Figure 12B***. Measurement progression is shown with means ± standard error of the mean (SEM). n = 5 Ctrl and 7 sPD clones, in triplicates. P values are determined by (***Table 16***). #, $p < 0.1$; *, $p < 0.05$; **, $p < 0.01$; ***, $p < 0.001$. In parts taken from a manuscript (Schmidt et al.) submitted to peer-reviewing journals.

The glycolytic flux was only analyzed in cells supplied with 25 mM glucose as an energy substrate. The basal rate or basal glycolysis is measured first. Subsequent injection of oligomycin inhibits mitochondrial ATP production which causes an increased glycolytic flux and ATP production to meet the cells' energy demand. This glycolytic flux rate is considered to be the maximal possible glycolytic flux, also referred to as glycolytic capacity. The difference between the glycolytic capacity and the basal glycolytic rate is defined as the glycolytic reserve. In the last step, 2-deoxyglucose (2-DG), an allosteric inhibitor of the enzyme

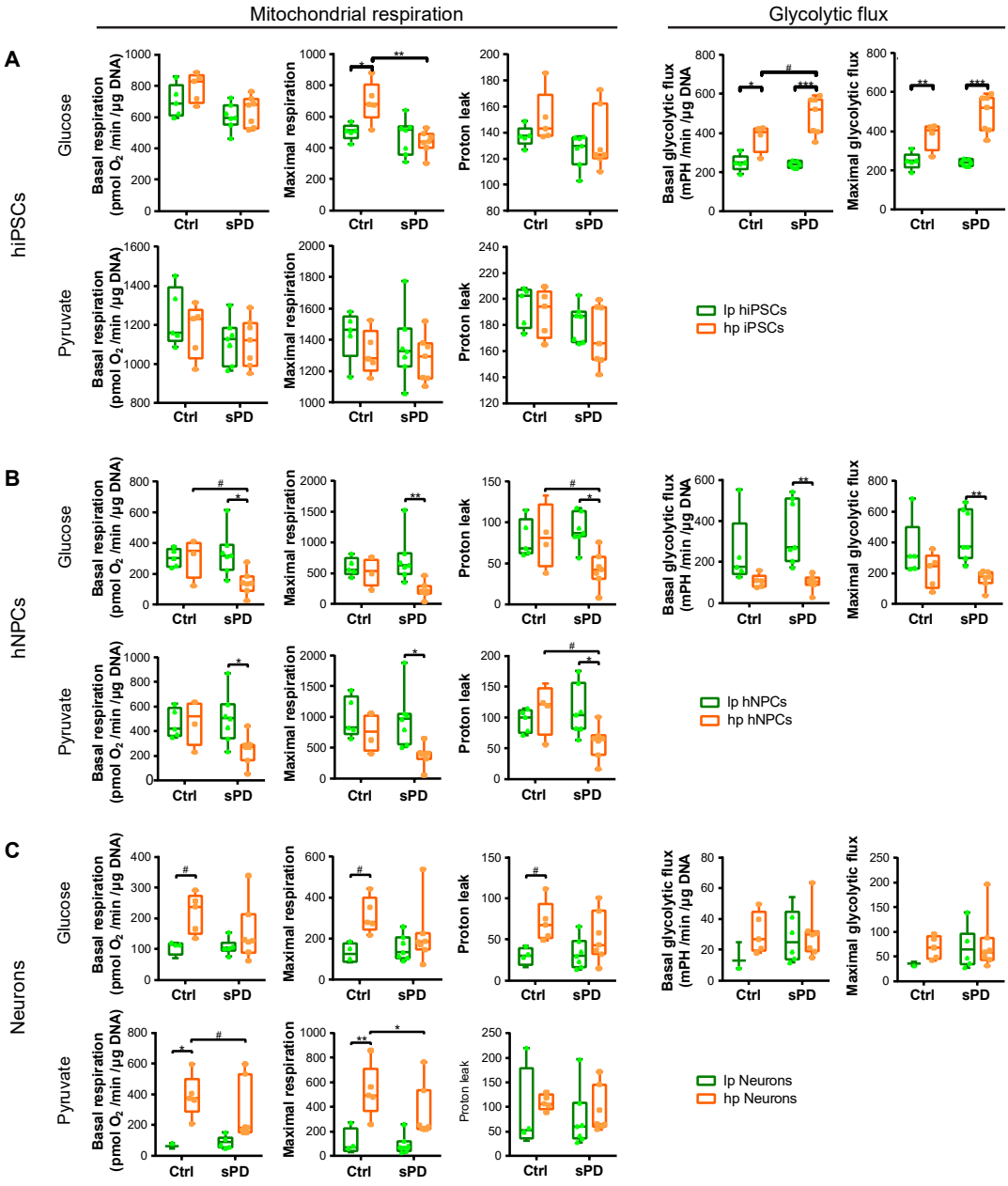

Figure 16 | Comparison of metabolic function between low- and high-passage cells. (A) Mitochondrial and glycolytic stress test performed in low-passage (lp) and high-passage (hp) hiPSCs (data provided by (*246*)), **(B)** hNPCs, and **(C)** DAns using a Seahorse XFe96 Extracellular Flux Analyzer. Cells were measured in Seahorse XF assay medium supplemented with 25 mM glucose or 5 mM pyruvate. n = 5 Ctrl and 7 sPD clones, in triplicates. Boxplots are displayed from min to max values with all data points shown. P values are determined by (two-way ANOVA and Tukey`s Post-hoc test) (***Table 17***). #, $p < 0.1$; *, $p < 0.05$; **, $p < 0.01$; ***, $p < 0.001$. In parts taken from a manuscript (Schmidt et al.) submitted to peer-reviewing journals.

hexokinase is injected which will completely shut down glycolysis. The resulting non-glycolytic acidification is subtracted from the cellular ECAR to obtain the ECAR solely linked to glycolytic rates. General analysis

across health state (Ctrl or sPD) and passage number (low-passage or high-passage) was evaluated using two-way ANOVA and Tukey`s Post-hoc test, an overview is given in **Figure *16*** (***Table 17***).
As expected, glycolytic flux analysis did not show significant differences in the ECAR between sPD and Ctrl neither in low-passage nor in high-passage cells (**Figure *15A*-*D***; ***Table 16***), supporting a defect in the mitochondrial citric acid cycle or respiratory chain. Basal and maximal glycolytic flux was increased in high-passage Ctrl and sPD hiPSCs compared to low-passage cells, which probably does not indicate an sPD specific phenotype, but rather a shift towards glycolysis upon long-term in vitro cultivation (**Figure *16A***; ***Table 17***). However, this is reversed in hNPCs (**Figure *16B***; ***Table 17***). Although not significantly for the Ctrls, both high-passage sPD and Ctrl hNPCs show a decrease in basal and maximal glycolytic flux compared to the corresponding low-passage cells. As glycolytic flux measurements did not differ between low and high-passage DAns (**Figure *16C***; ***Table 17***), high-passage hNPCs might be faster than low-passage hNPCs in the switch from glycolytic metabolism, typical for iPSCs, towards an oxidative metabolism which is characteristic for neurons.
Altogether, no major respiratory defects in hiPSCs downstream of glycolysis (***Figure 14B;*** **Figure *13B*** and **Figure *15B***; ***Table 16***) could be observed, thus any reduction in basal or maximal respiration with glucose as energy substrate is probably a substrate availability problem. Whereas upon entering neural lineage, metabolic deficits become specific for mitochondria and in contrast to hiPSCs occur only in sPD cells (***Figure 14C,E;*** **Figure *13C,E*** and **Figure *15C,E***; ***Table 16***).

2.3. Respiratory analysis of non-dopaminergic cell types

The cells that are mostly affected by degeneration in PD are the midbrain DAns located in the SNpc. To investigate neural lineage specificity, the same high-passage hNPCs that were used for DAn differentiation were differentiated into astrocytes. The respiratory metabolism of high-passage astrocytes was then also analyzed by mitochondrial stress test.
In functional brain tissues, the synaptic activity of neurons results in elevated extracellular concentrations of glutamate which is taken up by astrocytes to prevent excitotoxicity. The glutamate uptake is a highly energy-demanding process as the transport of one molecule of glutamate consumes one molecule of ATP. Therefore, astrocytes have high rates of oxidative metabolism, but can also metabolize glutamate which is converted to α-ketoglutarate and thereby enters the citric acid cycle. Hence, using glutamate instead of pyruvate as an energy substrate for astrocytes should be a further stressor and could reveal pathological features missed using only glucose as an energy substrate. In contrast to DAns, no difference in the basal or maximal mitochondrial respiration, proton leak, as well as basal or maximal glycolytic flux between sPD and Ctrls could be observed using glucose as energy substrate. Also, no difference in the basal or maximal mitochondrial respiration, as well as proton leak could be detected using glutamate as energy substrate (**Figure *17B***; ***Table 16***).
PD is viewed traditionally as a motor syndrome caused by nigrostriatal dopaminergic denervation. In addition to alterations in the dopaminergic system, there is also evidence for early alterations in cholinergic neurotransmission. A significant loss of cholinergic neurons in the nucleus basalis of Meynert in PD brains has been reported in several studies [reviewed in (*247*)]. This is thought to results in a reduced CHAT activity in the SNpc (*248*), hippocampus, and especially in the neocortex (*249*). To address the question if there is a neuronal cell-type specificity for metabolic alterations in our cellular model, also the

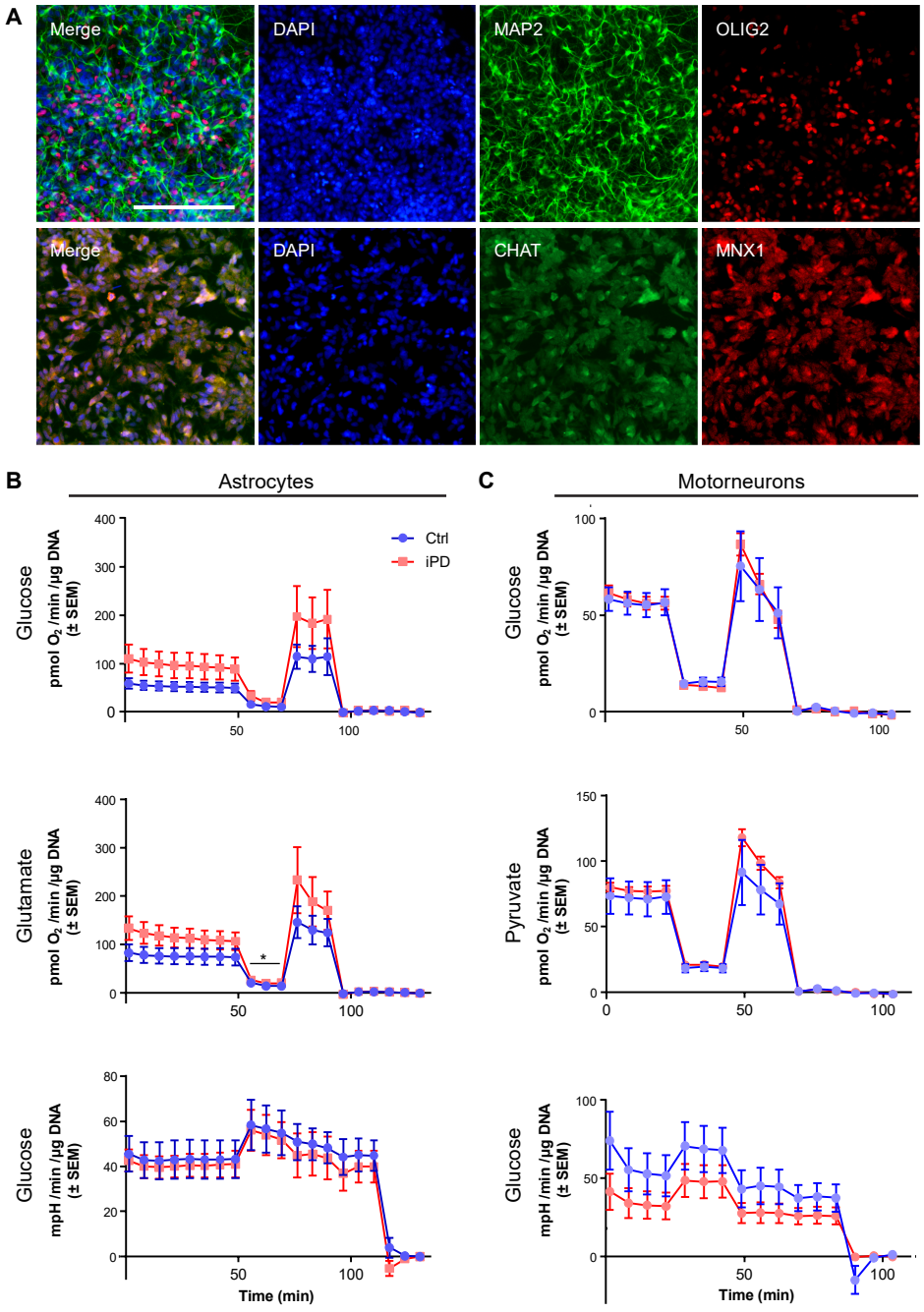

Figure 17 | Mitochondrial alterations of non-dopaminergic cell types derived from high-passage sPD lines. (A) Immunocytochemistry for motor neuron-specific markers (MAP2, CHAT, MNX1) and the oligodendrocyte-specific marker OLIG2. Motor neurons were differentiated from high-passage hiPSCs, exemplarily shown for iO3H-R1-003. Scale bar = 200 µm. **(B)** Mitochondrial stress test and glycolytic flux analysis performed in astrocytes (data provided by *(246)*), and **(C)** motor neurons using a Seahorse XFe96 Extracellular Flux Analyzer. Cells were measured in Seahorse XF assay medium supplemented with 25 mM glucose, 5 mM pyruvate, or 0.36 mM glutamate as described in ***Figure 12***. Measurement progression is shown with means ± standard error of the mean (SEM). n = 5 Ctrl and 7 sPD clones, in triplicates. P values are determined by (***Table 16***). *, $p < 0.05$; **, $p < 0.01$; ***, $p < 0.001$. In parts taken from a manuscript (Schmidt et al.) submitted to peer-reviewing journals.

cellular respiration of cholinergic neurons was analyzed. Therefore, high-passage hiPSCs were differentiated into motor neurons which showed correct expression of the motor neuron-specific markers MAP2, CHAT, and MNX1 (**Figure *17A***). Interestingly, no significant difference in basal and maximal mitochondrial respiration, proton leak, as well as basal and maximal glycolytic flux between Ctrl and sPD, could be detected in motor neurons using glucose as energy substrate. There was also no difference in the basal or maximal mitochondrial respiration, as well as in the proton leak could be detected using pyruvate as energy substrate (**Figure *17C***; ***Table 16***). Hence, the mitochondrial dysfunction is highly cell type-specific and only develops during differentiation towards the midbrain dopaminergic lineage, the cell type that is most prominently affected in PD.

2.4. Multiplexed single-cell RNA sequencing of high-passage hNPCs

To further unravel the molecular underpinnings of the cellular phenotype underlying the etiology of multifactorial sPD, we performed a pooled, droplet-based single-cell RNA sequencing (scRNA-seq) of hNPCs derived from high-passage hiPSCs using a 10xGenomics protocol (**Figure *18***).
In total, 16 different hiPSC clones derived from 14 individuals (7 sPD clones with 5 Ctrls, 1 *PINK1* ko, and 1 *PINK1* Q126P clone with their corresponding isogenic Ctrls) were used for scRNA-seq analysis. High-passage hiPSCs were differentiated to hNPCs and subsequently, hNPCs from different individuals were pooled to be analyzed in a single scRNA-seq library (**Table *3***). Pooled libraries from different individuals were demultiplexed based on SNPs, thereby avoiding confounding technical batch effects (see methods)

Table 3 | hiPSC clones used for scRNA-seq analysis. High-passage hiPSC clones were differentiated to hNPCs, which were pooled in two different cell mixes as indicated below. In total 15,650 hNPCs were loaded per flow cell lane to capture and sequence at least 9,000 cells per library. 6 scRNA-seq libraries were generated to sequence in total approximately 54,000 cells.

hiPSC clone ID	Health state	Cell numbers in scRNA-seq libraries 1 to 3	Cell numbers in scRNA-seq library 4 to 6
UKERi1JF-R1-018	Ctrl (sPD)	978	978
UKERiG3G-R1-039	Ctrl (sPD)	978	978
UKERi1E4-R1-003	Ctrl (sPD)	978	978
UKERiO3H-R1-005	Ctrl (sPD)	978	978
UKERi82A-R1-002	Ctrl (sPD)	978	978
UKERiJ2C-R1-015	sPD	978	978
UKERiM89-R1-005	sPD	978	978
UKERiC99-R1-007	sPD	978	978
UKERiR66-R1-007	sPD	978	978
UKERiAY6-R1-003	sPD	978	978
UKERiPX7-R1-001	sPD	978	978
UKERi88H-R1-002	sPD	978	978
K7.1	Ctrl (fPD - PINK1 knock-out)	1,956	0
Δ40.7	fPD - PINK1 knock-out	0	1,956
17/5 clone 2	Ctrl (fPD - PINK1 Q126P)	0	1,956
C4 clone 1	fPD - PINK1 Q126P	1,956	0

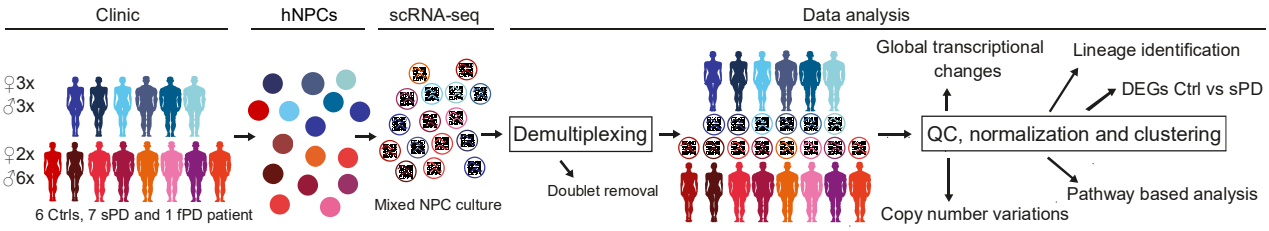

Figure 18 | scRNA-seq profiling. Experimental and bioinformatic workflow for multiplexing of 16 hNPC clones derived from 14 individuals. QC, quality control. In parts taken from a manuscript (Schmidt et al.) submitted to peer-reviewing journals.

(*250*). hNPCs derived from high-passage hiPSCs were chosen, as they are thought to be the earliest differentiation state that undergoes the metabolic switch associated with neuron differentiation. In addition, hNPCs can be used as an effective drug discovery model for neurological disorders and were also severely affected [see chapter 2.2.] (*251*).

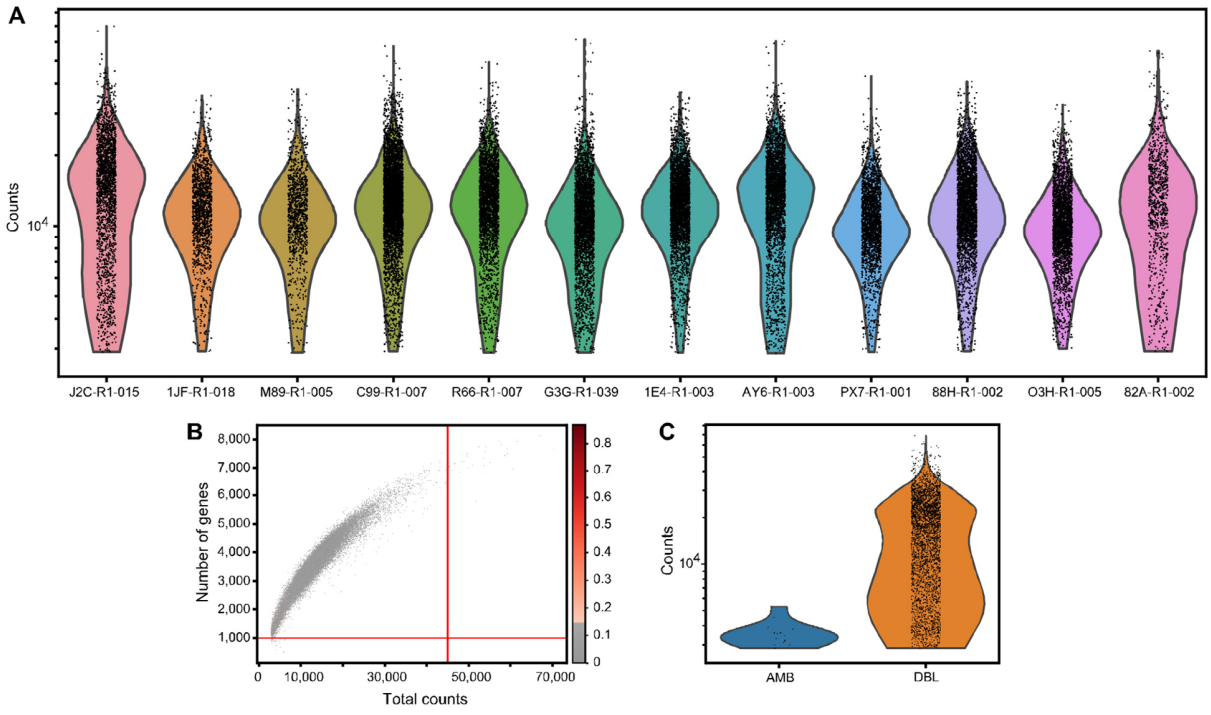

Figure 19 | scRNA-seq quality control. (A) Distribution of UMI counts per donor showing the consistent quality of cells. **(B)** Plot of number of detected genes per cell vs number of UMI counts per cell with implemented quality control thresholds shown as red lines. Data was filtered to have a minimum of 1,000 genes per cell at maximum 45,000 total counts. This also eliminates most cells with a high fraction of mitochondrial reads. **(C)** Distribution of UMI counts for cells that could not be assigned to a donor by demuxlet (AMB) and cells that were called as doublets (DBL). n = 30,557 hNPCs derived from 5 Ctrl and 7 sPD clones. In parts taken from a manuscript (Schmidt et al.) submitted to peer-reviewing journals. In collaboration with Malte Lücken.

2.4.1. Quality control

Pooled libraries from different individuals were demultiplexed based on SNPs, which allowed not only to avoid confounding technical batch effects but also to precisely identify and remove doublets (DBLs) and ambiguous cells (AMB) that could not be assigned to one specific donor (***Figure 19C***).
In total, 44,239 cells from six scRNA-seq libraries (6,602; 6,703; 6,958; 7,958; 7,964; 8,014; 7,998 cells, respectively) were sequenced. These cells were profiled with about 90,000 reads/cell, which allowed to identify in median 3,857; 3,889; 3,784; 3,339; 3,371; 3,254 genes per cell with 14,297; 14,621; 14,078; 11,461; 11,745; 11,208 unique molecular identifier (UMI) counts per cell.
After considering the joint distribution of count depth, the number of genes expressed, and mitochondrial read fraction per sample, cells with more than 45,000 counts, with fewer than 1,000 genes expressed, and with 15 % or more reads aligned to mitochondrial genes were filtered out (***Figure 19B***). Furthermore, genes that were measured in fewer than 20 cells were also removed from the dataset. Demultiplexing and quality control led to a dataset of 30,557 individual cells and 24,920 genes, which were profiled with about 90,000 reads/cell.
Further analysis of the visualization and clustering showed that none of these clusters was dominated by either disease state, gender, age, or individual donors (***Figure 20***). However, the Ctrl clone i1E4-R1-003 was slightly overrepresented in one cluster but also contributes to all other clusters with its remaining cells. Removal of this respective individual did not change the overall results. Therefore, clone i1E4-R1-003 was kept as part of the analysis.

2.4.2. Cluster annotation and RNA velocity

To classify distinct cell subpopulations within the hNPC cultures, cell clusters that produce a transcriptionally distinct cell population with highly consistent expression patterns across individuals should be identified and annotated (***Figure 21A***). These cellular populations were identified and annotated by the expression patterns of specific marker genes (***Figure 22***). In total, nine distinct clusters were annotated: neural crest stem cells (NCSC – marked by the expression of *LUM*, *LGALS1* and a high fraction of ribosome (*252*) and extracellular matrix (*253*) constituents), glial precursors (marked by the expression of *SOX10* and *S100B* (*254*)), apoptotic cells (marked by their low mitochondrial fraction, active cell death signaling and nonspecific marker genes), immature neurons (marked by the expression of *DCX* and *MAP2* (*255*)), and neural stem cells (NSCs) “proper” all of which expressed the marker gene *SOX2* (*256*). This NSC cluster could be subdivided into 4 sub-clusters based on differential expression of respective marker genes. The cluster NSC1a was marked by the expression of *DAAM1*, *FABP7*, *PTCH1*, and *DLL1*, whereas the cluster NSC2a was characterized by the expression of *SHH*, *FOXA2*, and *HES1*. The remaining two clusters NSC1b and NSC2b were characterized by the expression of similar genes as NSC1a and NSC2a, respectively, however, expressed also genes associated with the G2M phase of the cell cycle such as *CENPF*, *AURKB*, and *CDC20* (*257*). Interestingly, pathway analysis superimposed on the respective marker genes revealed that the NSC1 cluster was predominantly marked by the NOTCH and WNT signaling pathway, whereas the NSC2 cluster was predominantly marked by SHH expression and the FOXA transcription factor network. Temporal and spatial activation of these pathways plays an important role in the proliferation and

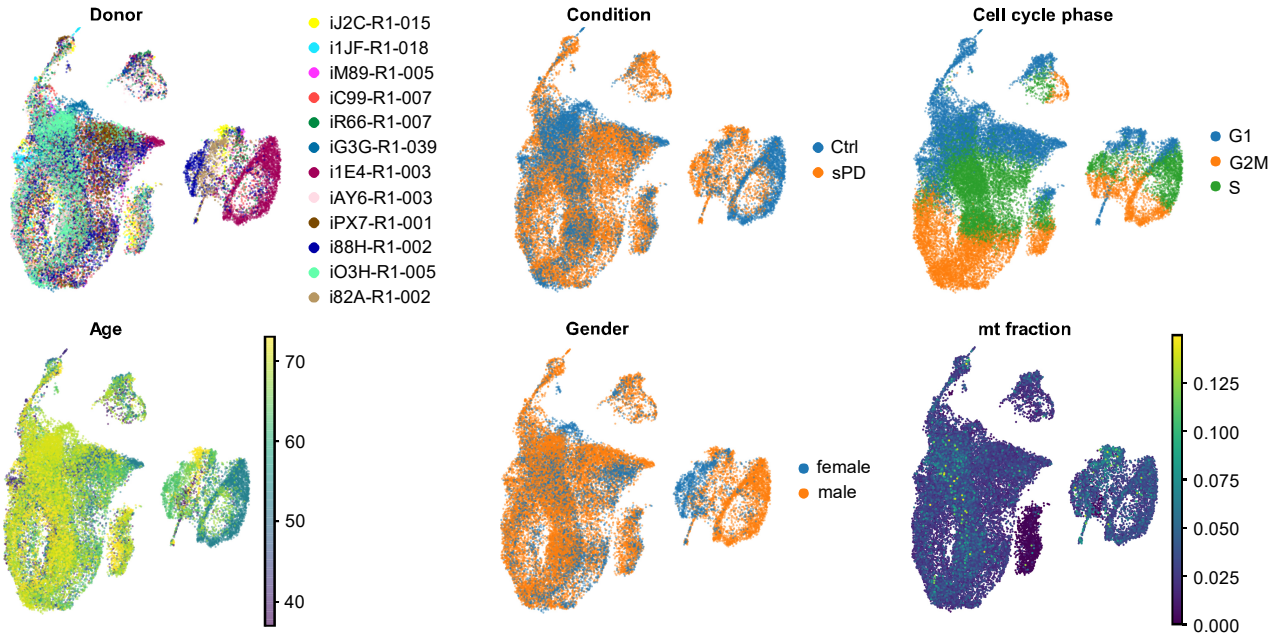

Figure 20 | scRNA-seq metadata visualization. UMAP visualizations of the processed scRNA-seq dataset with metadata annotations for donor, disease condition (Ctrl, sPD), cell cycle phase (G1-, G2/M-, S-phase), donor age, gender, and fraction of UMI counts from mitochondrial (mt) genes. n = 30,557 hNPCs derived from 5 Ctrl and 7 sPD clones. In parts taken from a manuscript (Schmidt et al.) submitted to peer-reviewing journals. In collaboration with Malte Lücken.

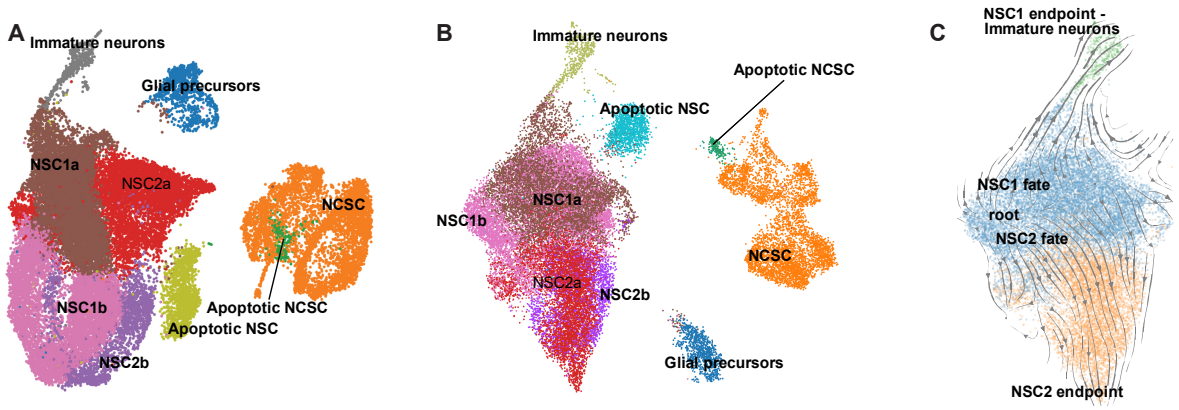

Figure 21 | scRNA-seq clustering and RNA velocity. (A) UMAP visualization of 30,557 annotated cells from 5 Ctrl and 7 sPD hNPC clones within the clusters NSC: neural stem cells, immature neurons, glial precursors, NCSC: neural crest stem cells, and apoptotic NSC / NCSC. **(B)** UMAP visualization of processed scRNA-seq dataset with cell cycle effects regressed out. Cells are colored by cell identity clusters. **(C)** RNA velocity analysis reveals two NSC trajectories on immature neurons (NSC1 fate) and NSC populations (NSC2 fate) as well as one developmental point of origin (root) after cell cycle effects are regressed out. In parts taken from a manuscript (Schmidt et al.) submitted to peer-reviewing journals. In collaboration with Malte Lücken.

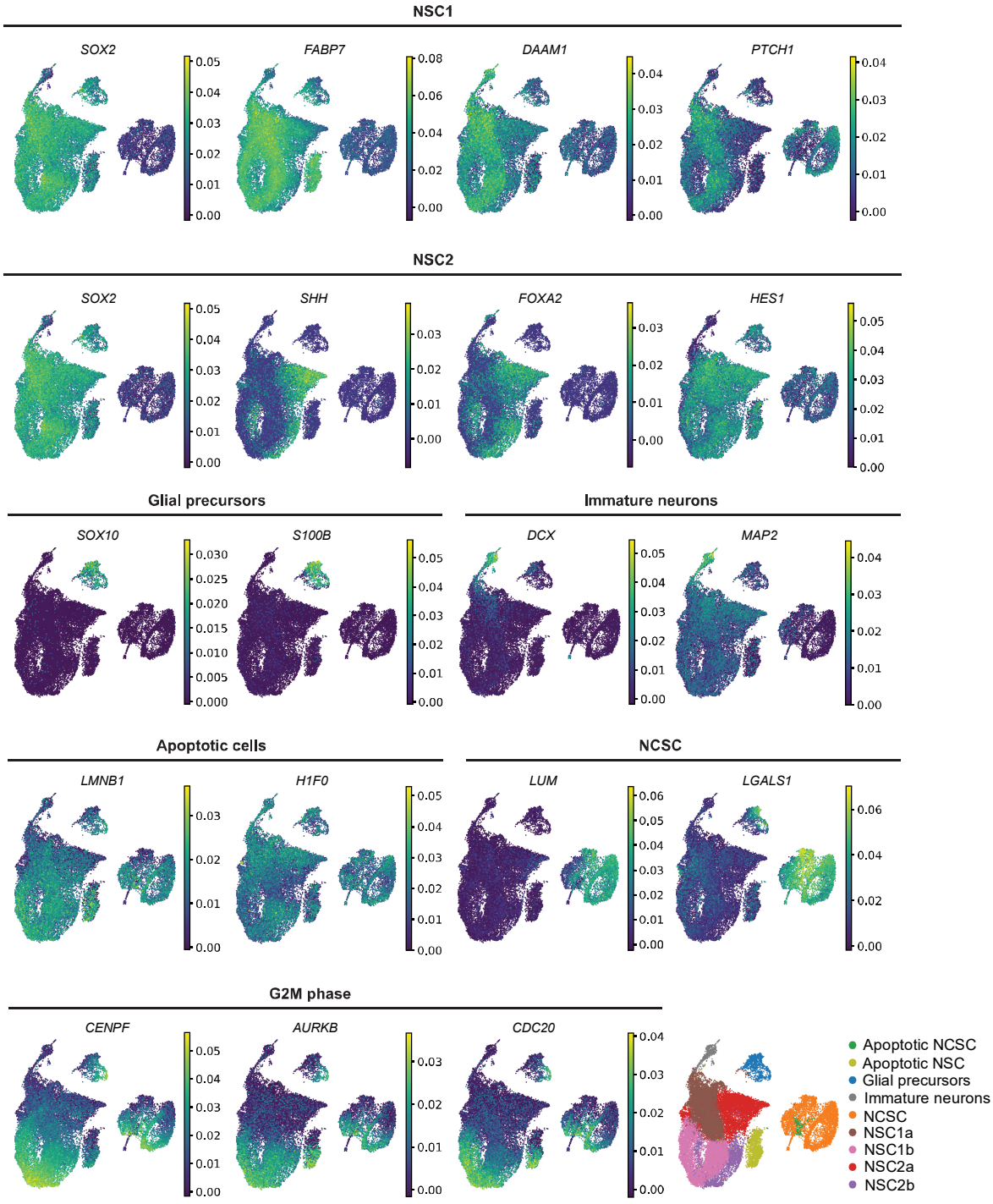

Figure 22 | scRNA-seq cluster annotation. UMAP visualization of mutual nearest neighbor (MNN)-corrected expression values of known cellular marker genes used to identify clusters. **NSC1:** SOX2, DAAM1, FABP7, PTCH1, DLL1; **NSC2:** SOX2, SHH, FOXA2, HES1; **Glial precursors:** SOX10, S100B; **immature neurons:** DCX, MAP2; **apoptotic cells:** LMNB1, H1F0; NCSC: LUM, LGALS1; **NSC1/2 G2M:** CENPF, AURKB, CDC20. Final cluster annotations are shown in the UMAP plot in the bottom right corner. n = 30,557 hNPCs derived from 5 Ctrl and 7 sPD clones. In parts taken from a manuscript (Schmidt et al.) submitted to peer-reviewing journals. In collaboration with Malte Lücken.

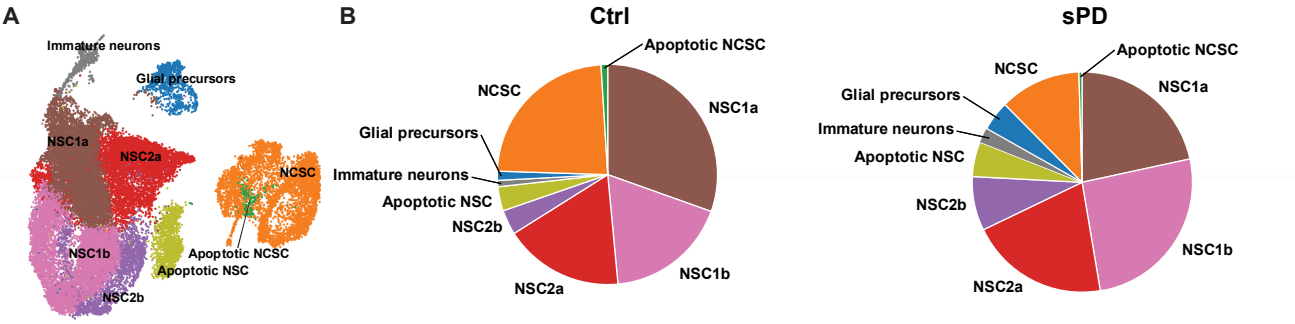

Figure 23 | Distribution to clusters. (A) UMAP visualization of 30,557 annotated cells from 5 Ctrl and 7 sPD hNPC clones. **(B)** Cells were distributed to the annotated clusters as follows, **Ctrl clones:** 30.5 % NSC1a (3,554), 18.0 % NSC1b (2,106), 17.5 % NSC2a (2,042), 3.7 % NSC2b (427), 3.6 % Apoptotic NSC (418), 0.9 % Immature neurons (109), 1.3 % Glial precursors (149), 23.6 % NCSC (2,758), 0.9 % Apoptotic NCSC (107); **PD clones:** 21.6 % NSC1a (4,076), 25.8 % NSC1b (4,874), 20.5 % NSC2a (3,872), 7.9 % NSC2b (1,496), 5.1 % Apoptotic NSC (970), 2.2 % Immature neurons (424), 4.4 % Glial precursors (824), 11.9 % NCSC (2,253), 0.5 % Apoptotic NCSC (98). Total cell counts per cluster and disease state are listed in brackets.

differentiation of NSCs in vivo, thus subdivision of the NSC population into these 4 clusters is biologically relevant (*258, 259*).

The different clusters were further validated by applying an RNA velocity analysis. RNA velocity predicts the future state of individual cells based on observed splicing kinetics. Splicing kinetics reveal gene-specific expression dynamics that can be projected onto existing low-dimensional embeddings indicating the direction of the gene expression changes and thus developmental trajectories. As cell cycle processes may mask such developmental trajectories, cell cycle effects were removed from the data. As expected, this led to the NSC population not being subdivided into four but instead two clusters, which could clearly be distinguished according to the expression of the marker genes of NSC1 and NSC2 (***Figure 21B***). Root cell analysis using the RNA velocity vectors indicated one bioinformatically determined developmental point of origin (root) within the NSC population from which two developmental trajectories arose (***Figure 21C***). Whereas the NSC1 fate clearly had its endpoint in the population of immature neurons, the NSC2 fate was within the NSC population itself, however, also exhibiting a clear endpoint. Still, RNA velocity analysis validated the initial subdivisions into the described clusters.

Furthermore, cells from both disease states contribute to all annotated clusters, however, with slightly different proportions (***Figure 23***). The Ctrl clone i1E4-R1-003 is overrepresented in the NCSC cluster [see chapter 2.4.1], consequently, the proportion of all Ctrl cells in this cluster (23.6 %) is slightly increased in comparison to the proportion of sPD cells (11.9 %), and in most other clusters slightly decreased. Furthermore, the proportion of sPD cells in the NSC1a and NSC1b clusters is shifted. Ctrl clones contribute more to the NSC1a than to the NSC1b cluster and inversely sPD clones contribute more to the NSC1b than to the NSC1a cluster.

Figure 24 (Next page) **| (A)** UMAP visualization of 30,557 annotated cells from 5 Ctrl and 7 sPD hNPC clones. **(B)** Q-Q plots for all detected gene - SNP interactions in relevant cell clusters. **(C)** Genome-wide Manhattan plots of the most significant variant for each gene across relevant cell clusters. Horizontal lines (red) indicate the significance thresholds (FDR = 0.05). **(D)** Gene - SNP interactions exemplarily shown for AC026111.1 – rs7128469 and WEE1 – rs7128469 across relevant cell clusters. Notable cis-eQTLs are marked with *(FDR < 0.05), **(FDR < 0.01), and ***(FDR < 0.001).

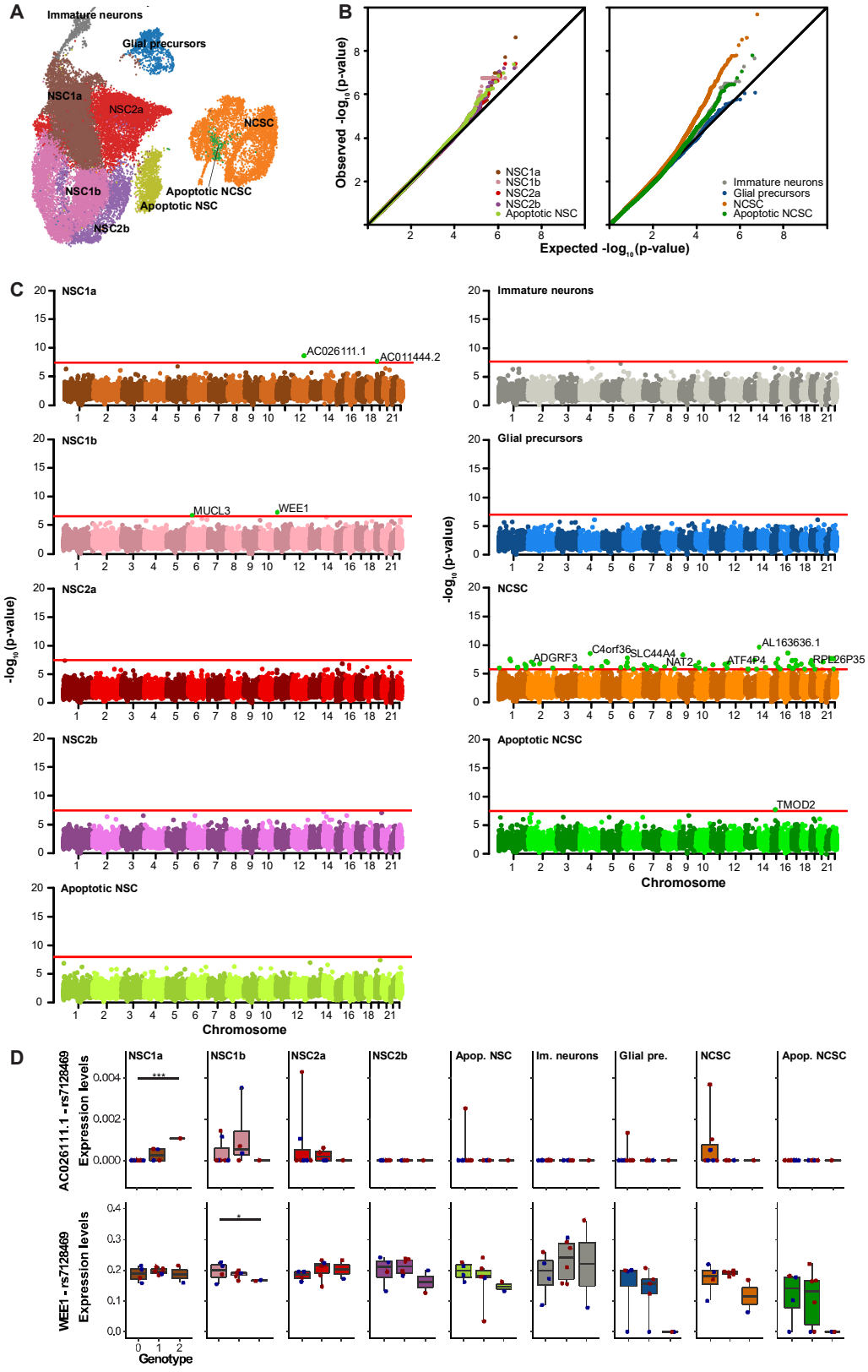

Figure 24 | Genetic control over gene expression. (Caption on the previous page)

2.4.3. Cell type-specific expression quantitative trait loci

Expression quantitative trait loci (eQTL) in disease-relevant tissues is an excellent approach to correlate genetic association with gene expression. To identify possibly disease-relevant genetic variants, eQTL analyses were performed for each cell cluster. In total, 180,183 SNPs as well as 24,736 (NSC1a), 24,707 (NSC1b), 24,474 (NSC2a), 21,478 (NSC2b), 20,646 (apoptotic NSCs), 23,609 (NCSC), 13,883 (apoptotic NCSC), 19,054 (glial precursors), 17,375 (immature neurons) genes for the respective clusters passed quality control. Local eQTLs were calculated by including all variants located within 100,000 base pairs up- or downstream of the transcription start site or the polyadenylation site of genes, respectively. With this approach, 76 independent local eQTLs - 2 in NSC1a; 2 in NSC1b; 71 in NCSC, and 1 in apoptotic NCSC – could be detected, all of which were present in exactly one cell cluster (***Figure 24***). Besides the NCSC cluster, genetic variation seems not to strongly impact gene expression variability. However, the accumulation of eQTLs in the NCSC cluster is astonishing and cannot be explained by experimental data so far. Possibly the NCSC cluster displays a reservoir for cells that may have lost their differentiation potential due to mutations that specifically affect gene expression. Nevertheless, the definition of this cluster as NCSCs requires further evaluation.
However, no genetic variant associated with cell type-specific gene expression is known to be associated with PD etiology, nor did any manually evaluated local eQTL correlate with the disease state.

2.4.4. Differentially expressed genes in sPD

Subsequently, these clusters and the root population identified via RNA-velocity analysis were used to identify PD-associated gene expression alterations and to assess qualitative differences in cluster-specific pathological responses. We were able to identify 12,806 unique differentially expressed genes (DEGs), among them 9,697 protein-coding genes, which were distributed over all clusters (***Table 4***). DEGs were robustly detected at different levels of expression. We selected 8 top down- and upregulated DEGs of the distinct clusters NSC1a and NSC2a - *BBS5* (Ctrl: 0.0108±0.0027; sPD: 0.0137±0.0037), *CFHR1* (Ctrl: $1.15*10^{-5}$±$9.56*10^{-6}$; sPD: $1.00*10^{-5}$±$3.71*10^{-6}$), *GET4* (Ctrl: 0.0298±0.0031; sPD: 0.0352±0.0037), *GRB14* (Ctrl: $4.34*10^{-4}$±$8.24*10^{-5}$; sPD: $2.62*10^{-4}$±$4.92*10^{-5}$), *LINGO2* (Ctrl: $8.24*10^{-4}$±$5.06*10^{-4}$; sPD: $5.34*10^{-4}$±$2.75*10^{-4}$), *PITX3* (Ctrl: $33.84*10^{-5}$±$40.28*10^{-5}$; sPD: $9.91*10^{-5}$±$5.10*10^{-5}$), *SLC1A2* (Ctrl: 0.0012±0.0003; sPD: 0.0007±0.0003), and *SRCAP* (Ctrl: 0.0494±0.0046; sPD: 0.0592±0.0066) – for validation by quantitative PCR with reverse transcription (RT–qPCR) in bulk hNPC cultures (***Figure 25B***). Analysis of DEGs in the root population revealed that already at this early developmental stage gene sets associated with “Parkinson's Disease” and “mitochondria” were significantly overrepresented in sPD lines (***Figure 21C***). In addition, in this root cluster, a subset of PD-associated risk genes (*CAB39L*, *FAM49B*, *GBF1*, *MBNL2*, *NUCKS1*, *RPS12*, *SYT17*, *UBTF*) (*30*) was dysregulated and significantly overrepresented (p = 0.013, Fisher's Exact Test). Also, in the NSC1a cluster dysregulated PD risk genes (*C5orf24*, *CAMK2D*, *FAM49B*, *GBF1*, *INPP5F*, *IP6K2*, *ITPKB*, *KPNA1*, *KRCITRIC ACID CYCLEP2*, *LCORL*, *MAP4K4*, *MBNL2*, *NUCKS1*, *PAM*, *RAB29*, *RPS12*, *SCAF11*, *SCARB2*, *SNCA*, *SPPL2B*, *VPS13C*) tended to be overrepresented (p = 0.053).
Overall and of note was the high number of repressed genes in NSC clusters e.g. in NSC1a and NSC2a irrespective of significance threshold (NSC1a – 88 %, NSC2a – 93 %; q < 0.05 and NSC1a – 62 %, NSC2a – 85 %; q < 0.01 and 0.83 > FC > 1.2) (***Figure 26C***,***D***). Analysis of DNA methylation levels in high-passage

hNPCs revealed that this was not due to a general DNA hypermethylation (Ctrl: 0.282±0.066; sPD: 0.236±0.071) (***Figure 26B***). This overrepresentation of downregulated genes was not as pronounced in other clusters e.g. in the immature neuron cluster (60 % ($q < 0.05$) and 48 % ($q < 0.01$ and $0.83 > FC > 1.2$)) (***Figure 26C***,***E***,***F***), which supports the notion of a heterogeneous differential response to the PD state per cluster. This heterogeneity is also visualized by the heat map of the top 10 DEGs per cluster based on average log fold-change, which also indicates a high degree of variability between the clusters (***Figure 26A***). Overall, these results suggested that all cell populations were affected by sPD pathology at the transcriptional level. Single-cell resolution is thereby critical as changes in gene expression can be dynamic and reversed across cell identities.

2.4.5. Pathway enrichment analysis of differentially expressed genes

To determine disease-associated cellular states, pathway enrichment analysis based on the identified DEGs was performed. This analysis pointed towards several significantly altered cellular processes and signaling pathways, which were specific to each cluster. In the four clusters encompassing the NSC population (NSC1a, NSC1b, NSC2a, NSC2b) a high proportion of cell cycle-associated processes was evident, specifically in the "b" clusters, which were associated with the G2M phase of the cell cycle. Enrichment of these pathways was, however, not too surprising due to the cycling nature of the original cell culture. Additionally, alterations in the 'DNA persistent repair Inhibits mTOR signaling' pathway were common to NSC clusters with varying significance (NSC1a $q = 0.144$; NSC1b $q = 0.048$; NSC2a $q = 0.046$; NSC2b $q = 0.029$).

Table 4 | Differentially expressed genes in sPD. Number of DEGs per cluster by negative binomial model fit and wald test over the condition covariate as implemented in diffxpy. FC, fold change. In collaboration with Malte Lücken.

Differentially expressed genes Ctrl vs sPD	Number of genes, q < 0.05	Number of protein coding genes, q < 0.05	Number of upregulated genes, q < 0.05	Number of downregulated genes, q < 0.05	Number of genes, FC > 1.2 or FC < 0.83, q < 0.01	Number of upregulated genes, FC > 1.2 or FC < 0.83, q < 0.01	Number of downregulated genes, FC > 1.2 or FC < 0.83, q < 0.01
NSC1a	4517	3708	535	3982	1220	462	758
NSC2a	5351	4593	368	4983	1497	224	1273
NSC1b	7094	5962	572	6522	1679	455	1224
NSC2b	3089	2618	335	2754	1047	263	784
Apoptotic NSC	706	608	182	524	440	170	270
Glial precursors	2135	1710	1370	765	1678	1240	438
Immature neurons	603	494	241	362	402	211	191
NCSC	2643	1587	2380	263	2128	1960	168
Apoptotic NCSC	571	495	107	464	450	98	352

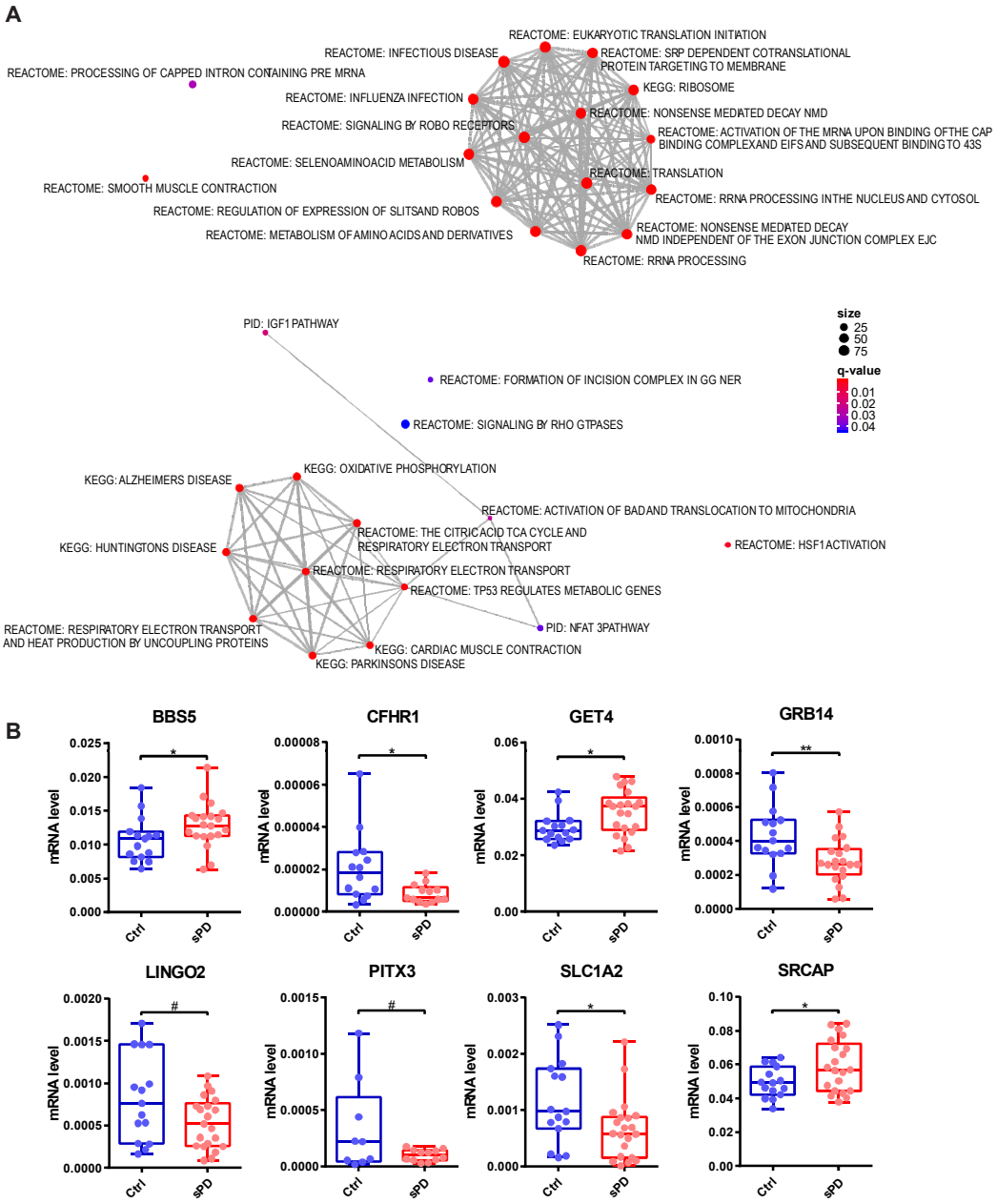

Figure 25 | Validation of top DEGs. (A) Network of enriched canonical pathways for DEGs of the root population with edges weighted by the ratio of overlapping gene sets. FDR corrected p-values are represented by q-values. **(B)** RT-qPCR validation of DEGs determined by scRNA-seq. Target gene mRNA levels are normalized to BestKeeper(*260*) calculated from GAPDH, HPRT1, and ACTB. n = 5 Ctrl and 7 sPD clones, in triplicates. Boxplots are displayed from min to max values. P values are determined by (t-test GRB14, PITX3, SRCAP; Welch-test LINGO2, SLC1A2; Mann-Whitney-U test BBS5, CFHR1, GET4). #, $p < 0.1$; *, $p < 0.05$; **, $p < 0.01$; ***, $p < 0.001$. In parts taken from a manuscript (Schmidt et al.) submitted to peer-reviewing journals.

Concerning enriched cellular and signaling pathways, the dramatically altered gene expression of members of the BBSome interaction pathway (*BBS5*, *BBS9*, *BBS4*, and *ARL6*) in the NSC1a cluster going along with

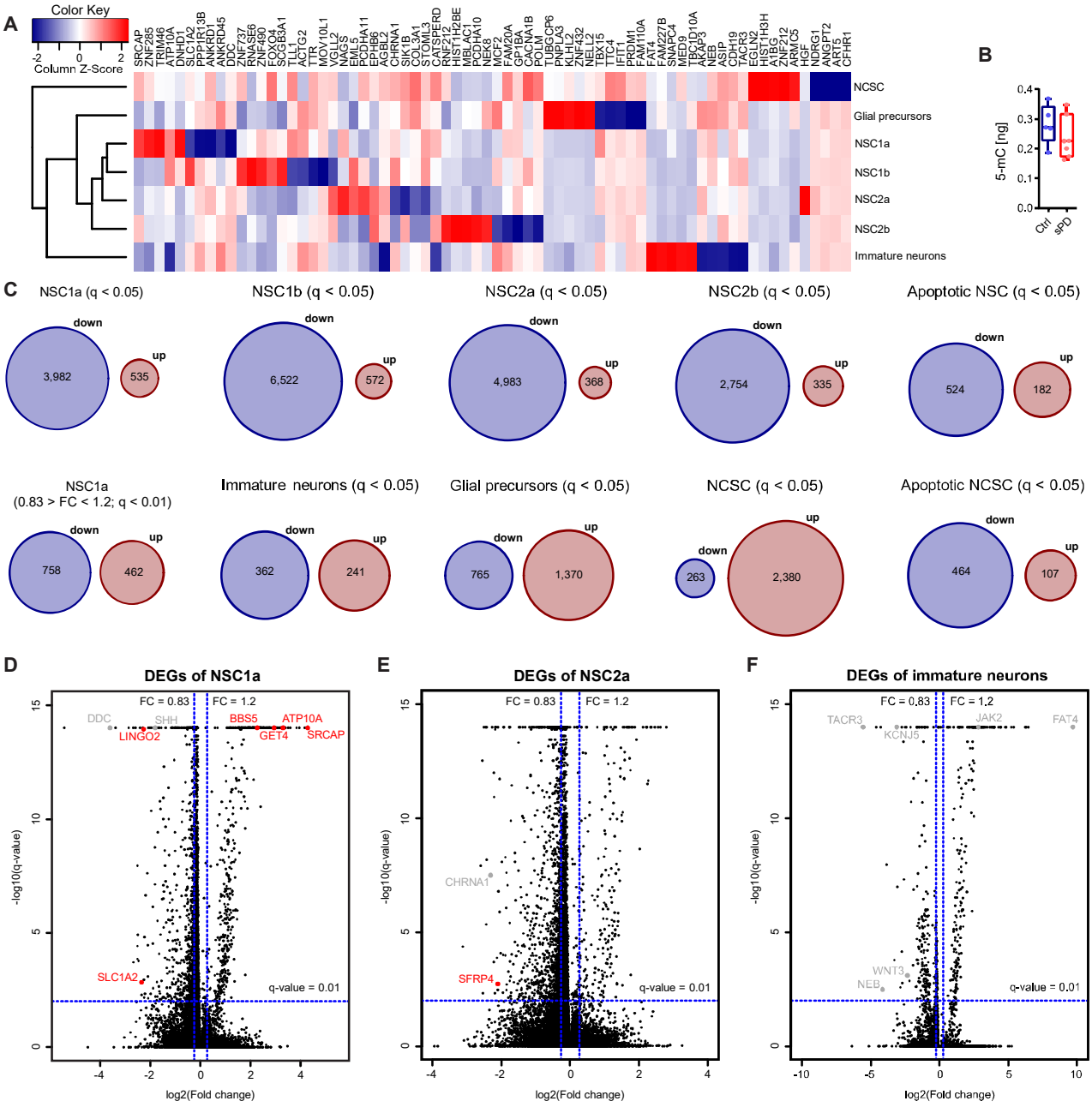

Figure 26 | Cluster-specific gene expression changes in sPD pathology. (A) Heatmap showing log2 transformed fold change with columns scaled by z-score for the top ten up- and downregulated DEGs of each cell type represented by red and blue color, respectively. Hierarchical clustering of cell types represented by the dendrogram on the left reveals their similarity across differential gene expression. **(B)** Analysis of DNA methylation levels (5-methylcytosine (5-mC) levels in [ng]) in hNPC clones. n = 5 Ctrl and 7 sPD clones, in triplicates. Boxplots are displayed from min to max values with all data points shown. P value is determined by analysis of variance (t-test). **(C)** Number of up- and downregulated DEGs in all clusters displayed as Venn diagrams. FC, fold change. **(D) – (F)** Volcano plots showing the significance and fold changes for DEGs of clusters NSC1, NSC2, and immature neurons, respectively, with RT-qPCR validated genes (***Figure 25***) colored in red and not validated DEGs with important biological function regarding PD in grey. In parts taken from a manuscript (Schmidt et al.) submitted to peer-reviewing journals. In collaboration with Dietrich Trümbach.

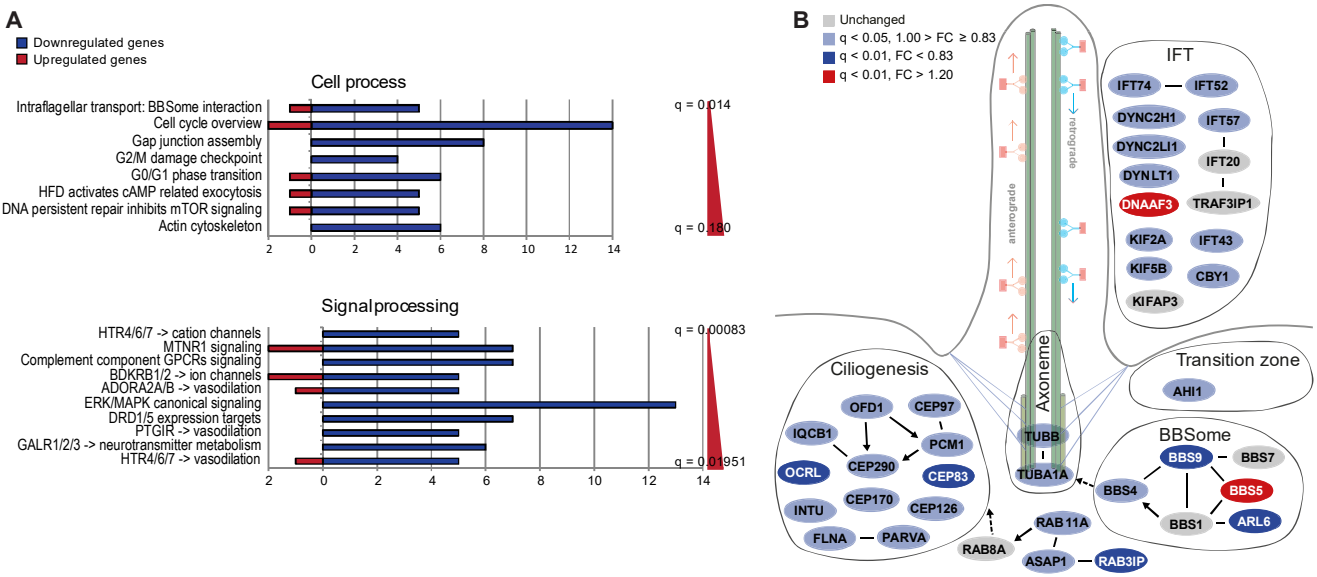

Figure 27 | Pathway enrichment analysis for cluster NSC1a. (A) Enriched pathways of the categories "Cell process" and "Signal processing" were analyzed using Pathway Studio for DEGs of NSC1a. FDR corrected p-values are represented by q-values. **(B)** Visualization of the ‚Intraflagellar transport: BBSome interaction' pathway with manual annotations. Up- (red) and downregulated (blue) genes are sorted into functional categories intraflagellar transport (IFT), transition zone, BBSome, axoneme, and ciliogenesis. Color intensity is proportional to fold change. In parts taken from a manuscript (Schmidt et al.) submitted to peer-reviewing journals. In collaboration with Dietrich Trümbach.

the enrichment of significantly altered GPCR signal processing pathways, e.g. serotonin signaling (HTR4/6/7 signaling) (*261*) and dopamine signaling (DRD1/5 signaling) (*262*), both of which are implicated in PD (***Figure 27A***), is of special interest. The BBSome is a component of the basal body of PC and is involved in trafficking cargos to the PC (*206, 226*). Intriguingly, GPCRs are normally localized to neural PC (*205*) and ciliary export of activated GPCRs for signal transduction is modulated by the BBSome (*197*). Furthermore, a high proportion of cilia-associated genes was dysregulated. These genes could be allocated into different categories according to their functions and localization within the cilia such as intraflagellar transport (IFT: e.g. *IFT74*, *IFT52*, *DYNC2H1*, *DYNC2LI1*), transition zone (e.g. *ASAP1*, *AHI1*), axoneme (*TUBA1A*, *TUBB*), and ciliogenesis (e.g. *INTU*, *CEP83*, *OCRL*) (***Figure 27D***). This suggests that the observed dysregulation of GPCR pathways was a consequence of ciliary dysfunction. This hypothesis is further supported by GPCRs such as serotonin and dopamine receptors themselves not being amongst the highest dysregulated genes. Instead, the respective downstream signaling components (e.g. *GNAS*, *GNB2*, *GNB5*, *ADCY9*, *ADCY5*, *PLCB1*) were affected.

Of note was again the overrepresentation of downregulated genes in the BBBsome (*BBS4*, *BBS9*) and other cilia associated categories with one exception the *BBS5*, which was also validated via qPCR in bulk hNPC cultures (***Figure 25B***). The upregulation of *BBS5* could be the result of compensation for the diminished expression of *BBS4* since it has been shown that at least these two BBS genes act in a functionally redundant manner (*263*). Furthermore, none of these dysregulated genes associated with PC formation and function were influenced by cis-eQTLs detected for the NSC1a cluster [see chapter 2.4.3].

The 'intraflagellar transport – anterograde transport' (q = 0.045) pathway was also significantly enriched

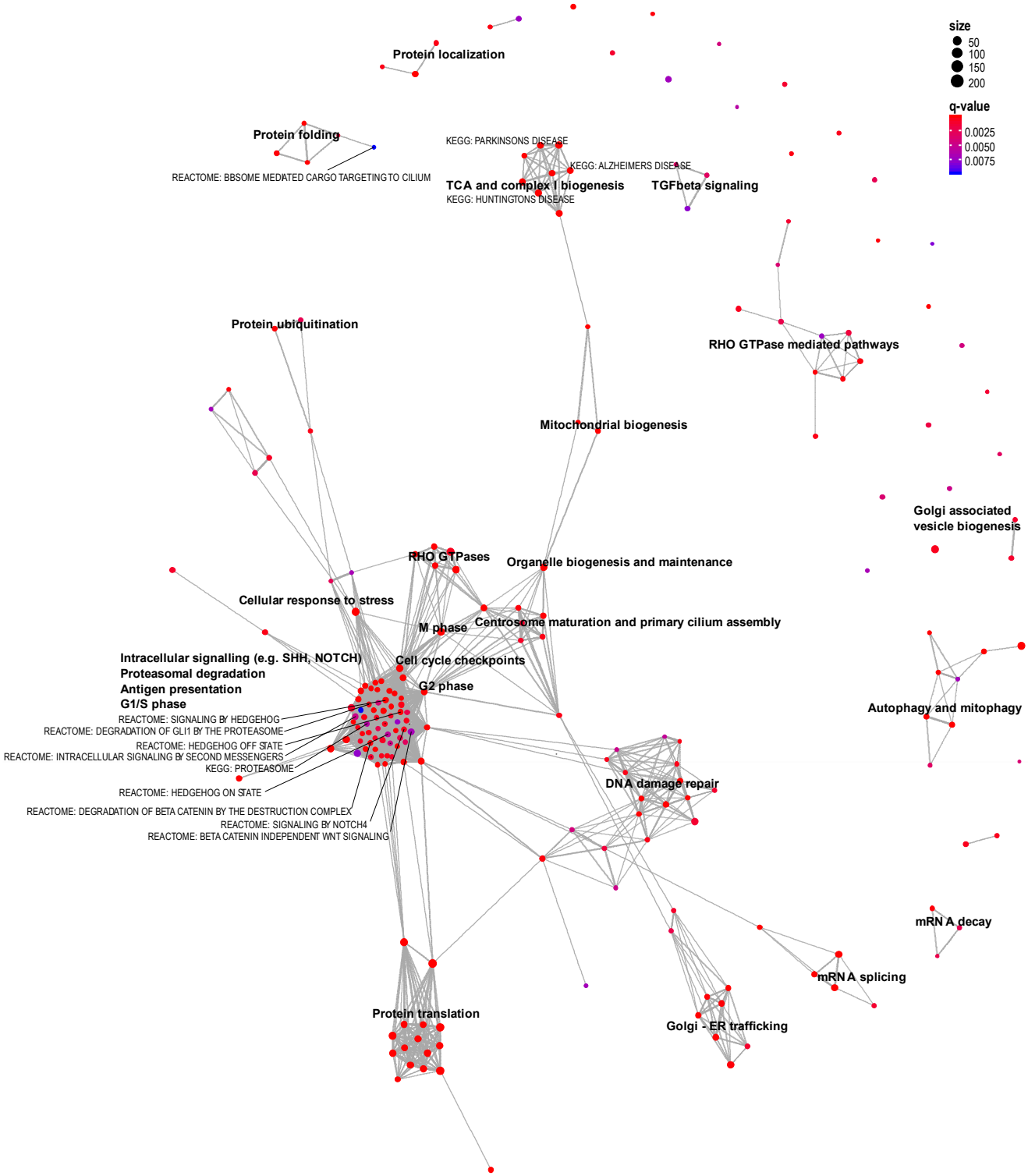

Figure 28 | Network of enriched canonical pathways for DEGs of the NSC1a population. Edges are weighted by the ratio of overlapping gene sets. FDR corrected p-values are represented by q-values.

in the NCSC population, next to 'histone ubiquitination (q = 0.045) and sumoylation' (q = 0.045), as well as 'NURF in chromatin remodeling' (q = 0.045). Thus, ciliary dysfunction could be also observed in one other cluster. Glial precursors on the other hand seemed to be affected by alterations in protein translation, as the 'rRNA (q = 0.00001) and tRNA (q = 0.006) transcription and processing' as well as 'protein folding' (q = 0.008) and 'Golgi to endosome transport' (q = 0.007) pathways were significantly enriched. However, no pathway of the category cell process or signal processing was significantly enriched in the immature neuron cluster, most likely due to the few immature neurons analyzed.
Similar results were obtained using varying databases such as the C2.CP collection (Molecular Signatures Database v7.0) (***Figure 28***) or wikipathways (***Figure 33***) for pathway enrichment analysis.
A network of significantly enriched pathways (C2.CP collection) for cluster NSC1a is displayed in ***Figure 28***. Of note was the overrepresentation of intracellular signaling pathways which overlapped with pathways associated with cell cycle, proteasomal degradation, and PC assembly. Interestingly, these pathways seemed to connect the pathway clusters associated with mitochondrial function, DNA damage repair, and protein translation, processes that are thought to be dysfunctional in sPD.
In conclusion, pathway enrichment analysis allowed to assign the numerous DEGs to pathways that are consequently thought to be dysfunctional in the present hNPCs. These hints, amongst others, at an impaired cilia formation and function in high-passage sPD hNPCs.

2.5. Ciliary dysfunction in neural cells derived from sPD patients

To validate the finding that PC function and formation is disturbed in sPD patients, PC length in high-passage hNPCs and post-mitotic human neurons was determined. Having the same fraction (20 – 55 %) of ciliated cells (hNPCs Ctrl: 0.456±0.082; sPD: 0.425±0.074) (neurons Ctrl: 0.350±0.100; sPD: 0.309±0.147) (***Figure 29A-C***) and similar proliferation rates (hNPCs Ctrl: 4926±289.3; sPD: 4850±272.1) (***Figure 30B***), sPD hNPC (Ctrl: 0.857±0.056; sPD: 0.796±0.062) and neurons (Ctrl: 2.453±0.624; sPD: 2.260±0.3018) exhibited significantly shorter PC as seen in distribution analysis (***Figure 29A-C***). Interestingly, in an astrocytic population derived from the same high-passage hNPCs neither alterations in PC morphology (Ctrl: 2.155±0.256; sPD: 2.114±0.319) nor in the fraction of ciliated cells (Ctrl: 0.378±0.129; sPD: 0.410±0.160) could be detected (***Figure 29D,E***).
PC are known as hubs for various signaling pathways, among which SHH signaling is very prominent. Thus, to validate the impact of altered ciliary morphology, it should be investigated whether an impaired ciliary function is reflected in alterations of SHH signaling in high-passage hNPCs (*205, 264*). For SHH signaling, three transcription factors are known to mediate signal transduction: GLI1, GLI2, and GLI3 (*207*). GLI1 acts as a transcriptional activator whose expression is low in hNPCs and its activity is thought to be neglectable during neural development (*208, 209*). In contrast GLI2 and GLI3 exhibit an evolutionarily conserved transcriptional duality - acting as activators or repressors depending on post-translational processing - and are thought to be the primary mediators of SHH signaling (*208, 210*). GLI2 expression was close to its detection limit in the present hNPC cultures suggesting that it does not play a major role in this disease network (data not shown). Therefore, to investigate the effect of PC length on SHH signal transduction in sPD, GLI3 expression, processing, and translocation was analyzed. SHH functions through its receptor PTCH1. Upon activation of PTCH1, SMO is translocated to the PC where subsequently the degradation of

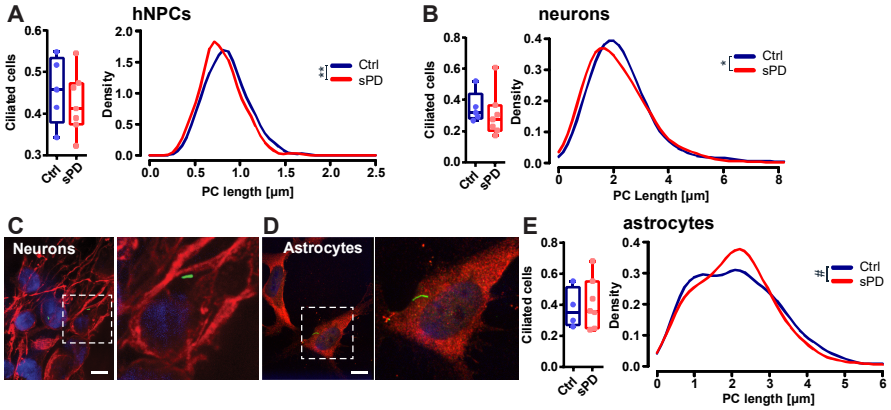

Figure 29 | Alterations in PC morphology in sPD. (A) (right) Density plot illustrating the distribution of PC length (in µm) in hNPCs. (left) Fraction of ciliated cells. PC length was measured in immunostainings of hNPCs with anti-ARL13B. n > 400 cells or PC per condition (data provided by (*265*)). **(B)** (right) Density plot illustrating distribution of PC length (in µm) in a neuron (in collaboration with Sina Hembach) and **(E)** astrocyte population (data provided by (*266*)). (left) Fractions of ciliated cells. PC length was measured in immunostainings of **(C)** neurons double positive for anti-TUBB3 (red) and anti-ARL13B (green) or **(D)** astrocytes double positive for anti-GFAP (red) and anti-ARL13B (green). n > 400 cells or PC per condition. All experiments were performed in triplicates, n = 5 Ctrl and 7 sPD clones. Boxplots are displayed from min to max values with all data points shown. P values are determined by (t-test **A** (left), **B** (left), **E** (left); bootstrap hypothesis test of equal distribution **A** (right), **B** (right), **E** (right)). #, $p < 0.1$; *, $p < 0.05$; **, $p < 0.01$; ***, $p < 0.001$. Scale bars = 10 µm. In parts taken from a manuscript (Schmidt et al.) submitted to peer-reviewing journals.

full-length GLI3 (GLI3-FL) to GLI3-repressor (GLI3-R) is prevented (*205, 212*). GLI3-FL is thought to be neutral or functions as a weak transcriptional activator, whereas the degradation product GLI3-R acts as a repressor. Interestingly, a large fraction of DEGs in the NSC1a cluster (~ 23 %) were predicted GLI3 target genes which were mostly repressed in sPD in the NSC1a cluster like *PKA*, hinting towards an altered SHH signal transduction (***Figure 30B***). From these DEGs, the dysregulation of the GLI3-R target *FOXA2* (*267*) in sPD hNPCs upon SHH stimulation and unstimulated conditions was specifically validated (***Figure 30C,D***). Under SHH stimulation, FOXA2 was upregulated in sPD in bulk analysis (Ctrl: 0.0366±0.0314; sPD: 0.1130±0.1092) and upon inhibition of SHH signal transduction by the SMO antagonist cyclopamine (*268*), *FOXA2* expression was repressed in Ctrl and sPD hNPCs (Ctrl: $8.39*10^{-4}$±$6.08*10^{-4}$; sPD: $14.44*10^{-4}$±$19.86*10^{-4}$) to similar levels, indicating that the expression of *FOXA2* was indeed mediated by SHH signaling in these cells. On the other hand, *GLI3* mRNA levels were upregulated upon stimulation with cyclopamine, albeit to similar extend in Ctrl and sPD hNPCs (unstimulated Ctrl: 0.030±0.022; fPD: 0.019±0.017) (stimulated Ctrl: 0.074±0.045; fPD: 0.079±0.045).

In particular, GLI3-FL (nf Ctrl: 1.03±0.26; sPD: 0.46±0.30), as well as GLI3-R (nf Ctrl: 1.00±0.41; sPD: 0.31±0.29) protein levels were reduced in the nucleus (nf), but not in the cytoplasm (cf) (GLI3-FL cf Ctrl: 0.85±0.65; sPD: 0.52±0.30) of sPD hNPCs, indicating impaired GLI3 processing (***Figure 30E,F***). Furthermore, in contrast to the reduced levels of GLI3-FL and GLI3-R in the nucleus, levels of ciliary GLI3 (FL and R) (Ctrl: 648,074±109,038; sPD: 591,495±122,214) and SMO (Ctrl: 498,076±116,800; sPD: 448,074±123,486) were not altered in sPD hNPCs (***Figure 30G,H***), supporting the hypothesis of impaired GLI3 processing.

Altogether, it could be shown that alterations in SHH signaling in hNPCs from sPD patients resulted in impaired GLI3 processing which might be evoked by shortened PC in these cells. This supports the

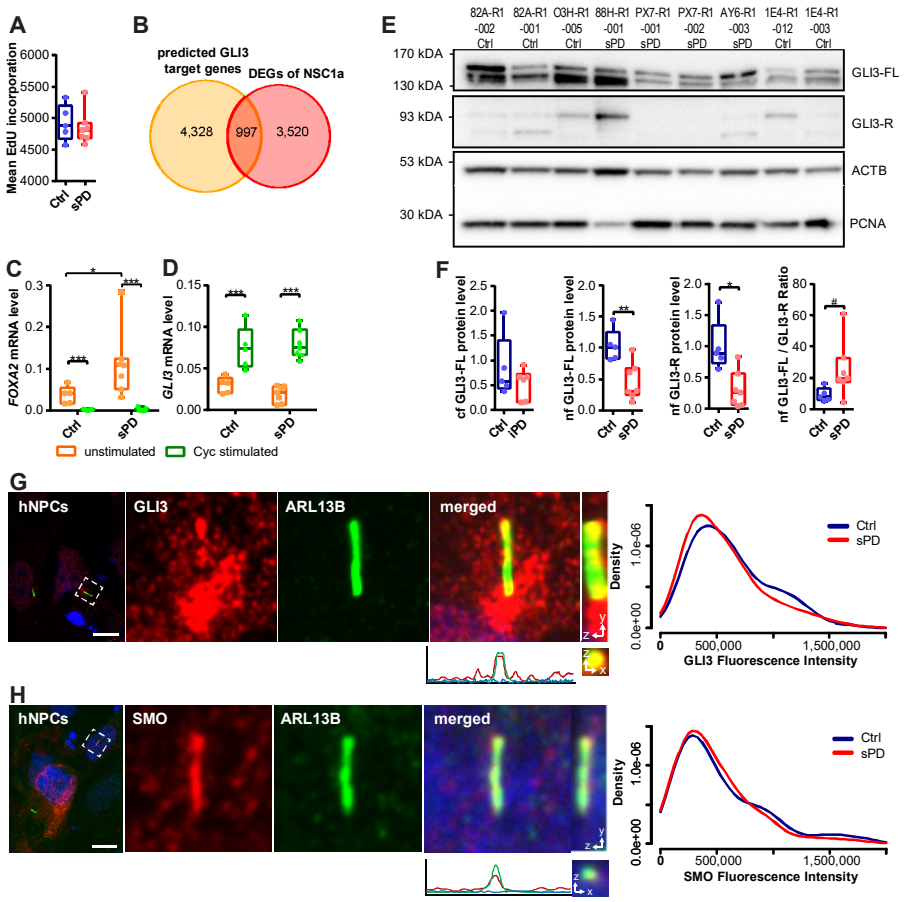

Figure 30 | Alterations in PC function in sPD. (A) Cell proliferation rate of high-passage hNPCs determined by EdU incorporation assay after a 2 h EdU treatment. **(B)** Overlap of genome-wide predicted GLI3 target genes using the MatInspector (Genomatix) with DEGs from NSC1a. **(C)** Normalized gene expression of the SHH signaling target *FOXA2* and **(D)** *GLI3*. mRNA expression levels of unstimulated (orange) and stimulated (cyclopamine (Cyc, green) for 8 days) high-passage hNPCs were analyzed by RT-qPCR. **(E)** Protein levels of GLI3-FL and GLI3-R were quantified by western blots. Data are shown exemplarily for Ctrl clones 1E4-R1-003, 1E4-R1-012, O3H-R1-005, 82A-R1-001, 82A-R1-002, and sPD clones AY6-R1-003, PX7-R1-001, PX7-R1-002, 88H-R1-001. Protein extracts were isolated from high-passage hNPCs and were immunoblotted using anti-GLI3, anti-ACTB, and anti-PCNA. **(F)** Quantification of full-length GLI3 (GLI3-FL) and GLI3 transcriptional repressor (GLI3-R) in the cytoplasmic (cf) or nuclear (nf) fraction of protein extracts from high-passage hNPCs analyzed by Western blot. **(G)** Ciliary GLI3 protein levels analyzed in hNPCs by immunostaining with anti-GLI3 and anti-ARL13B followed by quantitative imaging of z-stacks. n > 250 PC per condition (data provided by (*265*)). PC immunostaining is exemplarily shown for iG3G-R1-039. **(H)** Ciliary SMO protein levels analyzed in hNPCs by immunostaining with anti-SMO and anti-ARL13B followed by quantitative imaging of z-stacks. n > 250 PC per condition (data provided by (*265*)). PC immunostaining is exemplarily shown for iG3G-R1-039. All experiments were performed in triplicates, n = 5 Ctrl, and 7 sPD clones. Boxplots are displayed from min to max values with all data points shown. P values are determined by (*t*-test **A**, **F** (cf and nf GLI3-FL); Welch-test **F** (nf GLI3-R and GLI3-FL/GLI3-R ratio); two-way ANOVA and Tukey`s Post-hoc test **C**, **D**; bootstrap hypothesis test of equal distribution **G**, **H**). #, $p < 0.1$; *, $p < 0.05$; **, $p < 0.01$; ***, $p < 0.001$. Scale bars = 10 µm. In parts taken from a manuscript (Schmidt et al.) submitted to peer-reviewing journals.

hypothesis that ciliary mediated cell-cell communication is disrupted in specific cell types in sPD and may display an early convergence point in sPD etiology.

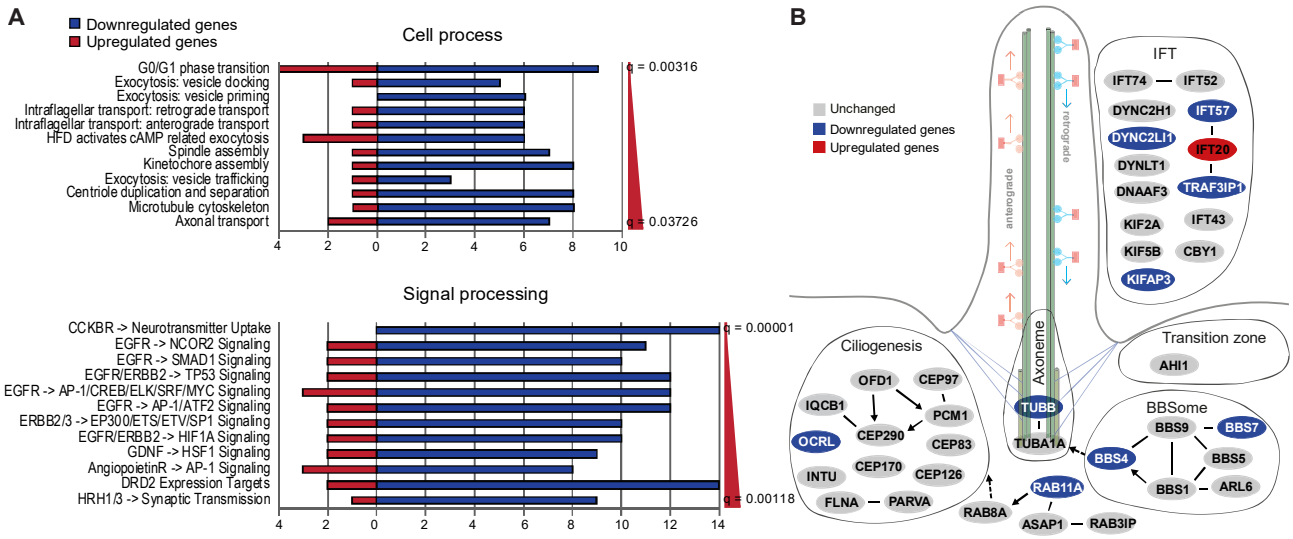

Figure 31 | Primary cilia associated genes are dysregulated in postmortem tissue of sPD patients. (A) Enriched pathways in the categories "Cell process" and "Signal processing" were identified using Pathway Studio for DEGs identified in a previously published meta-analysis (n= 83 PD patients and 70 Ctrl patients) of SN transcriptome studies (*269*). FDR corrected p-values are represented by q-values. **(B)** Visualization of cilia-associated DEGs. Up- (red) and downregulated (blue) genes are sorted into functional categories intraflagellar transport (IFT), transition zone, BBSome, axoneme, and ciliogenesis. In parts taken from a manuscript (Schmidt et al.) submitted to peer-reviewing journals.

2.6. Ciliary dysfunction is a hallmark of sPD patients

Nevertheless, the question arose whether ciliary dysfunction observed in a cellular model of sPD has any translational relevance. To answer this question, DEGs identified in the scRNA-seq were compared to previously published transcriptome data from postmortem SN tissues derived from sPD patients.

A recently published meta-analysis was chosen, as it combines the PD postmortem SN transcriptome studies available in the Gene Expression Omnibus database by employing a multiscale network biology approach (*269*). This yielded a global PD expression data set derived from 83 sPD patients and 70 Ctrl patients which was used to identify 946 genes that were dysregulated in sPD. Of note was the high proportion of repressed genes also in these datasets: approximately 72 % of DEGs were downregulated in sPD patients. This is remarkably similar to the high number of repressed genes identified by scRNA-seq in the neural stem cell clusters NSC1a and NSC2a (88 % and 93 % of DEGs) [see chapter 2.4].

Furthermore, pathway enrichment analysis using the same database as for the scRNA-seq data showed that DEGs were also significantly enriched for cell process pathways associated with ciliary function such as "Intraflagellar Transport: Retrograde and Anterograde" (q = 0.007) (***Figure 31A***), and a high proportion of cytoskeleton and cell cycle-associated processes were identified. Similar to our cellular model, several genes that were associated with the ciliary categories intraflagellar transport (IFT: e.g. *IFT57*, *DYNC2LI1*), BBSome (e.g. *BBS4*, *BBS7*), axoneme (*TUBB*), and ciliogenesis (*OCRL*) were dysregulated in sPD (***Figure 31B***). Interestingly, pathways of the category signal processing were dominated by receptor tyrosine kinase (EGFR, GDNF receptors), or GPCR (DRD2, CCKBR, HRH1/3) mediated signaling pathways, all of which

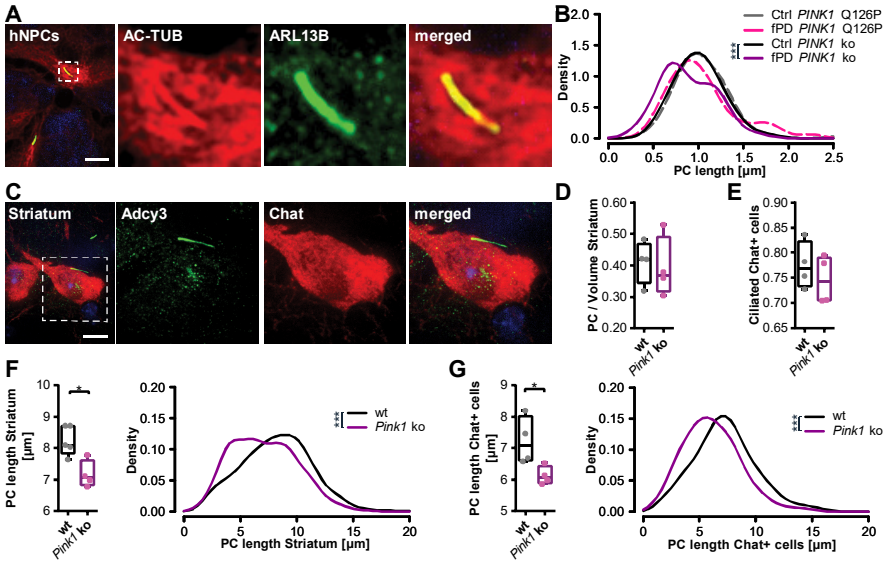

Figure 32 | Primary cilia in fPD. (A) PC immunostaining with anti-Acetylated Tubulin and anti-ARL13B exemplarily shown for the isogenic Ctrl of *PINK1* ko hNPCs. **(B)** Density plot illustrating the distribution of PC length (in µm) in a hNPC population. PC length was measured in immunostainings of *PINK1* ko hNPCs and its isogenic Ctrl, as well as of *PINK1* Q126P hNPCs with its isogenic Ctrl with anti-ARL13B. n > 90 cells or PC per condition from three independent differentiations (data provided by (*265*)). **(C)** PC immunostaining with anti-Chat and anti-Adcy3 exemplarily shown for a *Pink1* ko mouse (mice provided by Kristina Niedermeier). **(D)** The fraction of ciliated cells per striatal volume (115 µm x 87 µm x 40 µm). **(E)** The fraction of ciliated Chat+ cells. **(F)** Boxplot (left) illustrating the average PC length (in µm) per mouse and density plot (right) illustrating PC length distribution (in µm) in the mouse dorsal striatum. PC length was measured in 40 µm free-floating brain sections from 4 *Pink1* ko and 5 wt mice immunostained with anti-Adcy3. n > 900 PC per condition. **(G)** Boxplot (left) illustrating the average PC length (in µm) per mouse and density blot (right) illustrating PC length distribution (in µm) of Chat+ cells in mouse dorsal striatum. PC length was measured in 40 µm free-floating brain sections from 4 *Pink1* ko and 5 wt mice immunostained with anti-Chat and anti-Adcy3. n > 240 PC per condition. Boxplots are displayed from min to max values with all data points shown. P values are determined by (Mann-Whitney-U test **D**, **E**, **F** (left), **G** (left); bootstrap hypothesis test of equal distribution **B**, **F** (right), **G** (right)). *, $p < 0.05$; **, $p < 0.01$; ***, $p < 0.001$. Scale bar = 10 µm. In parts taken from a manuscript (Schmidt et al.) submitted to peer-reviewing journals.

rely on PC mediated signal transduction [reviewed in chapter 1.5]. Overall, these transcriptome data from postmortem sPD patients support our *in vitro* finding in PD patients and verify the hypothesis that ciliary dysfunction is a hallmark of sPD.

2.7. Altered ciliary morphology in familial forms of PD.

To address the question if ciliary dysfunction is also a hallmark of fPD, ciliary morphology was analyzed in hNPCs derived from *PINK1* knock-out (ko) hiPSCs provided by Julia Fitzgerald and *PINK1* Q126P hiPSCs which were generated and characterized in house by Annerose Kurz-Drexler. The *PINK1* ko clone derives from a wild-type hiPSC clone, thus the wild-type clone was used as isogenic Ctrl. The patient-derived *PINK1* Q126P hiPSC clone was gene-corrected to yield an adequate isogenic Ctrl (unpublished data). *PINK1* is, after *PARKIN*, the second most common cause for autosomal recessive fPD (*20*). Its function is to regulate proper mitophagy, but also mitochondrial transport (*24, 25*). Patients carrying *PINK1* mutations develop clinical phenotypes that resemble those suffering from sPD, including slow disease progression (*21, 22*). Interestingly, - while the percentage of ciliated cells did not change (Ctrl: 0.423±0.095; fPD: 0.310±0.061)

- the *PINK1* ko hNPC populations exhibited significantly shorter PC (Ctrl: 1.010±0.077; fPD: 0.608±0.460) (***Figure 32A***,***B***). In addition, with a similar proportion of ciliated cells (Ctrl: 0.473±0.139; fPD: 0.330±0.157), PC length of *PINK1* Q126P hNPCs (Ctrl: 1.046±0.116; fPD: 1.044±0.243) was shortened, albeit not reaching significant levels (p = 0.08). The *PINK1* ko leads to a loss of the protein, the *PINK1* Q126P represents a point mutation outside of the kinase domain close to its membrane-spanning domain and thus might result in a slightly different phenotype than the full ko (*266*).
Furthermore, having a similar proportion of ciliated cells (striatal cells Ctrl: 0.411±0.068; fPD: 0.315±0.071) (cholinergic neurons Ctrl: 0.775±0.047; fPD: 0.746±0.048), PC length was reduced in striatal cells (Ctrl: 8.234±0.470; fPD: 7.164±0.432) (***Figure 32D***,***F***), including striatal cholinergic neurons (Ctrl: 7.230±0.754; fPD: 6.122±0.286) of *Pink1* ko mice (***Figure 32C***,***E***,***G***). Cholinergic neurons were especially focused on as they are thought to respond to SHH. It has been described that SHH secretion by midbrain DAn is crucial for their maintenance and survival as striatal cholinergic neurons respond to SHH by secreting neurotrophic factors like GDNF which support the maintenance of substantia nigra DAn (*270*). Thus, an altered signal transduction in cholinergic neurons possibly affects the neurochemical homeostasis of nigrostriatal circuits over time.

2.8. Complex I misassembly may underlay mitochondrial dysfunction in sPD

Seahorse analysis indicated mitochondrial dysfunction that occurs specifically in sPD cells when entering the neuronal lineage. Mitochondrial function in high-passage hNPCs was further investigated, to address a possible mitochondrial defect. The amount of functional mitochondria within a cell was determined using MitoTracker which accumulates specifically in active mitochondria with a membrane potential. There was no difference between functional mitochondria in Ctrl and sPD hNPCs (Ctrl: 0.981±0.055; sPD: 0.948±0.060) (***Figure 33A***), suggesting that alterations in mitochondrial mass did not cause the respiratory deficiency that was observed in Seahorse analysis. Another parameter that could affect mitochondrial respiration is the abundance and activity of mitochondrial complexes involved in the respiratory chain. The abundance of the mitochondrial complexes I - V was determined by Western blot for labile subunits of each complex. sPD and Ctrl hNPCs expressed the same amount of complex I (Ctrl: 0.971±0.226; sPD: 1.023±0.197), complex II (Ctrl: 0.976±0.282; sPD: 0.941±0.369), complex III (Ctrl: 0.979±0.415; sPD: 1.007±0.256), complex IV (Ctrl: 0.886±0.717; sPD: 0.760±0.173) and complex V (Ctrl: 0.951±0.199; sPD: 0.982±0.269) subunits (***Figure 33B***, ***Figure 42***). Thus it can be concluded that the abundance of the respiratory chain complexes is also not altered in sPD.
However, analysis of the transcriptome data (bulk-like DEGs) for metabolic changes identified an enrichment of dysregulated genes between sPD patients and Ctrls in pathways associated with the respiratory chain. For example, 83 genes annotated in the “Electron Transport Chain (OXPHOS system in mitochondria)” and 47 genes annotated in the “Mitochondrial complex I assembly model OXPHOS system” were dysregulated in high-passage hNPCS from sPD patients (***Figure 33D***). Further analysis showed that most of the genes involved in the assembly of complex I and the function of complexes I-IV were downregulated in sPD hNPCs (***Figure 33E***). Although the abundance of mitochondrial complexes is not affected in sPD, their activity may be altered due to a different composition. Indeed, complex I activity was reduced by approximately 20 % in sPD hNPCs (Ctrl: 1.000±0.204; sPD: 0.784±0.130) (***Figure 33B***). This

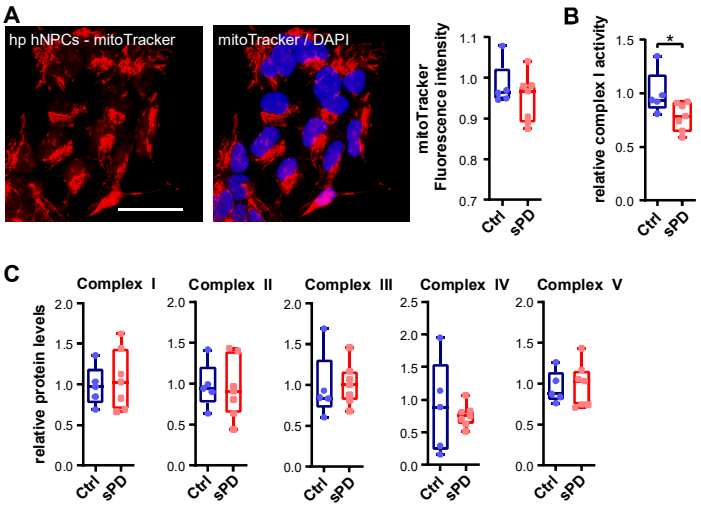

D

Pathways	Gene ratio	q-value
VEGFA-VEGFR2 Signaling Pathway	320/3850	2.55E-15
Cytoplasmic Ribosomal Proteins	85/3850	1.13E-14
mRNA Processing	113/3850	1.75E-12
Ciliary landscape	171/3850	5.17E-12
Integrated Breast Cancer Pathway	124/3850	3.78E-10
Cell Cycle	100/3850	2.67E-09
DNA IR-damage and cellular response via ATR	71/3850	3.92E-08
Retinoblastoma Gene in Cancer	74/3850	7.72E-08
Chromosomal and microsatellite instability in colorectal cancer	64/3850	8.39E-08
TGF-beta Signaling Pathway	103/3850	3.77E-07
EGF/EGFR Signaling Pathway	123/3850	4.05E-07
Insulin Signaling	120/3850	1.05E-06
Electron Transport Chain (OXPHOS system in mitochondria)	83/3850	3.25E-06
Nonalcoholic fatty liver disease	118/3850	3.25E-06
Base Excision Repair	30/3850	3.42E-06
Pancreatic adenocarcinoma pathway	71/3850	6.33E-06
Sterol Regulatory Element-Binding Proteins signalling	60/3850	7.34E-06
Nucleotide Excision Repair	39/3850	1.86E-05
G1 to S cell cycle control	53/3850	2.09E-05
Translation Factors	46/3850	2.12E-05
Androgen receptor signaling pathway	71/3850	2.37E-05
Pathways Affected in Adenoid Cystic Carcinoma	54/3850	3.04E-05
DNA Damage Response	56/3850	3.07E-05
Mitochondrial complex I assembly model OXPHOS system	47/3850	3.29E-05

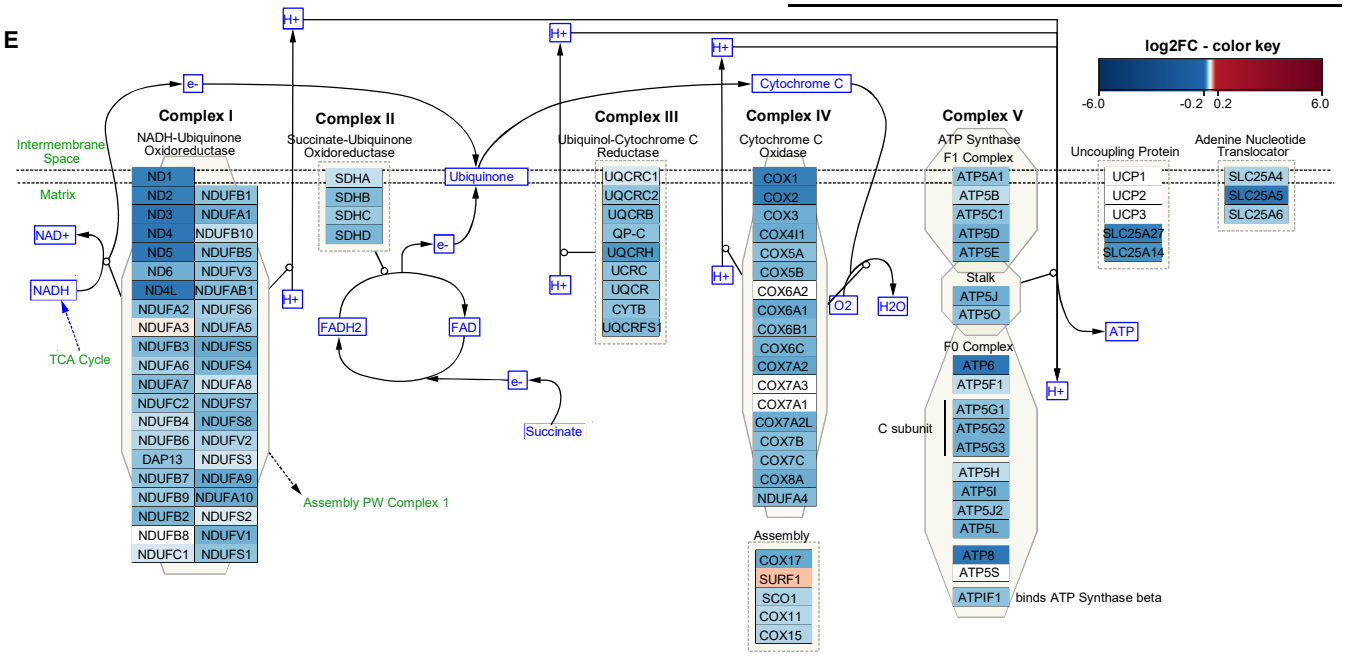

Figure 33 | Analysis of mitochondrial abundance and function. (A) Quantification of functional mitochondria in high-passage (hp) hNPC clones. Cells were incubated with MitoTracker (200 nM) and cytosolic fluorescence intensity was quantified. MitoTracker staining is exemplarily shown for UKERiAY6-R1-003. Scale bar = 5 µm. **(B)** Analysis of relative Complex I activity in hNPC clones normalized to Ctrl levels. **(C)** The abundance of mitochondrial complexes I - IV was quantified by Western blot with antibodies against the subunits NDUFB8 (complex I), Complex II Subunit 30 kDa, UQCRC2 (Complex III), COX2 (Complex IV), and ATP5A1 (Complex V). Expression levels were normalized to ACTB or α-Tubulin levels and the average expression of Ctrl clones. n = 5 Ctrl and 7 sPD clones, in triplicates. Boxplots are displayed from min to max values with all data points shown. P values are determined by (t-test **A**, **B**, **C**). *, $p < 0.05$; **, $p < 0.01$; ***, $p < 0.001$. **(D)** Pathways enriched in high-passage sPD hNPCs. FDR corrected p-values are represented by q-values. **(E)** Visualization of DEGs involved in the 'Electron Transport Chain (OXPHOS system in mitochondria)' pathway with manual annotations. Color intensities for up- (red) and downregulated (blue) genes are proportional to the fold change. In parts taken from a manuscript (Schmidt et al.) submitted to peer-reviewing journals.

corresponds well with literature describing complex I deficiency in different PD models as well as in postmortem brain tissues of PD patients (*165–167, 244*).

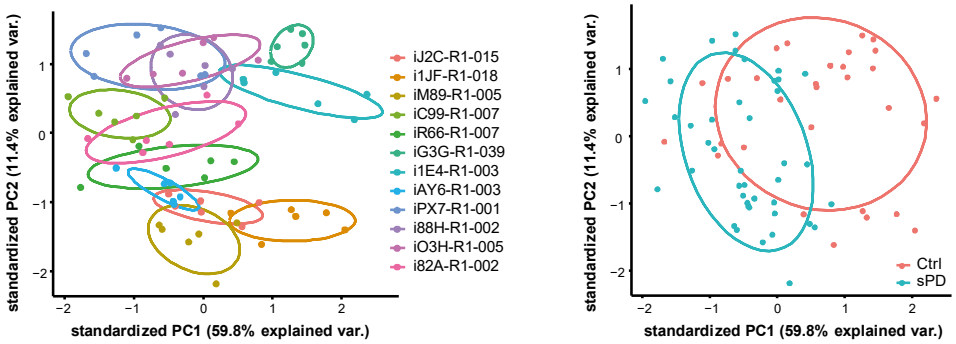

Figure 34 | Non-targeted metabolomics analysis. Principal component analysis scores plot of high-passage hNPC samples drawn with probability ellipses (0.68 of normal probability). n = 5 Ctrl and 7 sPD clones, in sextuplicates. In parts taken from a manuscript (Schmidt et al.) submitted to peer-reviewing journals.

2.9. The citric acid cycle is a bottleneck in sPD metabolism

Reduced activity of mitochondrial complexes may directly affect maximal mitochondrial respiratory capacity, but not necessarily interferes with basal metabolism. To gain a better understanding of metabolic alterations under basal conditions, a non-targeted metabolomics analysis was performed in high-passage hNPCs.

Principal Component Analysis (PCA) was used to visualize clusters within the samples to detect possible outliers (***Figure 34***). PCA is a multivariate data analysis that is used to reduce the dimension of data, to visualize the similarities between the biological samples and the variation in the data set. The observed variation between technical replicates seemed to be lower than the variation between samples from different patients, thus no sample was removed as an outlier. However, the variation could at least to some extent be explained by the disease state, as sPD samples clustered separately from Ctrl samples.

In total 223 metabolites passed quality control (***Figure 35A***) and 45 metabolites were significantly dysregulated in sPD. Interestingly, most of the metabolites detected and all significantly dysregulated metabolites were downregulated in sPD, similar to what was observed on the transcriptome level [see chapter 2.4.4]. scRNA-seq allowed to identify a heterogeneous differential response to the PD state per cell cluster. Of note was the high number of repressed genes in the neural stem cell clusters NSC1a and NSC2a (88 % and 93 % of differentially expressed genes). An integrated analysis of transcriptome (bulk-like DEGs) and metabolome (metabolites with q-value < 0.5) data allowed to refine pathway enrichment analysis of metabolic pathways (***Figure 35G***). This analysis pointed towards significantly altered processes associated with ‘pyruvate metabolism’ and the ‘citric acid cycle’. Both the abundance of 3 consecutive intermediate metabolites of the citric acid cycle, namely succinate (Ctrl: 3.271±0.477; sPD: 2.431±0.334), fumarate (Ctrl: 3.293±0.278; sPD: 2.637±0.214), and malate (Ctrl: 3.270±0.355; sPD: 2.651±0.223), as well as the expression levels of most citric acid cycle associated enzymes were reduced in sPD. However, levels of aconitate (cis and trans) (Ctrl: 3.374±0.587; sPD: 2.580±0.375), 2-oxoglutarate (Ctrl: 3.025±0.530; sPD: 2.636±0.600), citraconate (Ctrl: 3.354±0.505; sPD: 2.560±0.391), and glutamate (Ctrl: 3.287±0.519; sPD:

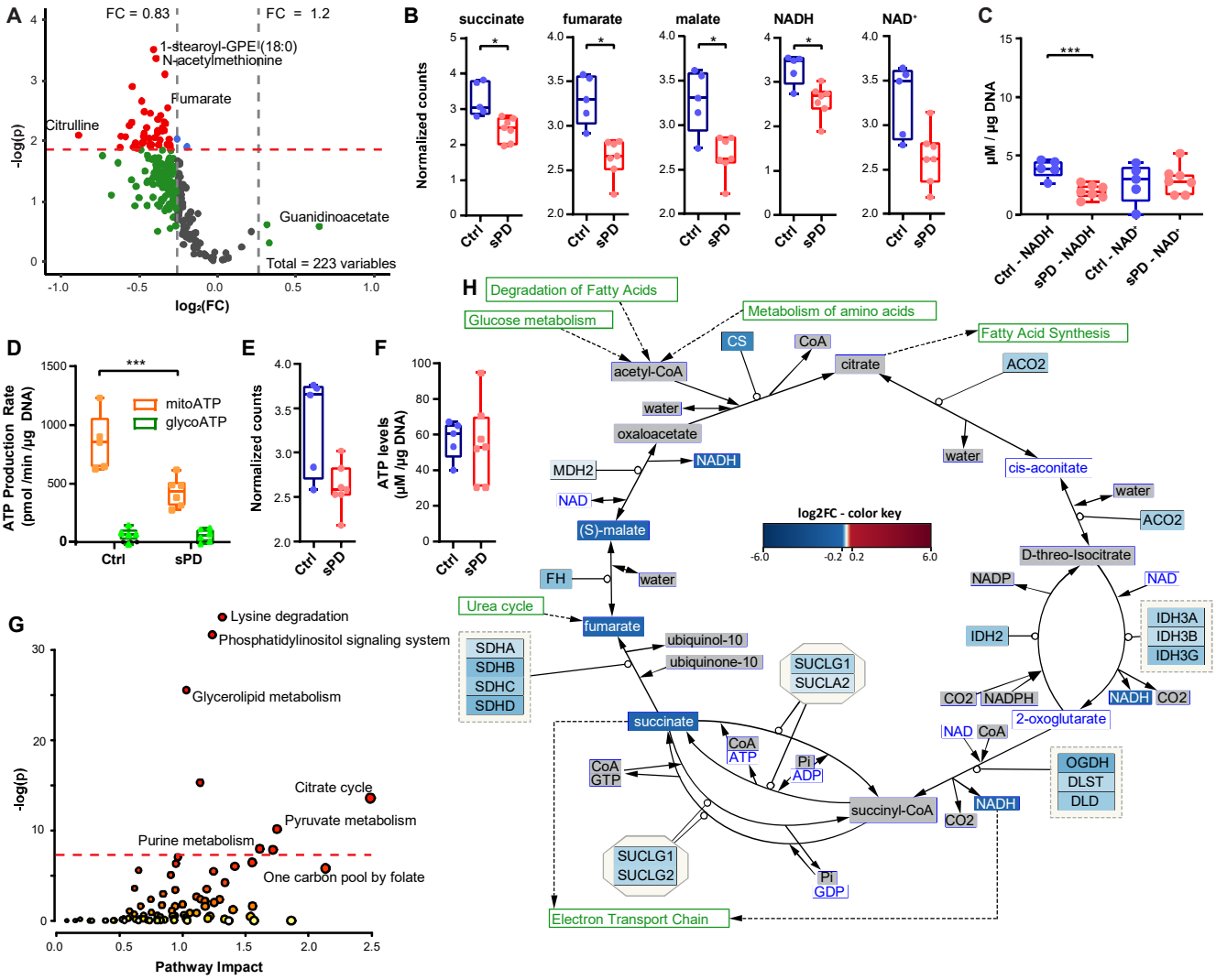

Figure 35 | Metabolic alterations affect citric acid cycle flux in sPD. (A) Non-targeted metabolomic analysis identified 45 metabolites (out of 223) that were dysregulated in high-passage sPD hNPCs. The red dotted line indicates the significance threshold ($q < 0.05$). **(B)** Boxplots showing levels of the citric acid cycle metabolites succinate, fumarate, malate, NADH, and NAD^+. *, $q < 0.05$. **(C)** Quantification of NADH and NAD^+ levels in high-passage hNPCs. **(D)** The ATP production rate was calculated from the basal glycolytic flux and mitochondrial respiration linked to ATP production measured in Seahorse XF analysis from high-passage hNPC clones (***Figure 14***, ***Figure 15***). **(E)** Cellular ATP levels were quantified by UPLC-MS/MS analysis. **(F)** Cellular ATP levels (in µM) were analyzed in high-passage hNPCs clones and normalized to the genomic DNA content. n = 5 Ctrl and 7 sPD clones, in triplicates. P values are determined by (t-test **A**, **B**, **C**; two-way ANOVA and Tukey`s Post-hoc test **D**). *, $p < 0.05$; **, $p < 0.01$; ***, $p < 0.001$. **(G)** Integrative analysis of transcriptome and metabolome data identified metabolic pathways enriched in high-passage sPD hNPCs. Node color is based on p-values and node radius on the pathway impact values. The dotted line indicates the significance threshold ($q < 0.05$). **(H)** Visualization of the 'citric acid cycle' pathway with manual annotations. Color intensities for up- (red) and downregulated (blue) genes or metabolites are proportional to the fold change, not quantified metabolites are colored in grey. In parts taken from a manuscript (Schmidt et al.) submitted to peer-reviewing journals.

2.732±0.488) were not affected. This suggests that the conversion of 2-oxoglutarate to succinate is a bottleneck in sPD metabolism, which may cause a reduced flux and thus results in a reduced abundance of citric acid cycle intermediates. Additionally, the abundance of the electron transport chain substrates

NADH (Ctrl: 3.297±0.343; sPD: 2.579±0.362) and succinate, produced within the citric acid cycle, was reduced in sPD (***Figure 35B***). Interestingly, NAD^+ (Ctrl: 3.276±0.407; sPD: 2.638±0.306) levels were not affected in sPD. Both NADH (Ctrl: 3.893±0.782; sPD: 1.959±0.577) and NAD^+ (Ctrl: 2.655±1.702; sPD: 2.962±1.221) levels could be validated independently in high-passage hNPCs (***Figure 35C***). Changes in the citric acid cycle may directly affect the flux through the electron transport chain and thus basal mitochondrial respiration. This is further supported by a decreased mitochondrial ATP production rate (calculated from the basal mitochondrial respiration) (Ctrl: 850.3±245.2; sPD: 426.3±126.6) in high-passage sPD hNPCs (***Figure 35D***), whereas the glycolytic ATP production rate (calculated from the basal glycolytic flux) (Ctrl: 62.82±62.6; sPD: 55.50±54.43) (***Figure 35D***) and the total ATP levels (Ctrl: 57.19±10.91; sPD: 55.50±22.51) (***Figure 35E, F***) were not affected. Taken together the data indicate the development of metabolic defects in the citric acid cycle and the electron transport chain specifically in high-passage neural cells derived from sPD patients.

2.10. Aging-associated genomic and epigenomic alterations develop specifically in sPD during long-term *in vitro* cultivation.

Mitochondrial dysfunction selectively affects high-passage neural cells from sPD patients, whereas low-passage cells seem not to be hindered. This raises the question about which molecular alterations happen to sPD cells during long-term *in vitro* cultivation, which cause them to specifically exhibit a PD phenotype. One major risk factor for PD is aging. As mitochondrial dysfunction is also associated with cellular aging, one hypothesis could be that long-term in vitro cultivation might recapitulate, at least to some extent, cellular aging processes. Therefore, patient-derived fibroblasts and neural cells differentiated from high-passage hiPSC were next analyzed for the appearance of different aging markers.

Associated with mitochondrial dysfunction and also characteristic for aged cells are elevated levels of ROS. However, there was no increase in ROS levels in high-passage sPD hNPCs (data not shown), most likely due to the high amount of antioxidants under cell culture conditions (*271*).

Other characteristics of cellular aging are epigenetic alterations, like DNA methylation, histone modifications, and chromatin remodeling [reviewed in chapter 1.2]. These alterations are highly cell-type-specific, but the heterochromatin markers H3K9me3 and H3K27me3 are often described to be altered during aging, e.g. these markers are lost in fibroblasts from old donor patients. Although an increase of H3K9me3 was observed in fibroblasts from sPD patients, the aging-associated heterochromatin markers H3K9me3 and H3K27me3 were specifically decreased in high-passage hNPCs (***Figure 36B***). Strikingly, in high-passage DAns these marks were only decreased in cells derived from sPD patients, while DAns derived from healthy age-matched Ctrls showed a similar abundance of the heterochromatin markers as low-passage Ctrl cells. The decrease observed in high-passage hNPC populations from both Ctrl and sPD patients compared to their low-passage counterparts may be due to the intermediate differentiation state of hNPCs, harboring a broader range of cells within a less defined differentiation stage. hNPCs derived from high-passage hiPSCs may display at the time of analysis an earlier or later differentiation state than low-passage cells, thus showing alterations in differentiation-associated epigenetic marks. Furthermore, the pattern of reduced expression levels specifically in high-passage hNPCs (Ctrl and sPD) and an sPD specific decrease in high-passage DAns was also observed for LAP2a (***Figure 36B***, ***Table 18***, ***Table 19***). LAP2a is a component of the nuclear lamina and structural changes of the nuclear lamina, e.g decrease

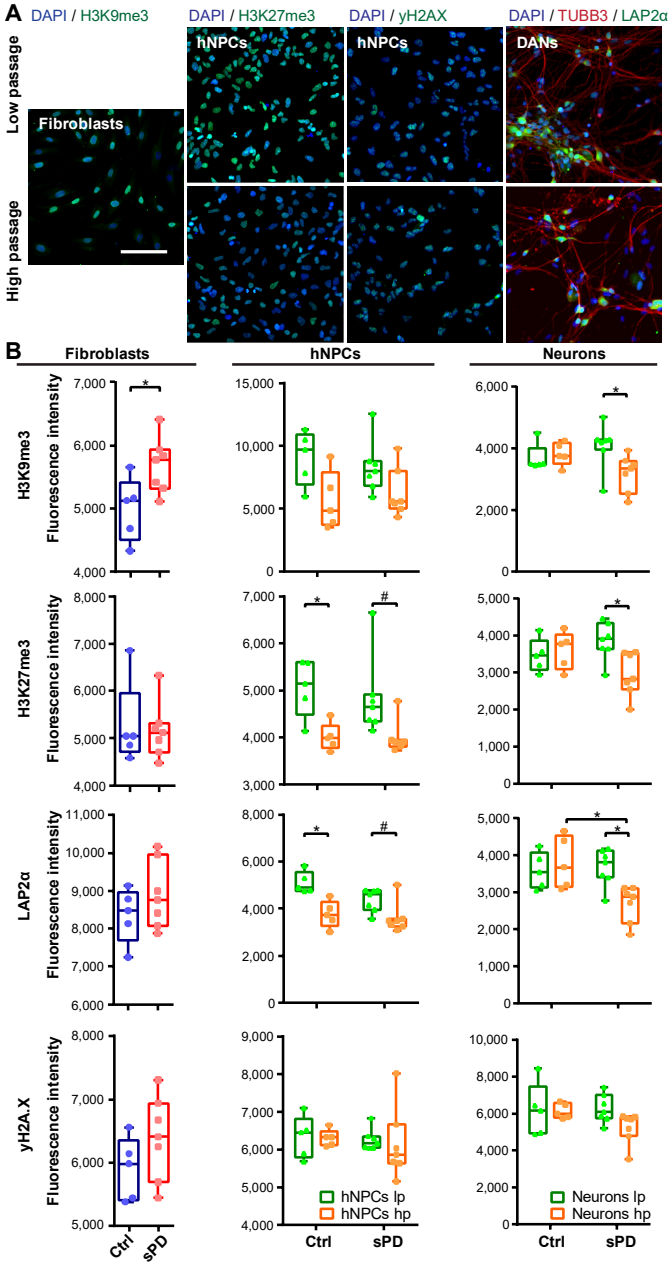

Figure 36 | Epigenetic and nuclear lamina alterations in high-passage sPD lines. (A) Immunocytochemistry for age-associated histone (H3K9me3, H3K27me3), DNA damage (γH2A.X), and laminar (LAP2α) markers. Stainings are exemplarily shown for the sPD fibroblast line UKERiAY6 (H3K9me3), for UKERiAY6-R1-003 low-passage and high-passage hNPCs (H3K27me3 and γH2AX) and DAns (LAP2α). Scale bar = 100 µm. **(B)** Boxplots show the quantification of immunostainings of age-associated markers. 7,000 cells per condition were analyzed from n = 5 Ctrl and 7 sPD clones, in triplicates (data for hNPCs and neurons provided by (*272*)). P values are determined by (two-way ANOVA and Tukey`s Post-hoc test **B**). *, $p < 0.05$; **, $p < 0.01$; ***, $p < 0.001$. In parts taken from a manuscript (Schmidt et al.) submitted to peer-reviewing journals.

of LAP2a, are further characteristics of cellular aging. Mutation in genes encoding components of the nuclear lamina, like lamin A, cause accelerated aging syndromes like HGPS, highlighting the importance of

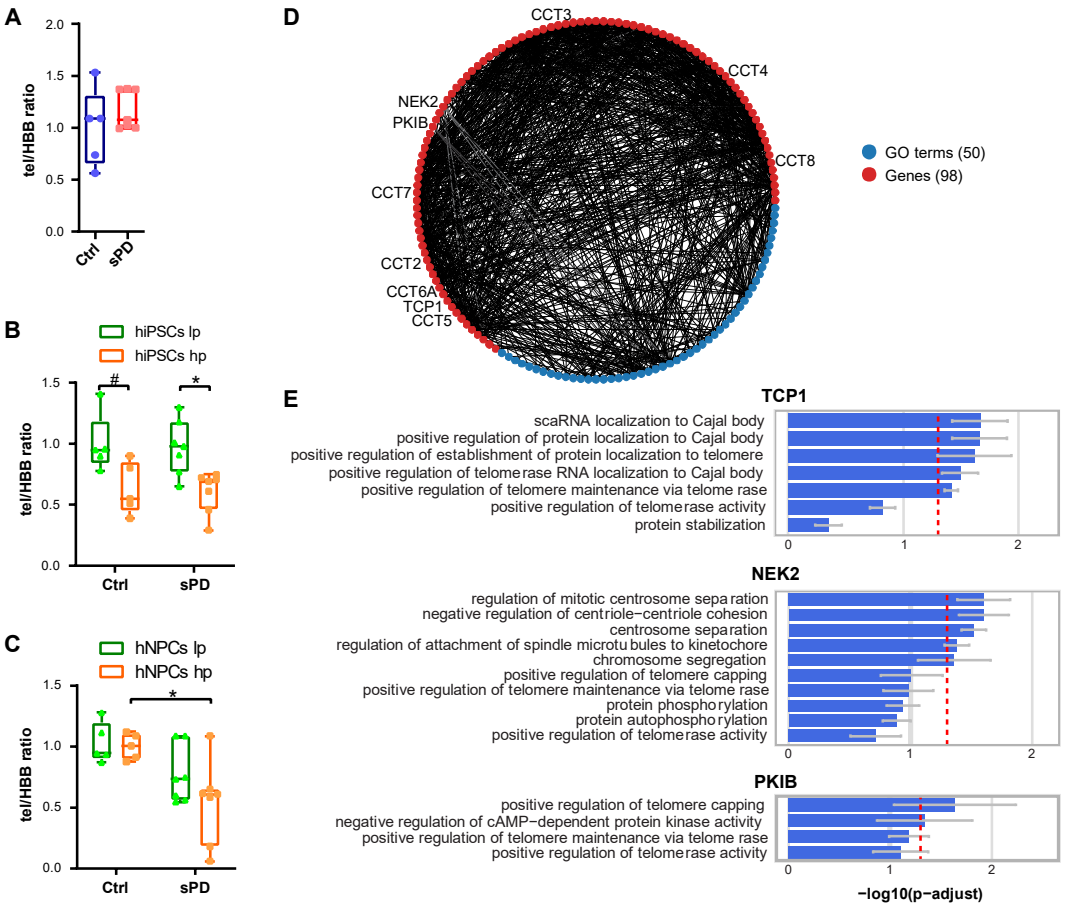

Figure 37 | Telomere attrition in high-passage sPD lines. (A) Telomere length analyzed in fibroblasts, **(B)** low and high-passage hiPSCs, and **(C)** hNPC clones (data provided by (*272*)). The telomere fragment to single-copy gene HBB ratio was determined by qPCR. n = 5 Ctrl and 7 sPD clones. P values are determined by (Welch-test **A**; two-way ANOVA and Tukey`s Post-hoc test **B**, **C**). *, $p < 0.05$; **, $p < 0.01$; ***, $p < 0.001$. **(D)** Differentially expressed genes that are associated with telomere function and maintenance in high-passage sPD hNPCs. **(E)** Annotated biological processes for selected genes associated with telomere function and maintenance are rank-ordered by mean FDR adjusted p-value. Error bars indicate 95 % confidence intervals of mean p-adjust, dotted lines indicate the significance threshold ($q < 0.05$). In parts taken from a manuscript (Schmidt et al.) submitted to peer-reviewing journals.

nuclear lamina integrity [reviewed in chapter 1.2]. One important function of the nuclear lamina is genomic maintenance. It provides a scaffold for chromatin and protein complexes involved in DNA repair and genomic stability (*273*). Although observing a decreased LAP2a expression in high-passage hNPCs and sPD DAns, the amount of γH2A.X foci, a marker for double-strand breaks, was similar between low- and high-passage cells as well as between Ctrl and sPD (***Figure 36B***, ***Table 18***, ***Table 19***).

The most characteristic feature of cellular aging, however, is still telomere attrition. It has been shown that telomerase deficiency leads to premature aging in mice which can be rescued by reactivation of telomerase in aged mice (*274*). In mitotic cells telomeres are shortened with every cell division, forcing cells eventually into replicative senescence to avoid DNA damage. In pluripotent cells like hiPSCs, telomerase activity maintains the telomeres allowing for unlimited proliferation (*275*). To further

investigate the aging phenotype, telomere length was analyzed in fibroblasts, hiPSCs, and hNPCs. As expected, there was no difference in telomere length between fibroblasts derived from sPD patients and healthy Ctrls (Ctrl: 1.00±0.37; sPD: 1.17±0.19) (***Figure 37A***). Long-term *in vitro* cultivation resulted in telomere attrition in hiPSCs, in both Ctrl and sPD cells (***Figure 37B***, ***Table 20***). However, telomere length in low-passage and high-passage Ctrl, as well as low-passage sPD cells, was reduced to similar levels during neural differentiation, whereas telomere attrition was more pronounced in high-passage hNPCs derived from sPD patients (***Figure 37C***, ***Table 20***). Genewalk analysis of the transcriptome data (bulk-like DEGs) of high-passage hNPCs allowed to identify some candidate genes that were dysregulated in sPD and in the cellular context most likely involved in telomere maintenance (***Figure 37D***,***E***). In total 98 genes assigned to telomere-associated GO terms (50 GO terms) were dysregulated. Amongst others, the genes *TCP1*, *CCT2*, *CCT3*, *CCT4*, *CCT5*, *CCT6A*, *CCT7,* and *CCT8*, all of which are components of the TCP1 Ring Complex (TRiC). A chaperone complex that consists of two rings of eight CCT subunits (CCT1-8) each, and is involved in the folding of numerous proteins e.g. the telomerase complex component WRAP53 as well as the BBSome. The depletion of TRiC results not only in decreased WRAP53 levels but also causes a mislocalization of the telomerase complex which finally leads to a failure of telomere elongation (*276*). Interestingly, expression of *CCT1*, *CCT2*, *CCT4*, and *CCT6* appears to be repressed in human brain tissue during aging as well as in Alzheimer's and Huntington's disease and with varying significance also in PD (*277*). This confirms the previous findings and indicates even further an aging phenotype that seems to be specific to neural cells derived from sPD patients after long-term *in vitro* cultivation.

2.11. Correlation of phenotypes and stratification of sPD patients

Neuronal populations derived from high-passage sPD hiPSC lines developed a PD-specific pattern that included mitochondrial, as well as ciliary dysfunction. To investigate a possible link between these two PD-associated phenotypes, a correlation analysis was performed including mitochondrial and ciliary parameters, as well as parameters associated with neurogenesis. A correlation analysis allows quantifying the strength of the relationship between two quantitative variables. A perfect negative or positive correlation has a correlation coefficient of -1 or 1, respectively, whereas 0 means that there is no relationship between the variables at all. The resulting correlation matrix is visualized in **Figure *38*** and the correlation coefficients are summarized in ***Table 21***.

As expected, mitochondrial respiration parameters quantified by Seahorse XF were positively correlated. These parameters also correlated with NAD^+ levels and cilia fraction. Interestingly, mitochondrial respiration parameters were not correlated with ciliary length, which was, however, negatively correlated with the abundance of the electron transport complexes I-IV, as well as their activity. In line with this, the imbalanced mitochondrial function has been shown to provoke aberrant ciliary function. For example, lowering or inhibition of complex I activity using rotenone elongates zebrafish PC, whereas increasing mitochondrial biogenesis was shown to result in cilia length reduction (*278*).

Ciliary length was also positively correlated with total ATP levels. Appropriate ATP levels are required for normal ciliary function since ATP-consuming motor proteins power the intraflagellar transport system [reviewed in chapter 1.5]. The energy required is provided amongst others by mitochondria which were found to assemble in close proximity to the basal body. Cilia-associated mitochondrial proteins are thought

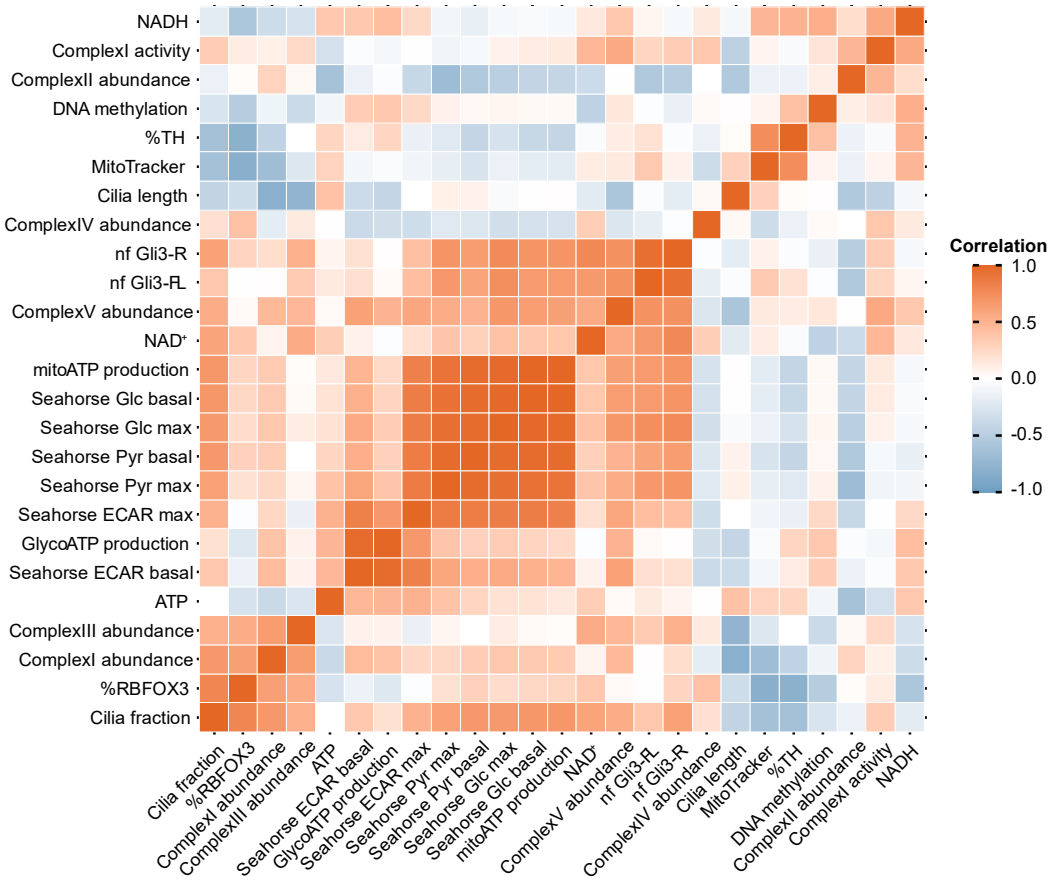

Figure 38 | Correlation matrix. The correlation matrix summarizes the correlation coefficients (***Table 10***) between variables quantified in high-passage hNPCs and thereof differentiated dopaminergic neurons. Each experiment was performed with n = 5 Ctrl and 7 sPD clones, in triplicates.

to recruit mitochondria to basal bodies to not only promote ATP delivery to the PC but also to coordinate calcium release, mitochondrial depolarization, or induction of mitophagy (*279*). For example, OFD2 is important for the centrosome conversion to the basal body, but also recruits TCHP (Mitostatin), which has been implicated in the recruitment of PRKN and thus PINK1 (*280*). Both are implicated in mitochondrial quality control by mediating mitophagy (*281*) but are also PD-associated risk genes (***Table 1***). This displays a possible link between mitochondrial (*266, 282*) and ciliary dysfunction observed in *PINK1* ko hiPSCs as well as *Pink1* ko mice.

Interestingly, cilia length was only weakly correlated with SHH signal transduction, which was instead positively correlated with mitochondrial respiration. This may suggest that GLI3 processing was dominated by other cellular processes than cilia length in hNPC and may affect mitochondrial respiration. This is in line with the observations that SHH pathway activation increases mitochondrial activity in hippocampal neurons amongst others (*283*).

Furthermore, the fraction of ciliated cells possibly affected neuronal differentiation efficiency. A high fraction of ciliated cells seemed to have a beneficial effect on neuronal differentiation, resulting in more

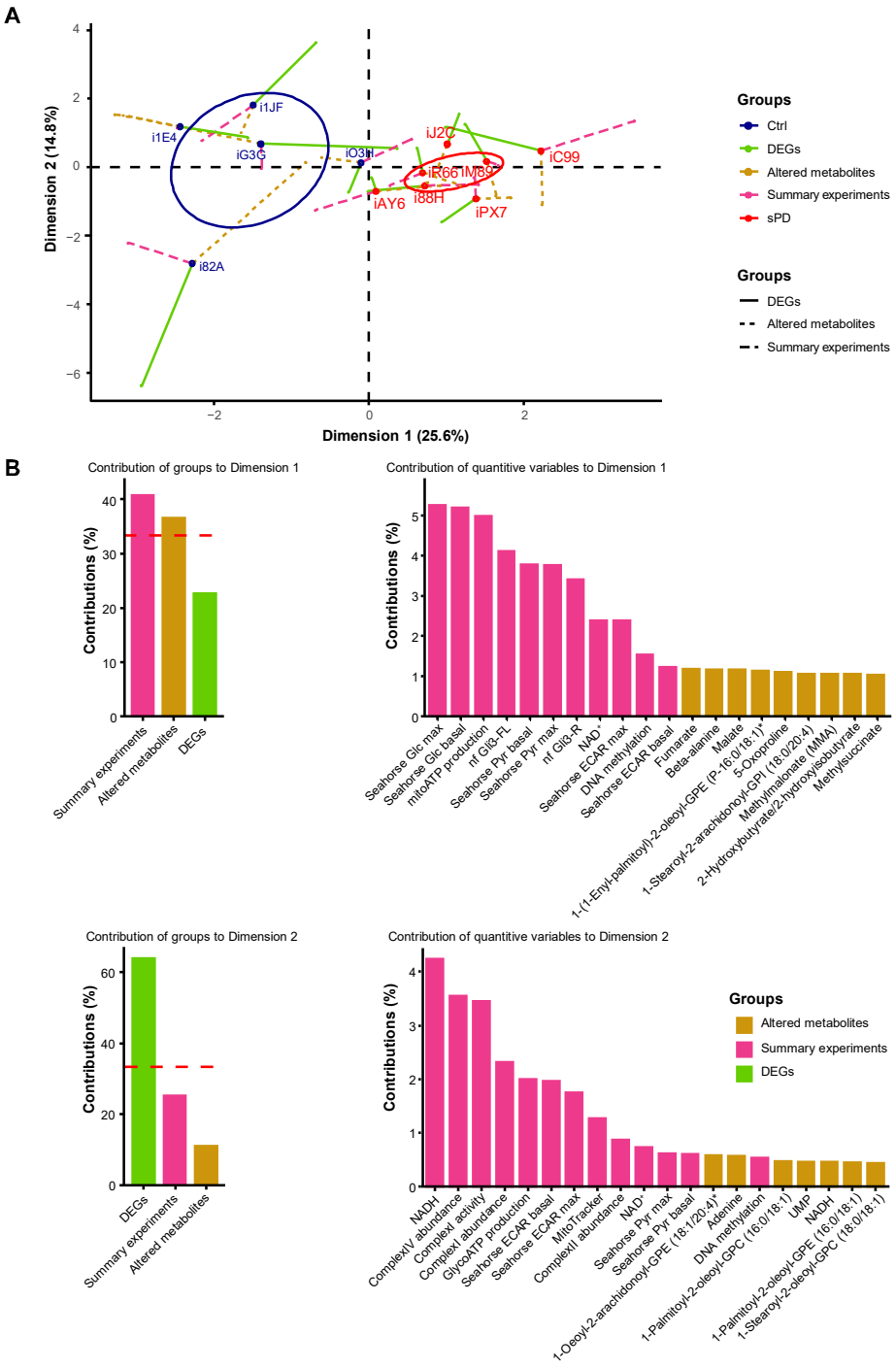

Figure 39 | Multiple factor analysis. (A) Integration of significantly altered metabolites (45 metabolites) quantified by non-targeted metabolomics, DEGs of the NSC1a cluster (4517 genes) identified by scRNA-seq, as well as all experimental variables (25 variables) displayed in ***Figure 38*** by MFA. The group colors represent the patient coordinates seen by only the group variables. **(B)** Contributions of quantitative variables of the categories “Altered metabolites”, “Summary experiments” and “DEGs” to the MFA dimension 1 and 2.

RBFOX3 (NeuN) positive cells. Neurogenesis involves a great variety of cell-extrinsic and cell-intrinsic signals which are thought to regulate patterning, the progression of the cell cycle, the timing of neurogenesis as well as dendritogenesis [reviewed in chapter 1.4 and in (*284*). PC as essential signaling hubs that fine-tune cellular responses to extrinsic signaling events may thereby be crucial in determining cell fate decisions. Surprisingly, the fraction of ciliated cells as well as the fraction of neurons negatively correlated with DAn differentiation efficiency. This suggests that the culturing conditions used for DAn differentiation may favor the neurogenesis of non-dopaminergic neurons from ciliated multipotent cells. Thus, further adaptions of the concentrations of signaling molecules in the differentiation protocol may be necessary to increase DAn differentiation efficiency.

In conclusion, this suggests that the presented data are inherently conclusive and that a link exists between mitochondrial and ciliary dysfunction, which is in line with previously published observations.

In the next step, these correlating data were used to further stratify and order the patients hierarchically according to the severity of their molecular alterations (phenotypes). Therefore, a multiple factor analysis (MFA) was performed to also include the detailed information gained from the scRNA-seq and non-targeted metabolomics analysis. MFA is a multivariate data analysis method for summarizing and visualizing data of individuals, which are described by a set of variables structured in groups. In total 4 groups of variables were used for the MFA (***Figure 39***): the significantly altered metabolites (45 metabolites) quantified by non-targeted metabolomics, DEGs of the NSC1a cluster (4517 genes) identified by scRNA-seq, all experimental variables (25 variables) used for the correlation analysis, and as a supplementary group, the information about the disease state (Ctrl or sPD).

Dimension 1 and 2 explain together about 40.4 % of the variability observed in patients (***Figure 39A***). The first dimension represents the experimental variables and altered metabolites (***Figure 39B***, ***Table 22***). Of particular interest is the separation of Ctrl and sPD patients by dimension 1, meaning that at least some metabolic phenotypes are negatively correlated between Ctrl and sPD patients. The larger the distance between an sPD patient and the average of Ctrl patients is, the larger are the alterations from the normally expected phenotype. Thus, indicating a more severe phenotype in distant sPD patients. The second dimension represents the DEGs and mainly separates the Ctrl patients, which seem to exhibit a higher variability than the sPD patients (***Figure 39A***,***B***, ***Table 22***). Especially one Ctrl patient (i82A) is separated from the remaining Ctrls by dimension 2. Another Ctrl patient (iO3H) seemed to cluster closer to the sPD patients than the remaining Ctrls.

Interestingly, the second dimension representing the DEGs splits the sPD patients into 2 subgroups, one with positive (iJ2C, iM89, and iC99) and one with negative coordinates (iAY6, i88H, iPX7). Thus, on the transcriptome levels, there are negative correlations for at least some genes that may be used to further group sPD patients. However, sPD patients clustered in close proximity of the second axis, meaning that the observed variation may be small, especially if compared to the Ctrl patients.

In conclusion, the first dimension representing mainly metabolic variations can be used to hierarchically order sPD patients according to the severity of their molecular alterations.

3. Discussion

Animal model systems carrying PD-associated mutations are widely used to harness the molecular and cellular mechanisms associated with PD such as mitochondrial impairment, autophagy, protein aggregation, proteasomal degradation, and lysosomal dysfunction [reviewed in chapter 1.1]. Still, the relevance of these molecular mechanisms for the etiology of sPD remains largely elusive due to the lack of suitable human models (*229*). This thesis aimed to establish a human cellular model for sPD, which should be used to explore molecular alterations underlying the etiology and progression of sPD. To unravel these cellular processes and molecular mechanisms contributing to sPD etiology unbiased molecular characterization methods such as a state-of-the-art single-cell transcriptome and non-targeted metabolomics analysis were used.

3.1. Parkinson's disease-specific aging signature after long-term *in vitro* cultivation.

To establish a more biological, not stress-induced human model that can be used to explore molecular alterations underlying the etiology of sPD, the effect of long-term *in vitro* cultivation on PD-related phenotypes like mitochondrial dysfunction was investigated. To address this question, fibroblasts from sPD patients and age- and sex-matched Ctrl individuals were reprogrammed into hiPSCs and cultivated for 25 to 70 passages to yield low- or high-passage hiPSCs, respectively. Low- and high-passage hiPSCs were then differentiated towards DAns and screened for known PD-associated phenotypes such as mitochondrial dysfunction. An overview of high-passage-associated phenotypes is displayed in **Figure *40***.
Low-passage hiPSCs and their derivatives did not display the expected PD-associated alterations in metabolism such as a reduced maximal mitochondrial respiration, nor did high-passage hiPSCs. These alterations only occurred upon the differentiation of high-passage hiPSCs into hNPCs and further into DAns. This raises the question about which molecular alterations happen to sPD cells during long-term *in vitro* cultivation that causes them to exhibit a phenotype deviating from the control state. As mitochondrial dysfunction is also associated with cellular aging, one hypothesis could be that long-term *in vitro* cultivation might recapitulate, at least to some extent, cellular aging processes that are enhanced in sPD cells. Indeed, high-passage cells developed also several other aging-associated alterations, of which telomere attrition is of particular interest. Again, the severity of aging-associated alterations seemed to be enhanced in sPD hNPCs and Dans. This aging phenotype may be suppressed in hiPSCs due to their stem cell characteristics but may visualize upon differentiation.
Telomere attrition is thought to accompany normal aging and the telomere shortening rate is a useful predictor of species lifespan (*128*). Similar telomere lengths were measured in low- and high-passage hiPSCs, however, the telomere shortening rate increased in sPD cells upon differentiation to DAns. If telomere length reaches a critical threshold, cells are normally forced into replicative senescence or apoptosis (*285*), which was, however, not observed in high-passage cells.
This increased telomere shortening rate in high-passage sPD hNPCs seems to be linked to other pathological hallmarks, namely: 1) Nuclear lamina alterations, 2) accumulation of DNA damage and 3) dysfunction of the TRiC complex.

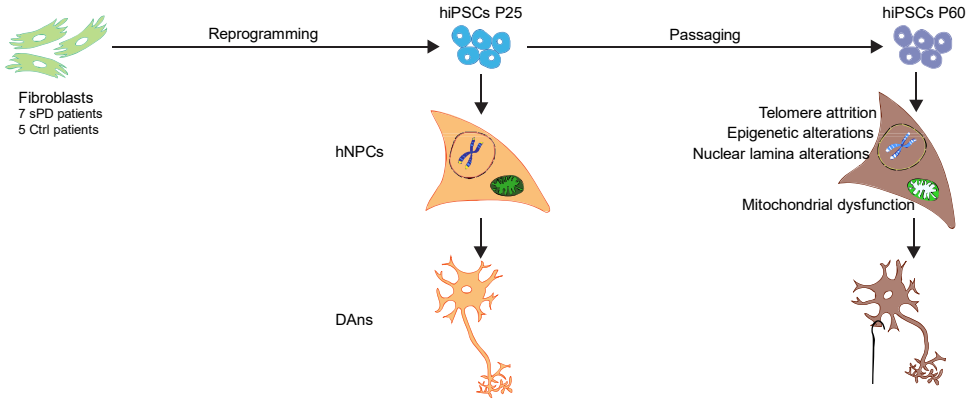

Figure 40 | sPD specific signature. Fibroblasts derived from 5 Ctrl and 7 sPD patients were reprogrammed to hiPSCs through retroviral transduction of POU5F1, SOX2, KLF4, and MYC. hiPSCs were cultivated in vitro for ~60 passages with passaging every 5-7 days and differentiated to hNPCs as well as DAns. Derivatives from high-passage sPD hiPSC lines developed a specific pattern that included telomere attrition, epigenetic and nuclear lamina alterations as well as mitochondrial dysfunction.

Alterations of A-type lamins have been shown to cause defects in various cellular pathways such as DNA replication and repair, gene transcription, and silencing. These defects are the result of altered lamin properties, which affect nuclear architecture and chromatin organization. For example, progerin, an abnormal version of lamin A that causes Hutchinson-Gilford progeria syndrome, has a lower affinity for LAPs such as LAP2α (*286*). These LAPs are thought to link specific chromatin regions, also telomeres, to the nuclear envelop, by doing so they structure the chromatin into functional domains and support the recruitment of specific factors involved in, amongst others, DNA repair (*287*). Telomere association to lamins has to be dynamic as it depends on the cell cycle phases. LAP2α is thought to be cytoplasmic in metaphase and associated with telomeres in anaphase. In telophase, telomeric LAP2α forms structures on chromatin adjacent to the spindle. During nuclear assembly, telomeres would be tethered at the nuclear periphery together with lamins and translocate to the nucleoplasm in interphase (*273, 288, 289*). Thus, altered levels of LAP2α as shown here in sPD cells will have a crucial effect on telomere dynamics and maintenance in high-passage sPD hNPCs and DAns. Also, lamins and LAP2α affect chromatin organization and epigenetics, for example, the levels of the heterochromatic mark H3K27me3 (*273, 286*). It has been shown that progerin or reduced levels of LAP2α can lead to heterochromatin loss, similar to the observed loss of H3K9me3 and H3K27me3 in high-passage sPD hNPCs and DAns.

Telomeres are not only progressively shortened during normal aging or in the absence of telomerase but can also be shortened in the presence of telomerase (*61*). Telomeres are bound by shelterin, which limits the access of the DNA repair machinery to telomeres and protects the chromosome ends from deterioration or fusion [reviewed in chapter 1.2.3]. As consequence, exogenous DNA damage to telomeres becomes invisible to the DNA repair machinery and accumulates, causing senescence or apoptosis. Furthermore, pathological telomere dysfunction was shown to accelerate aging in humans (*61*), which is accompanied by also PD-associated dysfunctions such as mitochondrial dysfunction (*290*).

The TRiC complex is a chaperone required for the folding of the telomerase cofactor TCAB1, which controls the trafficking of the telomerase to Cajal bodies and, subsequently, to telomeres. Consequently, alterations in TRiC function and impaired folding of TCAB1 result in telomerase mislocalization and failure of telomere elongation (*276*). Interestingly, also other clients of the TRiC chaperone complex were shown

to be dysfunctional in sPD such as the BBSome, which is essential for normal ciliary function [further discussed in chapter 3.2]. Furthermore, the TRiC complex is thought to restrict neuropathogenic protein aggregations via autophagy, a pathway that is also associated with PD pathology (*291, 292*). This possibly makes the TRiC complex an exciting new candidate for further sPD research, as it allows to link several PD-associated alterations.

Telomere attrition may not be useful as a biomarker for PD, as it couldn't be detected in patient-derived fibroblasts [this thesis] or blood samples (*293*). But it nicely correlates with accepted PD-associated phenotypes like mitochondrial dysfunction and, thus, could be used as a readout for further screening projects.

But is that enough to state that these hiPSCs aged in a dish? Well, that may depend on how aging is defined. If it is simply defined as the accumulation of damage over time that affects the function of various cellular pathways, the answer should be yes. However, it might be a little bit more complex. Firstly, it cannot be stated that hiPSCs in general age during long-term *in vitro* cultivation, as, especially in the more defined neuronal stage, only DAns derived from sPD patients displayed alterations. Furthermore, high-passage neuronal cells derived from sPD patients did not exhibit a complete aging phenotype, as hallmarks like increased mitochondrial ROS production or increased DNA damage could not be detected. Nevertheless, long-term *in vitro* cultivation is sufficient to trigger phenotypes observed in the late-onset disease.

To also address the controversial topic of pathogenic cell types contributing to sPD etiology and DAn degeneration, also the original patient-derived fibroblasts, as well as astrocytes and motor neurons derived from high-passage hNPCs were screened for mitochondrial alterations.

Although patients with sPD show no clinical signs of fibroblast pathology, these cells are often used as model systems to investigate PD-associated alterations (*294*). This model system is thought to have the advantage of comprising the chronological and biological aging of PD patients according to their predisposition and environmental influences. In most studies, a clear mitochondrial deficit e.g. a reduced basal or maximal respiration or a reduced complex I activity has been described (*295*). However, the largest study up to date including fibroblasts from 20 PD patients and 19 Ctrls couldn't recapitulate these findings also due to the large variability of complex activity between patients (*296*), nor could these findings be validated analyzing the fibroblasts used in this thesis. These controversial results suggest that fibroblasts may be unsuitable for studying the pathoetiology of sPD, as well as for the identification of biomarkers for diagnostics. It seems to be highly likely that fibroblasts are not necessarily subjected to alterations caused by PD. These alterations may be caused by somatic mutations in specific regions (*297*), or by environmental stimuli affecting only specific cell types.

This may not be the case for fibroblasts derived from fPD patients. These fibroblasts carry the same gene mutations responsible for fPD development and the PD-associated genes are also robustly expressed in fibroblasts. This may allow studying the involvement of these mutated genes on specific cellular processes on a human-specific background that also comprises to some extent the patients' age and environmental influences.

There is growing evidence that glial cells (microglia or astrocytes) contribute to PD pathoetiology by losing their normal homeostatic function, as well as by gaining neurotoxic functions. For example, it has been reported that PD-associated gene mutations can cause astrocytic cells to produce higher levels of SNCA, to have an increased sensitivity to inflammatory signaling, or to develop mitochondrial dysfunctions (*266, 298*). However, astrocytes differentiated from high-passage hNPCs did not exhibit the expected PD-associated mitochondrial alterations. Meaning that mitochondrial respiration seemed to be adjusted to the "normal" astrocytic state in both Ctrl and sPD cells during differentiation.

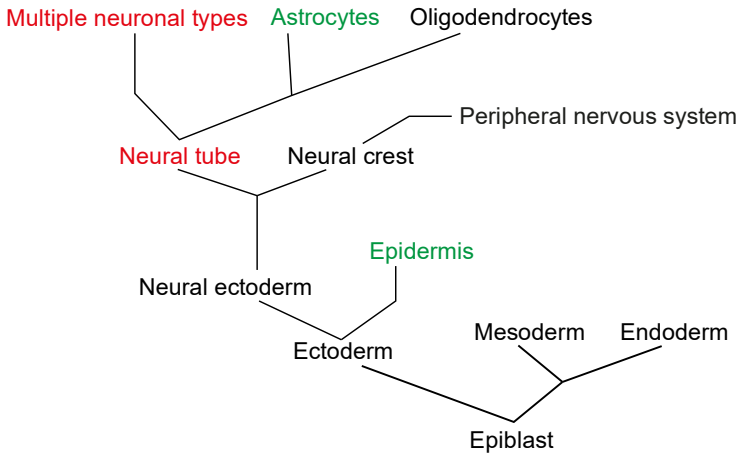

Figure 41 | Embryonic development. The ontology tree presents an overview of the epiblast development, through the germ layers (ectoderm, mesoderm, and endoderm) to their derived organs and tissues. Cell types exhibiting mitochondrial dysfunction are colored in red, whereas cell types with normal mitochondrial function are colored in green. Figure adapted from LifeMap Discovery (*299*).

This is in line with the analysis of fibroblasts derived from sPD patients. It strengthens the suspicion that especially in sPD the number of affected cell types is limited or even restricted to specific cell types, which possibly depends on the case-specific underlying causes (e.g. somatic mutations, environmental stimuli). The cellular model used in this thesis allowed to confine the pathogenic cell types to specific neural-tube-derived cells. PD-associated phenotypes were solely present in neural precursor cells with midbrain identity that are thought to mimic neuroepithelial cells, as well as a neuronal population containing multiple neuronal subtypes, amongst others, DAns (***Figure 41***). These phenotypes were not present in the ectoderm-derived epidermis (fibroblasts), glial cells (astrocytes), or other neuronal subtypes (motor neurons) than DAns, which suggests a lineage specificity for the development of cellular alterations during the prodromal phase of sPD.

Nevertheless, the question remains how these alterations are actually induced in sPD. The analysis of high-passage hNPCs and neurons allows some speculations to further refine the theory about disease etiology. Firstly, it is well established that sPD is a multifactorial disorder with seemingly random occurrence due to undetermined genetic or environmental bases (*300*). Interestingly, in this thesis, it could be shown that a PD-associated mitochondrial dysfunction developed also in a cellular model under standardized cultivation conditions. Under standardized environmental conditions, cells (fibroblasts, low-passage hiPSCs, and their derivatives) derived from sPD patients first behaved similarly to Ctrl clones, however, when cultivated for 45 or more passages developed sPD specific phenotypes. Thus, in this model, it can be excluded that environmental influences interfere with sPD progression.
However, it cannot be excluded that alterations caused by environmental influences were present in sPD fibroblasts and survived the reprogramming to rejuvenated hiPSCs (*234, 301*). It is thought that only a brief period in naïve pluripotency conditions would be sufficient for major epigenome remodeling but would allow preserving, amongst others, epigenetic imprints (*237*). This would mean that alterations observed in fibroblasts should also be present in hiPSCs and their derivatives right from the beginning. That these alterations are not present in fibroblasts or low-passage cells but develop over time and only after differentiation of high-passage hiPSC into neurons seems to be contradictory to the idea of pathogenic epigenetic imprints.

Secondly, transcriptome analysis of high-passage hNPCs was used to unravel the molecular underpinnings that might contribute to sPD etiology. Therefore, a state-of-the-art scRNA-seq analysis was performed. Pooled libraries from different individuals were demultiplexed based on SNPs, which allowed not only to avoid confounding technical batch effects but also to precisely identify and remove doublets (DBLs) and ambiguous cells (AMB) that could not be assigned to one specific donor. This allowed identifying 9 clusters that represent transcriptionally distinct cell populations present in the high-passage hNPC culture. Further analysis of the visualization and clustering showed that none of these clusters was dominated by either disease state, gender, age, or individual donors. Single-cell resolution is thereby critical to unravel molecular mechanisms contributing to sPD etiology in a cell-type-specific manner.
Especially three altered cellular processes are thereby of particular interest: 1) Mitochondrial dysfunction [further discussed in chapter 3.2.], 2) Alterations in PC mediated intracellular signaling [further discussed in chapter 3.3] and 3) DNA damage repair. These processes could be detected on the bulk-level but also in selected clusters, of which the NSC1a cluster is of particular interest as it is the most populated cluster (robust detection of DEGs) and also at the root of neuronal differentiation.
The contribution of DNA damage and repair to neurodegeneration is an exciting new research field. A decline in the DNA repair capacity and the accumulation of DNA damage have been proposed to be the main drivers of cellular aging but to also contribute to neurodegeneration (*302*). A DNA repair deficiency can be caused by mutations in DNA repair enzymes or their misexpression, which initiates a negative loop resulting in the accumulation of DNA damage or an incomplete repair (*302, 303*). The accumulation of DNA damage in genes relevant for critical cellular functions may further affect genomic stability, the epigenome, protein homeostasis, mitochondrial function, or cell-cell communication. However, neuronal complex I deficiency in PD patients was shown to be independent of at least mtDNA damage (*165*). Furthermore, it was also not possible to detect increased levels of DNA damage (yH2A.X foci) in PD cells. This analysis, however, provides only a snapshot and is not enough to allow conclusions about the cellular DNA repair capacity, nor about the frequency of DNA lesions. A DNA repair deficiency in PD cells could explain the observed phenotypes but has to be further characterized.
In conclusion, the cellular model described in this thesis is a suitable model system to study the etiology of sPD. It is the first cellular model available that recapitulates PD-associated phenotypes associated with mitochondrial function (*304*). Almost every stage of the prodromal phase is represented, from a no symptoms phase to severe mitochondrial alterations e.g. complex I deficiency. Yet one thing is missing: a neurodegeneration phenotype. Even though neuronal cells derived from PD patients exhibit severe mitochondrial alterations, these alterations did not interfere with DAn differentiation, maturation, nor maintenance. Interestingly, after long-term cultivation (>75 days), it has been shown that DAns differentiated from sPD hiPSC displayed morphological alterations, including reduced numbers of neurites and neurite arborization (*305*). It may be that DAns after 40 days of differentiation and maturation, as used in this thesis, are still too immature and “young” to display morphological alterations. Prolonged cultivation of DAns for up to 75 days may be useful to observe alterations in neurite morphology or even neurodegeneration. However, this has to be further investigated.

3.2. A pattern of global gene misexpression underlies Parkinson’s disease-associated phenotypes.

In this study, scRNA-seq was used to unravel regulatory defects in discrete cell subpopulations in sPD patient-derived high-passage hNPC lines. This offers the advantage of detecting disease-specific

impairments in cellular processes and pathways at early developmental stages independent of neuronal cell type specificity (as in hiPSC-derived neuronal cultures) and disease progression (as in human postmortem material). Indeed, it could be shown for the first time that already hiPSC derived hNPCs show cellular heterogeneity with PD-specific signatures. Interestingly, besides the overrepresentation of PD-associated risk genes, the root population of sPD hNPCs showed a specific enrichment of dysregulated genes associated with mitochondrial function supporting the assumption that mitochondrial dysfunction and bioenergetics failure are at the root of sPD etiology. Additionally, a pattern of global gene repression was observed. The gene expression changes are mostly small, albeit highly significant. Thus, they may not lead to an overt phenotype per se, but might be - according to the multiple hit theory (*306*) - the underlying cause of reduced compensatory capacity or reduced tolerance to further disturbances of cells derived from these hNPCs.

In general, this pattern of global gene repression could be explained by alterations in 1) DNA methylation, 2) Chromosome reorganization or histone modifications, and 3) signal transduction.

Alterations of DNA methylation at specific loci are thought to influence gene expression [reviewed in chapter 1.2.1]. However, to cause a pattern of global gene repression one would also expect a pattern of hypermethylation (*307*), which was not observed in sPD high-passage hNPCs. Interestingly, chromatin reorganization during neural development (*308*) and, thus, the silencing of alternative fate regions seemed to be impaired in sPD clones. Upon differentiation of hiPSCs into DAns, sPD clones exhibit reduced levels of the heterochromatin marks H3K9me3 and H3K27me3, indicating heterochromatin loss. However, it must be emphasized that the observed pattern of repression in NSC clusters cannot be explained by heterochromatin loss per se. The logical consequence of the loss of heterochromatin-induced gene silencing in sPD hNPCs and DAns would be gene activation and not repression. That high-passage hNPCs exhibit a strong pattern of gene repression is thus more likely the consequence of alterations in PC-mediated intracellular signaling. Both morphogen controlled genetic networks - *SHH-FOXA2* and *LMX1A*/*B-WNT1-OTX2* - that are involved in midbrain dopaminergic specification and survival [reviewed in chapter 1.4] are thought to function via PC (*205, 309–311*), which are known to be impaired in sPD hNPCs and DAns [discussed in chapter 3.2]. Especially for SHH signaling, it could be shown that the processing of the respective transcription factors was affected, which resulted in gene expression changes of transcription factor targets. Approximately 25 % of DEGs (NSC1a cluster) were predicted GLI3 target genes.

Although the exact cause of the global gene repression remains unknown, the consequences of these changes are severe, as they contribute to various cellular pathways, amongst others, associated with 1) Intracellular signaling and proteasomal degradation; 2) Cell cycle; 3) Protein translation; 4) DNA damage repair and 5) the citric acid cycle and ETC complex biogenesis.

Interestingly, the downregulation of mitochondrial proteins, especially of nuclear-encoded subunits of the ETC, that was observed in high-passage sPD hNPCs is also the most consistently reported alteration in aging, which is the greatest risk factor for developing sPD. These alterations have been reported in various species, including humans (*312–314*), rodents (*312, 315, 316*), and worms (*317, 318*) across a range of cell types from fibroblasts to neurons (*316, 319–321*). The reductions in mRNA level of mitochondrial proteins reported in these studies and this thesis are often small, but are clearly significant and pursue on the proteome level in mammals and worms (*322*). This may indicate that the development of mitochondrial dysfunction in sPD clones upon long-term *in vitro* cultivation occurs according to a predefined aging process that is conserved in various species and is somehow accelerated in sPD. This further strengthens the assumption that mitochondrial dysfunction and bioenergetics failure are at the root of sPD etiology.

The observed alterations in gene expression also allow drawing conclusions about the metabolic alterations underlying the mitochondrial respiration deficiency observed in sPD clones. Based on the expression changes of citric acid cycle enzymes and the abundance of citric acid cycle intermediates, it seems likely that the flux through the citric acid cycle is reduced in sPD, resulting in a decreased NADH production rate and, thus, mitochondrial respiration. This may be caused by a rerouting of intermediates from the energy-producing pathways glycolysis and citric acid cycle into branching pathways such as the pentose phosphate pathway, but also lactate production (preliminary data not shown). This may affect all cellular processes that rely on a constant energy supply, which is especially critical for highly energy-demanding cell types such as DAns.

These speculations are strengthened by the diminished levels of metabolites. Approximately 20 % of all detected metabolites were significantly dysregulated in sPD, and all of them were downregulated, indicating a state of hypometabolism. Hypometabolism is defined as an abnormally low metabolic rate and is hypothesized to predispose the development of various neurodegenerative diseases like PD or Alzheimer's disease (*323*). PD patients often exhibit a cortical hypometabolism, meaning reduced glucose consumption (*324–327*). A low cerebral glucose metabolic rate in brain regions of PD patients can be used as predictors for the severity and progression of PD and may even precede the onset of motor symptoms (*323*).

Taken together, the observed pattern of global gene repression is most likely the consequence of alterations in the expression and processing of transcription factors involved in cell fate decisions like e.g. GLI3. The consequences of these changes are severe, as they contribute to various cellular processes and all previously discussed sPD phenotypes (ETC complex deficiency, genomic instability, telomere attrition, and ciliary dysfunction). Especially PC dysfunction is thereby of interest, as it may enforce the gene misexpression observed in sPD, creating a negative feedback loop.

3.3. Ciliary dysfunction is a convergence point in Parkinson's disease etiology.

On the bulk-level but also in the NSC1a subpopulation - which gives rise to immature neurons - enrichment analysis reveals PC as a key hub of sPD. To maintain functional PC, correct length and shuttling of signaling molecules are essential, all of which are affected in sPD hNPCs (length, BBSome interaction, and IFT). Especially IFT is thereby of interest, as cilia typically lack the machinery that is necessary for protein synthesis. Hence, they rely on intracellular and intraflagellar transport systems for the delivery of new building material to their site of assembly, as well as the delivery of receptors/signal transducers and their export for a correct functionality (*188*). For example, IFT57 which is downregulated in sPD in the NSC1a cluster is not absolutely required for ciliogenesis and IFT per se but is required for ciliary elongation (*328*). IFT88 on the other hand is a core component of the IFT-B complex and essential for ciliogenesis (*329, 330*), however, not dysregulated in sPD in the NSC1a cluster. Thus, a mild reduction in the expression of IFT members that are not necessarily essential for ciliogenesis per se might explain the observed reduction in cilia length instead of alterations in PC abundance. Furthermore, mutations in genes associated with IFT or the sorting system (e.g. BBSome) are known to cause severe alterations in PC morphology (length, thickness), which is thought to be tightly regulated to maintain cell-specific lengths appropriate for their functions (*196*). These alterations are thought to underly various diseases [reviewed in chapter 1.5.3].

Interestingly in two recent reports performing either transcriptome analysis in NSCs of postmortem PD patients or hiPSC derived neurons from young-onset PD patients, downregulation of PC-associated pathways has also been observed (*331, 332*). In the present study, for the first time alterations in PC-associated pathways in hiPSC-derived neural cells from late-onset sPD patients have been described and additionally validated by showing that the length of PC is reduced and consequently PC-dependent signaling pathways are altered. It is worth noting that these changes seem to be restricted to neurons again since astrocytes do not exhibit significant changes in PC length. Most interestingly, also PC-related genes that are dysregulated in the postmortem SN of sPD patients based on a meta-analysis published by (*269*) have been identified.

The PC is a centriole-derived, membrane-ensheathed projection present in most mammalian cells. PC exhibit a microenvironment insulated from the cytosol compartment enriched for receptor tyrosine kinase (RTK) and GPCR membrane receptors and their downstream effectors (*206*). Thus, it is not surprising, that ciliary dysfunction is accompanied by dysregulation of several GPCR mediated signaling pathways amongst which is the PD relevant serotonergic and dopaminergic signaling via HTR4/6/7 and DRD1/5, respectively (*261, 262, 333*).

At first glance, an association of ciliary dysfunction with the pathoetiology of neurodegenerative diseases is not obvious. However, PC dysfunction starts to emerge as a pathoetiological component of Alzheimer's Disease, Huntington's Disease, ALS, and PD since the analysis of respective animal models have shown alterations in PC morphology (*332, 334–336*). The results of the present translational study corroborate these findings also in a human cellular model of sPD. Furthermore, a previously published meta-analysis of SN transcriptome studies strengthens the hypothesis that ciliary dysfunction is a common hallmark of PD patients, also in advanced stages of PD. Specifically in PD, a disruption of ciliary signaling might influence PD pathoetiology at several levels.

Firstly, loss of PC has been linked to loss of DAn during development due to its effect on early SHH signaling (*337*), a pathway impaired in the cellular model used in this study. However, in the present model differentiation from hNPCs to DAns is not affected. This might be due to the presence of PC in the hNPCs of sPD patients and thus SHH signaling not being completely abolished. Instead, GLI3 processing within a shortened cilium seems to be affected. Thus, there might be a functional distinction between the absence of PC versus alterations in PC morphology concerning cilia-mediated signaling. This hypothesis is strengthened by the correlation of the differentiation efficiency with the abundance of PC. To have more ciliated cells seemed to be beneficial for neurogenesis, whereas cilia morphology did not interfere with this process.

Secondly, focusing on the role of PC beyond neurogenesis and differentiation, several studies have reported intriguing findings that link slight ciliary alterations to disease progression. PC-mediated signaling pathways appear necessary for neuronal homeostasis and maintenance of e.g. DAn in adult brains (*270, 334*). As such, it has been described that loss of dopaminergic inputs on striatal neurons, which receive most of the dopaminergic projections from the midbrain, induces the elongation of neuronal PC in both hemiparkinsonian rats and *dopamine receptor D2* (*DRD2*)-null mice (*338*). In addition, striatal cholinergic neurons respond to SHH released by dopaminergic nerve terminals by secreting GDNF which in turn is crucial for the maintenance and survival of DAn projecting to the striatum (*270*).

Furthermore, over the last years *LRRK2* - a gene associated with fPD - has been implicated in ciliogenesis. Pathogenic mutations in the kinase domain of *LRRK2*, G2019S and R1441C, influence the ability of cells to respond to cilia-dependent SHH signaling. Cholinergic neurons in the striatum of *LRRK2* R1441C mice show

decreased ciliation, possibly diminishing the above-mentioned neuroprotective circuit supporting the survival of DAn (*335*). Additionally, in this thesis, it is shown that PINK1, another PD-associated gene that leads to early-onset fPD, affects PC length interestingly also on cholinergic neurons subjected to neuronal death (unpublished data from Kristina Niedermaier – not shown in this thesis). Both proteins are kinases and might therefore interfere with the phosphorylation of proteins critical for ciliogenesis, such as the Rabs, as has been shown for LRRK2 *(335, 339).* Additionally, PRKN and PINK1 are known to be recruited to the basal body by OFD2 and TCHP, which may link mitochondrial quality control to PC development and function. On the other hand, PINK1 has been associated with intracellular transport (*25*) mechanisms which might also include intraflagellar transport of which the underlying gene network is also affected (scRNA-seq data of *PINK1* ko and Q126P clones not shown). Of note, in most PD cases changes in PC length rather than loss of PC predominates. Further analysis will be necessary to elucidate the respective underlying mechanisms.

Taken together, dysfunctional PC and the respective signaling pathways are a common hallmark of sPD and fPD. Even though the functional consequences of altered cilia are numerous ranging from impaired neuronal homeostasis to mitochondrial dysfunction, altered signaling in PC emerge as a convergence point in PD etiology in human brain tissue, different human and mouse model systems as well as different forms of PD (sporadic and familial, early- and late-onset).

3.4. Conclusion

The cellular model system described in this thesis is a suitable model to study the etiology of sPD. It is the first cellular model available that recapitulates PD phenotypes associated with mitochondrial function (*304*). Almost every stage of the prodromal phase is represented, from a no symptoms phase to severe mitochondrial alterations e.g. complex I deficiency. Thus, this model system can provide unique insights into cellular processes and molecular mechanisms contributing to sPD etiology. A multiplexed scRNA-seq approach identified a pattern of global gene repression which might be the underlying cause of various PD phenotypes including mitochondrial complex I deficiency, ciliary dysfunction, and hypometabolism. This might create a positive feedback loop and a downward spiral of disease progression due to the reduced efficiency of almost every cellular pathway and compensatory capacity.

Based on the data presented in this thesis, it can be hypothesized that sPD etiology follows a predefined process that is at least in our cellular model independent of environmental stimuli and intensified or accelerated specifically in the midbrain dopaminergic lineage of sPD patients.

4. Material and Methods

4.1. Material.

Table 5 | Chemicals.

Chemicals	Catalogue number	Supplier
2-Deoxy-D-glucose GRADE II	D8375-25G	Sigma-Aldrich
2-Mercaptoethanol	31350010	Thermo Fisher Scientific
4 % paraformaldehyde (PFA)	P6148	Sigma-Aldrich
Acetic acid	W200603	Sigma-Aldrich
Antimycin A	A8674-50MG	Sigma-Aldrich
Ascorbic acid 2-phosphate	A8960-5G	Sigma-Aldrich
Bovine Serum Album (BSA)	A7906-500G	Sigma-Aldrich
Carbonyl cyanide 4-(trifluoromethoxy)phenylhydrazone (FCCP)	C2920-10MG	Sigma-Aldrich
CHIR 99021	4423/10	Tocris Bioscience
cOmplete Mini, EDTA-free	11836170001	Roche Diagnostics
Cyclopamine	C4116-1MG	Sigma-Aldrich
DAPI-Solution	62248	Thermo Fisher Scientific
Dimethyl sulfoxide, >=99.5 %	D5879-100ML	Sigma-Aldrich
DMH1	4126/10	Tocris
Dorsomorphin dihydrochloride	3093/10	Tocris Bioscience
EmbryoMax Ultra-Pure Water	TMS-006-B	Merck Millipore
Ethanol, absolute	1009832500	Merck Millipore
Ethylene glycol	2441.2	Roth
Ethylenediamintetraacetic acid (EDTA)	EDS-1KG	Sigma-Aldrich
Formalin, 10 %	F5554	Sigma-Aldrich
Gentamycinsulfat BioChemica	A1492,0005	AppliChem
Glucose	15023021	Thermo Fisher Scientific
Glycerine	G5516	Sigma-Aldrich
Hoechst 33342	H3570	Thermo Fisher Scientific
L-Glutamic acid	G1251-100G	Sigma-Aldrich
L-Glutamine	25030024	Thermo Fisher Scientific
Magnesiumchlorid	208337-100G	Sigma-Aldrich
Methanol	1.06009.2500	Merck Millipore
Methanol	361091	AppliChem
Milk powder	70166-500G	Sigma-Aldrich
N^6,2'-O-Dibutyryladenosine 3',5'-cyclic monophosphate sodium salt (dbcAMP)	D0627-1G	Sigma-Aldrich
Nonidet P40 Substitute	11754599001	Sigma-Aldrich
Oligomycin	O4876-5MG	Sigma-Aldrich
Penicillin-Streptomycin (10.000 U/ml)	15140122	Thermo Fisher Scientific
Phenylmethylsulfonyl fluoride	10837091001	Sigma-Aldrich
Proteinase K	A3830	AppliChem
Purmorphamine	4551	Tocris Bioscience
Pyruvic acid	P5280-25G	Sigma-Aldrich
Rotenone	R8875-1G	Sigma-Aldrich

Sodium chloride	106404	Merck Millipore
Sodium deoxycholate	D6750	Sigma-Aldrich
Sodium dodecyl sulfate (SDS)	L3771	Sigma-Aldrich
StemMACS DAPT	130-110-489	Miltenyi Biotec
StemMACS Retinoic Acid	130-117-339	Miltenyi Biotec
StemMACS SB431542	130-106-275	Miltenyi Biotec
Sucrose	S0389	Sigma-Aldrich
Tris (Trizma-Base)	93352	Sigma-Aldrich
Triton X-100	T9284	Sigma-Aldrich
Trizma hydrochloride	T3253	Sigma-Aldrich
Tween 20	P1379	Sigma-Aldrich
Y-27632 dihydrochloride	ALX-270333-M005	Enzo Life Sciences

Table 6 | Consumables.

Consumables	Catalogue number	Supplier
10x Tris/Glycine, 5 L cube	1610771	Bio-Rad
35 µm cell strainer	352235	Corning
Amersham ECL Western Blotting Detection Reagent	RPN2106OL/AF	GE Healthcare
Aqua-Poly/Mount	18606-20	Polysciences Inc.
Cell scraper	83.183	Sarstedt
Cover slips 15 mm Ø	41001115	Neolab
Criterion XT Bis-Tris Gel, 4-12 %, 18-well, 30 µl	3450124	Bio-Rad
Glass beads	VK-05	PeqLab
Immobilon – P Membranes	IPVH00010	Merck Millipore
Micro tubes	72.694	Sarstedt
Microplate 96/F-PP wh/bl	30601700	Neolab
Multi-well plate, 24 well	353047	Corning
Multi-well plate, 6 well	353046	Corning
Multi-well plate, 96 well	353072	Corning
Neubauer improved cell counting chamber	PK361	Carl Roth
NuPAGE™ LDS Sample Buffer (4X)	NP0007	Novex
Protein Marker VI	A8889	AppliChem
SafeSeal SurPhob Filtertips, 1250 µl, sterile	VT0270	Biozym
Seahorse XFe96 FluxPak	102416100	Agilent Technologies
Sterile filter 0.2 µM	INTG156608	VWR, Germany
SuperFrost Plus Glass Slides	4951PLUS4	Thermo Fisher Scientific
Whatman cellulose chromatography papers	WHA3030672	Sigma-Aldrich
XF96 cell culture microplates	101085004	Agilent Technologies
XT MOPS	1610788	Bio-Rad

Table 7 |Cell culture media and supplements.

Cell culture media and supplements	Catalogue number	Supplier
B-27 Supplement (50x), minus vitamin A-10 mL	12587010	Thermo Fisher Scientific
BMP-4	130-111-165	Miltenyi Biotec
CNTF	130-096-337	Miltenyi Biotec
CryoStor(R) cell cryopreservation media, CS10	C2874100ML	Sigma-Aldrich
DMEM/F-12, GlutaMAX Supplement-10x 500 ml	31331093	Thermo Fisher Scientific
EGF	130-093-825	Miltenyi Biotec
Fetal bovine serum	P30-1402	PAN-Biotech

FGF2	130-093-839	Miltenyi Biotec
GlutaMax	35050061	Thermo Fisher Scientific
Human BDNF, research grade	130-093-811	Miltenyi Biotec
Human FGF-8b, premium grade	130-095-741	Miltenyi Biotec
Human GDNF, research grade	130-096-291	Miltenyi Biotec
Human IGF-1	130-093-886	Miltenyi Biotec
Human SHH (C24II), research grade	130-095-718	Miltenyi Biotec
Human TGF-β3, research grade	130-094-008	Miltenyi Biotec
Insulin	I3536-100MG	Sigma-Aldrich
Knockout DMEM-500 ml	10829018	Thermo Fisher Scientific
KnockOut Serum Replacement-500 ml	10828028	Thermo Fisher Scientific
mTeSR1	85850	Stemcell Technologies
N2 supplement 5 ml	17502048	Thermo Fisher Scientific
Neuregulin1/Heregulin1	97642.1	Biomol
Neurobasal Medium-500 ml	21103049	Thermo Fisher Scientific
Non-essential amino acids	11140035	Thermo Fisher Scientific
PBS D´Beccos W/O CA, MG 500 ml	14190169	Thermo Fisher Scientific
Phosphate buffered saline with 10% BSA	SRE0036-250ML	Sigma-Aldrich
Seahorse XF base medium, 500 ml	103334-100	Agilent Technologies
Seahorse XF Calibrant Solution	100840000	Agilent Technologies
Trypsin 0,05 % EDTA 100 ml	25300096	Thermo Fisher Scientific

Table 8 | Coatings and passaging solutions.

Coatings and passaging solutions	Catalogue number	Supplier
Accutase	A6964-500ML	Sigma-Aldrich
Collagenase, Type IV, powder	17104019	Thermo Fisher Scientific
Geltrex	A1413302	Thermo Fisher Scientific
Laminin Mouse Protein, Natural	23017015	Thermo Fisher Scientific
Poly-L-ornithine hydrobromide	P3655	Sigma-Aldrich
StemMACS Passaging Solution XF	130-104-688	Miltenyi Biotec

Table 9 | Kits.

Kits	Catalogue number	Supplier
ACTB (Hs99999903_m1)	4331182	Thermo Fisher Scientific
BBS5 (Hs00537098_m1)	4331182	Thermo Fisher Scientific
CellROX	C10444	Thermo Fisher Scientific
CFHR1 (Hs00275663_m1)	4331182	Thermo Fisher Scientific
Chromium i7 Multiplex Kit	PN-120262	10xGenomics
Chromium Single Cell 3' Library & Gel Bead Kit v2	PN-120237	10xGenomics
Click-iT Plus EdU Alexa Fluor 488 Imaging Kit	C10420	Thermo Fisher Scientific
Complex I enzymatic activity microplate assay kit	ab109721	Abcam
FOXA2 (Hs05036278_s1)	4331182	Thermo Fisher Scientific
GAPDH (Hs99999905_m1)	4331182	Thermo Fisher Scientific
GET4 (Hs00944514_m)	4331182	Thermo Fisher Scientific
GLI1 (Hs00171790_m1)	4331182	Thermo Fisher Scientific
GLI2 (Hs01119974_m1)	4331182	Thermo Fisher Scientific
GLI3 (Hs00609233_m1)	4331182	Thermo Fisher Scientific
GRB14 (Hs00182949_m1)	4331182	Thermo Fisher Scientific
HPRT1 (Hs99999909_m1)	4331182	Thermo Fisher Scientific

Infinium CoreExome-24 v1.3 Kit	20024662	Illumina
LINGO2 (Hs01102041_s1)	4331182	Thermo Fisher Scientific
Luminescent ATP Detection Assay Kit	ab113849	Abcam
Methylated DNA Quantification Kit	ab117128	Abcam
MitoTracker Orange CMTMRos	M7510	Thermo Fisher Scientific
NAD/NADH Assay Kit	ab176723	Abcam
Pierce BCA Protein Assay Kit	23225	Thermo Fisher Scientific
PITX3 (Hs01013935_g1)	4331182	Thermo Fisher Scientific
Power SYBR Green mastermix	4368577	Thermo Fisher Scientific
QIAamp DNA Mini Kit	51304	Qiagen
Quant-iT PicoGreen dsDNA Assay Kit	P11496	Thermo Fisher Scientific
RNeasy Plus Mini Ki	74134	Qiagen
SLC1A2 (Hs01102423_m1)	4331182	Thermo Fisher Scientific
SRCAP (Hs00198472_m1)	4331182	Thermo Fisher Scientific
SuperScript VILO cDNA Synthesis Kit	11754050	Thermo Fisher Scientific
TaqMan universal PCR MM no Ung	4324018	Thermo Fisher Scientific

Table 10 | Antibodies.

Antibodies	Catalogue number	Supplier
ACTB	ABO145-200	OriGene
AC-TUB	T6793	Sigma-Aldrich
Adcy3	PA5-35382	Invitrogen
ARL13B	17711-1-AP	Proteintech
ATP5A	ab14748	Abcam
Chat	AB144P	Millipore
Complex II - Subunit 30	459230	Thermo Fisher Scientific
donkey-anti-goat IgG Alexa 488	A11055	Thermo Fisher Scientific
donkey-anti-goat IgG Alexa 594	A11058	Thermo Fisher Scientific
donkey-anti-mouse IgG Alexa 488	A21202	Thermo Fisher Scientific
donkey-anti-mouse IgG Alexa 594	A21203	Thermo Fisher Scientific
donkey-anti-rabbit IgG Alexa 488	A21206	Thermo Fisher Scientific
donkey-anti-rabbit IgG Alexa 594	A21207	Thermo Fisher Scientific
gamma H2A.X (phospho S139)	ab2893	Abcam
GFAP	MAB360	Millipore
GLI2	MAB35261	R&D
GLI3	AF3690	R&D
GLI3	AF3690	R&D
Histone H3 (tri methyl K27)	ab6002	Abcam
Histone H3 (tri methyl K9)	ab8898	Abcam
LAP2 alpha	ab5162	Abcam
MTCO2	ab110258	Abcam
NANOG	AF1997	R&D Systems
NDUFB8	459210	Novex
NDUFS1	ab157221	Abcam
NDUFS3	ab183733	Abcam
NES	Ma1110	Thermo Fisher Scientific
PAX6	Ab78545	Abcam
PCNA	ab29	Abcam
PITX3	38-2850	Invitrogen
POU5F1	2840S	Cell Signaling

rabbit-anti-goat IgG peroxidase	305-035-003	Dianova
rabbit-anti-mouse IgG peroxidase	GTX213112-01	GeneTex
RBFOX3	ab104224	Abcam
SLC1A3	NB100-1869	Novus Biologicals
SMO	sc1666685	Santa Cruz
SOX1	Ab87775	Abcam
SOX2	sc17320	Santa Cruz
TH	P40101	PelFreez
TUBA	GTX628802	Genetex
TUBB3	T5076	Sigma-Aldrich
UQCRC2	ab14745	Abcam

Table 11 | Oligonucleotides.

Description	Sequence (5' -> 3')
alb1	CGGCGGCGGGCGGCGCGGGCTGGGCGGaaatgctgcacagaatccttg
alb2	GCCCGGCC CGCCGCGCCCGTCCCGCCGgaaaagcatggtcgcctgtt
hbg1	CGGCGGCGGGCGGCGCGGGCTGGGCGGctcitric acid cycletccacgtcitric acid cyclecttg
hbg2	GCCCGGCCCGCCGCGCCCGTCCCGCCGg aggagaagtctgccgtt
tel1	ACACTAAGGTTTGGGTTTGGGTTTGGGTTTGGGTTAGTGT
tel2	TGTTAGGTATCCCTATCCCTATCCCTATCCCTATCCCTAACA

Table 12 | Mouse lines.

Description	Information
C57Bl6/N	Charles River
Pink1 3.5CreDel KO	generated at Helmholtz Zentrum München (IDG) by Anne Röthig

Table 13 | Media / buffer composition.

Media / Buffer	Composition
10x TBS, pH8	100 mM Tris 1.4 M NaCl in H2O Adjust to pH 8
1x TBS-T	10 % (v/v) 10x TBS 0.1 % (v/v) Tween20 in H_2O
1x Tris/Glycine transfer buffer	10 % (v/v) 10x Tris/Glycine Buffer (BioRad) 20 % (v/v) Methanol in H_2O
1x XT MOPS running buffer	5 % (v/v) 20x MOPS Buffer (BioRad) in H_2O

astrocyte differentiation medium	50 % (v/v) DMEM/F12-GlutaMAX 50 % (v/v) Neurobasal 1 % (v/v) B27 0.5 % (v/v) N2, 0.5 % (v/v) GlutaMaxx 0.5 % (v/v) non-essential amino acids 0.02 % (v/v) beta-mercaptoethanol 2.5 µg/ml human Insulin 5 ng/ml CNTF 10 ng/ml BMP4 10 ng/ml EGF 8 ng/ml FGF2 10 ng/ml Heregulin1/Neuregulin1b
blocking buffer (Immunocytochemistry)	1 % (w/v) BSA 0.5 % (v/v) Triton X-100 in PBS
blocking buffer (Western Blot)	5 % (w/v) skim milk powder in TBS-T
cell extraction buffer	1 mM PMSF 1x Protease Inhibitor Cocktail in H_2O
fibroblast growth medium	DMEM/F12-GlutaMAX 10 % fetal bovine serum
hypotonic buffer	20 mM Tris-HCl pH 7.4 10 mM NaCl 3 mM MgCl2 1x Protease Inhibitor Cocktail in H_2O
knockout serum replacement medium	80 % (v/v) KnockOut DMEM 20 % (v/v) Knockout serum replacement 10 µM SB431542 0.5 µM purmorphamine 1 µM dorsomorphin 3 µM CHIR99021 4.44 nM FGF-8b 1 % (v/v) non-essential amino acids 1 % (v/v) L-glutamine 150 µM ascorbic acid 2-phosphate 0.02 % (v/v) beta-mercaptoethanol
DAn differentiation medium	50 % (v/v) DMEM/F12-GlutaMAX 50 % (v/v) Neurobasal 1 % (v/v) B27 (minus vitamin A) 0.5 % (v/v) N2 0.1 mM ascorbic acid 2-phosphate 1 µM purmorphamine 4.44 nM FGF-8b

DAn maturation medium_1	50 % (v/v) DMEM/F12-GlutaMAX 50 % (v/v) Neurobasal 1 % (v/v) B27 (minus vitamin A) 0.5 % (v/v) N2 0.1 mM ascorbic acid 2-phosphate 0.5 µM purmorphamine 500 µM dbcAMP 10 ng/ml BDNF 10 ng/ml GDNF 1 ng/ml TGF-3ß
DAn maturation medium_2	50 % (v/v) DMEM/F12-GlutaMAX 50 % (v/v) Neurobasal 1 % (v/v) B27 (minus vitamin A) 0.5 % (v/v) N2 0.1 mM ascorbic acid 2-phosphate 500 µM dbcAMP 10 ng/ml BDNF 10 ng/ml GDNF 1 ng/ml TGF-3ß
motor neuron differentiation medium	50 % (v/v) DMEM/F12-GlutaMAX 50 % (v/v) Neurobasal 1 % (v/v) B27 (minus vitamin A) 0.5 % (v/v) N2 0.5 % (v/v) GlutaMAX 1 % (v/v) non-essential amino acids 0.02 % (v/v) beta-mercaptoethanol 2.5 µg/ml Insulin 0.1 mM ascorbic acid 2-phosphate 50 U/ml penicillin 50 mg/ml streptomycin 0.5 µM retinoic acid 0.1 µM purmorphamine 0.1 µM DAPT 10 ng/ml IGF-1 10 ng/ml BDNF 10 ng/ml CTNF
motor neuron neural induction medium	50 % (v/v) DMEM/F12-GlutaMAX 50 % (v/v) Neurobasal 1 % (v/v) B27 (minus vitamin A) 0.5 % (v/v) N2 0.5 % (v/v) GlutaMAX 1 % (v/v) non-essential amino acids 0.02 % (v/v) beta-mercaptoethanol 2.5 µg/ml Insulin 0.1 mM ascorbic acid 2-phosphate 50 U/ml penicillin 50 mg/ml streptomycin 3 µM CHIR99021 2 µM DMH1 2 µM SB431542

motor neuron specification medium	50 % (v/v) DMEM/F12-GlutaMAX 50 % (v/v) Neurobasal 1 % (v/v) B27 (minus vitamin A) 0.5 % (v/v) N2 0.5 % (v/v) GlutaMAX 1 % (v/v) non-essential amino acids 0.02 % (v/v) beta-mercaptoethanol 2.5 µg/ml Insulin 0.1 mM ascorbic acid 2-phosphate 1 µM CHIR99021 0.1 µM retinoic acid 0.5 µM purmorphamine 50 U/ml penicillin 50 mg/ml streptomycin 3 µM CHIR99021 2 µM DMH1 2 µM SB431542
motor neuron specification medium	50 % (v/v) DMEM/F12-GlutaMAX 50 % (v/v) Neurobasal 1 % (v/v) B27 (minus vitamin A) 0.5 % (v/v) N2 0.5 % (v/v) GlutaMAX 1 % (v/v) non-essential amino acids 0.02 % (v/v) beta-mercaptoethanol 2.5 µg/ml insulin 0.1 mM ascorbic acid 2-phosphate 50 U/ml penicillin 50 mg/ml streptomycin 0.5 µM retinoic acid 0.1 µM purmorphamine
neuronal precursor maintenance medium_1	50 % (v/v) DMEM/F12-GlutaMAX 50 % (v/v) Neurobasal 1 % (v/v) B27 (minus vitamin A) 0.5 % (v/v) N2 10 µM SB431542 1 µM dorsomorphin 4.44 nM FGF-8b 150 µM ascorbic acid 2-phosphate 0.02 % (v/v) beta-mercaptoethanol
neuronal precursor maintenance medium_2	50 % (v/v) DMEM/F12-GlutaMAX 50 % (v/v) Neurobasal 1 % (v/v) B27 (minus vitamin A) 0.5 % (v/v) N2 10 µM SB431542 1 µM dorsomorphin 0.5 µM purmorphamine 4.44 nM FGF-8b 150 µM ascorbic acid 2-phosphate 0.02 % (v/v) beta-mercaptoethanol

neuronal precursor medium	50 % (v/v) DMEM/F12-GlutaMAX 50 % (v/v) Neurobasal 1 % (v/v) B27 (minus vitamin A) 0.5 % (v/v) N2 10 µM SB431542 0.5 µM purmorphamine 1 µM dorsomorphin 3 µM CHIR99021 4.44 nM FGF-8b 150 µM ascorbic acid 2-phosphate 0.02 % (v/v) beta-mercaptoethanol
PBS	171 mM NaCl 3,4 mM KCl 10 mM Na2HPO4 1,8 mM KH2PO4 in H_2O Adjust to pH 7.4
RIPA buffer	50 mM Tris-HCL 150 mM NaCl 1% (v/v) Triton X-100 0.5% (w/v) Sodium-Deoxycholate 0.1% (w/v) SDS in H_2O

Table 14 | Cell lines.

Description	Information
PINK1 knockout (ko)	generated by Julia Fitzgerald, Tübingen
PINK1 knockout (ko) - isogenic Ctrl	generated by Julia Fitzgerald, Tübingen
PINK1 Q126P	generated at Helmholtz Zentrum München by Annerose Kurz-Drexler (IDG) and the reprogramming core facility
PINK1 Q126P - *isogenic Ctrl*	generated at Helmholtz Zentrum München (IDG) by Annerose Kurz-Drexler
UKERiJ2C-R1-012	ForIPS consortium
UKERiJ2C-R1-015	ForIPS consortium
UKERiM89-R1-005	ForIPS consortium
UKERiM89-R1-006	ForIPS consortium
UKERiC99-R1-007	ForIPS consortium
UKERiC99-R1-008	ForIPS consortium
UKERiR66-R1-007	ForIPS consortium
UKERiR66-R1-014	ForIPS consortium
UKERiAY6-R1-003	ForIPS consortium
UKERiAY6-R1-004	ForIPS consortium
UKERiPX7-R1-001	ForIPS consortium
UKERiPX7-R1-002	ForIPS consortium
UKERi88H-R1-001	ForIPS consortium
UKERi88H-R1-002	ForIPS consortium

UKERi1JF-R1-011	ForIPS consortium
UKERi1JF-R1-018	ForIPS consortium
UKERiG3G-R1-032	ForIPS consortium
UKERiG3G-R1-039	ForIPS consortium
UKERi1E4-R1-003	ForIPS consortium
UKERi1E4-R1-012	ForIPS consortium
UKERiO3H-R1-001	ForIPS consortium
UKERiO3H-R1-005	ForIPS consortium
UKERi82A-R1-001	ForIPS consortium
UKERi82A-R1-002	ForIPS consortium

Table 15 | Devices.

Devices	Supplier
AxioCam HRc camera	Zeiss
Axio Observer Z1 confocal microscope	Zeiss
Axioplan 2 Microscope	Zeiss
Axiovert 200 M	Zeiss
Biological Safety Cabinet, Herasafe	Thermo Fisher Scientific
Cellinsight NXT platform	Thermo Fisher Scientific
ChemiDoc Imager	Bio-Rad
Chromium controller	10xGenomics
Criterion Blotter	Bio-Rad
Criterion Vertical Electrophoresis Cell	Bio-Rad
GloMax Multi Detection System	Promega
HiSeq4000	Illumina
iScan system	Illumina
Microm HM 560 Cryostat	Thermo Fisher Scientific
Milli-Q Integral Water Purification System	Merck Millipore
Mr. Frosty™ Freezing Container	Thermo Fisher Scientific
NanoDrop Spectrophotometer ND-1000	Peqlab
Orbital Shaker (7-0030)	Neolab
Preccellys24	PeqLab
QuantStudio 7 Flex	Thermo Fisher Scientific
Seahorse XF96 Analyzer	Agilent Technologies
SpectraMax M5	Molecular Devices

4.2. Ethical compliance.

Work with human iPSCs was granted by the local ethics committees (No. 4485 and 4120, FAU Erlangen-Nuernberg, Germany; and No 422-13 and 357/19 S, Technical University Munich, Germany) and all participants or their legal guardians gave written informed consent. All related experiments and methods were performed in accordance with relevant guidelines and regulations.

All animal protocols and procedures were conducted with the approval for the ethical treatment of animals by the responsible animal welfare authority of the Regierung von Oberbayern (Government of Upper Bavaria) and considering the 3R principle.

sPD and Ctrl hiPSC lines were established, characterized and provided by the ForIPS consortium(*241*). hiPSC lines from 7 sPD patients and 5 Ctrls were used, in total 24 hiPSC lines with 2 clones per patient (Sup Table 1). To exchange selected sPD lines for research purposes the scientific board of the UKER biobank will consider each request. The TALEN induced *PINK1* knockout (ko) line and the isogenic Ctrl were established, characterized and provided by Julia Fitzgerald(*282*). The *PINK1* Q126P line and the isogenic Ctrl were established and characterized as described below. To exchange selected fPD lines for research purposes the scientific board of the Neuro-Biobank Tübingen will consider each request.

4.3. Cell culture.

4.3.1. Cell Culture Fibroblasts.

Primary human dermal fibroblasts were cultured in fibroblast growth medium (DMEM/F12-GlutaMAX (Life Technologies) supplemented with 10 % fetal bovine serum (PAN-Biotech)) at 37 °C, 5 % CO_2, 21 % O_2. At 60-70% confluency, fibroblasts were detached using 1 ml 0.05% trypsin-EDTA (Life Technologies) for 5 min at 37 °C, chopped with a 1000 µl pipette tip and diluted in 5 ml fibroblast growth medium. Fibroblasts were harvested at 200 g for 5 min, resuspended in 1 ml fibroblast growth medium and seeded 1:5 on Geltrex (Thermo Fisher Scientific) coated plates. Medium was changed every second day.

4.3.2. Culture of undifferentiated hiPSCs.

hiPSCs were maintained under feeder-free conditions on Geltrex (Thermo Fisher Scientific) coating and in mTesR1 medium (StemCell Technologies) at 37 °C, 5 % CO_2, 21 % O_2, if not indicated otherwise. At 70 % confluency, cells were detached using StemMACS Passaging Solution XF (Miltenyi Biotec) for 6 min at 37 °C. StemMACS Passaging Solution XF was aspirated and hiPSC colonies were harvested in 1 ml mTeSR1 and chopped using a 1000 µl pipette tip. Harvested hiPSCs were diluted and seeded on Geltrex coated plates. hiPSCs at passage 45-65 were used for all analyses. hiPSCs were screened regularly for pluripotency and stable karyotype (Extended Data Fig. 1).

4.3.3. Human neuronal precursor cell differentiation.

hiPSCs were differentiated into human small molecule neural progenitor cells (hNPCs) by embryoid body (EB) formation following the protocol described by(*340*) with minor adaptations. At 70 % confluency, hiPSC colonies were detached using 2 mg/ml collagenase type IV (Thermo Fisher Scientific) for 40 min at 37 °C, 5 % CO_2, 21 % O_2. Detached hiPSC colonies were harvested in knockout serum replacement medium (80 % KnockOut DMEM (Life Technologies) supplemented with 20 % Knockout serum replacement (Life Technologies), 10 µM SB431542 (Miltenyi Biotec), 0.5 µM purmorphamine (Tocris Bioscience), 1 µM dorsomorphin (Tocris Bioscience), 3 µM CHIR99021 (Tocris Bioscience), 4.44 nM FGF-8b (Miltenyi Biotec), 1 % non-essential amino acids (Life Technologies), 1 % L-glutamine (Life Technologies), 150 µM ascorbic acid 2-phosphate (Sigma) and 0.02 % beta-mercaptoethanol (Life Technologies)). hiPSCs were cultivated for two days on an orbital shaker at 37 °C, 5 % CO_2, 21 % O_2 and 80 rpm with daily media changes. At day

3, EBs were transferred into neuronal precursor medium (50 % DMEM/F12-GlutaMAX (Life Technologies), 50 % Neurobasal (Life Technologies) supplemented with 1 % B27 (minus vitamin A, 12587010, Life Technologies), 0.5 % N2 (Life Technologies), 10 µM SB431542, 0.5 µM purmorphamine, 1 µM dorsomorphin, 3 µM CHIR99021, 4.44 nM FGF-8b, 150 µM ascorbic acid 2-phosphate and 0.02 % beta-mercaptoethanol). EBs were cultivated for 4 days at 37 °C, 7 % CO_2, 21 % O_2 and 80 rpm with daily media changes. On day 6, EBs were transferred into neuronal precursor maintenance medium (neuronal precursor medium deprived of purmorphamine and CHIR99021). The following day, EBs were seeded unharmed on Geltrex coated plates and expanded for 3-4 days in neuronal precursor maintenance medium at 37 °C, 7 % CO_2, 21 % O_2 with daily media changes. At day 10-11 hNPCs were dissociated using Accutase (Sigma) for 10 min at 37 °C, 7 % CO_2, 21 % O_2, chopped with a 1000 µl pipette tip and diluted in 5 ml neuronal precursor maintenance medium. hNPCs were harvested at 200 g for 5 min, resuspended in 1 ml neuronal precursor maintenance medium and seeded on Geltrex coated plates. Thereafter, hNPCs were cultivated at 37 °C, 7 % CO_2, 21 % O_2 with daily medium changes and passaged with Accutase at 80 % confluency. After 2 passages, 0.5 µM purmorphamine was added to the maintenance medium.

4.3.4. Human dopaminergic neuron differentiation.

Human dopaminergic neuron differentiation was performed using 15 µg/mL poly-L-ornithine (Sigma) and 10 µg/mL laminin (Thermo Fisher Scientific) coating and differentiation steps were done precisely as described by(*340*) using the following growth factors and supplements: 10 ng/mL human BDNF (Miltenyi Biotec); 10 ng/mL human GDNF (Miltenyi Biotec); 1 ng/mL human Tgf-beta3 (Miltenyi Biotec); 100 ng/mL human FGF-8b (Miltenyi Biotec); 200 µM ascorbic acid 2-phosphate (Sigma); 1 µM purmorphamine (Tocris); 500 µM dbcAMP (Sigma). Human dopaminergic neurons were differentiated at 37 °C, 7 % CO_2, 21 % O_2 for at least 50 days.

4.3.5. Human astrocyte differentiation.

Human astrocyte differentiation was performed as described by(*341*) with minor adaptations. hNPCs were passaged with Accutase at 80 % confluency and counted using a Neubauer improved cell counting chamber (Carl Roth). Cells were resuspended in astrocyte differentiation medium (50 % DMEM/F12-GlutaMAX, 50 % Neurobasal supplemented with 1 % B27 (17504044, Life Technologies), 0.5 % N2, 0.5x GlutaMaxx (Thermo Fisher Scientific), 0.5x non-essential amino acids, 0.02 % beta-mercaptoethanol, 2.5 µg/ml human Insulin (Sigma), 5 ng/ml CNTF (Miltenyi Biotec), 10 ng/ml BMP4 (Miltenyi Biotec), 10 ng/ml EGF (Miltenyi Biotec), 8 ng/ml FGF2 (Miltenyi Biotec), 10 ng/ml Heregulin1/Neuregulin1b (Biomol)) containing 10 µM ROCK inhibitor Y27632 (Enzo Life Sciences) and were seeded on 15 µg/mL poly-L-ornithine and 10 µg/mL laminin coated 6-well plates at a density of 500.000 cells/well. Astrocytes were differentiated in astrocyte differentiation medium at 37 °C, 7 % CO_2, 21 % O_2 for at least 35 days with daily medium changes. At 80 % confluency, astrocytes were passaged with Accutase and seeded on 15 µg/mL poly-L-ornithine and 10 µg/mL laminin coated plates.

4.3.6. Motor neuron differentiation.

Human motor neuron differentiation was performed as described by (*342*) with minor adaptations. HiPSCs were dissociated into a single-cell suspension using Accutase and counted using a Neubauer improved cell counting chamber (Carl Roth). Single cells were seeded on Geltrex coated plates containing mTeST1 supplemented with 10 µM Y27632 at a density of 70,000 cells/cm^2. The next day, medium was changed to neural induction medium (50 % DMEM/F12-GlutaMAX, 50 % Neurobasal supplemented with 1 % B27 (minus vitamin A), 0.5 % N2, 0.5 % GlutaMAX, 1 % non-essential amino acids, 0.02 % beta-mercaptoethanol, 2.5 µg/ml Insulin (Sigma), 0.1 mM ascorbic acid 2-phosphate, 50 U/ml penicillin, 50 mg/ml streptomycin, 3 µM CHIR99021, 2 µM DMH1 (Tocris) and 2 µM SB431542) and maintained at 37 °C, 5 % CO_2, 21 % O_2 for 6 days with daily medium changes. At 80 % confluency, precursor cells were passaged using Accutase and seeded at a 1:6 ratio on Geltrex coated plates. For human motor neuron precursor (hMNP) differentiation, cells were subsequently cultivated in specification medium (neural induction medium containing 1 µM CHIR99021, 0.1 µM retinoic acid (Miltenyi Biotec) and 0.5 µM purmorphamine) at 37 °C, 5 % CO_2, 21 % O_2 for 6 days with daily medium changes. OLIG2$^+$ hMNPs were expanded in specification medium.

To induce motor neuron differentiation, hMNPs were cultivated in mn specification medium (50 % DMEM/F12-GlutaMAX, 50 % Neurobasal supplemented with 1 % B27 (minus vitamin A), 0.5 % N2, 0.5 % GlutaMAX, 1 % non-essential amino acids, 0.02 % beta-mercaptoethanol, 2.5 µg/ml Insulin, 0.1 mM ascorbic acid 2-phosphate, 50 U/ml penicillin, 50 mg/ml streptomycin, 0.5 µM retinoic acid and 0.1 µM purmorphamine) at 37 °C, 5 % CO_2, 21 % O_2 for 6 days with daily medium changes. At 80 % confluency, motor neurons were passaged using Accutase and seeded at a 1:6 ratio on Geltrex coated plates. Subsequently, motor neuron differentiation was induced with 0.5 µM retinoic acid, 0.1 µM purmorphamine, 0.1 µM DAPT (Miltenyi Biotec), 10 ng/ml IGF-1 (Miltenyi Biotec), 10 ng/ml BDNF and 10 ng/ml CNTF (Miltenyi Biotec) for at least 10 days.

4.4. Generation of fPD hiPSC clones.

4.4.1. Generation of *PINK1* ko hiPSC clones.

HiPSCs (previously described and characterized in(*340*)) were cultured in self-made E8 media on Vitronectin (VTN-N, Gibco) coated cell culture dishes. The hiPSCs were transfected with a TALEN and a homologous construct for *PINK1* exon1 to knockout the *PINK1* gene(*282*). Briefly, the transfection of healthy hiPSCs was performed using an Amaxa Nucleofector II with the Stem cell Nucleofection Kit (Lonza). The transfected hiPSCs were plated on VTN-N –coated 10 cm dishes in E8 medium containing 10 µM ROCK inhibitor Y27632. Homologous recombined hiPSC colonies were selected with 250 µg/ml G418 (Biochrom) or 10 µgml-1 Blasticidin (InvivoGen) in the second round of TALEN transfection and re-plated in 12-well plates. Resistant hiPSC colonies were characterized by sequencing, qRT-PCR and Western blot to confirm successful homozygous gene knockout. TALENs were designed with the online tool TAL Effector Nucleotide Targeter 2.0 (Cornell University). The following RVD sequences were used for the TALEN monomers: HD HD NI NH NH NG NH NI NH HD NH NH NH NH HD and NI NH HD NG HD HD NH NG HD HD NG HD HD NH HD. Colony-PCR after the first TALEN reaction was conducted with the primers pCR8_F1 (5'-TTGATGCCTGGCAGTTCCCT-3') and pCR8_R1 (5'-CGAACCGAACAGGCTTATGT-3'). After the second Golden

Gate reaction, the colony-PCR was performed with the primers TAL_F1 (5'-TTGGCGTCGGCAAACAGTGG-3') and TAL_R2 (5'-GGCGACGAGGTGGTCGTTGG-3').

4.4.2. Generation *PINK1* Q126P hiPSC clones.

Human fibroblasts were derived from a skin biopsy of a female PD patient with a *PINK1* Q126P mutation in Tübingen of which the family was previously described(*343*). Human samples were obtained with consent and prior ethical approval at The University of Tübingen and the Hertie Institute for Clinical Brain Research Biobank. The *PINK1* Q126P 15167 hiPSC line was generated by transient transgenic overexpression of six factors located on two episomal vectors CoMIP 4in1(*344*) and pCXLE- hMLN(*345*). CoMiP 4in1 for integration free expression of human OCT3 / 4, Sox2, Klf4, cMyc and shRNA against p53 and pCXLE- hMLN (Addgene Plasmid 27079) for integration free expression of human C-MYC, LIN28 and NANOG. Cells that showed morphological evidence of reprogramming were selected manually. The reprogramming was performed in the iPSC Core Facility of Helmholtz Zentrum München. hiPSC lines were screened for pluripotency using immunostainings of OCT4, SOX2, NANOG, LIN28 and for stable karyotype using chromosome counting and chromosomal microarray analysis. Chromosome counting was performed at chrombios (ChromBios GmbH) using a standard protocol. 30 cells in metaphase were analyzed showing no striking structural aberrations. Differentiation potential was verified by three lineage differentiation into ectoderm(*346*), mesoderm(*347*) and endoderm(*348*) lineage. At ~70 % confluency mTeSR was replaced by respective differentiation media (ectoderm: 50 % DMEM/F12-GlutaMAX, 50 % Neurobasal supplemented with 1 % B27, 0.5 % N2, 0.5 µM dorsomorphin, 10 µM SB431542 and 5 µg/ml insulin (Life Technologies); mesoderm: 50 % DMEM/F12-GlutaMAX, 50 % Neurobasal supplemented with 1 % B27 and 10 µM CHIR99021; endoderm day 1: 100 % DMEM/F12-GlutaMAX supplemented with 100 ng/ml Activin A (Tocris); endoderm days 2-5: 100 % DMEM/F12-GlutaMAX supplemented with 2 % B27 and 100 ng/ml Activin A) and cultivated for 5 days with daily media changes. Differentiation efficiency was quantified by RT-qPCR. Three lineage differentiation was performed in the iPSC Core Facility of Helmholtz Zentrum München.

4.4.3. Gene correction of *PINK1* Q126P hiPSC clone using CRISPR/Cas9.

PINK1 Q126P hiPSCs were electroporated with a modified pCAG-Cas9 vector (Addgene plasmid 84918) and a modified pEasy Flox donor vector (Addgene plasmid 11725) carrying a neo selection cassette flanked by a *PINK1* 5' homology arm (900 bp) containing the g.155732C>A and a 3' homology arm (700 bp). The pCAG-Cas9 vector expresses a Cas9 from *S. pyogenes* with a nuclear localization signal driven by a T7 promoter and two sgRNAs (sgRNA_fw: caccgggcggaggacggagctaagcg; sgRNA_rev: aaaccgcttagctccgtcctccgccc) driven by a human U6 promoter. hiPSCs were passaged using Accutase for 10 min at 37 °C, 5 % CO_2, 21 % O_2 and electroporated ($2x10^6$ hiPSCs, 2 µg pCAG-Cas9, 3 µg pEasy Flox) as single cells in a 100 µL cuvette using the program CB-150 with the P3 Primary Cell 4D-Nucleofector X Kit (Lonza Group Ltd) and the 4D Nucleofector X Unit (Lonza Group Ltd) according to the manufacturer's instructions. After nucleofection, hiPSCs were incubated in mTeSR supplemented with 10 µM Y27632 (Enzo Life Sciences) for 24 h and were allowed to recover to ~70 % confluency. Gene edited hiPSCs were selected by applying neomycin selection (Carl Roth) with 45 µg/ml for 3 days and with 30 µg/ml for 2 additional days. Subsequently, hiPSC colonies were

clonalized and expanded. For characterization genomic DNA was isolated using QIAamp DNA Mini Kit (Qiagen) according to the manufacturer's instructions for cultured cells. A double PCR with primer pairs P1-fw cggcctgcagctgggtcgag; P1-rev tcgcctcggccctcgatctg; P2-fw tttgttgtgaccggcggggg; P2-rev tttgctgtgctgcgacaggagc was performed using OneTaq 2X Master Mix with GC Buffer (NEB) and the sequence was verified by Sanger sequencing. Verification of pluripotency and normal karyotype of edited hiPSCs was performed as described above.

4.5. Immunocytochemistry and imaging of human cells.

Cells were cultured on Geltrex (fibroblasts, hiPSCs, hNPCs and motor neurons) or poly-L-ornithine/laminin (neurons and astrocytes) coated glass coverslips or 96 well plates (for high content analysis) for at least 72 h. Cells were fixed with 10 % Formalin (Sigma) for 20 min at 37 °C, washed twice with PBS and permeabilized/blocked with PBS containing 1 % BSA (Sigma-Aldrich) and 0.3 % Triton X-100 (Sigma-Aldrich) for 15 min at room temperature. Primary antibodies were diluted in PBS containing 1 % BSA and 0.3 % Triton X-100 and antibody incubation was performed at 4°C overnight. Cells were washed twice with PBS and incubated with secondary antibodies diluted in PBS containing 1 % BSA and 0.3 % Triton X-100 for 2 h at room temperature. Nuclei were stained using a 0.1 µg/ml DAPI (Thermo Fisher Scientific) - PBS solution for 10 min at room temperature. Cells were washed twice with PBS and coverslips were mounted using Aqua-Poly/Mount (Polysciences Inc.). Primary antibodies were diluted as follows: AC-TUB (T6793, Sigma-Aldrich; 1:1000), ARL13B (17711-1-AP, Proteintech; 1:500), GFAP (MAB360, Millipore; 1:250), GLI2 (MAB35261, R&D; 1:100), GLI3 (AF3690, R&D; 1:100), NANOG (AF1997, R&D Systems; 1:200), NES (Ma1110, Thermo Fisher Scientific; 1:250), PAX6 (Ab78545, Abcam; 1:200), PITX3 (38-2850, Invitrogen; 1:300), POU5F1 (2840S, Cell Signaling; 1:500), RBFOX3 (ab104224, Abcam; 1:800), SLC1A3 (NB100-1869, Novus Biologicals; 1:250), SMO (sc1666685, Santa Cruz; 1:500), SOX1 (Ab87775, Abcam; 1:500), SOX2 (sc17320, Santa Cruz; 1:500), TH (P40101, PelFreez; 1:600), TUBB3 (T5076, Sigma-Aldrich; 1:1000), gamma H2A.X (phospho S139) (ab2893, Abcam; 1:250), Histone H3 (tri methyl K27) (ab6002, Abcam; 1:100), Histone H3 (tri methyl K9) (ab8898, Abcam; 1:500), LAP2 alpha (ab5162, Abcam; 1:500). Secondary antibodies were diluted as follows: donkey-anti-goat IgG Alexa 488 (A11055, Thermo Fisher Scientific; 1:500), donkey-anti-mouse IgG Alexa 488 (A21202, Thermo Fisher Scientific; 1:500), donkey-anti-goat IgG Alexa 594 (A11058, Thermo Fisher Scientific; 1:500), donkey-anti-mouse IgG Alexa 594 (A21203, Thermo Fisher Scientific; 1:500), donkey-anti-rabbit IgG Alexa 488 (A21206, Thermo Fisher Scientific; 1:500), donkey-anti-rabbit IgG Alexa 594 (A21207, Thermo Fisher Scientific; 1:500). Fluorescence images were acquired using an Axiovert 200 M (ZEISS) with a 20 X / 63 X immersion objective or for z-stacks using a spinning disk Axio Observer Z1 confocal microscope (ZEISS) with a 100 X immersion objective. Images were analyzed using Fiji(*349*) and whenever necessary, z-stacks were collapsed to maximum intensity projections. For hNPCs and astrocytes, at least 30 primary cilia (PC) per cell line and replicate were analyzed blinded from random fields. The fraction of ciliated neurons, as well as the neuronal cilia length, was assessed using Neurolucida (MBF Bioscience) software and a Zeiss Axioplan 2 (Zeiss) microscope with a 100 X immersion objective. PC positive for cilia marker ARL13B and for the neuronal marker TUBB3 and RBFOX3 were selected for analysis. The analysis was performed blinded and an average of > 30 PC per cell line were analyzed from random fields.

4.6. Image (intensity and neurite) quantification.

For fluorescence intensity quantifications, images were acquired using a Cellinsight NXT platform (Thermo Fisher Scientific) with a 20 × 0.4 NA objective (field size of 454,41 by 454.41 µm) and analyzed using HCS Studio 2.0 (Thermo Fisher Scientific). Acquisition was configured individually for every analyzed antibody and chromophore. Nuclear DNA fluorescence intensity (DAPI) was assessed in channel 1 and a nuclear mask was created using the image analysis segmentation algorithm to identify viable cells as valid objects according to their object area and shape. The nuclear mask was used to quantify histone, genomic stability or neuron specific markers of valid objects in channel 2 with a fixed exposure time. A ring (thickness 13 pixels) was used to quantify the cytoplasmic marker CellROX, MitoTracker or neuron specific markers with a fixed exposure time. At least 2,000 valid objects per well and cell line were analyzed. An average fluorescence intensity per cell line was reported. Additionally, 100 cells per condition and replicate were selected randomly for distribution analysis. Distribution plots were generated and compared using the *sm.density.compare* function which applies a bootstrap hypothesis test of equal distribution (R package "sm: Smoothing Methods for Nonparametric Regression and Density Estimation" version 2.2-5.6, R version 3.6.3) and using the *ks.test* function to apply a two-sample Kolmogorov-Smirnov test.

Neurite outgrowth analysis was performed using a Cellinsight NXT platform with a 20 × 0.4 NA objective (field size of 454,41 by 454.41 µm) and analyzed using HCS Studio 2.0 (Neuronal Profiling Bioapplication). Twenty-five imaging fields were collected per well. Nuclei were identified by DAPI staining, while cell somas and neurites of dopaminergic neurons were identified by TH staining. Cells were classified as neurons if they had a DAPI and RBFOX3 (NEUN) -positive nucleus as well as a TH positive soma. Only neurites longer than 10 µm were included in the analysis.

4.7. Cell based assays.

4.7.1. CellROX staining.

hNPCs were maintained on Geltrex coated 96 well plates and in neuronal precursor maintenance medium at 37 °C, 7 % CO_2, 21 % O_2 for at least 48 h. Cells were washed with PBS and subsequently incubated with prewarmed neuronal precursor maintenance medium supplemented with 5 µM CellROX (C10444, Thermo Fisher Scientific) and 5 µm Hoechst 33342 (Thermo Fisher Scientific) for 30 min at 37 °C, 7 % CO_2, 21 % O_2. Cells were washed twice with PBS and fixed with 10 % Formalin (Sigma) for 20 min at 37 °C. High content analysis was performed within 24 h after CellROX incubation.

4.7.2. MitoTracker staining.

hNPCs were maintained on Geltrex coated 96 well plates and in neuronal precursor maintenance medium at 37 °C, 7 % CO_2, 21 % O_2 for at least 48 h. The same amount of prewarmed neuronal precursor medium supplemented with 200 nM MitoTracker Orange CMTMRos (M7510, Thermo Fisher Scientific) was added

per well and cells were stained for 20 min at 37 °C, 7 % CO_2, 21 % O_2. Cells were washed twice with PBS and fixed with 10 % Formalin (Sigma) for 20 min at 37 °C. DAPI staining was performed as described below.

4.7.3. EdU proliferation assay.

hNPCs were cultured on Geltrex coated 96 well plates for at least 72 h. 10 Ctrl and 14 sPD hNPC lines were incubated with 10 µM 5-ethynyl-2'-deoxyuridine (EdU) for 2 h at 37 °C, 7 % CO_2, 21 % O_2. Cells were fixed, EdU was detected and DNA was stained according to the Click-iT Plus EdU Alexa Fluor 488 Imaging Kit (Thermo Fisher Scientific) manual. Images were acquired using a Cellinsight NXT platform (Thermo Fisher Scientific) with a 20 × 0.4 NA objective (field size of 454,41 by 454.41 µm) and analyzed using HCS Studio 2.0 (Thermo Fisher Scientific). Nuclear DNA fluorescence intensity (Hoechst dye) was assessed in channel 1 and a nuclear mask was created using the image analysis segmentation algorithm to identify viable cells as valid objects according to their object area and shape. The nuclear mask was used to quantify EdU fluorescence intensity of valid objects in channel 2 with a fixed exposure time. At least 2000 valid objects per well and cell line were analyzed. EdU fluorescence intensity was normalized to the nuclear area and mean Ctrl fluorescence intensity, an average fluorescence intensity per cell line was reported.

4.7.4. Respiratory and glycolytic flux analysis.

Fibroblasts were cultured on Geltrex coating and in fibroblast growth medium at 37 °C, 5 % CO_2, 21 % O_2. At 60-70% confluency, fibroblasts were passaged using 0.05% trypsin-EDTA, cell number was determined using a Neubauer improved cell counting chamber and 25,000 cells per well with at least 8 replicates per cell line were seeded on Geltrex coated XF96 cell culture microplates and incubated for 48 h with daily medium changes.
hiPSCs were maintained on Geltrex coating and in mTesR1 medium at 37 °C, 5 % CO_2, 21 % O_2. At 70 % confluency, hiPSCs colonies were passaged using Accutase for 6 - 8 min at 37 °C, sheared to single cells by pipetting using a 1000 µl tip and diluted in mTeSR medium containing 10 µM ROCK inhibitor Y27632. hiPSCs were harvested at 100 g for 5 min and resuspended in 1 ml mTeSR medium containing 10 µM ROCK inhibitor Y27632. Cell number was determined and 5,000 cells per well with at least 8 replicates per cell line were seeded in mTeSR medium containing 10 µM ROCK inhibitor Y27632 on Geltrex coated XF96 cell culture microplates and incubated for 6 days with daily medium changes.
hNPCs were maintained on Geltrex coating and in neuronal precursor maintenance medium at 37 °C, 7 % CO_2, 21 % O_2. At 80% confluency, hNPCs were passaged, cell number was determined and 70,000 cells per well with at least 8 replicates per cell line were seeded on Geltrex coated XF96 cell culture microplates and incubated for 48 h with daily medium changes.
DAns were passaged on day 9 of differentiation according to the differentiation protocol, cell number was determined and 5,000 cells per well with at least 8 replicates per cell line were seeded on 15 µg/mL poly-L-ornithine and 10 µg/mL laminin coated XF96 cell culture microplates. DAns were matured for at least 30 days at 37 °C, 7 % CO_2, 21 % O_2 with medium changes every 2-5 days.
Astrocytes were cultured on 15 µg/mL poly-L-ornithine and 10 µg/mL laminin coating and in astrocyte differentiation medium at 37 °C, 7 % CO_2, 21 % O_2. At 70% confluency, astrocytes were passaged, cell number was determined and 50,000 cells per well with at least 8 replicates per cell line were seeded in

astrocyte differentiation medium containing 10 µM ROCK inhibitor Y27632 and on 15 µg/mL poly-L-ornithine and 10 µg/mL laminin coated XF96 cell culture microplates and incubated for 6 days with daily medium changes.
Motor neurons were passaged on day 30 of differentiation using Accutase and approximately 5,000-10,000 cells per well with at least 8 replicates per cell line were seeded on Geltrex coated XF96 cell culture microplates. Motor neurons were matured for additional 8 days at 37 °C, 5 % CO_2, 21 % O_2 with daily medium changes.
The respiratory and glycolytic flux analysis was performed using an XF96 Analyzer (Seahorse Bioscience) and XF Assay medium (Seahorse Bioscience) supplemented with 25 mM glucose (Sigma) or 5 mM pyruvate (Sigma). Prior to measurements, cells were washed once with XF Assay medium and at least 4 replicates per patient were incubated with XF Assay medium containing glucose or pyruvate for 1h at 37 °C, 0 % CO_2, 21 % O_2. XFe96 Sensor Cartridges (Seahorse Bioscience) were hydrated with 200 µl Calibrant (Seahorse Bioscience) per well overnight and ports were loaded with (A) 10 µg/mL oligomycin (Sigma), (B) 5 µM FCCP (Sigma), (C) 50 µM rotenone (Sigma) and 20 µM antimycin-A (Sigma) and (D) 1 M 2-deoxyglucose (Sigma). After equilibration, the analysis was performed with a total of 4 basal measuring points (mix for 1 min, time delay for 2 min and measure for 3 min). Subsequent to port injections, respiratory and glycolytic flux analysis was performed with 3 measuring points. Data were normalized to DNA content analyzed on an equally seeded and grown plate (fibroblasts, iPSCs, hNPCs) or the same plate (DAns, astrocytes, motor neurons) using the Quant-iT PicoGreen dsDNA Assay Kit (Thermo Fisher Scientific). The copy plate (medium aspirated) or the same plate was stored at -20 °C immediately after the Seahorse run was performed and thawed on ice for 30 min prior to analysis. For the copy plate, cells were lysed in 60 µl RIPA buffer (50 mM Tris-HCL (Sigma), 150 mM NaCl (Merck Millipore), 1 % Triton X-100, 0.5 % sodium deoxycholate (Sigma), 0.1 % SDS (Sigma), 3 mM EDTA (Sigma)) per well. For the same plate, 10 µl Proteinase K (20 mg/ml; AppliChem) was added per well and cells were lysed at 37 °C for 1h. The assay was performed according to the manufacturer's instructions. DNA concentrations were calculated with a linear regression curve using Lambda DNA standards. For statistical analysis of basal and maximal mitochondrial respiration as well as proton leak the mean OCR values per patient of measuring points prior to port A injection, after port B and prior to port C injection or after port A and prior to port B injection, respectively, were used. Basal glycolytic flux and glycolytic capacity were calculated from mean ECAR values per patient of measuring points prior to port A injection or after port A and prior to port B injection, respectively. The last two measuring points were used to subtract non-mitochondrial respiration or non-glycolytic acidification.

4.7.5. Analysis of complex I activity.

Complex I enzyme activity was measured using the complex I enzymatic activity microplate assay kit (Abcam) according to the manufacturer's instructions. Enzymatic kinetics were measured on a SpectraMax M5 (Molecular Devices) for 45 min. Values were normalized to total protein concentrations and average Ctrl levels.

4.7.6. Analysis of total ATP levels.

At 80% confluency, hNPCs were passaged, cell number was determined and 10,000 cells per well with at least 3 replicates per cell line were seeded on Geltrex coated white 96 well plates and incubated for 48 h with daily medium changes at 37 °C, 7 % CO_2, 21 % O_2. Total ATP levels were analyzed using a Luminescent ATP Detection Assay Kit (Abcam) according to the manufacturer's instructions. Values were normalized to DNA content analyzed on an equally seeded and grown copy plate using the Quant-iT PicoGreen dsDNA Assay Kit (Thermo Fisher Scientific) as described above for Respiratory and glycolytic flux analysis.

4.7.7. Analysis of NADH and NAD^+ levels.

At 80 % confluency, hNPCs were passaged, cell number was determined and 5,000,000 cells per sample were resuspended in 100 µl lysis buffer. Total NADH and NAD^+ levels were analyzed using a NAD/NADH Assay Kit (ab176723; Abcam) according to the manufacturer's instructions. Fluorescence intensity was quantified using a SpectraMax M5 (Molecular Devices). Values were normalized to DNA content analyzed using additional 5,000,000 cells that were lysed in 100 µl RIPA buffer using the Quant-iT PicoGreen dsDNA Assay Kit (Thermo Fisher Scientific) as described above for Respiratory and glycolytic flux analysis.

4.7.8. DNA methylation analysis.

Genomic DNA from 5 Ctrl and 7 sPD hNPC lines and from 3 different passages was extracted using the QIAamp DNA Mini Kit according to the manufacturer's instructions for cultured cells. DNA concentration was measured using Quant-iT™ PicoGreen according to the Infinium HTS Assay Protocol Guide (Illumina). DNA methylation was quantified using the Methylated DNA Quantification Kit (Colorimetric) (Abcam) according to the manufacturer's instructions. An amount of 100 ng sample genomic DNA was used per reaction. Absorbance was measured on a SpectraMax M5 at 450 nm after 10 min.

4.8. Isolation of RNA, cDNA synthesis and quantitative real-time PCR.

Gene expression was analyzed by RT-qPCR. When indicated, hNPCs were stimulated with 10 µM cyclopamine (Sigma-Aldrich) for 8 days at 37 °C, 7 % CO_2, 21 % O_2. Total RNA was extracted using RNeasy Plus Mini Kit (Qiagen) according to the manufacturer's instructions and reverse transcribed to cDNA using the SuperScript VILO cDNA Synthesis Kit (Thermo Fisher Scientific). For RT-qPCR 25 ng (2,78 ng/µl) cDNA was quantitatively amplified on a QuantStudio 7 Flex (Thermo Fisher Scientific) using TaqMan universal PCR MM no Ung (Thermo Fisher Scientific) and gene specific TaqMan primers (Thermo Fisher Scientific): ACTB (Hs99999903_m1); HPRT1 (Hs99999909_m1); GAPDH (Hs99999905_m1); GLI1 (Hs00171790_m1); GLI2 (Hs01119974_m1); GLI3 (Hs00609233_m1); FOXA2 (Hs05036278_s1); PITX3 (Hs01013935_g1); BBS5 (Hs00537098_m1); GET4 (Hs00944514_m); CFHR1 (Hs00275663_m1); GRB14 (Hs00182949_m1); LINGO2 (Hs01102041_s1); SLC1A2 (Hs01102423_m1); SRCAP (Hs00198472_m1). Comparative C_t method was used to analyze differences in gene expression, values were normalized to ACTB or BestKeeper(*260*) calculated from ACTB, GAPDH, MAPT1 expression levels.

4.9. Protein isolation and immunoblotting.

4.9.1. Cytoplasmic/nuclear fraction isolation.

For protein extraction hNPCs (5 x 10^6) were washed with ice cold PBS and collected by scraping in 100 µl ice cold Hypotonic buffer (20 mM Tris-HCl pH 7.4 (Sigma), 10 mM NaCl (Sigma), 3 mM $MgCl_2$ (Sigma)) containing Protease Inhibitor Cocktail (Roche Diagnostics). Cells were lysed on ice for 15 min, 5 µl 10 % NP_40 (Sigma) was added and the homogenate was centrifuged at 1,000 g, 4 °C for 10 min. The supernatant contained the cytoplasmic fraction. The nuclear pellet was washed with 500 µl Hypotonic buffer, centrifuged at 1,000 g, 4 °C for 10 min and resuspended in 20 µl Cell Extraction Buffer (Thermo Fisher Scientific) containing 1 mM PMSF (Sigma) and Protease Inhibitor Cocktail. Nuclei were lysed on ice for 50 min with vortexing at 10 min intervals. Debris were removed by centrifugation at 14,000 g, 4 °C for 30 min. The supernatant contained the nuclear fraction. Protein concentration was quantified using Pierce BCA Protein Assay Kit (Thermo Fisher Scientific) according to the manufacturer's instructions. 10 µg protein extract was diluted in RIPA and NuPAGE (Novex) and incubated for 5 min at 95 °C.

4.9.2. Total protein isolation.

hNPCs were maintained on Geltrex coating and in neuronal precursor maintenance medium at 37 °C, 7 % CO_2, 21 % O_2 for at least 72 h. Approximately 2 x 10^7 cells were lysed in RIPA buffer and subsequently stored at -80 °C. Protein concentration was quantified using the Pierce BCA Protein Assay Kit (Thermo Fisher Scientific) according to the manufacturer's instructions. 10 µg protein extract was diluted in RIPA and NuPAGE (Novex) and incubated for 5 min at 95 °C.

4.9.3. Immunoblotting.

Protein extracts from 5 Ctrl and 7 sPD hNPC lines and Protein Marker VI (AppliChem) were separated on a Criterion XT Bis-Tris Gel, 4-12% (Bio-Rad) using Tris/Glycine Buffer (Bio-Rad) and a Criterion Vertical Electrophoresis Cell (Bio-Rad) at 120 V for 70 min. Proteins were blotted on Immobilon – P Membranes (Millipore) using XT MOPS buffer (Bio-Rad) and a Criterion Blotter (Bio-Rad) at 20 V, 4 °C overnight. Membranes were blocked for 1 h with TBS containing 0.01 % Tween 20 (TBST) and 5 % milk. Primary antibodies against GLI3 (AF3690, R&D; 1:100), ACTB (ABO145-200, OriGene; 1:2,000), PCNA (ab29, Abcam; 1 µg/ml), NDUFB8 (459210, Novex; 1:500), NDUFS1 (ab157221, Abcam; 1:10,000), NDUFS3 (ab183733, Abcam; 1:10,000), Complex II - Subunit 30 (459230, Thermo Fisher Scientific; 1:500), UQCRC2 (ab14745, Abcam; 1:2,500), MTCO2 (ab110258, Abcam; 1:1,000), ATP5A (ab14748, Abcam; 1:4,000), TUBA (GTX628802, Genetex; 1:20,000) were incubated in blocking buffer overnight at 4 °C. Membrane was washed with TBST and secondary antibodies rabbit-anti-mouse IgG peroxidase (GTX213112-01, GeneTex; 1:10,000) and rabbit-anti-goat IgG peroxidase (305-035-003, Dianova; 1:10,000) were incubated in blocking buffer at room temperature for 2 h, respectively. Subsequently, the membrane was washed with TBST and incubated with ECL substrate (GE Healthcare) for 1 min. Protein bands were visualized using a ChemiDoc Imager (Bio-Rad) and quantified using Image Lab (Bio-Rad).

4.10. Analysis of telomere length.

Genomic DNA (gDNA) from 5 Ctrl and 7 sPD patient derived fibroblasts as well as from 5 Ctrl and 7 sPD hiPSC and hNPC lines in low and high-passage was extracted using the QIAamp DNA Mini Kit according to the manufacturer's instructions for cultured cells. DNA concentration was quantified using Quant-iT™ PicoGreen according to the Infinium HTS Assay Protocol Guide (Illumina). Telomere length was analyzed by calculating a relative telomere to single copy gene (T/S) ratio as described by (*350*)**.** For quantitative polymerase chain reaction, 200 ng (10 ng/µl) gDNA was quantitatively amplified on a QuantStudio 7 Flex (Thermo Fisher Scientific) using Power SYBR Green mastermix (Thermo Fisher Scientific) and telomere (tel1 ACACTAAGGTTTGGGTTTGGGTTTGGGTTTGGGTTAGTGT and tel2 TGTTAGGTATCCCTATCCCTATCCCTATCC CTATCCCTAACA), ALB (alb1 CGGCGGCGGGCGGCGCGGGCTGGGCGGaaatgctgcacagaatccttg and alb2 GCCCGGCCCGCCGCGCCCGTCCCGCCGgaaaagcatggtcgcctgtt) or HBG (hbg1 CGGCGGCGGGCGGCGCGGGC TGGGCGGctcitric acid cycletccacgtcitric acid cyclecttg and hbg2 GCCCGGCCCGCCGCGCCCGTCCCGCCG gaggagaagtctgccgtt) specific primers (500 nM each). The c_t values were used to calculate the telomere to ALB ratio and the telomere to HBG ratio per cell line. Values were normalized to the average ratio of (low-passage) ctrl lines.

4.11. SNP detection and CNV analysis.

Genomic DNA from 5 Ctrl and 7 sPD hNPC lines, as well as one PINK1 ko and one PINK1 Q126P line with their corresponding isogenic Ctrls, was extracted using the QIAamp DNA Mini Kit according to the manufacturer's instructions for cultured cells. DNA concentration was measured using Quant-iT™ PicoGreen according to the Infinium HTS Assay Protocol Guide (Illumina). SNPs from hNPC lines (200 ng DNA per sample) were detected in duplicates using an Infinium CoreExome-24 v1.3 Kit (20024662, Illumina) and an iScan system (Illumina) according to the Infinium HTS Assay Protocol Guide. The Infinium HTS Assay was performed in the genome analysis center of Helmholtz Zentrum München. Clustering, quality control, and SNP calling was done using GenomeStudio 2.0 (Illumina) as described by(*351*). The log2 R ratios (LRR) and B-allele frequencies (BAF) were used to identify copy number variations (CNVs) on autosomes for each cell line using cnvPartition v3.2.1 (Illumina) with regards to aberrations minimally sizing 100 kb. cnvPartition v3.2.1 was run with default settings, including a confidence threshold of 50. All SNPs were converted to the GRCh38 forward strand using a script developed by Robertson and Wrayner (https://www.well.ox.ac.uk/~wrayner/strand/; 12.11.2019). For multiplexed scRNA-seq, SNP files were converted to vcf files using PLINK 2.00 alpha(*352*). A custom-made perl script was used to extract exonic SNPs using exon boundaries obtained from BioMart (https://www.ensembl.org/info/data/biomart/index.html#biomartdoc, 12.11.2019).

4.12. Single-cell transcriptome library preparation and sequencing.

For multiplexed scRNA-seq analysis 5 Ctrl and 7 sPD lines, as well as one *PINK1* ko and one *PINK1* Q126P line with their corresponding isogenic Ctrls, were used. hNPCs were maintained on Geltrex coated plates containing neuronal precursor maintenance medium at 37 °C, 7 % CO_2, 21 % O_2. At 80% confluency, hNPCs were dissociated using Accutase for 10 min at 37 °C, chopped with a 1000 µl pipette tip and diluted in 5 ml PBS containing 10 % BSA (Sigma). hNPCs were harvested at 200 g for 5 min and resuspended in 1 ml PBS containing 10 % BSA. The hNPC solution was filtered through a 35 µm cell strainer (Corning) and

counted using a Neubauer improved cell counting chamber (Carl Roth). 978 hNPCs from each ForIPS line, 1,956 hNPCs from the *PINK1* ko line or isogenic Ctrl and 1,956 hNPCs from the *PINK1* Q126P line or isogenic Ctrl were mixed and used for multiplexed droplet single-cell library production. In total 6 libraries with 15,650 hNPCs each were generated in the 10X Genomics Chromium controller according to the manufacturer's instructions and using the Chromium Single Cell 3' Library & Gel Bead Kit v2 (PN-120237, 10xGenomics) and Chromium i7 Multiplex Kit (PN-120262, 10xGenomics). Libraries were pooled and sequenced on a HiSeq4000 (Illumina) according to the Chromium Single Cell v.2 specifications and with an average read depth of 90,000 aligned reads per cell. Sequencing was performed in the genome analysis center of Helmholtz Zentrum München.

4.13. Sequencing data processing.

Sequencing data was processed using Cell Ranger version 2.1.1. Read files were aligned against hg38 from Ensembl release 94 using default parameters. Spliced and unspliced counts for RNA velocity analysis were called using velocyto version 0.17.7 and samtools version 1.7.
We used Demuxlet(*250*) (retrieved 17th July 2018) and the obtained SNP data to demultiplex the pooled sequencing data. The SNP array data was reformatted to fit the chromosome ordering in the Cell Ranger output using vcf tools version 0.1.15. Demuxlet was run separately per sequencing batch (lane) with potential mixture proportion parameter alpha set to 0 and 0.5 and otherwise default parameters. Only cells called as singlets by demuxlet were used for further processing. The sPD clones and their respective Ctrls could be separated by SNP data, while *PINK1* ko and *PINK1* Q126P clones were run on different sequencing lanes as their isogenic Ctrls.

4.14. Single-cell transcriptome analysis.

Single cell gene expression data was processed according to a recently published best practices workflow(*353*). Data was loaded into Scanpy(*354*) version 1.4.3 commit 0075c62.

4.14.1. Quality control and pre-processing.

After considering the joint distribution of count depth, the number of genes expressed, and mt read fraction per sample, cells with more than 45,000 counts, with fewer than 1,000 genes expressed, and with 15 % or more reads aligned to mitochondrial genes were filtered out. Furthermore, genes that were measured in fewer than 20 cells were also removed from the dataset. This left a dataset of 30,557 cells and 24,920 genes. Normalization was performed by the pooling method implemented in the computeSumFactors() function in scran version 1.10.2. Normalized expression values were log+1-transformed.
To remove batch effects between donor samples in the dataset we used the python implementation of the matching mutual nearest neighbors algorithm(*355*), mnnpy (version 0.1.9.5; retrieved from https://github.com/chriscainx/mnnpy). MNNPY was run on a subset of highly variable genes (HVGs) that were shared by all batches. We selected 6000 HVGs per batch (donor) as implemented by the

highly_variable_genes method (with *flavor="cell_ranger"*) in Scanpy. Here, HVGs are selected by binning genes by mean expression and choosing the genes with the highest coefficient of variation per bin. The intersection of the set of HVGs per batch left 516 genes, which we used to find mutual nearest neighbors between batches in the dataset. Upon MNN data integration, we selected 4000 HVGs on the integrated dataset according to previously published best practices(*353*).
Low dimensional representations of the data were obtained by taking the top 50 principal components and calculating a k-nearest neighbor (KNN; k=15) graph using Euclidean distance on the principal component space as implemented in scanpy. The KNN graph was used as the basis on which to run UMAP(*356*) for visualization.

4.14.2. Cell cycle scoring and regression.

Cell cycle phases were called for each cell using Scanpy's *score_genes_cell_cycle* function with the gene list from(*357*). Scoring is performed by taking the mean expression of the gene sets for S and G2/M phases and subtracting a background gene expression score to obtain an S and G2/M phase score per cell. The background expression score is calculated by taking the mean expression of a random sample of 50 genes which are selected to have similar mean expression as the original gene set. Cells are assigned to S phase, G2/M phase, or G1 phase based on the relative S and G2M scores.
For trajectory and RNA velocity analysis, we used a version of the data with the cell cycle regressed out. For this we used Scanpy's regress_out function to jointly regress out the S G2/M phase scores on the MNN-corrected expression matrix.

4.14.3. Clustering, sub-clustering, marker gene detection, and cluster annotation.

We performed graph-based clustering on the computed KNN graph using the python implementation (version 0.6.1) of the Louvain algorithm(*358*) in Scanpy. As a first basis, we performed a coarse Louvain clustering at a resolution of 0.2. For each cluster, marker genes were determined by applying Welch's t-test (as implemented in Scanpy's *rank_genes_groups* function with default parameters) between the cells in the cluster and all other cells. Differential expression testing for marker gene detection was performed on the log-normalized, non-mnn-corrected expression values as recommended by published best practices(*353*). We annotated clusters by gathering evidence from four strategies: overlaps of data-derived marker genes with marker genes from the literature, literature-derived marker gene expression scores in our data, Gene Ontology(*359*) biological process term enrichment tests on data-derived marker genes via GProfiler(*360*), and cell cycle phases of cluster cells. Literature derived marker gene sets were obtained from(*252–259*). To gain a higher-resolution view on the cellular populations in the data, we sub-clustered larger clusters at a resolution of 0.2 using the restrict_to parameter in Scanpy's Louvain implementation. Sub-clusters were annotated in the way described above.
As clustering and sub-clustering frequently revealed a cluster structure that correlated with cell cycle phases, we performed a second Louvain clustering on the data after regressing out cell cycle effects (noCC data). Louvain clustering was performed at a resolution of 0.2 and broadly overlapped with results from the above clustering on original data. Sub-clustering was performed at a resolution of 0.3 and apoptotic sub-clusters were identified by data-derived marker genes and exhibit low mitochondrial read fractions.

Cluster annotations from the original and the noCC data were harmonized using the original clustering as a basis and adding annotations from the noCC data when the original cluster structure was determined by cell cycle phases. For example, the cluster "*Neuronal Stem Cells (G2M-phase)*" was divided into "*NSC1b*" and "*NSC2b*" in this way. Furthermore, the apoptotic sub-cluster labels from the noCC data annotation were kept.

4.14.4. RNA velocity and trajectory analysis.

RNA velocity analysis was performed using Scvelo(*361*) version 0.1.24 on commit e45a65a. Unspliced and spliced read data contained 71 % spliced counts, 22 % unspliced counts, and 7 % ambiguous reads. Merging of unspliced and spliced counts with our processed expression data resulted in a dataset containing 24,956 of the initial 30,557 cells. Unspliced and spliced count data were pre-processed by filtering out genes with fewer than 20 spliced counts and 10 unspliced counts. The resulting data was normalized (total count normalization) and log-transformed via Scvelo's *filter_and_normalize* function and smoothed via the *moments* method. To select only genes that were fit to a minimal degree of accuracy by the Scvelo model we used a threshold of 0.001 on the per-gene log-likelihood to determine our velocity gene set. This thresholding left 2,439 genes to fit the full dynamical model in Scvelo.
RNA velocity trajectories were determined by finding the root and end states shown by the velocity transition matrix. For this computation, we subsetted the data to the main neuronal cell population of interest (clusters *NSC1a*, *NSC1b*, *NSC2a*, *NSC2b*, and *immature neurons*) and determined the terminal states via Scvelo's *terminal_states* function. This function computes root and endpoint probabilities via a spectral decomposition of the velocity-inferred transition matrix. Specifically, the left eigenvectors of this matrix that correspond to a steady-state eigenvector of 1 determine the endpoint probabilities, while the root cell probabilities are obtained by using the transpose of the transition matrix for the same calculation. We obtained the root cell population by multiplying the root cell probabilities with the KNN graph connectivities to smooth the transitions and then selected cells with a score above 0.4. The resulting root cells were clustered by the *louvain* function at a resolution of 0.3. The dominant root cell cluster (>50 % of cells) was used to represent the root cell population and ignore outliers. Root cell sub-clusters with particular fates were identified by sub-clustering the main cluster at a resolution of 0.5 and assigning NSC1 and NSC2 fates based on velocity arrows. Endpoint clusters were obtained in a similar manner, using a threshold of 0.6, without prior KNN-smoothing. After Louvain clustering at a resolution of 0.3, we selected the two clusters that best correspond to the low dimensional embedding for further investigation.

4.14.5. Transcriptome analysis of *PINK1* clones.

As quality control (QC) metric distributions were similar between samples, we performed a joint QC across all *PINK1* clones. Cells with more than 39,000 counts, with fewer than 1000 genes expressed, and with 15 % or more reads aligned to mitochondrial genes were filtered out. Furthermore, genes that were measured in fewer than 20 cells were also removed from the dataset. This resulted in a dataset of 10,240 cells and 20,623 genes, with 6,569 *PINK1* Q126P cells and 3,671 *PINK1* ko cells. Normalization was performed jointly across all clones by the pooling method implemented in the computeSumFactors() function in scran version 1.10.2. Normalized expression values were log+1-transformed.

Further processing of the *PINK1* clone dataset was performed individually per clone. Cell cycle scoring was performed on a gene set(*357*) as described above. For the *PINK1* ko cell data, we first regressed out the cell cycle effect and then integrated the two conditions using mnnpy as described for the sPD clones. Here, the intersection of per-batch HVGs between batches left 5,328 HVGs on which the mnn data integration could be performed. The cell cycle effect was also regressed out for *PINK1* Q126P cells but no further batch effect removal was needed. Low dimensional embeddings for each *PINK1* clone dataset were computed via a KNN graph (k=15) calculated using Euclidean distances on the principal component-reduced expression space subsetted 4000 HVGs selected by Scanpy's *highly_variable_genes* function as described above.
Clustering by Louvain community detection was performed at a resolution of 0.3 for the *PINK1* ko dataset and 0.15 for the *PINK1* Q126P dataset. Marker genes were obtained by applying Scanpy's Welch's t-test implemented in the *rank_genes_groups* function in the same way as for the sPD clone data. Clusters were annotated by comparison of data-derived marker genes with the previously described literature curated marker gene list.

4.14.6. Differential expression analysis.

Differential expression analysis per cell identity cluster was performed via the Diffxpy package (https://github.com/theislab/diffxpy; version 0.6.1; dev branch). Diffxpy fits a negative binomial model to the raw count data and allows for adding covariates and constraints into the model. In the sPD clone dataset, we fit the model:

Y ~ 1 + condition + donor + size_factors,

for each annotated cluster. Here, *Y* represents the raw gene expression counts, *1* denotes the intercept, *condition* is the disease status (Parkinson vs control), *donor* is the patient from which the cell was obtained, and *size_factors* denote the scran pooling size factors. As the *donor* and *condition* covariates are perfectly confounded, we added the constraint that donor effects sum to 0 per condition (input as '*Donor:condition'* in Diffxpy) to make the model identifiable. As we only have a single sample per condition in the *PINK1* clone datasets, we instead fit the simplified model:

Y ~ 1 + condition + size_factors,

in these dataset. This simplified model did not require additional constraints.
The differential test was performed via a Wald test over the *condition* covariate per gene for all genes expressed in at least 50 cells in the tested cluster. Multiple testing correction was performed via the Benjamini-Hochberg method.(*362*)

4.15. Cis eQTL mapping.

Genotypes were filtered for a minor allele frequency (MAF) of > 0.2, resulting in a total of 180,183 SNPs. We calculated mean expression values per cluster and donor using the log+1-transformed, normalized expression data (normalized via scran-pooling). The expression matrix was filtered for genes detected in

at least 25 % of all individuals per cluster, resulting in a total of 24,736 genes in NSC1a; 24,707 genes in NSC1b; 24,474 genes in NSC2a; 21,478 genes in NSC2b; 20,646 genes in apoptotic NSCs; 23,609 genes in NCSC; 13,883 genes in apoptotic NCSC; 19,054 genes in glial precursors; 17,375 genes in immature neurons. Gene position informations for the genome assembly GRCh38 were obtained from BioMart (https://www.ensembl.org/info/data/biomart/index.html#biomartdoc, 12.11.2019). Linear regression was used to determine associations between each SNP within a 100 kb window of each gene with Matrix eQTL(*363*). Cis-eQTL analysis was performed seperatly for each cell cluster. Gender (male or female), disease state (Ctrl or sPD) and the first three principal components of the expression matrix were used as covariates.

4.16. Enrichment and pathway analysis.

DEGs (0.83 > FC > 1.2 and q < 0.01 or q < 0.05) were investigated for enrichment in the curated pathway categories "Cell Process" and "Signal Processing" of the Pathway Studio software (Elsevier) version 12.2.1.2 by using Fisher's exact test. Subsequently, p-value correction for multiple testing with the fdrtool program(*364*) was performed. The fdrtool function (*statistic* = "pvalue", *cutoff.method* = "fndr") within the fdrtool v1.2.15 package in R (R version 3.5.3, RStudio Desktop 1.2.5019) was used to calculate q-values. In case of smaller input datasets (i.e. number of DEGs < 450) into the Pathway Studio *cutoff.method* = "ptc0" was selected. We extended the literature-derived network of the intraflagellar transport BBSome interaction pathway in the category Cell Process from the Pathway Studio by manual literature searches. To further expand the BBSome interaction pathway a list of cilia associated genes were downloaded from the UniProtKB database (www.uniprot.org/keywords/ with the keywords Cilium biogenesis/degradation (KW-0970) and Cilium (KW-0969)) and compared to DEGs of cell clusters. DEGs of the root population were analyzed for enriched gene sets of the category curated canonical pathways by using the *enricher* function of the R package clusterProfiler v3.14.3(*365*) and the C2.CP collection of the Molecular Signatures Database v7.0(*366*). Bulk-like DEGs were analyzed for enriched gene sets by using the enricher function of the R v3.6.3 package clusterProfiler v3.14.3 and the wikipathways(*367*) collection (downloaded: 09.06.2020). p-values were adjusted for multiple testing by Benjamini and Hochberg(*362*). Enrichment maps were generated using the *emapplot* function of clusterProfiler v3.14.3.

4.17. Heatmap and volcano plot.

We represented log2 transformed fold changes of the top ten up- and downregulated DEGs from each cell cluster by a heatmap. This heatmap was generated by using the *heatmap.2* function within the gplots v3.0.1.1 package of R. Agglomerative hierarchical clustering by the *hclust* function (method = "complete") was applied to group cell clusters (rows) and a dendrogram was shown only for the rows. Log2 transformed fold changes of DEGs (columns) were scaled and represented as z-score. Based on the complete set of DEGs per cluster volcano plots were produced by plotting log2(fold change) versus –log10(q-value) on the x and y-axis, respectively. The q-value represents the differential expression p-value adjusted for multiple testing by Benjamini and Hochberg(*362*).

4.18. Transcription factor target gene prediction.

In silico prediction of GLI3 transcription factor binding sites in all human promoter sequences was performed by using the MatInspector program (Genomatix)(*368*). The corresponding position weight matrices V$GLI3.01 and V$GLI3.02 were applied to promoter analysis according to the Matrix Family Library Version 11.1 (February 2019). We used the maximum core similarity of 1.0 to exactly match the highest conserved bases of a matrix in the sequence. The threshold for the matrix similarity was set to 0.9 to minimize false positives.

4.19. Genewalk analysis.

Bulk-like DEGs (over all cells independent of cell clusters) identified in in high-passage sPD hNPCs were used as input for genewalk v1.2.1 (python v3.6.8) (*369*), which was run with default settings. Genewalk results were filtered for telomere associated GO terms. Identified GO terms and genes were visualized using networkx v2.4.

4.20. Primary cilia analysis in animal models.

For the analysis of neuronal PC in an animal model for genetic PD, five 12.5 ± 1.5 months old male homozygous *Pink1-/-* mice and four male wild type littermate *Pink1+/+* Ctrl animals were analyzed. *Pink1* KO mice were generated and characterized in our lab as previously described (*370*) and have been bred on a C57BL/J genetic background in the animal facility at the Helmholtz Zentrum München. In brief, in this mouse line, *Pink1* has been knocked out by excision of floxed exons 2 and 3 of the *Pink1* gene. Mice were kept under specific pathogen-free (SPF) conditions on a 12/12-hour dark-light cycle in a temperature (22 – 24 °C) and humidity (50 - 60 %) controlled environment and were provided food and water *ad libitum*. All protocols and procedures were conducted with the approval for the ethical treatment of animals by the responsible animal welfare authority of the Regierung von Oberbayern (Government of Upper Bavaria). Mice were sacrificed with CO_2 inhalation at the age of 12.5 months ± 1.5 months and perfused transcardially with 0.1 M phosphate buffered saline (PBS) (pH 7.4) followed by 4 % paraformaldehyde (PFA). Fixed brains were excised from the skull and post-fixed in 4 % PFA overnight at 4 °C and subsequently transferred to a 30 % (w/v) sucrose cryoprotectant solution until fully saturated. Brains were then sectioned at -20 °C into 40 µm thick horizontal sections using a freezing cryostat and collected free-floating in a cryoprotectant solution containing 25 % ethylene glycol and 25 % glycerine in 0.1 M PBS. Sections were stored in cryoprotectant solution at -20 °C until further processing. Immunofluorescent double labeling of Chat and Adcy3 was performed according to standard protocols. In brief, free-floating brain sections (1 in 6 series) were rinsed in 0.1 M PBS overnight at 4 °C on a platform shaker (100 rpm) to ensure that any residual cryoprotectant solution was washed off. Sections were incubated in blocking buffer containing 0.3 % Triton-X-100 in 0.1 M PBS with 2 % fetal bovine serum (FBS) for 1 hour to decrease unspecific background staining. After blocking, brain tissue was incubated in a primary antibody dilution in blocking buffer overnight at 4 °C on a platform shaker. The following primary antibodies were used: Adcy3 (PA5-35382, Invitrogen; 1:500) and Chat (AB144P, Millipore; 1:200). Following primary antibody

incubation, brain sections were washed three times in 0.1 M PBS for 10 min each at room temperature on a platform shaker. Brain tissue was then incubated in secondary antibody dilution in 0.3 % Triton-X-100 in 0.1 M PBS for 2h at room temperature on the platform shaker. Following secondary antibodies were used: Alexa Fluor 488-conjugated donkey anti-rabbit IgG (A21206, Invitrogen; 1:500) and Alexa Fluor 594-conjugated donkey anti-goat IgG (A11058, Invitrogen; 1:500). Sections were washed with 0.1 M PBS three times for 10 min each before they were mounted on slides and coverslipped using Aqua-PolyMount. PC of striatal Chat+ cells double-stained for Chat and Adcy3 were selected for cilia length quantification in a three dimensional space and analysis of fraction of ciliated cells using Neurolucida with a Zeiss Axioplan 2 microscope with a 63 X immersion objective. The analysis was performed blinded and an average of > 60 PC per mouse were analyzed from random fields. Additionally, striatal PC stained for Adcy3 were quantified in a three dimensional space (115 µm x 87 µm x 40 µm) with an average of > 210 PC per mouse from random fields.

4.21. Non-targeted metabolomics analysis.

4.21.1. Cell preparation.

hNPCs were seeded at a density of 700,000 cells / well in six replicates in Geltrex coated 6-well plates and cultured in neuronal precursor maintenance medium with daily medium changes at 37 °C, 7 % CO_2, 21 % O_2 for at least 72 h to achieve a desired cell number of 1,000,000 – 1,500,000 cells per well. One replicate was used to determine the cell number. hNPCs were dissociated using Accutase for 10 min at 37 °C, 7 % CO_2, 21 % O_2, chopped with a 1000 µl pipette tip and diluted in 5 ml neuronal precursor maintenance medium. Cell number was determined using a Neubauer improved cell counting chamber. The remaining replicates were used for metabolite extraction. Cells were washed twice with warm PBS and metabolism was quenched by adding precooled extraction solvent (80 % methanol (AppliChem)) which contained 4 standard compounds to monitor the extraction efficiency. The amount of extraction solvent used was adjusted to the cell count, 1 ml solvent was used for 1,000,000 cells. Cells were harvested by scrapping them with the extraction solvent, were collected in precooled micro tubes (Sarstedt) and stored at -80 °C. For Ctrl samples, Geltrex coated 6-well plates containing neuronal precursor maintenance medium were incubated at 37 °C, 7 % CO_2, 21 % O_2 for at least 72 h. Medium was changed daily. After 72 h, medium was collected in precooled micro tubes and stored at -80 °C. Geltrex coated wells were washed twice with warm PBS and 1 ml extraction solvent was added. After scraping, the Geltrex – extraction solvent mixture was collected in precooled micro tubes and stored at -80 °C.
For analysis, 80 mg glass beads (0.5 mm; VK-05, PeqLab) were added to the samples and cells were homogenized using a Preccellys24 (PeqLab) for two times 25 seconds at 5500 rpm, 4 °C. The homogenates were used for fluorometric DNA quantification and for metabolomic analysis.

4.21.2. Fluorometric DNA quantification.

Fluorometric DNA quantification in homogenates was performed as described by (*371*). In brief, 80 µl Hoechst 33342 (20 µg/ml in PBS; Thermo Fisher Scientific) were mixed with 20 µl of the homogenate or

88% Methanol (blank) in a black 96-well plate (Thermo Fisher Scientific) and incubated in the dark for 30 min at room temperature. Fluorescence intensity was quantified using a GloMax Multi Detection System (Promega) with an UV filter (λ_{Ex} 365 nm, λ_{Em} 410–460 nm; Promega). Values were normalized to blank levels and the average of 4 replicates per sample was used for normalization of metabolite levels.

4.21.3. LC-MS/MS based metabolomics analysis.

The cell homogenates were centrifuged for 5 minutes at 5380 rpm, 4 °C. Eight aliquots of 50 µl of the supernatant were loaded onto four 96-well microplate. Two (i.e., early and late eluting compounds) aliquots for analysis by ultra-high performance liquid chromatography-tandem mass spectrometry (UPLC-MS/MS) in positive ion mode electrospray ionization (ESI), one for analysis by UPLC-MS/MS in negative ion mode ESI, and one for analysis by (HILIC)/UPLC-MS/MS in negative ion mode ESI. Three types of quality control samples were included into each plate: samples generated from a pool of human plasma, samples generated from a small portion of each experimental samples served as technical replicate throughout the data set, and extracted water samples served as process blanks. Experimental samples and controls were randomized across the metabolomics analysis. The samples were dried on a TurboVap 96 (Zymark).
Prior to UPLC-MS/MS analysis, the dried samples were reconstituted in acidic or basic LC-compatible solvents, each of which contained a series of standard compounds at fixed concentrations to ensure injection and chromatographic consistency. The UPLC-MS/MS platform utilized a Waters Acquity UPLC with Waters UPLC BEH C18-2.1×100 mm, 1.7 µm columns and a Thermo Scientific Q-Exactive high resolution/accurate mass spectrometer interfaced with a heated electrospray ionization (HESI-II) source and Orbitrap mass analyzer operated at 35,000 mass resolution. One aliquot reconstituted in acidic positive ion conditions, chromatographically optimized for more hydrophilic compounds. In this method, the extract was gradient eluted from a C18 column (Waters UPLC BEH C18-2.1 x 100 mm, 1.7 µm) using water and methanol, containing 0.05% perfluoropentanoic acid (PFPA) and 0.1% formic acid (FA). Another aliquot was also analyzed using acidic positive ion conditions; however it was chromatographically optimized for more hydrophobic compounds. In this method, the extract was gradient eluted from the same afore mentioned C18 column using methanol, acetonitrile, water, 0.05% PFPA and 0.01% FA and was operated at an overall higher organic content. Another aliquot was analyzed using basic negative ion optimized conditions using a separate dedicated C18 column. The basic extracts were gradient eluted from the column using methanol and water, however with 6.5 mM Ammonium Bicarbonate at pH 8. The fourth aliquot was analyzed via negative ionization following elution from a HILIC column (Waters UPLC BEH Amide 2.1x150 mm, 1.7 µm) using a gradient consisting of water and acetonitrile with 10 mM Ammonium Formate, pH 10.8. The MS analysis alternated between MS and data-dependent MSn scans using dynamic exclusion. The scan range varied slighted between methods but covered 70-1000 m/z.
Raw data was extracted, peak-identified and QC processed using Metabolon's hardware and software (Metabolon, Inc., North Carolina, USA). Compounds were identified by comparison to library entries of purified standards or recurrent unknown entities, based on 3 criteria: retention index within a narrow RI window of the proposed identification, accurate mass match to the library +/- 10 ppm, and the MS/MS forward and reverse scores between the experimental data and authentic standards. The MS/MS scores are based on a comparison of the ions present in the experimental spectrum to the ions present in the

library spectrum. While there may be similarities between these molecules based on one of these factors, the use of all three data points can be utilized to distinguish and differentiate biochemicals.

4.21.4. Data analysis.

OrigScale values were median normalized, adjusted to DNA levels and imported into R v3.6.3. Only metabolites detected in more than 30 % of the samples were used for further analysis. To achieve normal distribution, values were $\log_2$ transformed. Unsupervised PCA was used to discover differential variation features and confirmed close relationship between replicates of samples. PCA was performed using the *prcomp* function in R and visualized using the R package ggbiplot v0.55 with probability ellipses (0.68 of normal probability). Thus, average values of all replicates per sample and metabolite were used for statistical analysis. Hypothesis testing was performed using student`s t-test (*t.test* function in R) and p-values were adjusted for multiple testing using the R package fdrtool v1.2.15 (*statistic* = "pvalue", *cutoff.method* = "ptc0"). Metabolites with a q-value < 0.5 were considered significantly altered in sPD. A volcano plot was produced using the R package EnhancedVolcano v1.6.0 by plotting the log2(fold change) versus the –log10(p-value). Integrated pathway enrichment analysis of transcriptome (bulk-like DEGs) and metabolome (metabolites with q-value < 0.5) data was performed in MetaboAnalyst v4.0 (Enrichment anlysis = Hypergeometric Test, Topology measure = Degree Centrality, Integration method = Combine queries) using KEGG (Oct2019) metabolic pathways. The 'CITRIC ACID CYCLE cycle' pathway (source: WikiPathways) was visualized and annotated using cytoscape v3.7.2 (installed apps: WikiPathways, CyTargetLinker and stringApp) and the R package RCy3 v3.11.

4.22. Statistics and reproducibility.

No statistical methods were used to predetermine the sample size. Statistical analysis was performed using GraphPad Prism 6 with mean values of n = 5 Ctrl and n = 7 sPD lines from 3 biological replicates, if not indicated otherwise. For two-group comparisons and in case of normal distribution, unpaired, two-tailed t-test was applied if a similar standard deviation could be assumed, otherwise, Welch-test was applied. In the case of non-Gaussian distribution, two-tailed Mann-Whitney-U test was applied. For comparison of multiple groups, two-way ANOVA with Tukey's Post-hoc test was performed. Data displaying a measurement progression are shown with mean ± standard error of the mean (SEM), boxplots are displayed from min to max values with all data points shown. Distribution plots were generated and compared using the *sm.density.compare* function which applies a bootstrap hypothesis test of equal distribution (R package "sm: Smoothing Methods for Nonparametric Regression and Density Estimation" version 2.2-5.6(*372*)). Additionally, the *ks.test* function in R was used to perform a two-sample Kolmogorov-Smirnov test. Venn diagrams were generated using the *draw.pairwise.venn* function (R package "VennDiagram" Version 1.6.20(*373*)). P-values or q-values below 0.05 are considered significant. Not-significant differences are not indicated.

5. References

1. World Health Organization, US National Institute of Aging, *Global health and ageing* (2011) (available at https://www.who.int/ageing/publications/global_health.pdf).
2. D. M. Vogt Weisenhorn, F. Giesert, W. Wurst, Diversity matters – heterogeneity of dopaminergic neurons in the ventral mesencephalon and its relation to Parkinson's Disease. *Journal of neurochemistry*. **139**, 8–26 (2016), doi:10.1111/jnc.13670.
3. S. Ovallath, P. Deepa, The history of parkinsonism: Descriptions in ancient Indian medical literature. *Movement Disorders*. **28**, 566–568 (2013), doi:10.1002/mds.25420.
4. B. Dániel, B. Árpád, P. Benedek, S. Szabolcs, International recognition of Ferenc Pápai Páriz as one of the first descriptors of all 4 cardinal signs of Parkinson's disease. *Bulletin of Medical Sciences*. **91**, 60–66 (2018), doi:10.2478/orvtudert-2018-0006.
5. J. Parkinson, An essay on the shaking palsy. 1817. *The Journal of neuropsychiatry and clinical neurosciences*. **14**, 223-36; discussion 222 (2002), doi:10.1176/jnp.14.2.223.
6. J. A. Obeso *et al.,* Past, present, and future of Parkinson's disease: A special essay on the 200th Anniversary of the Shaking Palsy. *Movement disorders : official journal of the Movement Disorder Society*. **32**, 1264–1310 (2017), doi:10.1002/mds.27115.
7. W. Poewe *et al.,* Parkinson disease. *Nature reviews. Disease primers*. **3**, 17013 (2017), doi:10.1038/nrdp.2017.13.
8. Van Den Eeden, Stephen K. *et al.,* Incidence of Parkinson's Disease: Variation by Age, Gender, and Race/Ethnicity. *Am J Epidemiol*. **157**, 1015–1022 (2003), doi:10.1093/aje/kwg068.
9. A. Reeve, E. Simcox, D. Turnbull, Ageing and Parkinson's disease: Why is advancing age the biggest risk factor?☆. *Ageing research reviews*. **14**, 19–30 (2014), doi:10.1016/j.arr.2014.01.004.
10. S. Fahn, Description of Parkinson's disease as a clinical syndrome. *Annals of the New York Academy of Sciences*. **991**, 1–14 (2003), doi:10.1111/j.1749-6632.2003.tb07458.x.
11. K. R. Chaudhuri, D. G. Healy, A. H. V. Schapira, Non-motor symptoms of Parkinson's disease: diagnosis and management (2006), doi:10.1016/S1474-4422(06)70373-8.
12. R. L. Doty, Olfactory dysfunction in Parkinson disease. *Nature Reviews Neurology*. **8**, 329–339 (2012), doi:10.1038/nrneurol.2012.80.
13. R. Savica *et al.,* Medical records documentation of constipation preceding Parkinson disease: A case-control study. *Neurology*. **73**, 1752–1758 (2009), doi:10.1212/WNL.0b013e3181c34af5.
14. N. Ball, W.-P. Teo, S. Chandra, J. Chapman, Parkinson's Disease and the Environment. *Frontiers in Neurology*. **10**, 218 (2019), doi:10.3389/fneur.2019.00218.
15. C. Klein, A. Westenberger, Genetics of Parkinson's Disease. *Cold Spring Harbor perspectives in medicine*. **2** (2012), doi:10.1101/cshperspect.a008888.
16. M. Kasten *et al.,* Genotype-Phenotype Relations for the Parkinson's Disease Genes Parkin, PINK1, DJ1: MDSGene Systematic Review. *Movement disorders : official journal of the Movement Disorder Society*. **33**, 730–741 (2018), doi:10.1002/mds.27352.
17. H. Deng, P. Wang, J. Jankovic, The genetics of Parkinson disease. *Ageing research reviews*. **42**, 72–85 (2018), doi:10.1016/j.arr.2017.12.007.
18. L. Cook Shukla *et al.*, *GeneReviews®*, *Parkinson Disease Overview* (Seattle (WA), 1993).
19. C. B. Lücking *et al.,* Association between early-onset Parkinson's disease and mutations in the parkin gene. *The New England journal of medicine*. **342**, 1560–1567 (2000), doi:10.1056/NEJM200005253422103.

20. L. V. Kalia, A. E. Lang, Parkinson's disease. *The Lancet*. **386**, 896–912 (2015), doi:10.1016/S0140-6736(14)61393-3.
21. A. Ferraris *et al.,* Olfactory dysfunction in Parkinsonism caused by PINK1 mutations. *Movement disorders : official journal of the Movement Disorder Society*. **24**, 2350–2357 (2009), doi:10.1002/mds.22816.
22. L. Ricciardi *et al.,* Phenotypic variability of PINK1 expression. *Movement disorders : official journal of the Movement Disorder Society*. **29**, 1561–1566 (2014), doi:10.1002/mds.25994.
23. S. Song *et al.,* Characterization of PINK1 (PTEN-induced Putative Kinase 1) Mutations Associated with Parkinson Disease in Mammalian Cells and Drosophila*. *The Journal of biological chemistry*. **288**, 5660–5672 (2013), doi:10.1074/jbc.M112.430801.
24. A. M. Pickrell, R. J. Youle, The roles of PINK1, parkin, and mitochondrial fidelity in Parkinson's disease. *Neuron*. **85**, 257–273 (2015), doi:10.1016/j.neuron.2014.12.007.
25. T. Das Banerjee *et al.,* PINK1 regulates mitochondrial trafficking in dendrites of cortical neurons through mitochondrial PKA. *Journal of neurochemistry*. **142**, 545–559 (2017), doi:10.1111/jnc.14083.
26. L. Aerts, K. Craessaerts, B. de Strooper, V. A. Morais, PINK1 Kinase Catalytic Activity Is Regulated by Phosphorylation on Serines 228 and 402*. *The Journal of biological chemistry*. **290**, 2798–2811 (2015), doi:10.1074/jbc.M114.620906.
27. M. Lazarou, S. M. Jin, L. A. Kane, R. J. Youle, Role of PINK1 binding to the TOM complex and alternate intracellular membranes in recruitment and activation of the E3 ligase Parkin. *Developmental Cell*. **22**, 320–333 (2012), doi:10.1016/j.devcel.2011.12.014.
28. K. Okatsu *et al.,* A dimeric PINK1-containing complex on depolarized mitochondria stimulates Parkin recruitment. *The Journal of biological chemistry*. **288**, 36372–36384 (2013), doi:10.1074/jbc.M113.509653.
29. Y.-C. Lai *et al.,* Phosphoproteomic screening identifies Rab GTPases as novel downstream targets of PINK1. *The EMBO Journal*. **34**, 2840–2861 (2015), doi:10.15252/embj.201591593.
30. M. A. Nalls *et al.,* Identification of novel risk loci, causal insights, and heritable risk for Parkinson's disease: a meta-analysis of genome-wide association studies. *The Lancet Neurology*. **18**, 1091–1102 (2019), doi:10.1016/S1474-4422(19)30320-5.
31. T. M. Dawson, T. E. Golde, C. L. Tourenne, Animal Models of Neurodegenerative Diseases. *Nature neuroscience*. **21**, 1370–1379 (2018), doi:10.1038/s41593-018-0236-8.
32. J. W. Langston, The MPTP Story. *Journal of Parkinson's disease*. **7**, S11-9, doi:10.3233/JPD-179006.
33. Le Weidong, C. Shen, J. Jankovic, Etiopathogenesis of Parkinson disease: a new beginning? *The Neuroscientist : a review journal bringing neurobiology, neurology and psychiatry*. **15**, 28–35 (2009), doi:10.1177/1073858408319974.
34. B. Ritz, P.-C. Lee, C. F. Lassen, O. A. Arah, Parkinson disease and smoking revisited: ease of quitting is an early sign of the disease. *Neurology*. **83**, 1396–1402 (2014), doi:10.1212/WNL.0000000000000879.
35. G. Hu, S. Bidel, P. Jousilahti, R. Antikainen, J. Tuomilehto, Coffee and tea consumption and the risk of Parkinson's disease. *Movement disorders : official journal of the Movement Disorder Society*. **22** (2007), doi:10.1002/mds.21706.
36. N. Palacios *et al.,* Caffeine and risk of Parkinson's disease in a large cohort of men and women. *Movement disorders : official journal of the Movement Disorder Society*. **27**, 1276–1282 (2012), doi:10.1002/mds.25076.
37. C. S. von Bartheld, J. Bahney, S. Herculano-Houzel, The search for true numbers of neurons and glial cells in the human brain: A review of 150 years of cell counting. *The Journal of comparative neurology*. **524**, 3865–3895 (2016), doi:10.1002/cne.24040.
38. K. L. Leenders *et al.,* The nigrostriatal dopaminergic system assessed in vivo by positron emission tomography in healthy volunteer subjects and patients with Parkinson's disease. *Archives of neurology*. **47**, 1290–1298 (1990), doi:10.1001/archneur.1990.00530120034007.
39. G. E. Alexander, M. D. Crutcher, M. R. DeLong, Basal ganglia-thalamocortical circuits: parallel substrates for motor, oculomotor, "prefrontal" and "limbic" functions. *Progress in brain research*. **85**, 119–146 (1990).

40. A. A. Kühn *et al.,* High-frequency stimulation of the subthalamic nucleus suppresses oscillatory beta activity in patients with Parkinson's disease in parallel with improvement in motor performance. *The Journal of neuroscience : the official journal of the Society for Neuroscience*. **28**, 6165–6173 (2008), doi:10.1523/JNEUROSCI.0282-08.2008.

41. N. Giguère, S. Burke Nanni, L.-E. Trudeau, On Cell Loss and Selective Vulnerability of Neuronal Populations in Parkinson's Disease. *Frontiers in Neurology*. **9** (2018), doi:10.3389/fneur.2018.00455.

42. S.-J. Lee, H.-S. Lim, E. Masliah, H.-J. Lee, Protein aggregate spreading in neurodegenerative diseases: Problems and perspectives. *Neuroscience research*. **70**, 339–348 (2011), doi:10.1016/j.neures.2011.05.008.

43. W. S. Kim, K. Kågedal, G. M. Halliday, Alpha-synuclein biology in Lewy body diseases. *Alzheimer's Research & Therapy*. **6**, 73 (2014), doi:10.1186/s13195-014-0073-2.

44. H. Braak *et al.,* Staging of brain pathology related to sporadic Parkinson's disease. *Neurobiology of Aging*. **24**, 197–211 (2003), doi:10.1016/S0197-4580(02)00065-9.

45. E. Angot *et al.,* Alpha-synuclein cell-to-cell transfer and seeding in grafted dopaminergic neurons in vivo. *PloS one*. **7**, e39465 (2012), doi:10.1371/journal.pone.0039465.

46. N. P. Visanji, P. L. Brooks, L.-N. Hazrati, A. E. Lang, The prion hypothesis in Parkinson's disease: Braak to the future. *Acta neuropathologica communications*. **1**, 2 (2013), doi:10.1186/2051-5960-1-2.

47. R. M. Ransohoff, How neuroinflammation contributes to neurodegeneration. *Science (New York, N.Y.)*. **353**, 777–783 (2016), doi:10.1126/science.aag2590.

48. A. Fani Maleki, S. Rivest, Innate Immune Cells: Monocytes, Monocyte-Derived Macrophages and Microglia as Therapeutic Targets for Alzheimer's Disease and Multiple Sclerosis. *Frontiers in cellular neuroscience*. **13** (2019), doi:10.3389/fncel.2019.00355.

49. F. L. Evans, M. Dittmer, A. G. de La Fuente, D. C. Fitzgerald, Protective and Regenerative Roles of T Cells in Central Nervous System Disorders. *Frontiers in Immunology*. **10** (2019), doi:10.3389/fimmu.2019.02171.

50. K. Li, J. Li, J. Zheng, S. Qin, Reactive Astrocytes in Neurodegenerative Diseases. *Aging and disease*. **10**, 664–675 (2019), doi:10.14336/AD.2018.0720.

51. P. L. McGeer, S. Itagaki, B. E. Boyes, E. G. McGeer, Reactive microglia are positive for HLA-DR in the substantia nigra of Parkinson's and Alzheimer's disease brains. *Neurology*. **38**, 1285–1291 (1988), doi:10.1212/wnl.38.8.1285.

52. N. J. Maragakis, J. D. Rothstein, Mechanisms of Disease: astrocytes in neurodegenerative disease. *Nature clinical practice. Neurology*. **2**, 679–689 (2006), doi:10.1038/ncpneuro0355.

53. J. P. Bolam, E. K. Pissadaki, Living on the edge with too many mouths to feed: why dopamine neurons die. *Movement disorders : official journal of the Movement Disorder Society*. **27**, 1478–1483 (2012), doi:10.1002/mds.25135.

54. D. J. Surmeier, J. A. Obeso, G. M. Halliday, Selective neuronal vulnerability in Parkinson disease. *Nature reviews. Neuroscience*. **18**, 101–113 (2017), doi:10.1038/nrn.2016.178.

55. P. Muñoz, S. Huenchuguala, I. Paris, J. Segura-Aguilar, Dopamine Oxidation and Autophagy. *Parkinson's Disease*. **2012** (2012), doi:10.1155/2012/920953.

56. J. Segura-Aguilar, I. Paris, in *Handbook of Neurotoxicity*, R. M. Kostrzewa, Ed. (Springer New York; Imprint; Springer, New York, NY, 2014), pp. 865–883.

57. J. Segura-Aguilar, D. Metodiewa, S. Baez, The possible role of one-electron reduction of aminochrome in the neurodegenerative process of the dopaminergic system. *Neurotoxicity research*. **3** (2001), doi:10.1007/BF03033188.

58. V. Dias, E. Junn, M. M. Mouradian, The Role of Oxidative Stress in Parkinson's Disease. *Journal of Parkinson's disease*. **3**, 461–491 (2013), doi:10.3233/JPD-130230.

59. B. G. Trist, D. J. Hare, K. L. Double, Oxidative stress in the aging substantia nigra and the etiology of Parkinson's disease. *Aging Cell*. **18** (2019), doi:10.1111/acel.13031.

60. N. S. Fedarko, The Biology of Aging and Frailty. *Clinics in geriatric medicine*. **27**, 27–37 (2011), doi:10.1016/j.cger.2010.08.006.

5. References

61. C. López-Otín, M. A. Blasco, L. Partridge, M. Serrano, G. Kroemer, The hallmarks of aging. *Cell*. **153**, 1194–1217 (2013), doi:10.1016/j.cell.2013.05.039.

62. T. C. Goldsmith, Evolution of Aging Theories: Why Modern Programmed Aging Concepts Are Transforming Medical Research. *Biochemistry. Biokhimiia*. **81**, 1406–1412 (2016), doi:10.1134/S0006297916120026.

63. T. Flatt, L. Partridge, Horizons in the evolution of aging. *BMC Biology*. **16** (2018), doi:10.1186/s12915-018-0562-z.

64. K. Jin, Modern Biological Theories of Aging. *Aging and disease*. **1**, 72–74 (2010).

65. S. Maynard, E. F. Fang, M. Scheibye-Knudsen, D. L. Croteau, V. A. Bohr, DNA Damage, DNA Repair, Aging, and Neurodegeneration. *Cold Spring Harbor perspectives in medicine*. **5** (2015), doi:10.1101/cshperspect.a025130.

66. D. E. Handy, R. Castro, J. Loscalzo, Epigenetic Modifications: Basic Mechanisms and Role in Cardiovascular Disease. *Circulation*. **123**, 2145–2156 (2011), doi:10.1161/CIRCULATIONAHA.110.956839.

67. E. Grazioli *et al.,* Physical activity in the prevention of human diseases: role of epigenetic modifications. *BMC Genomics*. **18** (2017), doi:10.1186/s12864-017-4193-5.

68. X. Wu *et al.,* Effect of tobacco smoking on the epigenetic age of human respiratory organs. *Clinical epigenetics*. **11**, 183 (2019), doi:10.1186/s13148-019-0777-z.

69. C. Pagiatakis, E. Musolino, R. Gornati, G. Bernardini, R. Papait, Epigenetics of aging and disease: a brief overview. *Aging clinical and experimental research* (2019), doi:10.1007/s40520-019-01430-0.

70. G. Almouzni, H. Cedar, Maintenance of Epigenetic Information. *Cold Spring Harbor Perspectives in Biology*. **8** (2016), doi:10.1101/cshperspect.a019372.

71. A. Bird, DNA methylation patterns and epigenetic memory. *Genes & development*. **16**, 6–21 (2002), doi:10.1101/gad.947102.

72. E. S. Lander *et al.,* Initial sequencing and analysis of the human genome. *Nature*. **409**, 860–921 (2001), doi:10.1038/35057062.

73. Y. Luo, X. Lu, H. Xie, Dynamic Alu methylation during normal development, aging, and tumorigenesis. *BioMed research international*. **2014**, 784706 (2014), doi:10.1155/2014/784706.

74. R. Lister, J. R. Ecker, Finding the fifth base: Genome-wide sequencing of cytosine methylation. *Genome Research*. **19**, 959–966 (2009), doi:10.1101/gr.083451.108.

75. A. M. Deaton, A. Bird, CpG islands and the regulation of transcription. *Genes & development*. **25**, 1010–1022 (2011), doi:10.1101/gad.2037511.

76. E. Louie, J. Ott, J. Majewski, Nucleotide frequency variation across human genes. *Genome Research*. **13**, 2594–2601 (2003), doi:10.1101/gr.1317703.

77. J. R. Edwards, O. Yarychkivska, M. Boulard, T. H. Bestor, DNA methylation and DNA methyltransferases. *Epigenetics & chromatin*. **10**, 23 (2017), doi:10.1186/s13072-017-0130-8.

78. C. Jiang, Z. Zhao, Mutational spectrum in the recent human genome inferred by single nucleotide polymorphisms. *Genomics*. **88**, 527–534 (2006), doi:10.1016/j.ygeno.2006.06.003.

79. M. W. Simmen, Genome-scale relationships between cytosine methylation and dinucleotide abundances in animals. *Genomics*. **92**, 33–40 (2008), doi:10.1016/j.ygeno.2008.03.009.

80. M. M. Suzuki, A. Bird, DNA methylation landscapes: provocative insights from epigenomics. *Nature reviews. Genetics*. **9**, 465–476 (2008), doi:10.1038/nrg2341.

81. L. Wen, F. Tang, Genomic distribution and possible functions of DNA hydroxymethylation in the brain. *Genomics*. **104**, 341–346 (2014), doi:10.1016/j.ygeno.2014.08.020.

82. L. Arcesi, P. G. La, A. Perico, Generalized electrostatic model of the wrapping of DNA around oppositely charged proteins. *Biopolymers*. **86** (2007), doi:10.1002/bip.20711.

83. A. Cutter, J. J. Hayes, A Brief Review of Nucleosome Structure. *FEBS letters*. **589**, 2914–2922 (2015), doi:10.1016/j.febslet.2015.05.016.

84. A. J. Bannister, T. Kouzarides, Regulation of chromatin by histone modifications. *Cell research*. **21**, 381–395 (2011), doi:10.1038/cr.2011.22.

85. J.-H. Lee, E. W. Kim, D. L. Croteau, V. A. Bohr, Heterochromatin: an epigenetic point of view in aging. *Experimental & molecular medicine* (2020), doi:10.1038/s12276-020-00497-4.

86. P. B. Singh, S. N. Belyakin, P. P. Laktionov, Biology and Physics of Heterochromatin-Like Domains/Complexes. *Cells*. **9** (2020), doi:10.3390/cells9081881.

87. J. Liu, M. Ali, Q. Zhou, Establishment and evolution of heterochromatin. *Annals of the New York Academy of Sciences* (2020), doi:10.1111/nyas.14303.

88. H. Kimura, Histone modifications for human epigenome analysis. *Journal of human genetics*. **58**, 439–445 (2013), doi:10.1038/jhg.2013.66.

89. A. T. Nguyen, Y. Zhang, The diverse functions of Dot1 and H3K79 methylation. *Genes & development*. **25**, 1345–1358 (2011), doi:10.1101/gad.2057811.

90. M. F. Fraga, M. Esteller, Epigenetics and aging: the targets and the marks. *Trends in genetics : TIG*. **23** (2007), doi:10.1016/j.tig.2007.05.008.

91. S. Han, A. Brunet, Histone methylation makes its mark on longevity. *Trends in cell biology*. **22**, 42–49 (2012), doi:10.1016/j.tcb.2011.11.001.

92. A. P. Siebold *et al.,* Polycomb Repressive Complex 2 and Trithorax modulate Drosophila longevity and stress resistance. *Proceedings of the National Academy of Sciences of the United States of America*. **107**, 169–174 (2010), doi:10.1073/pnas.0907739107.

93. C. Jin *et al.,* Histone demethylase UTX-1 regulates C. elegans life span by targeting the insulin/IGF-1 signaling pathway. *Cell metabolism*. **14** (2011), doi:10.1016/j.cmet.2011.07.001.

94. E. L. Greer *et al.,* Members of the H3K4 trimethylation complex regulate lifespan in a germline-dependent manner in C. elegans. *Nature*. **466**, 383–387 (2010), doi:10.1038/nature09195.

95. M. Jung, G. P. Pfeifer, Aging and DNA methylation. *BMC Biology*. **13** (2015), doi:10.1186/s12915-015-0118-4.

96. S. Horvath, DNA methylation age of human tissues and cell types. *Genome biology*. **14**, R115 (2013), doi:10.1186/gb-2013-14-10-r115.

97. A. A. Moskalev *et al.,* The role of DNA damage and repair in aging through the prism of Koch-like criteria. *Ageing research reviews*. **12**, 661–684 (2013), doi:10.1016/j.arr.2012.02.001.

98. J. H. J. Hoeijmakers, DNA damage, aging, and cancer. *The New England journal of medicine*. **361**, 1475–1485 (2009), doi:10.1056/NEJMra0804615.

99. M. A. Petr, T. Tulika, L. M. Carmona-Marin, M. Scheibye-Knudsen, Protecting the Aging Genome. *Trends in cell biology*. **30**, 117–132 (2020), doi:10.1016/j.tcb.2019.12.001.

100. R. Ren, A. Ocampo, G.-H. Liu, J. C. Izpisua Belmonte, Regulation of Stem Cell Aging by Metabolism and Epigenetics. *Cell metabolism*. **26**, 460–474 (2017), doi:10.1016/j.cmet.2017.07.019.

101. A. M. Fleming, C. J. Burrows, 8-Oxo-7,8-dihydroguanine, friend and foe: Epigenetic-like regulator versus initiator of mutagenesis. *DNA repair*. **56**, 75–83 (2017), doi:10.1016/j.dnarep.2017.06.009.

102. H. E. Krokan, M. Bjørås, Base Excision Repair. *Cold Spring Harbor Perspectives in Biology*. **5** (2013), doi:10.1101/cshperspect.a012583.

103. J. M. Pascal, The comings and goings of PARP-1 in response to DNA damage. *DNA repair*. **71**, 177–182 (2018), doi:10.1016/j.dnarep.2018.08.022.

104. R. de Leeuw, Y. Gruenbaum, O. Medalia, Nuclear Lamins: Thin Filaments with Major Functions. *Trends in cell biology*. **28**, 34–45 (2018), doi:10.1016/j.tcb.2017.08.004.

105. T. Shimi *et al.,* Structural organization of nuclear lamins A, C, B1, and B2 revealed by superresolution microscopy. *Molecular biology of the cell*. **26**, 4075–4086 (2015), doi:10.1091/mbc.E15-07-0461.

106. W. Xie *et al.,* A-type Lamins Form Distinct Filamentous Networks with Differential Nuclear Pore Complex Associations. *Current biology : CB*. **26**, 2651–2658 (2016), doi:10.1016/j.cub.2016.07.049.

107. T. Shimi *et al.,* The role of nuclear lamin B1 in cell proliferation and senescence. *Genes & development*. **25**, 2579–2593 (2011), doi:10.1101/gad.179515.111.

108. K. L. Wilson, R. Foisner, Lamin-binding Proteins. *Cold Spring Harbor Perspectives in Biology*. **2** (2010), doi:10.1101/cshperspect.a000554.

109. D. Dorner *et al.,* Lamina-associated polypeptide 2alpha regulates cell cycle progression and differentiation via the retinoblastoma-E2F pathway. *The Journal of cell biology*. **173**, 83–93 (2006), doi:10.1083/jcb.200511149.

110. Y. Y. Shevelyov, S. V. Ulianov, The Nuclear Lamina as an Organizer of Chromosome Architecture. *Cells*. **8** (2019), doi:10.3390/cells8020136.

111. T. Dechat, S. A. Adam, P. Taimen, T. Shimi, R. D. Goldman, Nuclear Lamins. *Cold Spring Harbor Perspectives in Biology*. **2** (2010), doi:10.1101/cshperspect.a000547.

112. J. Ahringer, S. M. Gasser, Repressive Chromatin in Caenorhabditis elegans: Establishment, Composition, and Function. *Genetics*. **208**, 491–511 (2018), doi:10.1534/genetics.117.300386.

113. M. Prokocimer *et al.,* Nuclear lamins: key regulators of nuclear structure and activities. *Journal of cellular and molecular medicine*. **13**, 1059–1085 (2009), doi:10.1111/j.1582-4934.2008.00676.x.

114. M. X. R. Foo, P. F. Ong, O. Dreesen, Premature aging syndromes: From patients to mechanism. *Journal of dermatological science*. **96**, 58–65 (2019), doi:10.1016/j.jdermsci.2019.10.003.

115. S. Vidak, N. Kubben, T. Dechat, R. Foisner, Proliferation of progeria cells is enhanced by lamina-associated polypeptide 2α (LAP2α) through expression of extracellular matrix proteins. *Genes & development*. **29**, 2022–2036 (2015), doi:10.1101/gad.263939.115.

116. N. Naetar, S. Ferraioli, R. Foisner, Lamins in the nuclear interior - life outside the lamina. *Journal of cell science*. **130**, 2087–2096 (2017), doi:10.1242/jcs.203430.

117. K. Cao *et al.,* Progerin and telomere dysfunction collaborate to trigger cellular senescence in normal human fibroblasts. *J Clin Invest*. **121**, 2833–2844 (2011), doi:10.1172/JCI43578.

118. A. Freund, R.-M. Laberge, M. Demaria, J. Campisi, Lamin B1 loss is a senescence-associated biomarker. *Molecular biology of the cell*. **23**, 2066–2075 (2012), doi:10.1091/mbc.E11-10-0884.

119. G. Hewitt *et al.,* Telomeres are favoured targets of a persistent DNA damage response in ageing and stress-induced senescence. *Nature communications*. **3**, 708 (2012), doi:10.1038/ncomms1708.

120. A. Sfeir, Telomeres at a glance. *Journal of cell science*. **125**, 4173–4178 (2012), doi:10.1242/jcs.106831.

121. S. M. Mir *et al.,* Shelterin Complex at Telomeres: Implications in Ageing. *Clinical interventions in aging*. **15**, 827–839 (2020), doi:10.2147/CIA.S256425.

122. M. Fumagalli *et al.,* Telomeric DNA damage is irreparable and causes persistent DNA-damage-response activation. *Nature cell biology*. **14**, 355–365 (2012), doi:10.1038/ncb2466.

123. A. Smogorzewska, T. de Lange, Regulation of telomerase by telomeric proteins. *Annual review of biochemistry*. **73**, 177–208 (2004), doi:10.1146/annurev.biochem.73.071403.160049.

124. J. W. Shay, W. E. Wright, Hayflick, his limit, and cellular ageing. *Nature reviews. Molecular cell biology*. **1**, 72–76 (2000), doi:10.1038/35036093.

125. E. Hiyama, K. Hiyama, Telomere and telomerase in stem cells. *British Journal of Cancer*. **96**, 1020–1024 (2007), doi:10.1038/sj.bjc.6603671.

126. R. A. Wu, H. E. Upton, J. M. Vogan, K. Collins, Telomerase Mechanism of Telomere Synthesis. *Annual review of biochemistry*. **86**, 439–460 (2017), doi:10.1146/annurev-biochem-061516-045019.

127. D. Tsoukalas *et al.,* Association of nutraceutical supplements with longer telomere length. *International journal of molecular medicine*. **44**, 218–226 (2019), doi:10.3892/ijmm.2019.4191.

128. K. Whittemore, E. Vera, Martínez-Nevado Eva, Sanpera Carola, A. Blasco Maria, Telomere shortening rate predicts species life span. *PNAS*. **116**, 15122–15127 (2019), doi:10.1073/pnas.1902452116.

129. J. Bhattacharyya, K. Mihara, D. Bhattacharjee, M. Mukherjee, Telomere length as a potential biomarker of coronary artery disease. *The Indian Journal of Medical Research*. **145**, 730–737 (2017), doi:10.4103/0971-5916.216974.

130. H. Xi, C. Li, F. Ren, H. Zhang, L. Zhang, Telomere, aging and age-related diseases. *Aging clinical and experimental research*. **25**, 139–146 (2013), doi:10.1007/s40520-013-0021-1.

131. S. Reichert, A. Stier, Does oxidative stress shorten telomeres in vivo? A review. *Biology letters*. **13** (2017), doi:10.1098/rsbl.2017.0463.

132. M. A. Shammas, Telomeres, lifestyle, cancer, and aging. *Current Opinion in Clinical Nutrition and Metabolic Care*. **14**, 28–34 (2011), doi:10.1097/MCO.0b013e32834121b1.

133. K.-I. Tomita *et al.,* Changes in telomere length with aging in human neurons and glial cells revealed by quantitative fluorescence in situ hybridization analysis. *Geriatrics & gerontology international*. **18**, 1507–1512 (2018), doi:10.1111/ggi.13500.

134. J. M. Berg, J. L. Tymoczko, L. Stryer, Eds., *Biochemistry. 5th edition* (W H Freeman, 2002).

135. P. Mergenthaler, U. Lindauer, G. A. Dienel, A. Meisel, Sugar for the brain: the role of glucose in physiological and pathological brain function. *Trends in neurosciences*. **36**, 587–597 (2013), doi:10.1016/j.tins.2013.07.001.

136. D. L. Nelson, M. M. Cox, B. on, *Lehninger principles of biochemistry* (W.H. Freeman and Company, New York, 2013).

137. P. E. Porporato, S. Dhup, R. K. Dadhich, T. Copetti, P. Sonveaux, Anticancer targets in the glycolytic metabolism of tumors: a comprehensive review. *Frontiers in pharmacology*. **2**, 49 (2011), doi:10.3389/fphar.2011.00049.

138. C. Granchi, S. Bertini, M. Macchia, F. Minutolo, Inhibitors of lactate dehydrogenase isoforms and their therapeutic potentials. *Current medicinal chemistry*. **17**, 672–697 (2010), doi:10.2174/092986710790416263.

139. H. Lodish *et al.*, *Molecular cell biology* (W.H. Freeman Macmillan Learning, New York, 2016).

140. A. R. D'Souza, M. Minczuk, Mitochondrial transcription and translation: overview. *Essays in Biochemistry*. **62**, 309–320 (2018), doi:10.1042/EBC20170102.

141. F. Fontanesi, in *Encyclopedia of life sciences*, J. W. &. S. Ltd, Ed. (Nature Pub. Group; Wiley, London, New York, Vols. 21-32, Chichester, West Sussex, U.K., 2002-2010), pp. 1–13.

142. M. W. Gray, Mitochondrial Evolution. *Cold Spring Harbor Perspectives in Biology*. **4** (2012), doi:10.1101/cshperspect.a011403.

143. C. Perier, M. Vila, Mitochondrial biology and Parkinson's disease. *Cold Spring Harbor perspectives in medicine*. **2** (2012), doi:10.1101/cshperspect.a009332.

144. A. M. van der Bliek, Q. Shen, S. Kawajiri, Mechanisms of Mitochondrial Fission and Fusion. *Cold Spring Harbor Perspectives in Biology*. **5** (2013), doi:10.1101/cshperspect.a011072.

145. B. Westermann, Bioenergetic role of mitochondrial fusion and fission. *Biochimica et Biophysica Acta (BBA) - Bioenergetics*. **1817**, 1833–1838 (2012), doi:10.1016/j.bbabio.2012.02.033.

146. R. J. Youle, A. M. van der Bliek, Mitochondrial fission, fusion, and stress. *Science (New York, N.Y.)*. **337**, 1062–1065 (2012), doi:10.1126/science.1219855.

147. D. Safiulina, A. Kaasik, Energetic and dynamic: how mitochondria meet neuronal energy demands. *PLoS biology*. **11**, e1001755 (2013), doi:10.1371/journal.pbio.1001755.

148. Z. Li, K.-I. Okamoto, Y. Hayashi, M. Sheng, The importance of dendritic mitochondria in the morphogenesis and plasticity of spines and synapses. *Cell*. **119**, 873–887 (2004), doi:10.1016/j.cell.2004.11.003.

149. Z.-H. Sheng, Q. Cai, Mitochondrial transport in neurons: impact on synaptic homeostasis and neurodegeneration. *Nature reviews. Neuroscience*. **13**, 77–93 (2012), doi:10.1038/nrn3156.

150. D. M. Arduíno, A. R. Esteves, S. M. Cardoso, Mitochondrial Fusion/Fission, Transport and Autophagy in Parkinson's Disease: When Mitochondria Get Nasty. *Parkinson's Disease*. **2011** (2011), doi:10.4061/2011/767230.

151. M. D. Brand, A. L. Orr, I. V. Perevoshchikova, C. L. Quinlan, The role of mitochondrial function and cellular bioenergetics in ageing and disease. *The British journal of dermatology*. **169**, 1–8 (2013), doi:10.1111/bjd.12208.

152. M. P. Murphy, How mitochondria produce reactive oxygen species. *Biochemical Journal*. **417**, 1–13 (2008), doi:10.1042/BJ20081386.

153. G. Karamanlidis *et al.,* Mitochondrial Complex I Deficiency Increases Protein Acetylation and Accelerates Heart Failure. *Cell metabolism*. **18**, 239–250 (2013), doi:10.1016/j.cmet.2013.07.002.

154. D. Harmon, Aging: a theory based on free radical and radiation chemistry. *Journal of gerontology*. **11**, 298–300 (1956), doi:10.1093/geronj/11.3.298.

155. M. A. Birch-Machin, A. Bowman, Oxidative stress and ageing. *The British journal of dermatology*. **175 Suppl 2**, 26–29 (2016), doi:10.1111/bjd.14906.

156. A. S. Tan *et al.,* Mitochondrial genome acquisition restores respiratory function and tumorigenic potential of cancer cells without mitochondrial DNA. *Cell metabolism*. **21**, 81–94 (2015), doi:10.1016/j.cmet.2014.12.003.

157. C. Guo, L. Sun, X. Chen, D. Zhang, Oxidative stress, mitochondrial damage and neurodegenerative diseases. *Neural Regeneration Research*. **8**, 2003–2014 (2013), doi:10.3969/j.issn.1673-5374.2013.21.009.

158. A. B. Salmon, A. Richardson, V. I. Pérez, Update on the oxidative stress theory of aging: Does oxidative stress play a role in aging or healthy aging? *Free radical biology & medicine*. **48**, 642 (2009), doi:10.1016/j.freeradbiomed.2009.12.015.

159. J. M. van Raamsdonk, S. Hekimi, Deletion of the mitochondrial superoxide dismutase sod-2 extends lifespan in Caenorhabditis elegans. *PLoS genetics*. **5**, e1000361 (2009), doi:10.1371/journal.pgen.1000361.

160. A. Mesquita *et al.,* Caloric restriction or catalase inactivation extends yeast chronological lifespan by inducing H2O2 and superoxide dismutase activity. *Proceedings of the National Academy of Sciences of the United States of America*. **107**, 15123–15128 (2010), doi:10.1073/pnas.1004432107.

161. M. Rango, N. Bresolin, Brain Mitochondria, Aging, and Parkinson's Disease. *Genes*. **9** (2018), doi:10.3390/genes9050250.

162. J. W. Langston, P. Ballard, J. W. Tetrud, I. Irwin, Chronic Parkinsonism in humans due to a product of meperidine-analog synthesis. *Science (New York, N.Y.)*. **219**, 979–980 (1983), doi:10.1126/science.6823561.

163. C. Berry, C. La Vecchia, P. Nicotera, Paraquat and Parkinson's disease. *Cell death and differentiation*. **17**, 1115–1125 (2010), doi:10.1038/cdd.2009.217.

164. X.-S. Zeng, W.-S. Geng, J.-J. Jia, Neurotoxin-Induced Animal Models of Parkinson Disease: Pathogenic Mechanism and Assessment. *ASN neuro*. **10**, 1759091418777438 (2018), doi:10.1177/1759091418777438.

165. I. H. Flønes *et al.,* Neuronal complex I deficiency occurs throughout the Parkinson's disease brain, but is not associated with neurodegeneration or mitochondrial DNA damage. *Acta neuropathologica*. **135**, 409–425 (2018), doi:10.1007/s00401-017-1794-7.

166. N. Exner, A. K. Lutz, C. Haass, K. F. Winklhofer, Mitochondrial dysfunction in Parkinson's disease: molecular mechanisms and pathophysiological consequences. *The EMBO Journal*. **31**, 3038–3062 (2012), doi:10.1038/emboj.2012.170.

167. R. Banerjee, A. A. Starkov, M. F. Beal, B. Thomas, Mitochondrial dysfunction in the limelight of Parkinson's disease pathogenesis. *Biochimica et biophysica acta*. **1792**, 651–663 (2008), doi:10.1016/j.bbadis.2008.11.007.

168. R. Vartak, J. Deng, H. Fang, Y. Bai, Redefining the roles of mitochondrial DNA-encoded subunits in respiratory Complex I assembly. *Biochimica et biophysica acta*. **1852**, 1531–1539 (2015), doi:10.1016/j.bbadis.2015.04.008.

169. A. Bender *et al.,* High levels of mitochondrial DNA deletions in substantia nigra neurons in aging and Parkinson disease. *Nature genetics*. **38** (2006), doi:10.1038/ng1769.

170. B. Zheng *et al.,* PGC-1α, A Potential Therapeutic Target for Early Intervention in Parkinson's Disease. *Science translational medicine*. **2**, 52ra73 (2010), doi:10.1126/scitranslmed.3001059.

171. H. Chen *et al.,* Reductions in the mitochondrial enzyme α-ketoglutarate dehydrogenase complex in neurodegenerative disease - beneficial or detrimental? *Journal of neurochemistry*. **139**, 823–838 (2016), doi:10.1111/jnc.13836.

172. M. J. Kumar, D. G. Nicholls, J. K. Andersen, Oxidative alpha-ketoglutarate dehydrogenase inhibition via subtle elevations in monoamine oxidase B levels results in loss of spare respiratory capacity: implications for Parkinson's disease. *The Journal of biological chemistry*. **278**, 46432–46439 (2003), doi:10.1074/jbc.M306378200.

173. H. E. Moon, S. H. Paek, Mitochondrial Dysfunction in Parkinson's Disease. *Experimental Neurobiology*. **24**, 103–116 (2015), doi:10.5607/en.2015.24.2.103.

174. M. A. P. Oliveira, R. Balling, M. P. Smidt, R. M. T. Fleming, Embryonic development of selectively vulnerable neurons in Parkinson's disease. *NPJ Parkinson's disease*. **3**, 21 (2017), doi:10.1038/s41531-017-0022-4.

175. E. Arenas, M. Denham, J. C. Villaescusa, How to make a midbrain dopaminergic neuron. *Development (Cambridge, England)*. **142**, 1918–1936 (2015), doi:10.1242/dev.097394.

176. V. Broccoli, E. Boncinelli, W. Wurst, The caudal limit of Otx2 expression positions the isthmic organizer. *Nature*. **401**, 164–168 (1999), doi:10.1038/43670.

177. S. Millet *et al.,* A role for Gbx2 in repression of Otx2 and positioning the mid/hindbrain organizer. *Nature*. **401**, 161–164 (1999), doi:10.1038/43664.

178. Q. Deng *et al.,* Specific and integrated roles of Lmx1a, Lmx1b and Phox2a in ventral midbrain development. *Development (Cambridge, England)*. **138**, 3399–3408 (2011), doi:10.1242/dev.065482.

179. M. P. Smidt *et al.,* A second independent pathway for development of mesencephalic dopaminergic neurons requires Lmx1b. *Nature neuroscience*. **3**, 337–341 (2000), doi:10.1038/73902.

180. M. Götz, Y.-A. Barde, Radial glial cells defined and major intermediates between embryonic stem cells and CNS neurons. *Neuron*. **46**, 369–372 (2005), doi:10.1016/j.neuron.2005.04.012.

181. M. Götz, W. B. Huttner, The cell biology of neurogenesis. *Nature reviews. Molecular cell biology*. **6**, 777–788 (2005), doi:10.1038/nrm1739.

182. V. Martínez-Cerdeño, S. C. Noctor, Neural Progenitor Cell Terminology. *Frontiers in Neuroanatomy*. **12** (2018), doi:10.3389/fnana.2018.00104.

183. J. A. Cooper, Molecules and mechanisms that regulate multipolar migration in the intermediate zone. *Frontiers in cellular neuroscience*. **8**, 386 (2014), doi:10.3389/fncel.2014.00386.

184. K. N. Alavian *et al.,* The lifelong maintenance of mesencephalic dopaminergic neurons by Nurr1 and engrailed. *Journal of biomedical science*. **21**, 27 (2014), doi:10.1186/1423-0127-21-27.

185. K. L. Tucker, T. Caspary, *Cilia and Nervous System Development and Function* (Springer, Dordrecht, 2013).

186. J. J. Malicki, C. A. Johnson, The Cilium: Cellular Antenna and Central Processing Unit. *Trends in cell biology*. **27**, 126–140 (2017), doi:10.1016/j.tcb.2016.08.002.

187. K. B. Schou, L. B. Pedersen, S. T. Christensen, Ins and outs of GPCR signaling in primary cilia. *EMBO reports*. **16**, 1099–1113 (2015), doi:10.15252/embr.201540530.

188. J. L. Rosenbaum, G. B. Witman, Intraflagellar transport. *Nature reviews. Molecular cell biology*. **3**, 813–825 (2002), doi:10.1038/nrm952.

189. D. K. Breslow, E. F. Koslover, F. Seydel, A. J. Spakowitz, M. V. Nachury, An in vitro assay for entry into cilia reveals unique properties of the soluble diffusion barrier. *The Journal of cell biology*. **203**, 129–147 (2013), doi:10.1083/jcb.201212024.

190. H. L. Kee *et al.,* A size-exclusion permeability barrier and nucleoporins characterize a ciliary pore complex that regulates transport into cilia. *Nature cell biology*. **14** (2012), doi:10.1038/ncb2450.

191. F. R. Garcia-Gonzalo, J. F. Reiter, Scoring a backstage pass: Mechanisms of ciliogenesis and ciliary access. *J Cell Biol*. **197**, 697–709 (2012), doi:10.1083/jcb.201111146.

192. J. Malicki, T. Avidor-Reiss, From the cytoplasm into the cilium: Bon voyage. *Organogenesis*. **10**, 138–157 (2014), doi:10.4161/org.29055.

193. B. Prevo, J. M. Scholey, E. J. Peterman, Intraflagellar Transport: Mechanisms of Motor Action, Cooperation and Cargo Delivery. *The FEBS journal*. **284**, 2905–2931 (2017), doi:10.1111/febs.14068.

194. H. Jin *et al.,* The conserved Bardet-Biedl Syndrome proteins assemble a coat that traffics membrane proteins to cilia. *Cell*. **141**, 1208–1219 (2010), doi:10.1016/j.cell.2010.05.015.

195. H. Jin, M. V. Nachury, The BBSome. *Current biology : CB*. **19**, R472-3 (2009), doi:10.1016/j.cub.2009.04.015.

196. H. Ishikawa, W. F. Marshall, Intraflagellar Transport and Ciliary Dynamics. *Cold Spring Harbor Perspectives in Biology*. **9** (2017), doi:10.1101/cshperspect.a021998.

197. F. Ye, A. R. Nager, M. V. Nachury, BBSome trains remove activated GPCRs from cilia by enabling passage through the transition zone. *The Journal of cell biology*. **217**, 1847–1868 (2018), doi:10.1083/jcb.201709041.

198. S. M. Park, H. J. Jang, J. H. Lee, Roles of Primary Cilia in the Developing Brain. *Frontiers in cellular neuroscience*. **13**, 218 (2019), doi:10.3389/fncel.2019.00218.

199. J. F. Reiter, M. R. Leroux, Genes and molecular pathways underpinning ciliopathies. *Nature reviews. Molecular cell biology*. **18**, 533–547 (2017), doi:10.1038/nrm.2017.60.

200. I. Izawa, H. Goto, K. Kasahara, M. Inagaki, Current topics of functional links between primary cilia and cell cycle. *Cilia*. **4**, 12 (2015), doi:10.1186/s13630-015-0021-1.

201. D. K. Breslow, A. J. Holland, Mechanism and regulation of centriole and cilium biogenesis. *Annual review of biochemistry*. **88**, 691–724 (2019), doi:10.1146/annurev-biochem-013118-111153.

202. H. Ishikawa, W. F. Marshall, Ciliogenesis: building the cell's antenna. *Nature reviews. Molecular cell biology*. **12**, 222–234 (2011), doi:10.1038/nrm3085.

203. D. Wloga, J. Gaertig, Post-translational modifications of microtubules. *Journal of cell science*. **123**, 3447–3455 (2010), doi:10.1242/jcs.063727.

204. M. Mirvis, K. A. Siemers, W. J. Nelson, T. P. Stearns, Primary cilium loss in mammalian cells occurs predominantly by whole-cilium shedding. *PLoS biology*. **17**, e3000381 (2019), doi:10.1371/journal.pbio.3000381.

205. G. Wheway, L. Nazlamova, J. T. Hancock, Signaling through the Primary Cilium. *Frontiers in Cell and Developmental Biology*. **6** (2018), doi:10.3389/fcell.2018.00008.

206. Z. Anvarian, K. Mykytyn, S. Mukhopadhyay, L. B. Pedersen, S. T. Christensen, Cellular signalling by primary cilia in development, organ function and disease. *Nature reviews. Nephrology*. **15**, 199–219 (2019), doi:10.1038/s41581-019-0116-9.

207. C.-C. Hui, S. Angers, Gli proteins in development and disease. *Annual review of cell and developmental biology*. **27**, 513–537 (2011), doi:10.1146/annurev-cellbio-092910-154048.

208. H. Sasaki, Y. Nishizaki, C. Hui, M. Nakafuku, H. Kondoh, Regulation of Gli2 and Gli3 activities by an amino-terminal repression domain. *Development (Cambridge, England)*. **126**, 3915–3924 (1999).

209. C. B. Bai, W. Auerbach, J. S. Lee, D. Stephen, A. L. Joyner, Gli2, but not Gli1, is required for initial Shh signaling and ectopic activation of the Shh pathway. *Development (Cambridge, England)*. **129**, 4753–4761 (2002).

210. J. Jacob, J. Briscoe, Gli proteins and the control of spinal-cord patterning. *EMBO reports*. **4**, 761–765 (2003), doi:10.1038/sj.embor.embor896.

211. A. P. McMahon, P. W. Ingham, C. J. Tabin, in *Current Topics in Developmental Biology*, G. P. Schatten, Ed. (Elsevier textbooks, s.l., ed. 1, 2002), vol. **53,** pp. 1–114.

212. E. Pak, R. A. Segal, Hedgehog Signal Transduction. *Developmental Cell*. **38**, 333–344 (2016), doi:10.1016/j.devcel.2016.07.026.

213. P. Niewiadomski *et al.,* Gli protein activity is controlled by multisite phosphorylation in vertebrate Hedgehog signaling. *Cell reports*. **6**, 168–181 (2014), doi:10.1016/j.celrep.2013.12.003.

214. P. Niewiadomski, A. Zhujiang, M. Youssef, J. A. Waschek, Interaction of PACAP with Sonic hedgehog reveals complex regulation of the hedgehog pathway by PKA. *Cellular signalling*. **25**, 2222–2230 (2013), doi:10.1016/j.cellsig.2013.07.012.

215. T. Kotani, Protein kinase A activity and Hedgehog signaling pathway. *Vitamins and hormones*. **88**, 273–291 (2012), doi:10.1016/B978-0-12-394622-5.00012-2.

216. E. W. Humke, K. V. Dorn, L. Milenkovic, M. P. Scott, R. Rohatgi, The output of Hedgehog signaling is controlled by the dynamic association between Suppressor of Fused and the Gli proteins. *Genes & development*. **24**, 670–682 (2010), doi:10.1101/gad.1902910.

217. J. Briscoe, P. P. Thérond, The mechanisms of Hedgehog signalling and its roles in development and disease. *Nature reviews. Molecular cell biology*. **14**, 416–429 (2013), doi:10.1038/nrm3598.

218. A. Boukhalfa, C. Miceli, Y. Ávalos, E. Morel, N. Dupont, Interplay between primary cilia, ubiquitin-proteasome system and autophagy. *Biochimie*. **166**, 286–292 (2019), doi:10.1016/j.biochi.2019.06.009.

219. Y. H. Youn, Y.-G. Han, Primary Cilia in Brain Development and Diseases. *The American journal of pathology*. **188**, 11–22 (2018), doi:10.1016/j.ajpath.2017.08.031.

220. J. Baranova *et al.,* Autism Spectrum Disorder: Signaling Pathways and Prospective Therapeutic Targets. *Cellular and molecular neurobiology* (2020), doi:10.1007/s10571-020-00882-7.

221. C.-Y. Chang *et al.,* Induced Pluripotent Stem Cell (iPSC)-Based Neurodegenerative Disease Models for Phenotype Recapitulation and Drug Screening. *Molecules (Basel, Switzerland)*. **25** (2020), doi:10.3390/molecules25082000.

222. D. A. Braun, F. Hildebrandt, Ciliopathies. *Cold Spring Harbor Perspectives in Biology*. **9** (2017), doi:10.1101/cshperspect.a028191.

223. E. Forsythe, P. L. Beales, Bardet–Biedl syndrome. *European Journal of Human Genetics*. **21**, 8–13 (2013), doi:10.1038/ejhg.2012.115.

224. S. Seo *et al.,* BBS6, BBS10, and BBS12 form a complex with CCT/TRiC family chaperonins and mediate BBSome assembly. *Proceedings of the National Academy of Sciences of the United States of America*. **107**, 1488–1493 (2010), doi:10.1073/pnas.0910268107.

225. S. K. Singh, M. Gui, F. Koh, M. C. Yip, A. Brown, Structure and activation mechanism of the BBSome membrane protein trafficking complex. *eLife*. **9** (2020), doi:10.7554/eLife.53322.

226. N. F. Berbari, J. S. Lewis, G. A. Bishop, C. C. Askwith, K. Mykytyn, Bardet-Biedl syndrome proteins are required for the localization of G protein-coupled receptors to primary cilia. *Proceedings of the National Academy of Sciences of the United States of America*. **105**, 4242–4246 (2008), doi:10.1073/pnas.0711027105.

227. T. B. Stoker, J. C. Greenland, Eds., *Parkinson's disease*, *Pathogenesis and clinical aspects* (Codon Publications, Brisbane, Australia, December 2018).

228. B. H. Falkenburger, T. Saridaki, E. Dinter, Cellular models for Parkinson's disease. *Journal of neurochemistry*. **139 Suppl 1**, 121–130 (2016), doi:10.1111/jnc.13618.

229. K. Takahashi *et al.,* Induction of pluripotent stem cells from adult human fibroblasts by defined factors. *Cell*. **131**, 861–872 (2007), doi:10.1016/j.cell.2007.11.019.

230. E.-A. Chang, S.-W. Jin, M.-H. Nam, S.-D. Kim, Human Induced Pluripotent Stem Cells : Clinical Significance and Applications in Neurologic Diseases. *Journal of Korean Neurosurgical Society*. **62**, 493–501 (2019), doi:10.3340/jkns.2018.0222.

231. K. Simmnacher, J. Lanfer, T. Rizo, J. Kaindl, B. Winner, Modeling Cell-Cell Interactions in Parkinson's Disease Using Human Stem Cell-Based Models. *Frontiers in cellular neuroscience*. **13**, 571 (2019), doi:10.3389/fncel.2019.00571.

232. X. Hu *et al.,* Modeling Parkinson's Disease Using Induced Pluripotent Stem Cells. *Stem cells international*. **2020**, 1061470 (2020), doi:10.1155/2020/1061470.

233. M. Ke, C.-M. Chong, H. Su, Using induced pluripotent stem cells for modeling Parkinson’s disease. *World Journal of Stem Cells*. **11**, 634–649 (2019), doi:10.4252/wjsc.v11.i9.634.

234. L. Studer, E. Vera, D. Cornacchia, PROGRAMMING AND REPROGRAMMING CELLULAR AGE IN THE ERA OF INDUCED PLURIPOTENCY. *Cell stem cell*. **16**, 591–600 (2015), doi:10.1016/j.stem.2015.05.004.

235. J. D. Miller *et al.,* Human iPSC-based modeling of late-onset disease via progerin-induced aging. *Cell stem cell*. **13**, 691–705 (2013), doi:10.1016/j.stem.2013.11.006.

236. J. L. Carter, J. A. N. M. Halmai, K. D. Fink, The iNs and Outs of Direct Reprogramming to Induced Neurons. *Front. Genome Ed.* **2** (2020), doi:10.3389/fgeed.2020.00007.

237. A. Smith, Formative pluripotency: the executive phase in a developmental continuum. *Development (Cambridge, England)*. **144**, 365–373 (2017), doi:10.1242/dev.142679.

238. H. Fu *et al.,* Dynamics of Telomere Rejuvenation during Chemical Induction to Pluripotent Stem Cells. *Stem cell reports*. **11**, 70–87 (2018), doi:10.1016/j.stemcr.2018.05.003.

239. K. Kalmbach, L. G. Robinson, F. Wang, L. Liu, D. Keefe, Telomere length reprogramming in embryos and stem cells. *BioMed research international*. **2014**, 925121 (2014), doi:10.1155/2014/925121.

240. J. Mertens, D. Reid, S. Lau, Y. Kim, F. H. Gage, Aging in a Dish: iPSC-Derived and Directly Induced Neurons for Studying Brain Aging and Age-Related Neurodegenerative Diseases. *Annual review of genetics*. **52**, 271–293 (2018), doi:10.1146/annurev-genet-120417-031534.

241. B. Popp *et al.,* Need for high-resolution Genetic Analysis in iPSC: Results and Lessons from the ForIPS Consortium. *Scientific reports*. **8**, 17201 (2018), doi:10.1038/s41598-018-35506-0.

242. C. Patthey, T. Edlund, L. Gunhaga, Wnt-regulated temporal control of BMP exposure directs the choice between neural plate border and epidermal fate. *Development (Cambridge, England)*. **136**, 73–83 (2009), doi:10.1242/dev.025890.

243. S. Petrini *et al.,* Aged induced pluripotent stem cell (iPSCs) as a new cellular model for studying premature aging. *Aging (Albany NY)*. **9**, 1453–1466 (2017), doi:10.18632/aging.101248.

244. A. H. Schapira *et al.,* Anatomic and disease specificity of NADH CoQ1 reductase (complex I) deficiency in Parkinson's disease. *Journal of neurochemistry*. **55**, 2142–2145 (1990), doi:10.1111/j.1471-4159.1990.tb05809.x.

245. A. Navarro *et al.,* Human brain cortex: mitochondrial oxidative damage and adaptive response in Parkinson disease and in dementia with Lewy bodies. *Free radical biology & medicine*. **46**, 1574–1580 (2009), doi:10.1016/j.freeradbiomed.2009.03.007.

246. C. A. Stautner, *Mitochondrial Function in Cellular Models of Idiopathic Parkinson's Disease* (Universitätsbibliothek der TU München, München, 2018).

247. N. I. Bohnen, R. L. Albin, The Cholinergic System and Parkinson Disease. *Behavioural brain research*. **221**, 564–573 (2011), doi:10.1016/j.bbr.2009.12.048.

248. M. Ruberg, A. Ploska, F. Javoy-Agid, Y. Agid, Muscarinic binding and choline acetyltransferase activity in Parkinsonian subjects with reference to dementia. *Brain research*. **232** (1982), doi:10.1016/0006-8993(82)90615-1.

249. K. W. Lange, F. R. Wells, P. Jenner, C. D. Marsden, Altered muscarinic and nicotinic receptor densities in cortical and subcortical brain regions in Parkinson's disease. *Journal of neurochemistry*. **60** (1993), doi:10.1111/j.1471-4159.1993.tb05838.x.

250. H. M. Kang *et al.,* Multiplexed droplet single-cell RNA-sequencing using natural genetic variation. *Nature biotechnology*. **36**, 89–94 (2018), doi:10.1038/nbt.4042.

251. C. Lorenz *et al.,* Human iPSC-Derived Neural Progenitors Are an Effective Drug Discovery Model for Neurological mtDNA Disorders. *Cell stem cell*. **20**, 659-674.e9 (2017), doi:10.1016/j.stem.2016.12.013.

252. S. Thomas *et al.,* Human neural crest cells display molecular and phenotypic hallmarks of stem cells. *Human molecular genetics*. **17**, 3411–3425 (2008), doi:10.1093/hmg/ddn235.

253. N. Nagy *et al.,* Collagen 18 and agrin are secreted by neural crest cells to remodel their microenvironment and regulate their migration during enteric nervous system development. *Development (Cambridge, England)*. **145** (2018), doi:10.1242/dev.160317.

254. J. T. Campanelli *et al.,* Expression profiling of human glial precursors. *BMC developmental biology*. **8**, 102 (2008), doi:10.1186/1471-213X-8-102.

255. D. E. Korzhevskii, M. N. Karpenko, O. V. Kirik, Microtubule-Associated Proteins as Indicators of Differentiation and the Functional State of Nerve Cells. *Neurosci Behav Physi*. **42**, 215–222 (2012), doi:10.1007/s11055-012-9556-4.

256. P. Ellis *et al.,* SOX2, a persistent marker for multipotential neural stem cells derived from embryonic stem cells, the embryo or the adult. *Developmental neuroscience*. **26**, 148–165 (2004), doi:10.1159/000082134.

257. T. Ly *et al.,* Proteomic analysis of cell cycle progression in asynchronous cultures, including mitotic subphases, using PRIMMUS. *eLife*. **6** (2017), doi:10.7554/eLife.27574.

258. E. Navarro Quiroz *et al.,* Cell Signaling in Neuronal Stem Cells. *Cells*. **7** (2018), doi:10.3390/cells7070075.

259. A. Ruiz i Altaba, V. Palma, N. Dahmane, Hedgehog-Gli signalling and the growth of the brain. *Nature reviews. Neuroscience*. **3**, 24–33 (2002), doi:10.1038/nrn704.

260. M. W. Pfaffl, A. Tichopad, C. Prgomet, T. P. Neuvians, Determination of stable housekeeping genes, differentially regulated target genes and sample integrity. *Biotechnology letters*. **26**, 509–515 (2004), doi:10.1023/b:bile.0000019559.84305.47.

261. P. Huot, S. H. Fox, J. M. Brotchie, The serotonergic system in Parkinson's disease. *Progress in neurobiology*. **95**, 163–212 (2011), doi:10.1016/j.pneurobio.2011.08.004.

262. S. Hisahara, S. Shimohama, Dopamine receptors and Parkinson's disease. *International journal of medicinal chemistry*. **2011**, 403039 (2011), doi:10.1155/2011/403039.

263. Q. Xu *et al.,* BBS4 and BBS5 show functional redundancy in the BBSome to regulate the degradative sorting of ciliary sensory receptors. *Scientific reports*. **5**, 11855 (2015), doi:10.1038/srep11855.

264. Y. Chen, J. Jiang, Decoding the phosphorylation code in Hedgehog signal transduction. *Cell research*. **23**, 186–200 (2013), doi:10.1038/cr.2013.10.

265. N. Wenck, *Analysis of an iPSC-based Model of Parkinson's Disease Regarding SHH Signalling in Primary Cilia and Neuronal Outgrowth* (Universitätsbibliothek der TU München, München, 2019).

266. K. Pflügler, *Metabolic Analysis of iPSC derived Astrocytes from idiopathic Parkinson`s Disease Patients using Seahorse XF* (Universitätsbibliothek der TU München, München, 2020).

267. S. A. Vokes *et al.,* Genomic characterization of Gli-activator targets in sonic hedgehog-mediated neural patterning. *Development (Cambridge, England)*. **134**, 1977–1989 (2007), doi:10.1242/dev.001966.

268. B. Jung *et al.,* Novel small molecules targeting ciliary transport of Smoothened and oncogenic Hedgehog pathway activation. *Scientific reports*. **6**, 22540 (2016), doi:10.1038/srep22540.

269. Q. Wang *et al.,* The landscape of multiscale transcriptomic networks and key regulators in Parkinson's disease. *Nature communications*. **10**, 5234 (2019), doi:10.1038/s41467-019-13144-y.

270. L. E. Gonzalez-Reyes *et al.,* Sonic hedgehog maintains cellular and neurochemical homeostasis in the adult nigrostriatal circuit. *Neuron*. **75**, 306–319 (2012), doi:10.1016/j.neuron.2012.05.018.

271. L. Tretter, I. Sipos, V. Adam-Vizi, Initiation of neuronal damage by complex I deficiency and oxidative stress in Parkinson's disease. *Neurochemical research*. **29** (2004), doi:10.1023/b:nere.0000014827.94562.4b.

272. L. Steinert, *Profiles of aging markers in iPSCs from idiopathic Parkinson`s Disease patients during long term in vitro cultivation* (Universitätsbibliothek der TU München, München, 2019).

273. R. Burla, M. La Torre, I. Saggio, Mammalian telomeres and their partnership with lamins. *Nucleus*. **7**, 187–202 (2016), doi:10.1080/19491034.2016.1179409.

274. M. Jaskelioff *et al.,* Telomerase reactivation reverses tissue degeneration in aged telomerase deficient mice. *Nature*. **469**, 102–106 (2010), doi:10.1038/nature09603.

275. Y. Huang, P. Liang, D. Liu, J. Huang, Z. Songyang, Telomere regulation in pluripotent stem cells. *Protein & Cell*. **5**, 194–202 (2014), doi:10.1007/s13238-014-0028-1.

276. A. Freund *et al.,* Proteostatic control of telomerase function through TRiC-mediated folding of TCAB1. *Cell*. **159**, 1389–1403 (2014), doi:10.1016/j.cell.2014.10.059.

277. M. Brehme *et al.,* A chaperome subnetwork safeguards proteostasis in aging and neurodegenerative disease. *Cell reports*. **9**, 1135–1150 (2014), doi:10.1016/j.celrep.2014.09.042.

278. M. D. Burkhalter *et al.,* Imbalanced mitochondrial function provokes heterotaxy via aberrant ciliogenesis. *The Journal of clinical investigation*. **129**, 2841–2855 (2019), doi:10.1172/JCI98890.

279. G. Walz, Role of primary cilia in non-dividing and post-mitotic cells. *Cell Tissue Res*. **369**, 11–25 (2017), doi:10.1007/s00441-017-2599-7.

280. T. Neill, L. Schaefer, R. V. Iozzo, Oncosuppressive functions of decorin. *Molecular & cellular oncology*. **2**, e975645 (2015), doi:10.4161/23723556.2014.975645.

281. S. M. Jin, R. J. Youle, PINK1- and Parkin-mediated mitophagy at a glance. *Journal of cell science*. **125**, 795–799 (2012), doi:10.1242/jcs.093849.

282. C. Bus *et al.,* PINK1 Regulates Dopamine and Lipids at Mitochondria to Maintain Synapses and Neuronal Function. *bioRxiv* (2019), doi:10.1101/814343.

283. P. J. Yao *et al.,* Sonic hedgehog pathway activation increases mitochondrial abundance and activity in hippocampal neurons. *Molecular biology of the cell*. **28**, 387–395 (2017), doi:10.1091/mbc.E16-07-0553.

284. P. Lepanto, J. L. Badano, F. R. Zolessi, Neuron's little helper: The role of primary cilia in neurogenesis. *Neurogenesis*. **3** (2016), doi:10.1080/23262133.2016.1253363.

285. S. Victorelli, J. F. Passos, Telomeres and Cell Senescence - Size Matters Not. *EBioMedicine*. **21**, 14–20 (2017), doi:10.1016/j.ebiom.2017.03.027.

286. A. Chojnowski *et al.,* Progerin reduces LAP2α-telomere association in Hutchinson-Gilford progeria. *eLife*. **4** (2015), doi:10.7554/eLife.07759.

287. J. D. Robin, F. Magdinier, Physiological and Pathological Aging Affects Chromatin Dynamics, Structure and Function at the Nuclear Edge. *Frontiers in Genetics*. **7** (2016), doi:10.3389/fgene.2016.00153.

288. T. Dechat *et al.,* LAP2alpha and BAF transiently localize to telomeres and specific regions on chromatin during nuclear assembly. *Journal of cell science*. **117**, 6117–6128 (2004), doi:10.1242/jcs.01529.

289. N. Naetar *et al.,* LAP2alpha maintains a mobile and low assembly state of A-type lamins in the nuclear interior. *eLife*. **10** (2021), doi:10.7554/eLife.63476.

290. Y. Zhu, X. Liu, X. Ding, F. Wang, X. Geng, Telomere and its role in the aging pathways: telomere shortening, cell senescence and mitochondria dysfunction. *Biogerontology*, 1–16 (2019), doi:10.1007/s10522-018-9769-1.

291. M. Pavel *et al.,* CCT complex restricts neuropathogenic protein aggregation via autophagy. *Nature communications*. **7**, 13821 (2016), doi:10.1038/ncomms13821.

292. M. A. Lynch-Day, K. Mao, K. Wang, M. Zhao, D. J. Klionsky, The Role of Autophagy in Parkinson's Disease. *Cold Spring Harbor perspectives in medicine*. **2** (2012), doi:10.1101/cshperspect.a009357.

293. D. A. Forero *et al.,* Telomere length in Parkinson's disease: A meta-analysis. *Experimental gerontology*. **75**, 53–55 (2016), doi:10.1016/j.exger.2016.01.002.

294. G. Auburger *et al.,* Primary Skin Fibroblasts as a Model of Parkinson's Disease. *Molecular Neurobiology*. **46**, 20–27 (2012), doi:10.1007/s12035-012-8245-1.

295. G. Ambrosi *et al.,* Bioenergetic and proteolytic defects in fibroblasts from patients with sporadic Parkinson's disease. *Biochimica et Biophysica Acta (BBA) - Molecular Basis of Disease*. **1842**, 1385–1394 (2014), doi:10.1016/j.bbadis.2014.05.008.

296. P. del Hoyo *et al.,* Oxidative stress in skin fibroblasts cultures from patients with Parkinson's disease. *BMC neurology*. **10**, 95 (2010), doi:10.1186/1471-2377-10-95.

297. H.-J. Kim, B. S. Jeon, Hypothesis: Somatic Mosaicism and Parkinson Disease. *Experimental Neurobiology*. **23**, 271–276 (2014), doi:10.5607/en.2014.23.4.271.

298. T.-M. Sonninen *et al.,* Metabolic alterations in Parkinson's disease astrocytes. *Scientific reports*. **10**, 14474 (2020), doi:10.1038/s41598-020-71329-8.

299. R. Edgar *et al.,* LifeMap Discovery™: the embryonic development, stem cells, and regenerative medicine research portal. *PloS one*. **8**, e66629 (2013), doi:10.1371/journal.pone.0066629.

300. J.-S. Park, R. L. Davis, C. M. Sue, Mitochondrial Dysfunction in Parkinson's Disease: New Mechanistic Insights and Therapeutic Perspectives. *Current Neurology and Neuroscience Reports*. **18** (2018), doi:10.1007/s11910-018-0829-3.

301. T. J. Sarkar, V. Sebastiano, in *Pluripotent Stem Cells - From the Bench to the Clinic*, M. Tomizawa, Ed. (InTech, 2016).

302. C. P. Gonzalez-Hunt, L. H. Sanders, DNA damage and repair in Parkinson's disease: Recent advances and new opportunities. *Journal of neuroscience research* (2020), doi:10.1002/jnr.24592.

303. L. Bermúdez-Guzmán, A. Leal, DNA repair deficiency in neuropathogenesis: when all roads lead to mitochondria. *Translational neurodegeneration*. **8**, 14 (2019), doi:10.1186/s40035-019-0156-x.

304. J. Tran, H. Anastacio, C. Bardy, Genetic predispositions of Parkinson's disease revealed in patient-derived brain cells. *npj Parkinsons Dis.* **6**, 8 (2020), doi:10.1038/s41531-020-0110-8.

305. A. Sánchez-Danés *et al.,* Disease-specific phenotypes in dopamine neurons from human iPS-based models of genetic and sporadic Parkinson's disease. *EMBO molecular medicine*. **4**, 380–395 (2012), doi:10.1002/emmm.201200215.

306. D. Sulzer, Multiple hit hypotheses for dopamine neuron loss in Parkinson's disease. *Trends in neurosciences*. **30**, 244–250 (2007), doi:10.1016/j.tins.2007.03.009.

307. M. Ehrlich, DNA hypermethylation in disease: mechanisms and clinical relevance. *Epigenetics*. **14**, 1141–1163 (2019), doi:10.1080/15592294.2019.1638701.

308. Y. Kishi, Y. Gotoh, Regulation of Chromatin Structure During Neural Development. *Frontiers in neuroscience*. **12** (2018), doi:10.3389/fnins.2018.00874.

309. B. Liu, S. Chen, D. Cheng, W. Jing, J. A. Helms, Primary Cilia Integrate Hedgehog and Wnt Signaling during Tooth Development. *Journal of Dental Research*. **93**, 475–482 (2014), doi:10.1177/0022034514528211.

310. S. Saito, B. Tampe, G. A. Müller, M. Zeisberg, Primary cilia modulate balance of canonical and non-canonical Wnt signaling responses in the injured kidney. *Fibrogenesis & Tissue Repair*. **8** (2015), doi:10.1186/s13069-015-0024-y.

311. H. L. May-Simera, M. W. Kelley, Cilia, Wnt signaling, and the cytoskeleton. *Cilia*. **1**, 7 (2012), doi:10.1186/2046-2530-1-7.

312. J. P. de Magalhães, J. Curado, G. M. Church, Meta-analysis of age-related gene expression profiles identifies common signatures of aging. *Bioinformatics (Oxford, England)*. **25**, 875–881 (2009), doi:10.1093/bioinformatics/btp073.

313. M. J. Peters *et al.,* The transcriptional landscape of age in human peripheral blood. *Nature communications*. **6**, 8570 (2015), doi:10.1038/ncomms9570.

314. E. B. van den Akker *et al.,* Meta-analysis on blood transcriptomic studies identifies consistently coexpressed protein-protein interaction modules as robust markers of human aging. *Aging Cell*. **13**, 216–225 (2014), doi:10.1111/acel.12160.

315. J. M. Zahn *et al.,* AGEMAP: a gene expression database for aging in mice. *PLoS genetics*. **3**, e201 (2007), doi:10.1371/journal.pgen.0030201.

316. J. M. Zahn *et al.,* Transcriptional profiling of aging in human muscle reveals a common aging signature. *PLoS genetics*. **2**, e115 (2006), doi:10.1371/journal.pgen.0020115.eor.

317. X. Ma *et al.,* Analysis of C. elegans muscle transcriptome using trans-splicing-based RNA tagging (SRT). *Nucleic acids research*. **44**, e156 (2016), doi:10.1093/nar/gkw734.

318. S. A. McCarroll *et al.,* Comparing genomic expression patterns across species identifies shared transcriptional profile in aging. *Nature genetics*. **36**, 197–204 (2004), doi:10.1038/ng1291.

319. D. Glass *et al.,* Gene expression changes with age in skin, adipose tissue, blood and brain. *Genome biology*. **14**, R75 (2013), doi:10.1186/gb-2013-14-7-r75.

320. T. Hamatani *et al.,* Age-associated alteration of gene expression patterns in mouse oocytes. *Human molecular genetics*. **13**, 2263–2278 (2004), doi:10.1093/hmg/ddh241.

321. A. Kumar *et al.,* Age-associated changes in gene expression in human brain and isolated neurons. *Neurobiology of Aging*. **34**, 1199–1209 (2013), doi:10.1016/j.neurobiolaging.2012.10.021.

322. S. Frenk, J. Houseley, Gene expression hallmarks of cellular ageing. *Biogerontology*. **19**, 547–566 (2018), doi:10.1007/s10522-018-9750-z.

323. Y. Zilberter, M. Zilberter, The vicious circle of hypometabolism in neurodegenerative diseases: Ways and mechanisms of metabolic correction. *Journal of neuroscience research*. **95**, 2217–2235 (2017), doi:10.1002/jnr.24064.

324. P. Borghammer, Perfusion and metabolism imaging studies in Parkinson's disease. *Danish medical journal*. **59**, B4466 (2012).

325. P. Borghammer *et al.,* Cortical hypometabolism and hypoperfusion in Parkinson's disease is extensive: probably even at early disease stages. *Brain structure & function*. **214**, 303–317 (2010), doi:10.1007/s00429-010-0246-0.

326. L. Dunn *et al.,* Dysregulation of glucose metabolism is an early event in sporadic Parkinson's disease. *Neurobiology of Aging*. **35**, 1111–1115 (2014), doi:10.1016/j.neurobiolaging.2013.11.001.

327. Y. Xu *et al.,* Low Cerebral Glucose Metabolism: A Potential Predictor for the Severity of Vascular Parkinsonism and Parkinson's Disease. *Aging and disease*. **6**, 426–436 (2015), doi:10.14336/AD.2015.0204.

328. B. L. Krock, B. D. Perkins, The intraflagellar transport protein IFT57 is required for cilia maintenance and regulates IFT-particle-kinesin-II dissociation in vertebrate photoreceptors. *Journal of cell science*. **121**, 1907–1915 (2008), doi:10.1242/jcs.029397.

329. J. Kim *et al.,* Functional genomic screen for modulators of ciliogenesis and cilium length. *Nature*. **464**, 1048–1051 (2010), doi:10.1038/nature08895.

330. L. Shao *et al.,* Genetic reduction of cilium length by targeting intraflagellar transport 88 protein impedes kidney and liver cyst formation in mouse models of autosomal polycystic kidney disease. *Kidney international*, 1225–1241 (2020), doi:10.1016/j.kint.2020.05.049.

331. V. Donega *et al.,* Transcriptome and proteome profiling of neural stem cells from the human subventricular zone in Parkinson's disease. *Acta neuropathologica communications*. **7**, 84 (2019), doi:10.1186/s40478-019-0736-0.

332. A. H. Laperle *et al.,* iPSC modeling of young-onset Parkinson's disease reveals a molecular signature of disease and novel therapeutic candidates. *Nature medicine* (2020), doi:10.1038/s41591-019-0739-1.

333. S. Vegas-Suarez *et al.,* Dysfunction of serotonergic neurons in Parkinson's disease and dyskinesia. *International review of neurobiology*. **146**, 259–279 (2019), doi:10.1016/bs.irn.2019.06.013.

334. M. Álvarez-Satta, L. Moreno-Cugnon, A. Matheu, Primary cilium and brain aging: role in neural stem cells, neurodegenerative diseases and glioblastoma. *Ageing research reviews*. **52**, 53–63 (2019), doi:10.1016/j.arr.2019.04.004.

335. H. S. Dhekne *et al.,* A pathway for Parkinson's Disease LRRK2 kinase to block primary cilia and Sonic hedgehog signaling in the brain. *eLife*. **7** (2018), doi:10.7554/eLife.40202.

336. M. Kaliszewski, A. B. Knott, E. Bossy-Wetzel, Primary cilia and autophagic dysfunction in Huntington's disease. *Cell death and differentiation*. **22**, 1413–1424 (2015), doi:10.1038/cdd.2015.80.

337. M. Gazea *et al.,* Primary cilia are critical for Sonic hedgehog-mediated dopaminergic neurogenesis in the embryonic midbrain. *Developmental biology*. **409**, 55–71 (2016), doi:10.1016/j.ydbio.2015.10.033.

338. K. Miyoshi *et al.,* Lack of dopaminergic inputs elongates the primary cilia of striatal neurons. *PloS one*. **9**, e97918 (2014), doi:10.1371/journal.pone.0097918.

339. A. B. West, M. R. Cookson, Identification of bona-fide LRRK2 kinase substrates. *Movement disorders : official journal of the Movement Disorder Society*. **31**, 1140–1141 (2016), doi:10.1002/mds.26647.

340. P. Reinhardt *et al.,* Derivation and expansion using only small molecules of human neural progenitors for neurodegenerative disease modeling. *PloS one*. **8**, e59252 (2013), doi:10.1371/journal.pone.0059252.

341. J. Tcw *et al.,* An Efficient Platform for Astrocyte Differentiation from Human Induced Pluripotent Stem Cells. *Stem cell reports*. **9**, 600–614 (2017), doi:10.1016/j.stemcr.2017.06.018.

342. Z.-W. Du *et al.,* Generation and expansion of highly pure motor neuron progenitors from human pluripotent stem cells. *Nature communications*. **6**, 6626 (2015), doi:10.1038/ncomms7626.

343. J. Prestel *et al.,* Clinical and molecular characterisation of a Parkinson family with a novel PINK1 mutation. *Journal of neurology*. **255**, 643–648 (2008), doi:10.1007/s00415-008-0763-4.

344. S. Diecke *et al.,* Novel codon-optimized mini-intronic plasmid for efficient, inexpensive, and xeno-free induction of pluripotency. *Scientific reports*. **5**, 8081 (2015), doi:10.1038/srep08081.

345. K. Okita *et al.,* A more efficient method to generate integration-free human iPS cells. *Nature methods*. **8**, 409–412 (2011), doi:10.1038/nmeth.1591.

346. Y. Shi, P. Kirwan, F. J. Livesey, Directed differentiation of human pluripotent stem cells to cerebral cortex neurons and neural networks. *Nature protocols*. **7**, 1836–1846 (2012), doi:10.1038/nprot.2012.116.

347. B. Borchin, J. Chen, T. Barberi, Derivation and FACS-mediated purification of PAX3+/PAX7+ skeletal muscle precursors from human pluripotent stem cells. *Stem cell reports*. **1**, 620–631 (2013), doi:10.1016/j.stemcr.2013.10.007.

348. K. A. D'Amour *et al.,* Efficient differentiation of human embryonic stem cells to definitive endoderm. *Nature biotechnology*. **23**, 1534–1541 (2005), doi:10.1038/nbt1163.

349. J. Schindelin *et al.,* Fiji. *Nature methods*. **9**, 676–682 (2012), doi:10.1038/nmeth.2019.

350. R. M. Cawthon, Telomere length measurement by a novel monochrome multiplex quantitative PCR method. *Nucleic acids research*. **37**, e21 (2009), doi:10.1093/nar/gkn1027.

351. Y. Guo *et al.,* Illumina human exome genotyping array clustering and quality control. *Nature protocols*. **9**, 2643–2662 (2014), doi:10.1038/nprot.2014.174.

352. C. C. Chang *et al.,* Second-generation PLINK. *GigaScience*. **4**, 7 (2015), doi:10.1186/s13742-015-0047-8.

353. M. D. Luecken, F. J. Theis, Current best practices in single-cell RNA-seq analysis. *Molecular systems biology*. **15**, e8746 (2019), doi:10.15252/msb.20188746.

354. F. A. Wolf, P. Angerer, F. J. Theis, SCANPY. *Genome biology*. **19**, 15 (2018), doi:10.1186/s13059-017-1382-0.

355. L. Haghverdi, A. T. L. Lun, M. D. Morgan, J. C. Marioni, Batch effects in single-cell RNA-sequencing data are corrected by matching mutual nearest neighbors. *Nature biotechnology*. **36**, 421–427 (2018), doi:10.1038/nbt.4091.

356. L. McInnes, J. Healy, J. Melville, "UMAP, Uniform Manifold Approximation and Projection for Dimension Reduction". (; http://arxiv.org/pdf/1802.03426v2).

357. I. Tirosh *et al.,* Dissecting the multicellular ecosystem of metastatic melanoma by single-cell RNA-seq. *Science (New York, N.Y.)*. **352**, 189–196 (2016), doi:10.1126/science.aad0501.

358. V. D. Blondel, J.-L. Guillaume, R. Lambiotte, E. Lefebvre, Fast unfolding of communities in large networks. *J. Stat. Mech.* **2008**, P10008 (2008), doi:10.1088/1742-5468/2008/10/P10008.

359. M. Ashburner *et al.,* Gene ontology: tool for the unification of biology. The Gene Ontology Consortium. *Nature genetics*. **25**, 25–29 (2000), doi:10.1038/75556.

360. U. Raudvere *et al.,* g:Profiler: a web server for functional enrichment analysis and conversions of gene lists (2019 update). *Nucleic acids research*. **47**, W191-W198 (2019), doi:10.1093/nar/gkz369.

361. V. Bergen, M. Lange, S. Peidli, F. A. Wolf, F. J. Theis, Generalizing RNA velocity to transient cell states through dynamical modeling. *bioRxiv* (2019), doi:10.1101/820936.

362. Y. Benjamini, Y. Hochberg, Controlling the False Discovery Rate. *Journal of the Royal Statistical Society: Series B (Methodological)*. **57**, 289–300 (1995), doi:10.1111/j.2517-6161.1995.tb02031.x.

363. A. A. Shabalin, Matrix eQTL: ultra fast eQTL analysis via large matrix operations. *Bioinformatics (Oxford, England)*. **28**, 1353–1358 (2012), doi:10.1093/bioinformatics/bts163.

364. K. Strimmer, fdrtool. *Bioinformatics (Oxford, England)*. **24**, 1461–1462 (2008), doi:10.1093/bioinformatics/btn209.

365. G. Yu, L.-G. Wang, Y. Han, Q.-Y. He, clusterProfiler. *Omics : a journal of integrative biology*. **16**, 284–287 (2012), doi:10.1089/omi.2011.0118.

366. A. Subramanian *et al.,* Gene set enrichment analysis. *Proceedings of the National Academy of Sciences of the United States of America*. **102**, 15545–15550 (2005), doi:10.1073/pnas.0506580102.

367. D. N. Slenter *et al.,* WikiPathways: a multifaceted pathway database bridging metabolomics to other omics research. *Nucleic acids research*. **46**, D661-D667 (2018), doi:10.1093/nar/gkx1064.

368. K. Cartharius *et al.,* MatInspector and beyond. *Bioinformatics (Oxford, England)*. **21**, 2933–2942 (2005), doi:10.1093/bioinformatics/bti473.

369. R. Ietswaart, B. M. Gyori, J. A. Bachman, P. K. Sorger, L. S. Churchman, GeneWalk identifies relevant gene functions for a biological context using network representation learning. *Genome Biol*. **22**, 55 (2021), doi:10.1186/s13059-021-02264-8.

370. L. Glasl *et al.,* Pink1-deficiency in mice impairs gait, olfaction and serotonergic innervation of the olfactory bulb. *Experimental neurology*. **235**, 214–227 (2012), doi:10.1016/j.expneurol.2012.01.002.

371. C. Muschet *et al.,* Removing the bottlenecks of cell culture metabolomics: fast normalization procedure, correlation of metabolites to cell number, and impact of the cell harvesting method. *Metabolomics : Official journal of the Metabolomic Society*. **12**, 151 (2016), doi:10.1007/s11306-016-1104-8.

372. A. W. Bowman, A. Azzalini, *R package 'sm': nonparametric smoothing methods (version 2.2-5.6)* (2018).

373. H. Chen, P. C. Boutros, VennDiagram. *BMC bioinformatics*. **12**, 35 (2011), doi:10.1186/1471-2105-12-35.

6. Appendix

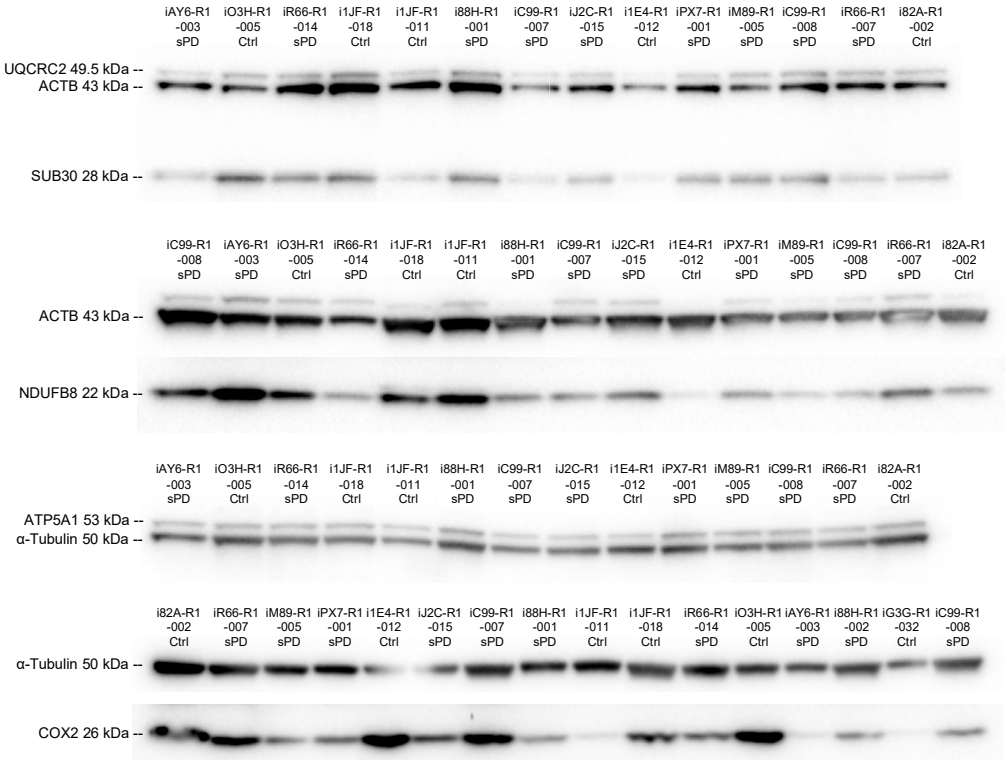

Figure 42 | Analysis of mitochondrial abundance and function. The abundance of mitochondrial complexes I - IV was quantified by Western blot with antibodies against the subunits NDUFB8 (complex I), Complex II Subunit 30 kDa (SUB30), UQCRC2 (Complex III), COX2 (Complex IV) and ATP5A1 (Complex V). Expression levels were normalized to ACTB or α-Tubulin levels. Western blots are exemplary shown for one replicate. In parts taken from a manuscript (Schmidt et al.) submitted to peer-reviewing journals.

Table 16 | Analysis of variance of Seahorse XF measurements. Comparison of health state. Values are displayed as means ± standard deviation (SD). n = 5 Ctrl and 7 sPD clones, in triplicates.

Cell type	Seahorse measurement		Statistical test	p-value	Average Ctrl [pmol O_2/min /µg DNA]	Average sPD [pmol O_2/min /µg DNA]
Fibroblast	OCR, Glucose	basal respiration	t-test	0.44	765.70±119.30	824.20±160.60
		maximal respiration	t-test	0.59	1,662.00±258.80	1,694.00±170.90
		proton leak	Mann-Whitney	0.79	47.47±31.77	55.48±10.71
	OCR, Pyruvate	basal respiration	t-test	0.74	1,111.00±185.40	1,129.00±159.60
		maximal respiration	Mann-Whitney	0.79	1,581.00±255.00	1,675.00±352.00
		proton leak	Mann-Whitney	0.89	75.50±8.65	85.42±17.58
	ECAR, Glucose	basal glycolytic flux	t-test	0.68	535.20±100.50	611.50±145.80
		maximal glycolytic flux	Welch-test	0.62	952.90±113.00	964.70±99.22

hiPSCs, lp	OCR, Glucose	basal respiration	t-test	0.0004	693.52±120.52	606.56±111.32
		maximal respiration	t-test	0.3272	443.11±70.25	411.80±106.34
		proton leak	t-test	0.0894	133.98±13.42	126.12±13.21
	OCR, Pyruvate	basal respiration	t-test	0.0004	1,236.59±169.99	1,116.68±150.02
		maximal respiration	t-test	0.1713	1,323.28±155.91	1,229.84±222.48
		proton leak	t-test	0.0195	194.59±17.21	181.49±14.72
	ECAR, Glucose	basal glycolytic flux	t-test	0.1502	248.84±39.43	239.66±17.11
		maximal glycolytic flux	t-test	0.4916	384.04±60.98	366.59±20.59
hiPSCs, hp	OCR, Glucose	basal respiration	t-test	< 0,0001	761.41±110.73	637.94±134.09
		maximal respiration	t-test	< 0,0001	695.89±132.18	437.26±83.92
		proton leak	Mann-Whitney	0.0831	150.99±30.25	133.89±26.34
	OCR, Pyruvate	basal respiration	t-test	0.0566	1,169.25±145.86	1,111.72±142.65
		maximal respiration	t-test	0.4951	1,320.29±173.47	1,280.91±165.65
		proton leak	t-test	0.0428	189.32±24.00	171.80±25.04
	ECAR, Glucose	basal glycolytic flux	Mann-Whitney	< 0,0001	362.50±56.84	469.14±86.14
		maximal glycolytic flux	t-test	0.4282	643.70±224.51	729.87±139.04
hNPCs, lp	OCR, Glucose	basal respiration	t-test	0.66	304.44±59.08	335.94±144.05
		maximal respiration	t-test	0.5	602.13±146.24	727.89±381.54
		proton leak	t-test	0.44	80.28±23.29	90.57±20.54
	OCR, Pyruvate	basal respiration	t-test	0.71	463.52±119.12	502.77±206.22
		maximal respiration	t-test	0.93	990.21±331.98	969.11±458.64
		proton leak	t-test	0.44	94.64±18.77	110.51±41.08
	ECAR, Glucose	basal glycolytic flux	Mann-Whitney	0.27	248.89±174.52	350.77±157.10
		maximal glycolytic flux	Mann-Whitney	0.34	354.22±189.55	451.25±167.91
hNPCs, hp	OCR, Glucose	basal respiration	t-test	0.023	308.59±128.77	140.97±77.17
		maximal respiration	t-test	0.02	517.86±222.03	224.99±129.73
		proton leak	t-test	0.51	83.08±39.41	42.88±21.12
	OCR, Pyruvate	basal respiration	t-test	0.035	475.37±180.01	252.45±120.69
		maximal respiration	t-test	0.026	745.18±290.89	377.35±175.74
		proton leak	t-test	0.026	113.67±41.56	59.81±26.55
	ECAR, Glucose	basal glycolytic flux	t-test	0.72	107.04±33.00	99.23±37.63
		maximal glycolytic flux	Welch-test	0.38	215.94±112.94	164.11±55.00
Neurons, lp	OCR, Glucose	basal respiration	Mann-Whitney	0.61	105.13±22.50	108.54±25.71
		maximal respiration	t-test	0.49	130.50±46.60	155.96±61.56
		proton leak	t-test	0.75	29.66±10.59	33.11±18.63
	OCR, Pyruvate	basal respiration	Welch-test	0.21	64.43±17.05	90.30±39.17
		maximal respiration	Mann-Whitney	0.93	111.17±108.03	94.20±78.21
		proton leak	Mann-Whitney	1	88.99±87.69	75.86±59.28
	ECAR, Glucose	basal glycolytic flux	Welch-test	0.16	15.23±8.67	28.66±16.68
		maximal glycolytic flux	Welch-test	0.1	35.00±3.91	68.83±41.34
Neurons, hp	OCR, Glucose	basal respiration	t-test	0.23	217.42±64.80	155.25±93.33
		maximal respiration	Mann-Whitney	0.07	313.15±87.12	217.17±148.77
		proton leak	t-test	0.29	71.49±24.72	52.89±30.52
	OCR, Pyruvate	basal respiration	Welch-test	0.02	389.52±138.27	282.10±194.24

		maximal respiration	Welch-test	0.04	528.85±216.02	348.42±215.84
		proton leak	Welch-test	0.43	109.05±15.79	93.33±46.78
	ECAR, Glucose	basal glycolytic flux	t-test	0.93	31.01±13.38	30.19±16.11
		maximal glycolytic flux	Mann-Whitney	0.76	67.92±23.20	75.03±56.33
Astrocytes	OCR, Glucose	basal respiration	t-test	0.21	52.55±17.34	96.97±59.99
		maximal respiration	Welch-test	0.33	112.40±55.32	190.10±135.90
		proton leak	t-test	0.23	11.92±3.34	19.13±8.63
	OCR, Glutamate	basal respiration	Mann-Whitney	0.26	59.98±6.72	116.00±48.11
		maximal respiration	Mann-Whitney	0.26	133.30±56.18	176.30±94.54
		proton leak	Mann-Whitney	0.014	14.62±3.62	22.04±7.19
	ECAR	basal glycolytic flux	t-test	0.78	43.22±14.61	40.54±11.81
		maximal glycolytic flux	t-test	0.72	56.56±19.11	53.85±20.07
Motor neurons	OCR, Glucose	basal respiration	t-test	0.84	56.52±11.26	57.89±9.09
		maximal respiration	Mann-Whitney	0.23	63.23±30.72	66.78±20.98
		proton leak	t-test	0.38	15.13±3.66	13.15±3.18
	OCR, Pyruvate	basal respiration	Welch-test	0.71	72.09±23.26	77.59±9.16
		maximal respiration	Welch-test	0.38	78.82±38.18	99.69±19.80
		proton leak	t-test	0.66	18.42±6.05	20.28±6.30
	ECAR, Glucose	basal glycolytic flux	Welch-test	0.16	58.35±28.30	35.02±24.52
		maximal glycolytic flux	t-test	0.76	69.08±27.03	48.02±26.43

Table 17 | Analysis of variance of Seahorse XF measurements. Comparison of health state and passage number using two-way ANOVA and Tukey`s Post-hoc test. n = 5 Ctrl and 7 sPD clones, in triplicates.

Cell type	Seahorse measurement		Health state, F (DFn, DFd); P-value	Passage, F (DFn, DFd); P-value	P-value (Ctrl vs sPD, lp)	P-value (Ctrl vs sPD, hp)	P-value (Ctrl, lp vs hp)	P-value (sPD, lp vs hp)
hiPSCs	OCR, Glucose	basal respiration	F (1, 20) = 10.29; P = 0.004	F (1, 20) = 2.38; P = 0.14	0.31	0.06	0.48	0.91
		maximal respiration	F (1, 20) = 13.04; P = 0.002	F (1, 20) = 3.89; P = 0.06	0.93	0.00	0.03	0.93
		proton leak	F (1, 20) = 3.67; P = 0.07	F (1, 20) = 2.09; P = 0.16	0.72	0.37	0.62	0.86
	OCR, Pyruvate	basal respiration	F (1, 20) = 2.70; P = 0.12	F (1, 20) = 0.45; P = 0.51	0.42	0.87	0.85	1.00
		maximal respiration	F (1, 20) = 0.61; P = 0.44	F (1, 20) = 1.67; P = 0.21	0.89	0.98	0.75	0.85
		proton leak	F (1, 20) = 4.00; P = 0.06	F (1, 20) = 0.96; P = 0.34	0.63	0.39	0.97	0.76
	ECAR, Glucose	basal glycolytic flux	F (1, 19) = 3.39; P = 0.08	F (1, 19) = 46.24; P < 0.0001	0.99	0.06	0.04	< 0.0001
		maximal glycolytic flux	F (1, 20) = 0.13; P = 0.72	F (1, 20) = 41.76; P < 0.0001	0.99	0.87	0.01	0.00
hNPCs	OCR, Glucose	basal respiration	F (1, 19) = 2.14; P = 0.16	F (1, 19) = 4.20; P = 0.05	0.96	0.10	1.00	0.02
		maximal respiration	F (1, 19) = 0.60; P = 0.45	F (1, 19) = 7.37; P = 0.01	0.83	0.28	0.96	0.01
		proton leak	F (1, 19) = 1.92; P = 0.18	F (1, 19) = 4.32; P = 0.05	0.90	0.08	1.00	0.01

	OCR, Pyruvate	basal respiration	F (1, 19) = 1.76; P = 0.20	F (1, 19) = 2.96; P = 0.10	0.98	0.16	1.00	0.04
		maximal respiration	F (1, 19) = 1.82; P = 0.19	F (1, 19) = 8.44; P = 0.009	1.00	0.33	0.70	0.02
		proton leak	F (1, 19) = 1.78; P = 0.20	F (1, 19) = 1.24; P = 0.28	0.85	0.08	0.83	0.05
	ECAR, Glucose	basal glycolytic flux	F (1, 20) = 0.91; P = 0.35	F (1, 20) = 15.96; P = 0.0007	0.48	1.00	0.27	0.00
		maximal glycolytic flux	F (1, 20) = 0.16; P = 0.70	F (1, 20) = 13.82; P = 0.001	0.63	0.92	0.41	0.00
Neurons	OCR, Glucose	basal respiration	F (1, 18) = 1.11; P = 0.31	F (1, 18) = 8.11; P = 0.01	1.00	0.37	0.08	0.57
		maximal respiration	F (1, 19) = 0.67; P = 0.42	F (1, 19) = 7.98; P = 0.01	0.98	0.39	0.06	0.67
		proton leak	F (1, 19) = 0.57; P = 0.46	F (1, 19) = 9.38; P = 0.006	1.00	0.54	0.07	0.41
	OCR, Pyruvate	basal respiration	F (1, 19) = 0.76; P = 0.39	F (1, 19) = 6.59; P = 0.02	0.99	0.54	0.02	0.09
		maximal respiration	F (1, 19) = 1.70; P = 0.21	F (1, 19) = 13.09; P = 0.002	1.00	0.29	0.01	0.05
		proton leak	F (1, 19) = 0.22; P = 0.65	F (1, 19) = 19.21; P = 0.0003	0.98	0.96	0.95	0.93
	ECAR, Glucose	basal glycolytic flux	F (1, 17) = 0.84; P = 0.37	F (1, 17) = 1.58; P = 0.23	0.59	1.00	0.49	1.00
		maximal glycolytic flux	F (1, 17) = 1.14; P = 0.30	F (1, 17) = 1.04; P = 0.32	0.67	0.99	0.71	0.99

Table 18 | Analysis of variance of aging markers. Values are displayed as means ± standard deviation (SD). n = 5 Ctrl and 7 sPD clones, in triplicates.

Cell type	Aging marker	Average Ctrl [FI]	Average sPD [FI]	Statistical test	P-value
Fibroblasts	H3K9me3	4,992.00±504.40	5,687.00±436.70	t-test	0.03
	H3K27me3	5,279.00±900.10	5,160.00±591.70	Mann-Whitney	0.88
	LAP2α	8,352.00±718.20	8,893.00±887.20	t-test	0.29
	γH2A.X	5,898.00±497.40	6,386.00±663.10	t-test	0.20
hNPCs, lp	H3K9me3	9,082.74±2,141.21	8,329.74±2,116.32	ANOVA	
	H3K27me3	5,066.80±607.77	4,841.74±841.38	ANOVA	
	LAP2α	5,114.38±460.40	4,377.25±491.58	ANOVA	
	γH2A.X	6,326.73±560.24	6,257.69±280.39	ANOVA	
hNPCs, hp	H3K9me3	5,614.65±2,311.80	6,232.78±1,943.41	ANOVA	
	H3K27me3	4,007.25±292.22	3,997.09±350.79	ANOVA	
	LAP2α	3,774.52±565.90	3,604.41±641.18	ANOVA	
	γH2A.X	6,302.26±219.35	6,145.49±942.11	ANOVA	
Neurons, lp	H3K9me3	3,682.54±457.72	4,085.51±723.34	ANOVA	
	H3K27me3	3,463.40±452.32	3,847.43±508.87	ANOVA	
	LAP2α	3,594.95±497.34	3,681.22±502.49	ANOVA	
	γH2A.X	6,187.25±1,446.73	6,273.34±769.06	ANOVA	
Neurons, hp	H3K9me3	3,818.17±374.46	3,186.03±595.39	ANOVA	
	H3K27me3	3,601.58±504.91	2,952.60±591.35	ANOVA	

LAP2α	3,806.29±702.25	2,686.51±490.22	ANOVA
γH2A.X	6,144.98±411.10	5,231.53±850.24	ANOVA

Table 19 | Analysis of variance of aging markers. Comparison of health state and passage number using two-way ANOVA and Tukey`s Post-hoc test. n = 5 Ctrl and 7 sPD clones, in triplicates.

Cell type	Aging marker	Health state, F (DFn, DFd); P-value	Passage, F (DFn, DFd); P-value	P-value (Ctrl vs sPD, lp)	P-value (Ctrl vs sPD, hp)	P-value (Ctrl, lp vs hp)	P-value (sPD, lp vs hp)
hNPCs	H3K9me3	F (1, 20) = 0.006; P = 0.94	F (1, 20) = 10.12; P = 0.005	0.93	0.96	0.08	0.28
	H3K27me3	F (1, 20) = 0.24; P = 0.63	F (1, 20) = 15.54; P = 0.0008	0.91	1.00	0.04	0.06
	LAP2α	F (1, 20) = 3.97; P = 0.06	F (1, 20) = 21.53; P = 0.0002	0.13	0.95	0.005	0.07
	γH2A.X	F (1, 20) = 0.21; P = 0.66	F (1, 20) = 0.08; P = 0.79	1.00	0.97	1.00	0.99
Neurons	H3K9me3	F (1, 20) = 0.23; P = 0.64	F (1, 20) = 2.55; P = 0.13	0.64	0.27	0.98	0.04
	H3K27me3	F (1, 20) = 0.37; P = 0.55	F (1, 20) = 3.04; P = 0.10	0.60	0.18	0.97	0.02
	LAP2α	F (1, 20) = 5.26; P = 0.03	F (1, 20) = 3.02; P = 0.10	0.99	0.01	0.93	0.01
	γH2A.X	F (1, 20) = 1.18; P = 0.29	F (1, 20) = 2.02; P = 0.17	1.00	0.35	1.00	0.18

Table 20 | Analysis of variance of telomere length. Comparison of health state and passage number using two-way ANOVA and Tukey`s Post-hoc test. Values are displayed as means ± standard deviation (SD). n = 5 Ctrl and 7 sPD clones, in triplicates.

Cell type	Average length Ctrl	Average length sPD	Health state, F (DFn, DFd); P-value	Passage, F (DFn, DFd); P-value	P-value (Ctrl vs sPD, lp)	P-value (Ctrl vs sPD, hp)	P-value (Ctrl, lp vs hp)	P-value (sPD, lp vs hp)
hiPSC, lp	1.00±0.24	0.97±0.22	F (1, 20) = 0.11; P = 0.75	F (1, 20) = 17.98; P = 0.0004	1.00	1.00	0.05	0.02
hiPSC, hp	0.63±0.21	0.60±0.17						
hNPCs, lp	1.00±0.16	0.74±0.23	F (1, 20) = 13.09; P = 0.0017	F (1, 20) = 1.589; P = 0.2219	0.28	0.02	1.00	0.33
hNPCs, hp	0.97±0.10	0.53±0.33						

Table 21 | Correlation matrix. Correlation coefficients between variables quantified in high-passage hNPCs and thereof differentiated dopaminergic neurons. Each experiment was performed with n = 5 Ctrl and 7 sPD clones, in triplicates.

	ComplexI activity	ComplexI abundance	ComplexII abundance	ComplexIII abundance	ComplexIV abundance	ComplexV abundance	MitoTracker	Seahorse Glc basal	Seahorse Glc max	Seahorse Pyr basal	Seahorse Pyr max	Seahorse ECAR basal	Seahorse ECAR max	GlycoATP production	mitoATP production	ATP	NAD+	NADH	DANN methylation	Cilia length	Cilia fraction	%RBFOX3	%TH	nf Gli3-FL	nf Gli3-R
ComplexI activity	1	0.10	0.48	0.24	0.37	0.57	0.07	0.13	0.09	-0.06	-0.10	-0.03	-0.01	-0.07	0.14	-0.30	0.47	0.57	0.17	-0.46	0.33	0.12	-0.05	0.27	0.33
ComplexI abundance	0.10	1	0.29	0.65	-0.18	0.46	-0.67	0.35	0.37	0.33	0.26	0.44	0.26	0.39	0.34	-0.38	0.07	-0.35	-0.11	-0.81	0.68	0.63	-0.44	0.01	0.22
ComplexII abundance	0.48	0.29	1	0.04	0.00	-0.01	-0.14	-0.42	-0.48	-0.56	-0.68	-0.14	-0.40	-0.03	-0.41	-0.62	-0.36	0.22	0.11	-0.55	-0.14	0.02	-0.13	-0.56	-0.50
ComplexIII abundance	0.24	0.65	0.04	1	0.14	0.47	-0.24	0.03	0.12	0.00	0.06	0.09	-0.15	0.09	0.02	-0.26	0.55	-0.29	-0.37	-0.76	0.52	0.54	0.00	0.34	0.52
ComplexIV abundance	0.37	-0.18	0.00	0.14	1	-0.25	-0.35	-0.30	-0.32	-0.24	-0.22	-0.37	-0.34	-0.33	-0.29	-0.01	0.32	0.14	0.03	0.04	0.21	0.40	-0.14	-0.17	-0.02
ComplexV abundance	0.57	0.46	-0.01	0.47	-0.25	1	0.14	0.64	0.69	0.50	0.54	0.62	0.58	0.50	0.63	0.03	0.56	0.37	0.16	-0.59	0.54	0.03	0.12	0.72	0.73
MitoTracker	0.07	-0.67	-0.14	-0.24	-0.35	0.14	1	-0.18	-0.14	-0.28	-0.17	-0.08	-0.10	-0.04	-0.19	0.29	0.12	0.48	0.07	0.30	-0.63	-0.82	0.75	0.35	0.09
Seahorse Glc basal	0.13	0.35	-0.42	0.03	-0.30	0.64	-0.18	1	0.99	0.97	0.93	0.52	0.85	0.28	1.00	0.18	0.37	-0.05	0.04	-0.01	0.69	0.26	-0.40	0.66	0.70
Seahorse Glc max	0.09	0.37	-0.48	0.12	-0.32	0.69	-0.14	0.99	1	0.97	0.95	0.56	0.85	0.33	0.98	0.19	0.40	-0.06	0.06	-0.05	0.67	0.23	-0.29	0.74	0.77
Seahorse Pyr basal	-0.06	0.33	-0.56	0.00	-0.24	0.50	-0.28	0.97	0.97	1	0.97	0.53	0.86	0.30	0.97	0.27	0.31	-0.16	0.05	0.09	0.68	0.30	-0.41	0.60	0.65
Seahorse Pyr max	-0.10	0.26	-0.68	0.06	-0.22	0.54	-0.17	0.93	0.95	0.97	1	0.59	0.87	0.38	0.92	0.39	0.38	-0.09	0.09	0.10	0.62	0.20	-0.22	0.68	0.70
Seahorse ECAR basal	-0.03	0.44	-0.14	0.09	-0.37	0.62	-0.08	0.52	0.56	0.53	0.59	1	0.84	0.97	0.49	0.47	0.09	0.36	0.33	-0.36	0.36	-0.13	0.13	0.21	0.20
Seahorse ECAR max	-0.01	0.26	-0.40	-0.15	-0.34	0.58	-0.10	0.85	0.85	0.86	0.87	0.84	1	0.68	0.83	0.51	0.21	0.25	0.25	0.00	0.51	-0.02	-0.15	0.43	0.42
GlycoATP production	-0.07	0.39	-0.03	0.09	-0.33	0.50	-0.04	0.28	0.33	0.30	0.38	0.97	0.68	1	0.24	0.48	-0.02	0.43	0.36	-0.41	0.20	-0.23	0.27	0.03	0.01
mitoATP production	0.14	0.34	-0.41	0.02	-0.29	0.63	-0.19	1.00	0.98	0.97	0.92	0.49	0.83	0.24	1	0.15	0.37	-0.06	0.04	0.01	0.69	0.27	-0.41	0.66	0.71
ATP	-0.30	-0.38	-0.62	-0.26	-0.01	0.03	0.29	0.18	0.19	0.27	0.39	0.47	0.51	0.48	0.15	1	0.32	0.36	-0.09	0.40	0.00	-0.29	0.27	0.14	0.07
NAD+	0.47	0.07	-0.36	0.55	0.32	0.56	0.12	0.37	0.40	0.31	0.38	0.09	0.21	-0.02	0.37	0.32	1	0.15	-0.45	-0.20	0.60	0.36	-0.04	0.67	0.78
NADH	0.57	-0.35	0.22	-0.29	0.14	0.37	0.48	-0.05	-0.06	-0.16	-0.09	0.36	0.25	0.43	-0.06	0.36	0.15	1	0.53	-0.07	-0.19	-0.58	0.50	0.06	-0.06
DANN methylation	0.17	-0.11	0.11	-0.37	0.03	0.16	0.07	0.04	0.06	0.05	0.09	0.33	0.25	0.36	0.04	-0.09	-0.45	0.53	1	0.01	-0.27	-0.51	0.41	-0.02	-0.15
Cilia length	-0.46	-0.81	-0.55	-0.76	0.04	-0.59	0.30	-0.01	-0.05	0.09	0.10	-0.36	0.00	-0.41	0.01	0.40	-0.20	-0.07	0.01	1	-0.43	-0.34	0.02	-0.03	-0.18
Cilia fraction	0.33	0.68	-0.14	0.52	0.21	0.54	-0.63	0.69	0.67	0.68	0.62	0.36	0.51	0.20	0.69	0.00	0.60	-0.19	-0.27	-0.43	1	0.80	-0.64	0.37	0.62
%RBFOX3	0.12	0.63	0.02	0.54	0.40	0.03	-0.82	0.26	0.23	0.30	0.20	-0.13	-0.02	-0.23	0.27	-0.29	0.36	-0.58	-0.51	-0.34	0.80	1	-0.80	-0.01	0.28
%TH	-0.05	-0.44	-0.13	0.00	-0.14	0.12	0.75	-0.40	-0.29	-0.41	-0.22	0.13	-0.15	0.27	-0.41	0.27	-0.04	0.50	0.41	0.02	-0.64	-0.80	1	0.19	-0.03
nf Gli3-FL	0.27	0.01	-0.56	0.34	-0.17	0.72	0.35	0.66	0.74	0.60	0.68	0.21	0.43	0.03	0.66	0.14	0.67	0.06	-0.02	-0.03	0.37	-0.01	0.19	1	0.95
nf Gli3-R	0.33	0.22	-0.50	0.52	-0.02	0.73	0.09	0.70	0.77	0.65	0.70	0.20	0.42	0.01	0.71	0.07	0.78	-0.06	-0.15	-0.18	0.62	0.28	-0.03	0.95	1

Table 22 | Multiple factor analysis. Squared cosine and coordinates of the top 20 variables per dimension.

Variables	squared cosine (cos2)		coordinates (coord)	
	Dimension 1	Dimension 2	Dimension 1	Dimension 2
fumarate	0.82	0.06	-0.91	0.25
Seahorse Glc max	0.8	0	-0.9	-0.03
beta-alanine	0.8	0.06	-0.9	0.25
malate	0.8	0.07	-0.9	0.26
TMEM160	0.8	0.01	0.89	0.08
Seahorse Glc basal	0.79	0.01	-0.89	-0.08
HPS1	0.79	0	0.89	0.06
1-(1-enyl-palmitoyl)-2-oleoyl-GPE (P-16:0/18:1)*	0.78	0.06	-0.88	0.24
mitoATP production	0.76	0	-0.87	0.04
5-oxoproline	0.76	0.06	-0.87	0.25
1-stearoyl-2-arachidonoyl-GPI (18:0/20:4)	0.74	0.12	-0.86	0.35
PEX13	0.74	0.01	0.86	0.09
2-hydroxybutyrate/2-hydroxyisobutyrate	0.73	0.09	-0.85	0.3
methylmalonate (MMA)	0.73	0.03	-0.86	0.18
1-palmitoyl-2-stearoyl-GPC (16:0/18:0)	0.72	0.15	-0.85	0.39
1-palmitoyl-2-oleoyl-GPC (16:0/18:1)	0.72	0.19	-0.85	0.44
methylsuccinate	0.72	0.04	-0.85	0.21
HNRNPM	0.72	0	0.85	0
3-hydroxyisobutyrate	0.71	0.09	-0.84	0.3
FKBP7	0.71	0.03	0.84	0.16
GRIA4	0	0.94	-0.03	-0.97
MAN1A2	0.03	0.89	-0.19	-0.94
EBNA1BP2	0.01	0.88	0.11	0.94
HIRA	0	0.88	0.01	-0.94
EIF3L	0	0.87	-0.04	0.93
NDUFB2	0.01	0.85	0.11	-0.92
VANGL2	0	0.85	0.06	-0.92
HDDC3	0	0.85	-0.01	0.92
PIN1	0.06	0.84	0.25	0.92
QKI	0.05	0.84	-0.23	-0.92
PJA1	0.03	0.84	-0.16	0.92
TK1	0.02	0.84	0.12	0.92
RPLP0	0.05	0.83	0.23	0.91
PPP4C	0.04	0.83	0.19	0.91
UFM1	0.02	0.83	0.15	0.91
EMP3	0	0.83	-0.04	0.91
CRABP2	0.13	0.82	0.36	0.9
TRMT112	0.07	0.82	0.25	0.91
STX10	0.02	0.82	0.14	0.9
RAN	0.01	0.82	0.12	0.9

List of Figures

List of Tables

Acronyms

2-DG	2-deoxyglucose
5-hmC	5-hydroxymethylcytosine
5-mC	5-methylcytosine
8-oxoG	8-oxo-7,8-dihydroguanine
AA	antimycin a
AD	autosomal dominant
ADP	adenosine diphosphate
ALS	Amyotrophic lateral sclerosis
AMB	ambiguous cell
AMP	adenosine monophosphate
ANOVA	analysis of variance
AP	abasic site
Apop.	apoptotic
AR	autosomal recessive
ATP	adenosine triphosphate
BAF	B-allele frequency
BBB	blood-brain-barrier
BBS	Bardet-Biedl syndrome
bp	base pair(s)
BSA	bovine serum albumin
CCT	Chaperonin Containing TCP1 Subunit
cDNA	complementary DNA
cf	cytoplasmic fraction
CNV	copy number variation
CO_2	carbon dioxide
CoA	Coenzyme A
CpA	cytosine-adenine dinucleotide
CpG	cytosine-guanine dinucleotide
CRISPR	clustered regularly interspaced short palindromic repeats
ct	threshold cycle
Ctrl	control
Cyc	cyclopamine
Cyt c	cytochrome c
DAn	dopaminergic neuron
dbcAMP	dibutyryl cyclic adenosine monophosphate
DEG	differentially expressed gene
DMEM	Dulbecco's Modified Eagle Medium
DNA	deoxyribonucleic acid
EB	embyoid body
ECAR	extracellular acidification rate
ECL	electrochemiluminescence
EDTA	ethylenediaminetetraacetic acid
EdU	5-ethynyl-2´-deoxyuridine
eQTL	expression quantitative trait loci
ER	endoplasmatic reticulum
ESI	electrospray ionization
ETC	electron transport chain

FA	formic acid
$FAD/FADH_2$	flavin adenine dinucleotide
FBS	fetal bovine serum
fc	fold change
FC	fold change
FCCP	carbonyl cyanide-4-(trifluoromethoxy)phenylhydrazone
FDR	false discovery rate
FP	floor plate
fPD	familial Parkinson's disease
G0	gap 0
G1	gap 1
G2	gap 2
G2M	gap 2, mitosis
GABA	γ-aminobutric acid
GABA	gamma-aminobutyric acid
gDNA	genomic DNA
GDP	guanosine diphosphate
Glc	glucose
GLI	glioma-Associated Oncogene
GLI3-FL	GLI3 full length
GLI3-R	GLI3 repressor
glycoATP	glycolytic ATP
GO	gene ontology
GPCR	G-protein coupled receptor
GRCh37	Genome Reference Consortium Human Build 37
GTP	guanosine-5'-triphosphate
GWAS	genome-wide association studies
H^+	proton
H^2O	water
H3K16ac	acetylation at the 16th lysine residue of the histone H3
H3K20me3	tri-methylation at the 20th lysine residue of the histone H3
H3K27	27th lysine residue of the histone H3
H3K27ac	acetylation at the 27th lysine residue of the histone H3
H3K27me3	tri-methylation at the 27th lysine residue of the histone H3
H3K4	4th lysine residue of the histone H3
H3K4me3	tri-methylation at the 4th lysine residue of the histone H3
H3K79me2	di-methylation at the 79th lysine residue of the histone H3
H3K9	9th lysine residue of the histone H3
H3K9me	methylation at the 9th lysine residue of the histone H3
H3K9me2	di-methylation at the 9th lysine residue of the histone H3
H3K9me3	tri-methylation at the 9th lysine residue of the histone H3
HGPS	Hutchinson-Gilford progeria syndrome
HILIC	hydrophilic interaction chromatography
hiPSC	human induced pluripotent stem cell
hNPC	human neuronal precursor cell
hp	high-passage
HVG	highly variable gene
ID	identifier
IFT	intraflagellar transport
IMM	inner mitochondrial membrane
IMS	intermembrane space

iPSC	induced pluripotent stem cell
IsO	IsO
KNN	k-mearest neighbor
ko	knock-out
kp	kilo base pair(s)
LAP	lamina associated protein
LAP2α	lamina-associated polypeptide 2alpha
LB	Lewy bodies
L-DOPA	levodopa
lp	low-passage
LRR	log2 R ratios
M	male
MAF	minor allele frequency
MAO-A	Monoamine oxidase A (MAOA)
MAO-B	Monoamine oxidase B (MAOB)
mBP	midbrain basal plate
MFA	multiple factor analysis
mFP	midbrain floor plate
MHB	midbrain-hindbrain boundary
mitoATP	mitochondrial ATP
MMP	mitochondrial membrane potential
MNN	mutual nearest neighbor
MPP+	1-methyl-4-phenylpyridinium
MPTP	1-methyl-4-phenyl-1,2,3,6-tetrahydropyridine
mRNA	messenger RNA
MS/MS	tandem mass spectrometry
mt	mitochondia
mtDNA	mitochondrial DNA
NAD^+/NADH	nicotinamide adenine dinucleotide
NADPH	nicotinamide adenine dinucleotide phosphate
NCSC	neural crest stem cell
nf	nuclear fraction
noCC data	data after regressing out cell cycle effects
NPC	neuronal precursor cell
NSC	neural stem cell
O_2	oxygen
OCR	oxygen consumption rate
OH-	hydroxide
Olig	oligomycin
OMM	outer mitochondrial membrane
OXPHOS	oxidative phosphorylation
PBS	phosphate buffered saline
PC	primary cilium/cilia
PC1	principal component 1
PC2	principal component 2
PCA	principal component analysis
PCR	polymerase chain reaction
PD	Parkinson's disease
PFA	paraformaldehyde
PFPA	perfluoropentanoic acid
pH	potential of hydrogen

P_i	phosphate group
PPP	pentose phosphate pathway
Pyr	pyruvate
Q	ubiquinone
QC	quality control
qPCR	quantitative PCR
Q-Q plot	quantile-quantile plot
RBD	REM-sleep-behavior-disorder
REM	Rapid eye movement
RG	radial glia
RIPA	radioimmunoprecipitation assay buffer
RNA	ribonucleic acid
ROS	reactive oxygen species
Rot	rotenone
rRNA	ribosomal RNA
RT-qPCR	quantitative PCR with reverse transcription
S	synthesis
scRNA-seq	single-cell RNA sequencing
SDS	sodium dodecyl sulfate
SEM	standard error of the mean
SN	substantia nigra
SNP	single-nucleotide polymorphism
SNpc	substantia nigra pars compacta
sPD	sporadic Parkinson's disease
SPF	specific pathogen-free
T	thymine
T/S	telomere to single copy gene ratio
TALEN	transcription activator-like effector nucleases
TBS	Tris-buffered saline
TCA	trichloroacetic acid
TpG	thymine-guanine dinucleotide
TRiC	TCP1 Ring Complex
tRNA	transfer RNA
UMAP	uniform manifold approximation and projection
UMI	unique molecular identifier
UPLC-MS/MS	ultra performance liquid chromatography - tandem mass spectrometer
UPS	ubiquitin-proteasome system
yH2A.X	phosphorylated form of histone H2A.X

Acknowledgements

Als Erstes möchte ich mich bei Prof. Wolfgang Wurst und Dr. Daniela Vogt Weisenhorn für die Möglichkeit bedanken, meine Doktorarbeit am IDG zu absolvieren. Vielen Dank euch beiden für die tolle Betreuung und die unzähligen, meist fachlichen Diskussionen. Besonderen Dank auch an Daniela für deine Unterstützung, dein Verständnis und dein offenes Ohr während den letzten Jahren!

Danke auch an den vielbeschäftigten Dr. Florian Giesert, der sich trotz Stress immer die Zeit genommen hat mir zu helfen.

Ebenfalls bedanken möchte ich mich bei meinen Thesis Committee Mitgliedern Prof. Heiko Lickert und Dr. Julia Fuchs für ihre Unterstützung, ihren Input während der jährlichen Treffen und die gute Zusammenarbeit.

Einen großen Dank an Dr. Dietrich Trümbach und Dr. Malte Lücken für eine angenehme und produktive Zusammenarbeit. Danke euch beiden für eure großartige Hilfe und Unterstützung!

In diesem Sinn möchte ich mich auch bei Dr. Anika Böttcher, Dr. Anna Artati und Daniel Lamp für die tollen Kollaborationen bedanken.

Danke an meine Bürokollegen Petra, Constantin, Artem, Kristina und Sina dafür das ihr die herausfordernden Zeiten der letzten Jahre in schöne und lustige Momente verwandelt habt. Besonderen Dank auch an Consti für deine Betreuung in den ersten Monaten!

Ein besonderes Dankeschön an Annerose Kurz-Drexler, Tanja Orschmann und Susanne Badeke für eure tatkräftige Unterstützung, und eine lustige Zeit in der Zellkultur.

Besonderen Dank auch an Letyfee Steinert, Nicole Wenck und Klaus Pflügler. Es war mir eine Ehre euch während euren Masterarbeiten zu begleiten und zu unterstützen. Zum Glück konnte man euch immer mit Schokolade bestechen, und der angedrohte Arbeitsstreik konnte abgewendet werden :) Es war eine wunderschöne Zeit! Ich wünsche euch nur das Beste für eure Zukunft, wissenschaftlich und privat!

Großen Dank auch an meine Freunde, auf die ich mich immer verlassen kann! Insbesondere an Christian, Daniel, Florian, Isabel und Michael für unzählige lustige und aufmunternde Erinnerungen!

Das Beste an meiner Doktorarbeit allerdings war, dass ich Sina gefunden habe. Danke das du immer für mich da bist und dir tapfer mein Gejammer anhörst. Danke das du der kleine Engelchen auf meiner rechten Schulter bist, der mich antreibt und immer in die richtige Richtung bugsiert :D

Zuletzt möchte ich meiner Familie danken, meiner Schwester Verena, meinen Großeltern Michael, Crescentia und Erna und vor allem meinen Eltern Manfred und Christa. Danke, dass ihr keine Mühen gescheut habt, um mir alles zu ermöglichen. Ohne euch wäre all das nicht möglich gewesen. Danke für all die Liebe und Unterstützung!

Danke!